PHYSIOLOGICAL MRI FOR NEUROPHARMACOLOGICAL AND
ADVANCED CEREBRAL HAEMODYNAMIC STUDIES

REBECCA SUSAN DEWEY MPhys (Hons)

Thesis submitted to The University of Nottingham
for the degree of Doctor of Philosophy

JULY 2012

Abstract

This thesis investigates the application of physiological measures made using magnetic resonance imaging (MRI) to study cerebral haemodynamics and pharmacological modulation of brain activity. In particular, this thesis has an emphasis on the technical developments of Arterial Spin Labelling (ASL), and their applications in neuroimaging.

Blood Oxygen Level Dependent (BOLD) fMRI methods, together with ASL, were applied to a pharmacological study of the effect of beta-blockers on the brain's response to emotional visual stimuli, ASL being performed for improved quantitative understanding. The study aimed to test the James-Lange theory, which states that emotions result from the perception of bodily arousal. Autonomic nervous system responses to emotional stimuli can be predicted by the level of activity in the limbic system (including amygdala, brainstem and salience network), and previous studies have demonstrated reduced amygdala response to emotional memory encoding and retrieval under the influence of centrally acting beta-blockade. However, this modulation may be a direct central effect. To disentangle these possible confounds, this thesis assesses the action of the peripherally acting beta-blocker, nadolol, on the fMRI response to neutral, pleasant and unpleasant visual stimuli, and during rest; the hypothesis being that nadolol suppresses the neuronal response to emotional stimuli in comparison to neutral stimuli. BOLD and ASL contrasts were exploited for the application of pharmacological functional MRI at 3 T. 80 mg nadolol and placebo tablets were administered to twenty healthy subjects in a double blinded, randomised, placebo controlled crossover design. In addition, resting state perfusion was assessed for drug induced changes, and resting state BOLD for beta-blocker modulation of resting state functional connectivity. Drug induced reduction in insula response to emotional stimuli supports results from previously published studies, and the James-Lange theory. The preliminary finding of drug induced increase in amygdala response is contradictory.

ASL methods were applied to the techniques of Territorial ASL (TASL) and multi-phase ASL for advanced investigation of the vascular territories, and quantitative perfusion and blood transit times. Territorial ASL and multi-phase ASL were first implemented and optimised for use at 3 T during the course of a pilot study. Further, TASL and multi-phase ASL were used in combination for the assessment of the location and haemodynamic properties of the cerebral watershed regions. Watershed region masks formed from the combined assessment of TASL and multi-phase ASL exhibited reduced perfusion and lengthened transit times compared to other cortical regions. Each technique in isolation provided approximate location of watershed regions, while the accuracy of the two techniques was shown to be enhanced by their combined use. Furthermore, territorial ASL is developed and implemented at 7 T. Alternative labelling schemes were compared and parameters optimised for control condition efficiency, and TASL assessment was performed in three healthy volunteers. The benefits of this preliminary study at ultra-high magnetic field strength were discussed, along with the challenges still to be overcome.

List of accepted conference abstracts

1.   Dewey RS, Pollatos O, Hosseini AA, Francis ST, Auer DP. Does neural processing of emotional stimuli depend on bodily arousal? British Chapter Intl. Soc. Mag. Reson. Med. (2011).

2.   Dewey RS, Auer DP, Francis ST. Territorial Arterial Spin Labelling at 7T using PICORE. . Intl. Soc. Mag. Reson. Med. (2011).

3.   Dewey RS, Auer DP, Francis ST. Haemodynamic characterisation of cerebral arterial watershed regions using Arterial Spin Labelling. Proceedings BSNR Annual Conference, Paper 3.2 (2010).

4.   Dewey RS, Auer DP, Francis ST. Feasibility of Territorial Arterial Spin Labelling at 7T. British Chapter Intl. Soc. Mag. Reson. Med. (2010).

5.   Dewey RS, Auer DP, Francis ST. Combined assessment of vascular territories and haemodynamic parameter maps. Intl. Soc. Mag. Reson. Med. (2010).

6.   Dewey RS, Steward C, Koumellis P, Alexakis C, Auer DP. Caffeine Modulation of Breath-Hold Neurovascular Response using phMRI. Neuroradiology (Proceedings BSNR Annual Conference) 52:421–440, Paper 5.34 (2010).

7.   Dewey RS, Steward C, Koumellis P, Alexakis H, Auer DP. On the importance of placebo-control in studying caffeine-induced modulation of BOLD signal changes. British Chapter Intl. Soc. Mag. Reson. Med. (2009).

Acknowledgements

Contents

1   Introduction

People have always yearned to understand the processes that happen inside the body and, until the last century, the only way to do that was by dissection. The discovery of x-rays led to advances in medical imaging but it was later found that substantial exposure to x-rays was harmful. Early medical imaging used techniques derived from the introduction of an ionising radiation emitting contrast agent [1]. Contemporary medical imaging methods include positron emission tomography (PET), computed tomography of x-rays (CT) and single-photon emission computed tomography (SPECT), which still depend on ionising radiation, thus care must be taken with long term exposure. The technique of nuclear magnetic resonance (NMR) was first developed for observing nuclei in a thin gaseous state in 1938 [2] and further modified for the study of nuclei in other materials in 1946 [3]. Magnetic Resonance Imaging (MRI) is non-invasive and has not been shown to cause any long term side effects, and thus is deemed safe.

Early advances in magnetic resonance imaging (MRI), demonstrated that it was possible to acquire an image of a slice through the body non-invasively, marking the advent of high speed imaging [4]. Today, MRI provides a non-invasive way of obtaining information about the internal structure of the body, allowing the identification of pathological tissue boundaries. Functional neuroimaging is an advancing field that allows us to study processes such as blood flow and neuronal activation using inferences about measurable parameters to quantify changes over time. It is now possible to observe patterns of regional changes in deoxygenated haemoglobin and cerebral perfusion that are associated with neuronal activity. This is used to determine which areas of the brain are activated by the external application of a stimulus or by performing a task. Blood flow in the brain can be measured quantitatively using endogenous contrast arterial spin labelling (ASL), which applies an inversion pulse to label inflowing blood to the brain, and images the blood as it is perfused into the tissue. Further, it is possible to observe modulations in patterns measured using blood oxygen level dependent contrast (BOLD) or ASL that are caused by pharmacological intervention or disease.

Many studies reported in the literature use MRI to study drug modulation of resting state BOLD or perfusion measurements or the neuronal response to a stimulus [5]. Magnetic resonance imaging now has broad applications in, for example, psychology, psychiatry, pharmacology and medicine.

MRI is commonly used for the investigation of complex brain function; one relevant example is to observe the processing of emotional stimuli. Further, MRI can be used to study the pharmacological modulation of such a neuronal process, thus allowing the testing of theories such as the James-Lange [6] and two factor [7] theories of emotion, as reported later in this thesis.

1.1   The scope of this thesis

The work presented in this thesis took place at the University of Nottingham between September 2008 and November 2011. During my time at the University of Nottingham, I have been affiliated with both the division of Radiological and Imaging Sciences (formerly the division of Academic Radiology), School of Clinical Sciences and the Sir Peter Mansfield Magnetic Resonance Centre (SPMMRC), School of Physics and Astronomy. The initial remit of the PhD funding was to study the pharmacological modulation of brain function and functional connectivity using advanced neuroimaging techniques, including functional magnetic resonance imaging (fMRI). During the course of my study, I have performed experiments on healthy adult volunteers using the non-invasive MRI methods of BOLD and ASL to gain information on resting perfusion and both resting and task-induced neuronal activity within the healthy human brain.

Chapter 2 of this thesis introduces the concepts in physics required to understand nuclear magnetic resonance and magnetic resonance imaging. Further, current state of the art technology is explained, including the source of image contrasts.

Chapter 3 introduces the relevant principles of neurophysiology and how these properties of the human brain can give additional sources of contrast, such as

blood oxygen level dependent (BOLD) contrast and arterial spin labelling (ASL). The techniques outlined in this chapter provide insight into processes occurring in the brain, such as cerebral perfusion, neuronal activity or functional connectivity between spatially disparate brain regions. Further, this chapter will explain the interpretation of images acquired using such techniques and outline the applications of these techniques.

Chapter 4 presents the methods and results from a study investigating the effect of the peripherally acting beta blocker, nadolol, on both the activity associated with an emotional visual stimulus task, and the functional connectivity during resting state. Study design, recruitment, data acquisition, processing, analysis, results and their interpretation are described in this chapter. The aims of this chapter are:

- To determine whether nadolol modulates activity in brain regions within the salience network during the presentation of emotional visual stimuli;
- To determine whether any drug induced differences in activity are specific to the valence of the stimulus (pleasant or unpleasant);
- To determine whether BOLD changes are associated with perfusion changes as measured using ASL;
- To determine whether nadolol modulates activity in regions not implicated in the salience network or the processing of emotional stimuli, indicative of a confound by direct central action of a beta-blocker;
- To determine whether there are changes in resting perfusion or resting functional connectivity in response to nadolol, which could explain the differences in response to stimuli, if found.

In Chapter 5, a study using Territorial Arterial Spin Labelling and multi-phase Arterial Spin Labelling at 3 T in healthy volunteers is described. The vascular territories associated with the major cerebral blood vessels are mapped and blood transit times and perfusion rates are considered. The methods of data

acquisition, processing, analysis and interpretation are described. Here, the experimental aims are:

- To acquire selective maps of the vascular territories of the internal carotid arteries and basilar artery and to define the vascular territory boundary of the anterior cerebral arteries;

- To compare the locations and boundaries of the watershed regions at a group level using the three different methods of territorial ASL, and arterial and tissue transit time maps;

- To assess transit time variance across a range of cortical areas, providing useful information for planning future ASL studies and for functional MRI studies using perfusion weighted contrast.

The development of territorial arterial spin labelling for use at ultra-high field (7 T) is described in Chapter 6. This involved optimising the techniques for use at 7 T. The advantages and challenges of applying such a technique at ultra-high field are discussed. The processes used in optimisation are described, along with results in healthy volunteers. The aim of this chapter is:

- To develop a technique for performing TASL at 7 T, and further to optimise this technique for assessment of vascular territories in healthy adults.

Chapter 7 provides a general discussion of the results obtained in this thesis, strengths and weaknesses of experimental design and implementation and concludes with a discussion of the impact of this work, and possibilities for future research in these areas.

References

1.   Dyson, NA. Characteristic X-rays-A Still Developing Subject. Phys. Med. Biol. 20(1):1-29 (1975).

2.   Rabi, II, Zacharias, JR, Millman, S, Kusch, P. A New Method of Measuring Nuclear Magnetic Moment. Physical Review, 53 (4): 318 (1938).

3.   Purcell, E. M., Torrey, H. C. and Pound, R. V. Resonance Absorption by Nuclear Magnetic Moments in a Solid. Physical Review, 69,37-38 (1946).

4.   Mansfield, P., Multi-planar image formation using NMR spin echoes. J. Phys. C: Solid State Phys. 10:L55-L58 (1977).

5.   Honey, G, Bullmore, E. Human pharmacological MRI. Trends in Pharmacological Sciences, 25(7):366-374 (2004).

6.   Fehr, FS, Stern, JA. Peripheral physiological variables and emotion: the James-Lange theory revisited. Psychol Bull, 74(6):411-24 (1970).

7.   Schachter, S. and Singer, J. E. Cognitive, social and physiological determinants of emotional states, Psychological Review, 69, 379-399 (1962).

2 NMR theory and Magnetic Resonance Imaging (MRI)

This chapter provides an overview of the nuclear magnetic resonance (NMR) theory and magnetic resonance imaging (MRI) techniques necessary to understand and reproduce the work presented in this thesis. The chapter begins with an explanation of the physics of nuclear magnetic resonance, which is followed by the specific physics of magnetic resonance imaging. Finally, this chapter will outline the different applications of magnetic resonance imaging used in this thesis, describing how images of different contrast are formed and interpreted.

2.1 The NMR signal

Nuclear magnetic resonance (NMR) refers to the behaviour of a nucleus or nuclei in the presence of a magnetic field. Principally, nuclei will absorb and re-emit energy in the form of electromagnetic (EM) radiation with specific properties. This phenomenon was first described by Isidor Rabi in 1938 in the paper titled "A New Method of Measuring Nuclear Magnetic Moment" [1]. Rabi was awarded the Nobel Prize in Physics in 1944 for results obtained in an experiment using an adaptation of Stern's molecular beam method to observe the magnetic properties of atomic nuclei in a thin gaseous state. A similar technique was developed by Bloch and Purcell in 1946 [2], which allowed the study of matter in other states without causing any disturbance to the composition of the sample, thus opening the technique up to much broader applications. Bloch and Purcell were jointly awarded the Nobel Prize in 1952 for their work.

2.1.1 The concept of spin

It is not just protons that are MR sensitive, but many nuclei with odd-numbered atomic mass, such as ^{13}C [3]. Currently, the vast majority of magnetic resonance imaging of the human body is acquired using hydrogen nucleus (proton) excitations. This is because the hydrogen nucleus is highly abundant in the human body (being present in every water molecule). It is

now possible to achieve nuclear magnetic resonance using a wide range of nuclei, including much heavier nuclei such as xenon, krypton and fluorine; however discussion of these experiments is not within the capacity of this thesis.

In quantum mechanics, an elementary particle is conventionally described in terms of the fundamental properties of charge, mass, spin (also known as intrinsic angular momentum) and spin quantum number. The simplest nucleus is that of a hydrogen atom; a single proton with charge (Q) 1.6×10^{-19} Coulombs, mass (m) 1.7×10^{-27} kg and spin (I) ½. The intrinsic spin quantum number is represented by I, where the magnitude of I is described by Eqn. [2.1]. A nucleus can also have orbital angular momentum, J. J and I are related thus; where ħ is h (Planck's constant) divided by 2π, as described in Eqn. [2.2]. I can take integral and half integral values as follows; for example hydrogen (^{1}H), I = ½, carbon-13 (^{13}C), I = ½, oxygen-17 (^{17}O), I = $^{5}/_{2}$.

$$I = \sqrt{I(I + 1)}$$ Eqn. [2.1]

$$|J| = \hbar\sqrt{I(I + 1)}$$ Eqn. [2.2]

When a magnetic field is applied, a particular spin quantum number, I, can take different spin states, m_I. I can take the discrete values $–I, (-I+1), ... , (I-1), I$. There are $(2I + 1)$ spin eigenstates (energy levels), each corresponding to a particular direction of spin [4].

The z component of the orbital angular momentum, J_z is a measurable quantity that represents the projection of the orbital angular momentum onto the axis of the intrinsic angular momentum. J_z is related to the spin quantum number, m_I as shown in Eqn. [2.3]. Therefore, for the proton of $m_I = \pm$½, $J_z = \pm$ ½ħ, as demonstrated in Figure 2.1.

$$J_z = \hbar m_I$$ Eqn. [2.3]
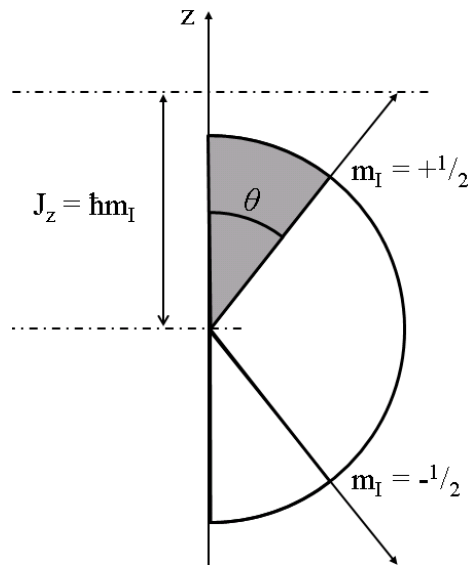
Figure 2.1: Orientation of the intrinsic angular momentum vector.

2.1.2 The magnetic dipole moment

A moving charge will generate a magnetic field. As the hydrogen nucleus, or proton, has a charge, and is rotating, it will generate a nuclear magnetic dipole moment, $\boldsymbol{\mu}$. $\boldsymbol{\mu}$ is proportional to the proton's orbital angular momentum, $\boldsymbol{J}$, where $\boldsymbol{\mu}$ and $\boldsymbol{J}$ are vectors:

$$\boldsymbol{\mu} = \gamma \boldsymbol{J}$$
Eqn. [2.4]

where γ refers to the gyromagnetic ratio, or magnetogyric ratio, of units rad s^{-1} T^{-1} or MHzT^{-1}. For a charge, q, of mass, m, in classical mechanics the gyromagnetic ratio is calculated as follows:

$$\gamma = \frac{q}{2m}$$
Eqn. [2.5]

In quantum mechanics, this is multiplied by the *g factor*, a dimensionless quantity that characterises the properties of that particular nucleus. For a proton, the *g factor* takes a value of approximately 5.585. Table 2.1 gives some example values of the gyromagnetic ratio for different nuclei [5].

Nucleus	Intrinsic Spin, I	γ (MHzT^{-1})
^{1}H	½	42.58
^{13}C	½	10.71
^{17}O	$^5/_2$	5.77
^{19}F	½	40.08
^{31}P	½	17.25

Table 2.1: Intrinsic spin quantum numbers and gyromagnetic ratio for nuclei [5].

In the presence of a static magnetic field (**B**$_0$), the magnetic moments will all align parallel or antiparallel to **B**$_0$. Therefore, the z-component of the orbital angular momentum of a proton in a **B**$_0$ field can take one of two values:

$$J_z = \pm \frac{\hbar}{2}$$

Eqn. [2.6]

In classical theory, this nucleus placed in a magnetic field, **B**$_0$, will have an energy represented by:

$$E = -\boldsymbol{\mu}.\boldsymbol{B_0}$$

Eqn. [2.7]

Combining with Eqn. [2.2] and Eqn. [2.3] gives:

$$E = -\boldsymbol{\mu_z}.\boldsymbol{B_0} = -\gamma \hbar m_I B_0$$

Eqn. [2.8]

There are two possible energy values corresponding to the two possible values of m_I ($\pm$½ for a proton); the nucleus can align parallel (taking the lower energy state) or antiparallel (higher energy state) with **B**$_0$. This splitting into multiple discrete energy states in the presence of a magnetic field is known as Zeeman splitting, with the two different energy levels for a proton taking the values $E_{1,2} = \pm$½$\gamma \hbar B_0$, and the difference between energy states being described by Eqn. [2.9] (see Figure 2.2 illustrating Zeeman splitting). NMR is concerned with inducing changes in the quantum state of a system by applying electromagnetic radiation. For transitions between the two states, we can use Planck's law that is equated to the energy, ΔE, to determine the frequency of the applied electromagnetic radiation:

$$\Delta E = \gamma \hbar B_0 = h\nu \qquad\qquad\qquad\qquad \text{Eqn. [2.9]}$$

where ν is the frequency of the electromagnetic radiation needed to move the proton from one spin state to another.
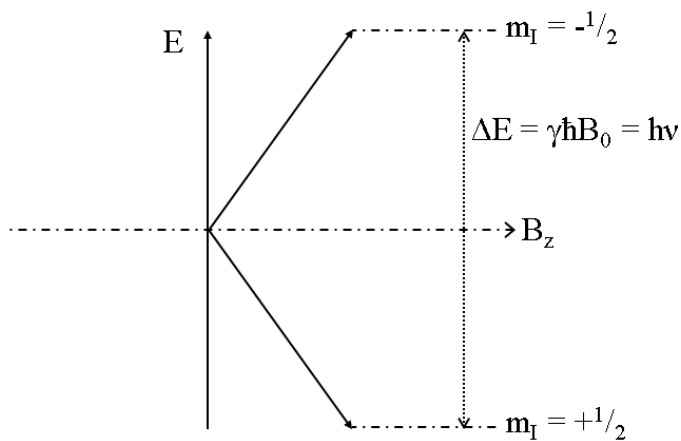
Figure 2.2: Illustration of Zeeman splitting caused by the presence of a static magnetic field along the B_z axis.

2.1.3   Precession of spins

Quantum theory dictates that the magnetic moments of the protons do not exactly align to the direction of the combined magnetic field, **B**, but that they precess about **B** at a frequency, ω (see Figure 2.3 illustrating precession).
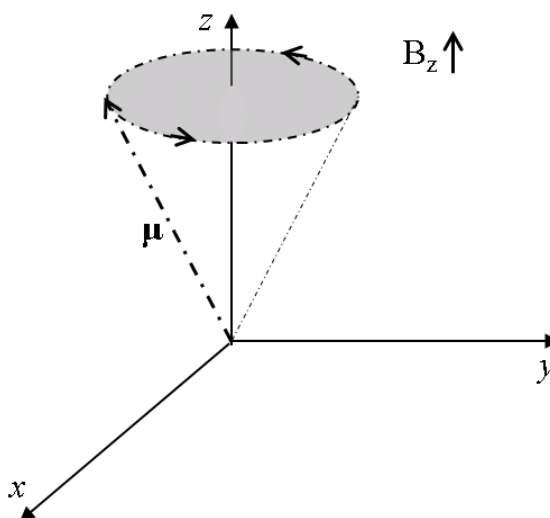
Figure 2.3: Precession of the magnetic moment vector about the axis of the static magnetic field, B_z.

A proton experiences a torque, $\boldsymbol{\tau}$, when placed in a magnetic field, equal to the rate of change of its orbital angular momentum ($\boldsymbol{J}$) with respect to time. In addition, the torque can also be expressed in terms of a vector product of the magnetic moment, $\boldsymbol{\mu}$, and the magnetic field, $\boldsymbol{B}$. These relationships are represented in Eqn. [2.10].

$$\boldsymbol{\tau} = \frac{d\boldsymbol{J}}{dt} = \boldsymbol{\mu} \times \boldsymbol{B} \qquad\qquad \text{Eqn. [2.10]}$$

Substituting Eqn. [2.4] for $\boldsymbol{\mu}$ into Eqn. [2.10] and rearranging gives a form of the Bloch equation, which describes how a magnetic moment behaves under the influence of a magnetic field. It holds true under the assumption that any changes in the orientation of the magnetic moment vector are caused by its interaction with an external magnetic field [5]:

$$\frac{d\boldsymbol{\mu}}{dt} = \gamma \boldsymbol{\mu} \times \boldsymbol{B} \qquad\qquad \text{Eqn. [2.11]}$$

2.1.4   Boltzmann Statistics

So far, this thesis has only described the behaviour of a single proton. However, it is more common to deal with the protons found in matter, for which the number of protons is of the order of Avogadro's number; 6.02×10^{23}. In quantum mechanics it is possible to explain the behaviour associated with NMR. This is acceptable for a single nucleus but becomes complicated when dealing with matter that contains several nuclei, each undergoing interactions with the magnetic field and with each other. Therefore it is usually appropriate to refer to a classical description of bulk magnetisation.

Boltzmann statistics can be used to predict the behaviour of many protons. By applying Boltzmann's methods to a system with a temperature above absolute zero, one can consider the net magnetisation as the sum of the magnetic moments in the sample. This is shown in Eqn. [2.12], where $N\uparrow$ is the number of protons in the lower energy state with magnetic moment parallel to B_0 and $N\downarrow$ is the number of protons in the higher energy state with magnetic moments

antiparallel to B_0. This ratio is dependent on the temperature of the sample, T, and Boltzmann's constant k_B:

$$\frac{N\downarrow}{N\uparrow} = e^{\frac{\Delta E}{k_B T}} = e^{-\frac{\gamma\hbar B_0}{k_B T}}$$

Eqn. [2.12]

The expression can be expanded using a power series which, if $\gamma\hbar B_0 << k_B T$ approximates to give Eqn. [2.13].

$$\frac{N\downarrow}{N\uparrow} \approx 1 + \frac{\gamma\hbar B_0}{k_B T}$$

Eqn. [2.13]

Further, the number of spins in the sample that result in NMR signal is determined by the fractional difference between the populations of the two states, as given in Eqn. [2.14], which is linearly dependent on the strength of the magnetic field, B_0. At a typical imaging field strength of 3 T, this fraction is approximately 3×10^{-6} (3 parts per million).

$$\frac{N\downarrow - N\uparrow}{N\uparrow} \approx \frac{\gamma\hbar B_0}{k_B T}$$

Eqn. [2.14]

At room temperature, the population difference between the two states is small, so the ratio given in Eqn. [2.14] will be small. However, the ratio is also dependent on ΔE, the energy difference between the two states. From Eqn. [2.9] it is clear that ΔE is proportional to B_0, the magnetic field strength – thus greater sensitivity is achieved at higher field strengths.

2.1.5   Bulk Magnetisation

To describe the effect of large numbers of protons in magnetic fields, we deal with a quantity known as the *bulk magnetisation*, **M**, which is the vector sum of all the magnetic moments of the constituent protons:

$$M_0 = \sum \mu$$

Eqn. [2.15]

Hence the Bloch equation can be modified to give the form of bulk magnetisation. The rate of change of bulk magnetisation can be described thus:

$$\frac{d\boldsymbol{M_0}}{dt} = \gamma \boldsymbol{M_0} \times \boldsymbol{B} \qquad \text{Eqn. [2.16]}$$

This states that the rate of precession increases linearly with the magnetic field strength, and also that the bulk magnetisation increases with magnetic field strength. Using Eqn. [2.4], and the concept of bulk magnetisation, the following equation can be deduced:

$$\boldsymbol{\omega} = \gamma \boldsymbol{B} \qquad \text{Eqn. [2.17]}$$

Substituting the above equation into the Bloch equation for bulk magnetisation gives:

$$\frac{d\boldsymbol{M_0}}{dt} = \boldsymbol{\omega} \times \boldsymbol{M_0} \qquad \text{Eqn. [2.18]}$$

2.1.6   Excitation

The energy level of protons in the sample can be manipulated by introducing a specific amount of energy in the form of electromagnetic radiation that matches the Zeeman splitting energy, ΔE. This is achieved by applying a pulse of an additional magnetic field of lower amplitude than B_0; this additional field is a non-static magnetic field that oscillates at the same precession frequency, in phase with the rotation of the nuclei within the sample. This oscillating magnetic field is referred to as a $\boldsymbol{B_1}$-field and can be described as a pulse of amplitude $B_1 = |\boldsymbol{B_1}|$ with its time dependence given in Eqn. [2.19].

$$B_1 = \begin{pmatrix} B_1 \cos\omega t \\ B_1 \sin\omega t \\ 0 \end{pmatrix} \qquad \text{Eqn. [2.19]}$$

As the frequency of this B_1-field (designed to be similar to the frequency of precession) is in the radiofrequency range, it is often described as a radiofrequency (RF) field and RF pulse. The amount of energy required to move protons from one energy state to another is proportional to the magnetic field strength, $\mathbf{B_0}$, as demonstrated in Eqn. [2.9], therefore while higher field strength provides greater sensitivity, it also causes an increase in the amount of energy required to excite protons from the lower to the higher state.

We can describe the frequency of the RF pulses needed to be absorbed from or emitted by a proton to make a transition from one energy state to another (see Eqn. [2.9]).

$$\nu = \frac{\Delta E}{\hbar} = \gamma B \qquad\qquad \text{Eqn. [2.20]}$$

The specific frequency that allows transitions is described as the *resonant frequency* of the system, hence the use of the term *magnetic resonance*, and is also referred to as the Larmor frequency, ω_L.

The application of the $\mathbf{B_1}$ field causes the magnetic moments to precess at angular frequency, ω, at an angle, θ, about the $\boldsymbol{B}$ vector. The total angular displacement effect of the magnetisation is dependent on the amplitude and duration of the applied B_1 pulse.

It is conventional to describe the effect of an applied B_1-field using a rotating frame of reference as opposed to the laboratory frame (x, y, z). In the laboratory frame, the spin precesses, whereas in the rotating frame (x', y', z), the spin and the $\mathbf{B_1}$ vector become stationary, with $\mathbf{B_1}$ pointing along the x' axis. The bulk magnetisation vector, $\mathbf{M_0}$, now appears to rotate about the $\mathbf{B_1}$ vector, as shown in Figure 2.4 (A). The rotating frame of reference thus vastly simplifies the mathematics required to understand the process of excitation. This is pictured in Figure 2.4 (B).
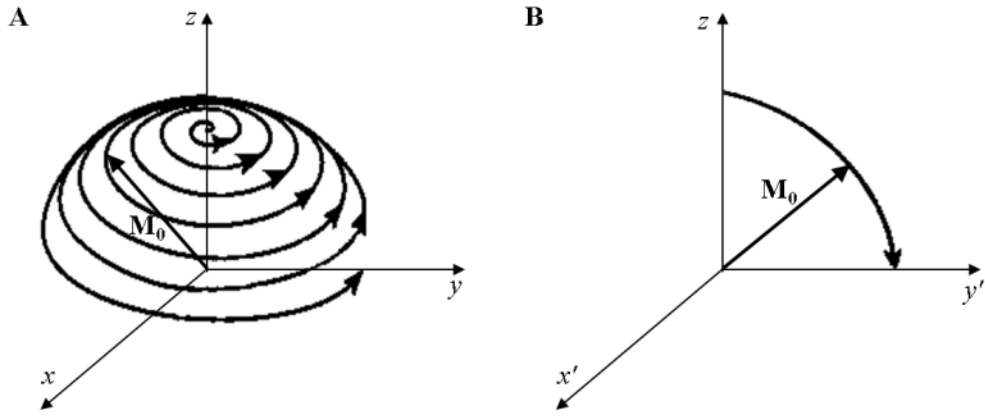
Figure 2.4: The motion of the bulk magnetisation vector, M_0, when influenced by a radiofrequency (B_1) pulse. The two diagrams represent the same motion in (A) the laboratory frame and (B) the rotating frame.

The angle by which the magnetic moment vector is displaced in the rotating frame of reference is now given by Eqn. [2.21].

$$\theta = \int_0^T \gamma B_1(t) dt$$ Eqn. [2.21]

where the additional pulse of B1 is applied for a given duration, T.

RF pulses are conventionally referred to by the angle through which they tip the bulk magnetisation, the "flip angle". For example, a pulse with a 90° flip angle refers to a B_1 pulse that displaces the bulk magnetisation by 90°. As shown in the Eqn. [2.21], this angle can be manipulated simply by controlling either the amplitude or the duration of the B_1 pulse. Sinc pulses are often used for this purpose as the Fourier transform of a sinc pulse gives a sharp profile.

2.1.7   Relaxation

Following the application of a B_1 RF pulse, the magnetisation vector, M_0, is displaced; the magnetisation precesses about the magnetic field vector and is in a non-equilibrium state. The perturbation will then decay as the spins relax back into their lower energy, or equilibrium state. The magnetisation at equilibrium (M_0) has a given z value (as described previously by Boltzmann

statistics) with random phase. The behaviour of relaxation is described mathematically by the Bloch equations and is called free induction decay (FID). This behaviour can be easier to visualise when separated into the two components in the rotating frame of reference; a *longitudinal* component, describing relaxation along the z axis, and a *transverse* component, describing relaxation in the xy-plane [6]. Relaxation curves are time (t) dependent and conventionally start from time, t = 0 s referring to the moment that the RF pulse ceases to be applied. The decay of the longitudinal magnetisation is due to interactions between the magnetic dipole moment and the thermal motion of nuclei within the lattice structure of the sample material (spin-lattice interactions), and is described by the longitudinal relaxation time constant, T_1. The transverse magnetisation decay is largely due to the magnetic dipole moments interacting with other magnetic dipole moments (spin-spin interactions), and the mathematics of this is dependent on the transverse relaxation time constant, T_2 or T_2* (see Section 2.1.7.2). T_1 and T_2 / T_2* relaxation processes are mutually independent. The Bloch equation given above for the time dependent change of bulk magnetisation can now be augmented with these time constants to give an equation representative of the FID (below). Figure 2.5 gives a graphical representation of these two types of exponential decay phenomena using values T_1 = 600 ms, T_2 = 100 ms and off-resonance frequency, $\Delta\omega$ = 10 Hz.

$$\frac{d\boldsymbol{M}}{dt} = \gamma \boldsymbol{M} \times \boldsymbol{B} - \begin{pmatrix} \boldsymbol{M}_{x\prime}/T_2 \\ \boldsymbol{M}_{y\prime}/T_2 \\ (\boldsymbol{M}_z - \boldsymbol{M_0})/T_1 \end{pmatrix} \qquad \text{Eqn. [2.22]}$$
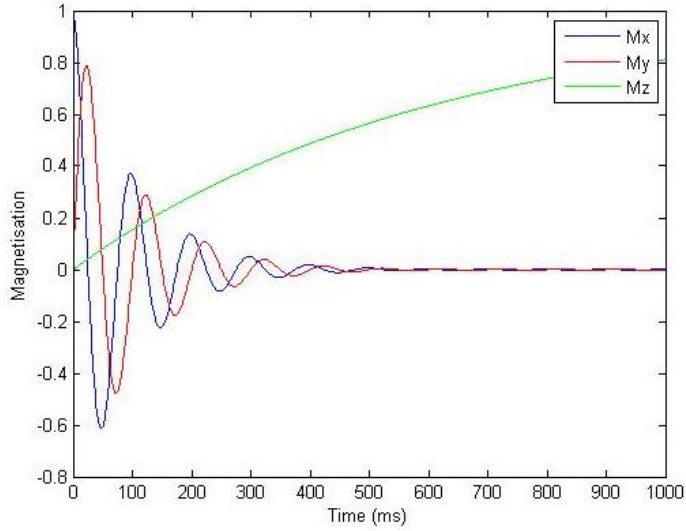
Figure 2.5: Simulation of free precession (relaxation) of magnetisation following excitation [7].

As suggested earlier in this chapter, relaxation causes the emission of electromagnetic radiation, Eqn. [2.9]. This induces a voltage in a radiofrequency coil through the principle of Faraday induction. In the case of the 90° pulse described earlier, the magnetisation is tipped into the transverse plane and a signal that oscillates at the Larmor frequency is emitted [8].

Relaxation is represented by an exponential function using the relaxation times T_1 and T_2 [5]. By looking at the rate of change of magnetisation with respect to time, we can derive a set of differential equations that describe the rate of change of the magnetisation vector over time. These are known as the Bloch equations [5], and are given below as three inter-dependent equations modelling the magnetisation in each Cartesian direction:

$$\frac{dM_x(t)}{dt} = \gamma \left(M_y(t)B_z(t) - M_z(t)B_y(t) \right) - \frac{M_x}{T_2}$$
$$\frac{dM_y(t)}{dt} = \gamma \left(M_z(t)B_x(t) - M_x(t)B_z(t) \right) - \frac{M_y}{T_2} \qquad \text{Eqn. [2.23]}$$
$$\frac{dM_z(t)}{dt} = \gamma \left(M_x(t)B_y(t) - M_y(t)B_x(t) \right) - \frac{(M_z(t) - M_0)}{T_1}$$

Terms can be added to the equations above, for example to account for the resonance offset and for the effects of flow, as outlined in Chapter 3.

The three dimensional vector for the magnetisation can then be rewritten in terms of components of transverse magnetisation, M_{xy}, and longitudinal magnetisation, M_z, as demonstrated in Eqn. [2.24].

$$M'_{xy} = M_{xy} e^{-\frac{t}{T_2}}$$
$$M'_z = M_0 - [M_0 - M_z] e^{-\frac{t}{T_1}}$$

Eqn. [2.24]

2.1.7.1   Longitudinal relaxation (T_1)

Longitudinal relaxation (i.e. the decay of the z component of the bulk magnetisation to return it to the equilibrium state after the application of a radiofrequency pulse in the rotating frame of reference), can be described by the following Bloch equation:

$$\frac{dM_z}{dt} = \frac{M_0 - M}{T_1}$$

Eqn. [2.25]

Two common imaging sequences that utilise T_1 contrast are saturation recovery and inversion recovery. A saturation recovery sequence uses a 90° pulse to tip the bulk magnetisation entirely into the transverse plane so that the z component of the magnetisation in the rotating frame of reference is saturated (nulled) and allowed to recover.

Inversion recovery inverts the bulk magnetisation so that the magnetic moments are antiparallel to their equilibrium position. Solving Eqn. [2.25] gives the following expression for the relaxation of the longitudinal relaxation following an inversion pulse, as shown in Figure 2.6.

$$M_z(t) = M_0 \left(1 - 2e^{-t/T_1} \right)$$

Eqn. [2.26]
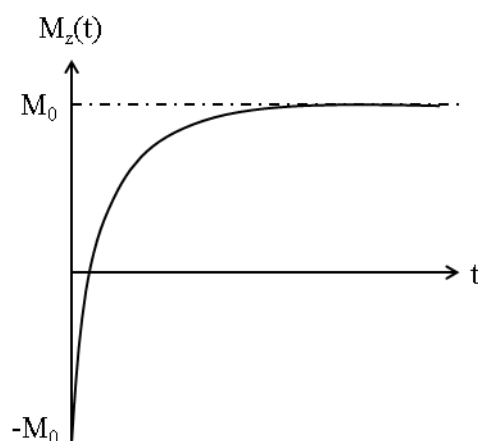
Figure 2.6: Relaxation curve of the longitudinal magnetisation following an inversion pulse, described by Eqn. [2.26].

T_1, the time constant of longitudinal relaxation varies as an intrinsic property of the material being imaged, depending on the interaction of the proton magnetic moments with the lattice of the material. For example it takes a value of approximately 1.6s in grey matter at 3T [9]. T_1 weighted contrast uses a short TE and short to intermediate TR. In these images, voxels with short T_1 relaxation times (e.g. white matter) are bright, and voxels with long T_1 relaxation times are dark (e.g. cerebrospinal fluid, CSF). This can be enhanced by using an inversion recovery sequence. To enhance image contrast even further, an exogenous paramagnetic ion, such as gadolinium, can be introduced into the imaging region. This significantly shortens the longitudinal relaxation time of any tissue that absorbs it and so is often used for clinical diagnostic imaging.

2.1.7.2   Transverse relaxation (T_2, T_2^*)

T_2 is the time constant of the decay of transverse magnetisation, and represents the decay of the proton magnetic dipoles that is caused by their interactions with each other (also known as dipole-dipole interactions). Like T_1, its relaxation curve is also derived by solving the Bloch equations for transverse magnetisation (Eqn. [2.27]), with the relaxation curve following a 90° pulse shown in Figure 2.7.

$$M_{xy}(t) = M_0 e^{-t/T_2}$$
<div align="right">Eqn. [2.27]</div>
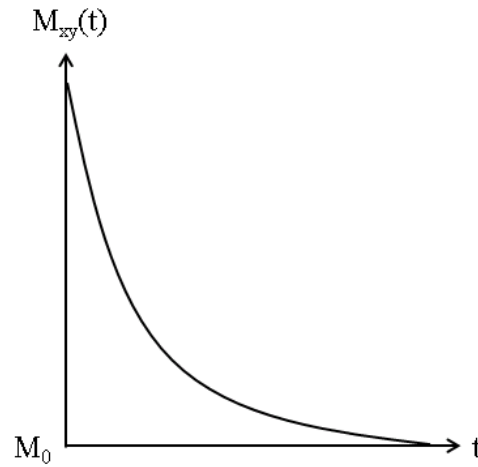
Figure 2.7: Relaxation curve of the transverse magnetisation, given in Eqn. [2.27].

However, spins are greatly affected by inhomogeneities in the external magnetic field which serve to further dephase the motion of the magnetic moments in the transverse plane, increasing the rate of decay. T_2^*, or effective T_2, is a time constant that accounts for the effects of these inhomogeneities, and is always less than T_2 itself. The relationship between T_2^* and T_2 is described in Eqn. [2.28], where T_2' is the correction that needs to be made to T_2 due to the dephasing effect caused by the external magnetic field inhomogeneities [6].

$$\frac{1}{T_2*} = \frac{1}{T_2} + \frac{1}{T_2'}$$
<div align="right">Eqn. [2.28]</div>

Both T_2 and T_2^* image contrast require sequences with a long repetition time (TR > T_1) and intermediate to long echo time. T_2-weighted images are typically acquired using a spin echo sequence, whereas T_2^*-weighted images are collected using a gradient echo sequence. In a T_2^* weighted image, voxels with short T_2^* relaxation times (e.g. those that contain iron) are dark and voxels with long T_2^* relaxation times (e.g. cerebrospinal fluid) are bright. T_2^* decreases with field strength, and this reduces the amount of time available in which to acquire a signal. T_2 weighted imaging is frequently used as a diagnostic method in brain MRI studies due to its high sensitivity to cerebral

pathology, such as tumours or arteriovenous malformations. Conversely, T_2^* weighted contrast is commonly used in functional MRI due to its sensitivity to blood oxygen level dependent (BOLD) contrast, which is associated with observing the haemodynamic response of brain tissue to neuronal activity, as described in Chapter 3.

2.1.8   Spin Echo

Magnetic dipole moments will naturally decay with random phase. In order to ensure that the magnetic dipole moments decay coherently, they must first be refocused, using an additional gradient or radiofrequency pulse after the excitation. The process of bringing the magnetic dipole moments back into phase is known as an *echo*. One form of an echo is the spin echo, whereby the excitation pulse is followed by a 180° refocusing pulse. This was first performed in 1950 using two consecutive 90° pulses [10]. Hahn's spin echo method was then improved by replacing the second of the two 90° pulses with a single 180° pulse [11]. Following the 90° excitation pulse, the bulk magnetisation vector decays freely for a time, t, after which the second pulse is applied. This causes the decaying bulk magnetisation vector to be rotated by 180°. Now further "decay" will result in accumulation of phase coherence rather than phase loss. After a further time, t, the bulk magnetisation will have returned to a coherent state, forming a spin echo [12]. Signal is acquired at this point in the free induction decay, as shown in Figure 2.8.
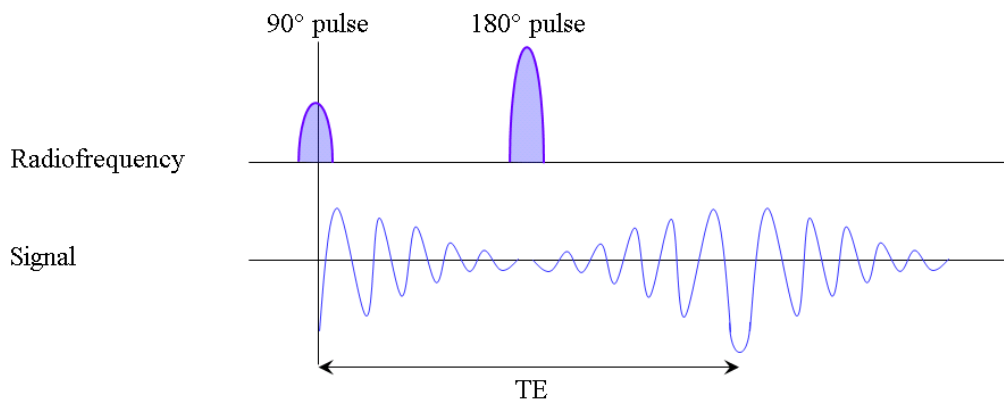
Figure 2.8: Diagram showing a basic spin echo sequence.

2.2   Physics of Magnetic Resonance Imaging

A magnetic resonance imaging scanner is a versatile instrument and can be used to create a wide variety of different image types that are adaptable to various purposes depending on the sequence, for example if speed of acquisition, sensitivity or insensitivity to specific materials or high resolution is required. The work presented in this thesis uses *gradient echo – echo planar imaging*, which is a fast two dimensional imaging technique where contrast is formed from the differences in $T_2{}^*$ of the material being imaged. This section outlines how pulse sequences are used to produce images with a wide variety of different types of contrast.

2.2.1   Gradient echo and encoding

In order to gain information from an array of adjacent, spatially distinct regions simultaneously, there needs to be a way to distinguish between the signals obtained from each voxel. For this purpose a combination of linear magnetic field gradients can be used to make the signal received from each voxel unique. The three schemes that are commonly used are slice selection, frequency encoding, and phase encoding [13], which are overviewed in the next sections. Linear gradients are applied using additional electromagnetic induction coils known as gradient coils. The direction and amplitude of the gradient is dependent on the direction and amplitude of the electric current flowing through the gradient coil, and the number of loops of wire in the coil. A gradient vector, *G(t)*, can be expressed in terms as the gradient derivative of the scalar field, B_z, and represented in three spatial dimensions, in units of millitesla per metre (mT/m):

$$\boldsymbol{G}(t) = \frac{\partial B_z(t)}{\partial x}\boldsymbol{i} + \frac{\partial B_z(t)}{\partial y}\boldsymbol{j} + \frac{\partial B_z(t)}{\partial z}\boldsymbol{k} \qquad\qquad \text{Eqn. [2.29]}$$

Gradients used on contemporary commercial systems have strength of the order 40 mT/m.

2.2.2 Slice selection

The application of an additional gradient simultaneous to the excitation pulse can be used to limit the effect of the radiofrequency pulse to exciting only those nuclei that rotate at a frequency within a given bandwidth, i.e. spatially confining the response of the system to a thin slab of the desired orientation. The thickness of the slice selected is inversely proportional to the gradient strength, stronger gradients allowing for thinner slabs of selective excitation [14]. The location of the slice can be manipulated by altering the central frequency and bandwidth ($\Delta\omega$) of the RF pulse, Figure 2.9. The relationship between the slice thickness and gradient strength are shown in Eqn. [2.30].

$$\Delta z = \frac{\Delta\omega}{\gamma G_z} \qquad\qquad \text{Eqn. [2.30]}$$
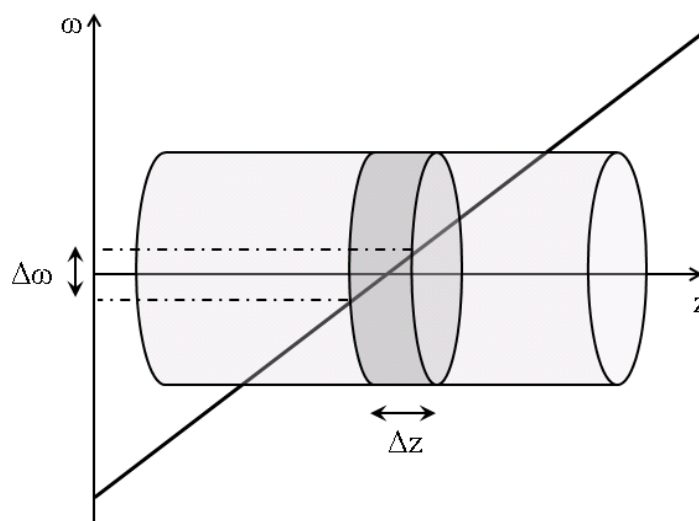
Figure 2.9: Application of a slice-selection gradient to selectively excite spins in the region Δz using a radiofrequency pulse of bandwidth Δω.

2.2.3 Phase encoding

Spatial location of a source of NMR signal may be gained from spatially varying the phase of the magnetisation. This requires the application of an additional gradient that introduces a spatially specific phase to the magnetic moments in that region dependent on their position along the axis of the phase

encoding gradient. Typically the phase encoding gradient, $\mathbf{G}_y$ is applied after the excitation pulse and before the readout gradient. If $\mathbf{G}_y$ is applied for duration, t, it will introduce a phase shift, Φ, given by Eqn. [2.31]:

$$\Phi = \gamma G_y yt \qquad\qquad \text{Eqn. [2.31]}$$

This describes the phase in terms of gradient strength, $G(t)$, duration, t, and displacement along the y axis. $G(t)$ is changed incrementally to allow sampling of additional lines in k-space (see Section 0). Figure 2.10 depicts an example of a 2 dimensional Fourier sequence, such as spin warp imaging.
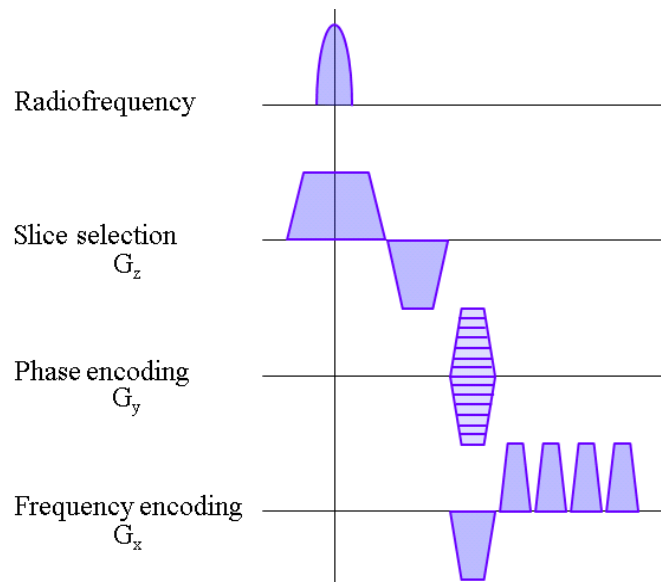
Figure 2.10: Pulse sequence showing phase encoding for a 2D Fourier sequence such as spin warp imaging. Frequency encoding is also shown (see Section 0).

2.2.4   Frequency encoding and k-space

Frequency encoding is a form of spatial encoding that uses the concept of frequency space (also known as k-space, using the symbol, k, to represent wavenumber). A frequency encoding gradient is applied following the phase encoding gradient, also shown in Figure 2.10. This manipulates the precession of the excited spins so that they will precess at a range of frequencies, dependent on the strength of the gradient. Spins in different regions of the gradient will absorb *and therefore radiate* at different frequencies. If several

voxels are excited at different frequencies then the received radiofrequency signal will be a function of the sum of several different frequencies. It was observed that taking the inverse Fourier transform of this signal will give the different frequencies at which signal is being received [15], which is equivalent to the locations of the signal sources. Therefore, there is an intrinsic relationship between frequency and gradient, which can be exploited to give a frequency dependent expression for the location of the signal source along a given axis. Moving the centre of the voxel by a distance Δx causes the magnetic field experienced at the centre of the voxel to change as shown in Eqn. [2.32], where in this case the vector x can take an arbitrary direction. This results in the change in angular frequency as expressed in Eqn. [2.33].

$$\Delta B_z = G \cdot \Delta x \qquad \text{Eqn. [2.32]}$$

$$\Delta \omega = \gamma G \cdot \Delta x \qquad \text{Eqn. [2.33]}$$

It is possible to transform these expressions into those that use the concept of wave number, k. The relationship between k and the wavelength λ is given in Eqn. [2.34].

$$k = \frac{2\pi}{\lambda} \qquad \text{Eqn. [2.34]}$$

If the signal, $S(t)$ received at a time, t, after the refocusing pulse, during the application of a gradient, is in the form of a free induction decay, then it can be treated as if it is a Fourier transform of the proton density function $\rho(r)$ at a vector r, i.e. $S(t) = \rho(k(t))$. Eqn. [2.35] shows the expression for the signal as it is recorded in real time, t.

$$S(t) = \int \rho(r) e^{i\gamma \int_0^t r \cdot G(t')dt'} \, dr \qquad \text{Eqn. [2.35]}$$

If the signal, $S(t)$, is to be a function of time, then $k(t')$ must also be a function of time, as it is a vector in Fourier transformed space (now known as k-space) and is dependent on the applied B_z and the gradient $G(t)$ as follows, where t' denotes time in the Fourier transformed domain:

$$k(t) = \gamma \int_0^t G(t')dt'$$

As Eqn. [2.35] is described as an inverse Fourier transform, then applying a Fourier transform gives the transform of the proton density function in terms of k:

$$S(k) = transform(\rho(k)) = \int \rho(r)e^{ik\cdot r}dr$$

Taking the inverse Fourier transform of this then gives the proton density function, thus:

$$\rho(r) = \int S(\boldsymbol{k})e^{-ik\cdot r}d\boldsymbol{r}$$

Therefore, by acquiring sufficient signals $S(t)$ at different frequencies, k-space can be sufficiently populated. Figure 2.11 shows the k-space trajectory for spin warp imaging. The arrow signifies the trajectory through k-space that sampling will take; i.e. the direction in which k-space is being sampled and the range of frequencies sampled.
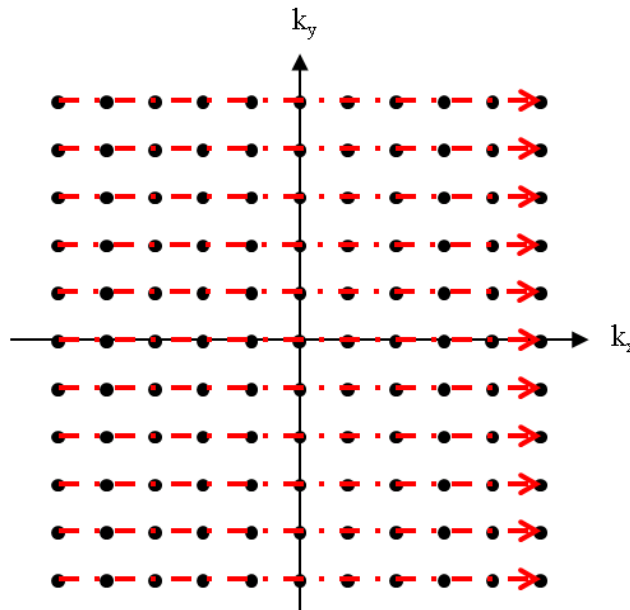
Figure 2.11: The k-space trajectory commonly used for spin warp imaging.

2.2.5 Echo planar imaging

Filling k-space as described in Section 0 will only encode one k-space line. Researchers at the University of Nottingham showed that all of k-space could be sampled after a single excitation pulse [16]. This was a great improvement on previous methods that only allowed for the equivalent of one line of k-space to be sampled following each individual radiofrequency excitation. Due to the sequence's high signal-to-noise ratio and sensitivity to transverse relaxation time and temporal resolution, this pulse scheme provides a good way of forming images weighted to blood oxygen level dependent contrast (BOLD), used for functional MRI (fMRI), which is discussed at length later in this thesis.
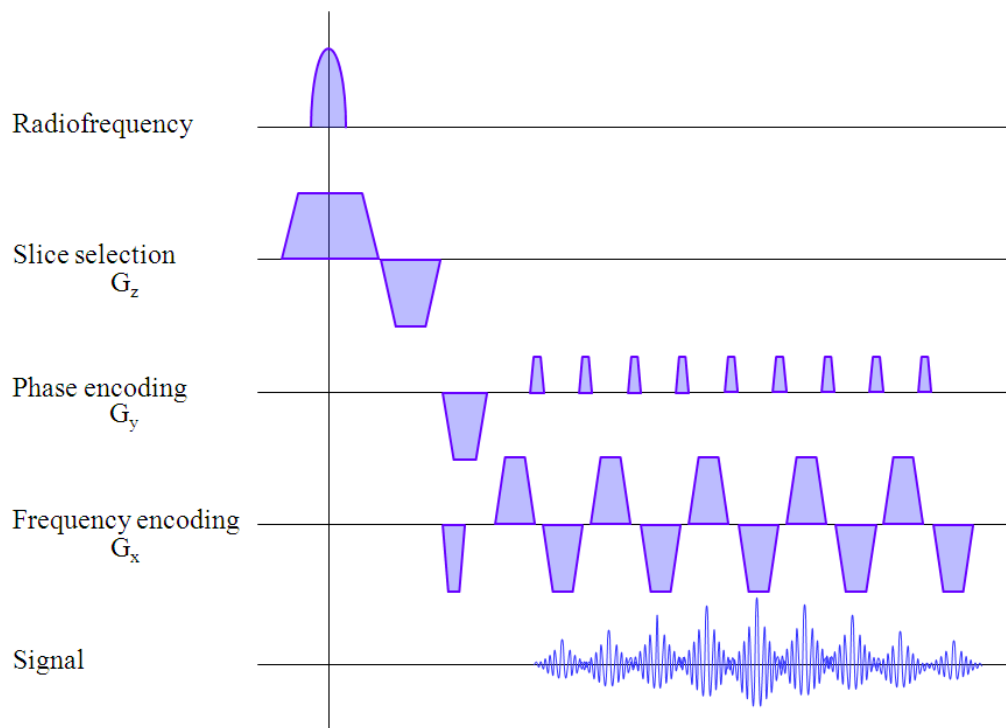
Figure 2.12: Pulse sequence diagram for the gradient echo – echo planar imaging acquisition. Note that the phase encoding and frequency encoding gradients correspond to the trajectory of k-space sampling shown in Figure 2.13.

The radiofrequency pulses and gradients used in a standard gradient echo – echo planar image acquisition are shown in Figure 2.12. The radiofrequency pulse and slice selection gradient facilitate the excitation of a slice. Immediately following this, two further short gradients, G_x and G_y align the

frequency and phase to the extreme edge of k-space prior to the start of measurement. Then, the first gradient echo in the echo train represents the sampling of k-space from $-k_x$ to 0 during the frequency encoding gradient, G_x. This is followed by a short phase encode gradient, G_y, and sampling progresses from 0 to $+k_x$ under another frequency encoding gradient, G_x of the opposite polarity. The next phase encode gradient, G_y, moves sampling incrementally up to the next line of k-space, (i.e. from k_y to $k_{y+\Delta y}$). The application of frequency and phase encoding gradients is repeated until the whole of k-space is sampled, as shown in Figure 2.13. As alternate lines of k-space are sampled in reverse (i.e. from $+k_x$ to $-k_x$ as opposed to from $-k_x$ to $+k_x$), the sampled data must be time-reversed on those lines before the data undergoes Fourier transform to form an image, as described earlier in this chapter.
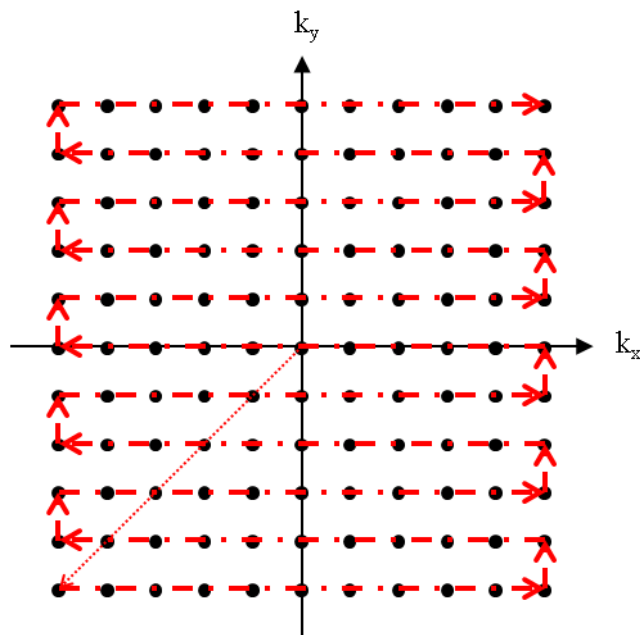
Figure 2.13: Schematic showing the trajectory under which k-space is sampled during echo planar imaging (Figure 2.12). Initial phase and frequency encoding gradients move the start of k-space to ($-k_{x,max}$,$-k_{y,max}$). Transition along horizontal lines is caused by the switching of frequency encoding gradients. Incremental vertical transitions are caused by phase encoding gradients.

Fourier transform mathematics can be time consuming for even a powerful computer to perform, and there are several Fast Fourier Transform algorithms

used in image reconstruction. For maximum efficiency of these methods, acquisition matrix sizes are confined to 2^n in each dimension.

2.2.6 Proton density image contrast

Chemicals present in the source tissue, e.g. proteins, will alter the proton density of the volume surrounding the resonating nuclei, changing the dynamics of the FID and thus change its magnitude. This provides the most basic contrast, proton density contrast. Here the bulk magnetisation of the sample is known and the applied gradient is optimised to elicit nuclear precession only in hydrogen nuclei. The signal produced by a voxel varies linearly with the concentration of hydrogen nuclei present; i.e. if the concentration of hydrogen nuclei in a sample is doubled, then the proton density signal also increases by a factor of two.

Proton density contrast is suitable for use in tissue that contains a high proportion of water and protein molecules as it provides a high signal-to-noise ratio, however the contrast-to-noise ratio is often limited as proton density is relatively uniform across different tissue types. Therefore, proton density contrast is often augmented by weighting it with a relaxation time contrast that provides greater differences between tissue types, as described in Sections 0 and 2.1.7.2.

2.2.7 Image artefacts

Magnetic resonance imaging is very sensitive to regional accuracy in the values of B_0 and B_1. While the types of artefact are wide ranging and numerous, outlined here are a few that are relevant to the techniques used in this thesis.

One artefact that is commonly seen in echo planar imaging is the Nyquist ghost, also known as N/2. As the direction of trajectory taken when sampling k-space is antiparallel for each consecutive line through k-space, alternate lines in k-space can have systematic sampling errors due to inhomogeneities.

This is manifest in a ghost of the image appearing overlaid on top of the real image, but shifted in the phase encoding direction by N/2. Solutions to this problem include the acquisition of an extra image where k-space is oppositely sampled in order to calculate phase correction.

Aliasing is where a copy of the image is wrapped back onto itself, and is caused by under-sampling of k-space. The Nyquist digital sampling theorem states that the highest frequency that can accurately be sampled to avoid aliasing, or the Nyquist frequency, f_N, is calculated using Eqn. [2.39], where f_s is the sampling frequency. To avoid aliasing, k-space should be sampled at a frequency equal to or greater than half the maximum frequency of the system.

$$f_N = \frac{f_s}{2}$$
<div style="text-align:right">Eqn. [2.39]</div>

Susceptibility occurs at tissue boundaries where adjacent tissue types have different magnetic properties. This causes inhomogeneities in the magnetic field in that area, resulting in phase changes. These effects are greater at high field strength, where field inhomogeneities are greater, for example at a tissue-air boundary, phase changes cause the data to be incorrectly sampled in k-space and ultimately results in signal drop-out and degradation of the signal-to-noise ratio. However, where the inhomogeneities, and thus the phase changes are more controlled, for example around blood vessel walls, the effect can be exploited to give susceptibility weighted contrast. In the extreme case, metal causes susceptibility artefacts across a wide portion of the images due to the magnetic field inhomogeneities caused by its presence.

At tissue boundaries between two different types of tissue, particularly fatty tissue interfaces, the difference in precession rates of the proton magnetic moments causes the frequency encoding of the signal to incur an error. This is known as chemical shift and is manifest as the two regions of tissue appearing spatially shifted relative to each other. A fat-water shift artefact is commonly removed by saturating either the water signal or the fat signal using a selective saturation pulse.

2.2.8   Beyond two dimensional EPI acquisition

Three dimensional echo planar imaging (3D-EPI) provides higher signal-to-noise ratio and allows higher resolution to be achieved in comparison to multi-slice imaging by virtue of the fact that data are acquired using an additional phase encoding gradient along the slice direction. This allows for signal to be collected from the entire volume, which is reconstructed using a 3D Fourier transform, instead of a 2D one. Despite the advantageous SNR increase, this lengthens the time required for a single acquisition, which can be problematic where temporal resolution is important.

2.3   Practical Magnetic Resonance Imaging

This section will outline the nuclear magnetic resonance (NMR) hardware. While the intricate details of scanner design vary from manufacturer to manufacturer, and can depend on the specialised purpose of the MR system, most scanners will have the same set of basic components; a large superconducting magnet, shim coils, gradient coils and coils for transmitting and receiving radiofrequency radiation, together with a high level of computing power. A simplified schematic of the entire system is given in Figure 2.14. This section will describe these main components.
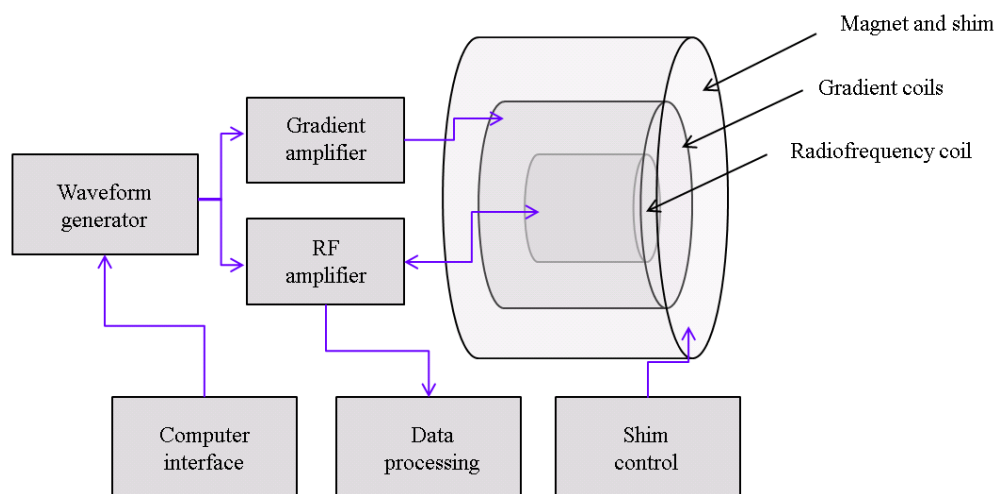
Figure 2.14: Simplified schematic of the components of a modern MR scanner.

Clinical systems used in hospitals typically operate at a static field of either 1.5 T or 3 T. Recent technological developments have seen the production of 7 T scanners, but their use is currently limited to research institutions. The work presented in this thesis has mainly been acquired using a 3 T system, with the work in Chapter 6 using a 7 T system. Both of these systems were produced by Philips Healthcare [17].

2.3.1   Magnet

In order to form an MR image of an object, it must be placed in a homogeneous magnetic field. When imaging the human body, this requires that the field covers a large three dimensional volume. The field needs to be stable in time and homogeneous in space, with a tolerance for inhomogeneity of around 1 in 1,000,000. Early magnetic resonance scanners used low magnetic fields, of the order 0.1 T, and for these it was sufficient to use a permanent iron magnet. For higher fields (greater than around 0.5 T), it is necessary to use a superconducting electromagnet. This works on the principle of a solenoid coil, whereby a magnetic field is generated inside a toroid coil, which forms the bore of the magnet into which the subject is placed. The field produced is dependent on the size of the electrical current in the coiled wire. Wire made from superconducting metal allows a very large current to pass through with very low resistance when they are cooled below a certain temperature. In modern systems, the superconducting metal alloy Niobium-Titanium is used; cooled to a temperature of around 10K by liquid helium. In the past, liquid nitrogen has been used to maintain the low temperature of the helium, but in recent systems this is done using air or water chillers. Initially supplying enough power to generate such a high magnetic field is extremely costly and time consuming. The act of maintaining a very low temperature in the superconductor means that once the static field is achieved, the current in the superconducting coils can be maintained merely by maintaining a low temperature in the coil using water and air coolers.

The imaging area of the magnet is inside the bore of the toroid coil. However, this generates a fringe field extending outside the scanner. In order to

minimise the spatial extent of this field, shielding is used. Current technology typically uses passive shielding, where a metal with a high magnetic permeability such as iron limits the extent of the field outside the bore of the scanner. To minimise the space and additional mass of the iron shielding, it is now possible to use active shielding, where additional electromagnetic coils generate fields that neutralise the fringe field [18].

2.3.2   Shim Coils

The static field produced by the superconducting magnet alone is typically not homogeneous enough for the purpose of imaging over a large volume, and so it is necessary to make adjustments to this field to ensure homogeneity. This process is known as the *shimming* of the MRI scanner. Passive shimming is performed at the installation of the magnet, where the magnetic field throughout the volume of the bore is calculated, and any inhomogeneities are identified by comparing the measured field with that of the final target field. This is done when the magnet is *in-situ*, as inhomogeneities may be due to the environment around the magnet or due to flaws in the magnet itself. Any differences between the two fields are known as the residual of the field. Residual fields are reversed by inserting pieces of a metal with high magnetic permeability, such as iron into the appropriate regions of the magnet [19].

In addition, the subject can introduce inhomogeneities into the magnetic field due to naturally occurring exogenous paramagnetic and diamagnetic materials in the body. These are accounted for by the process of active shimming, which is performed at the start of each scan session. Incorporated within the bore of the MRI scanner is an additional set of copper shimming coils that produce temporary magnetic fields to modify the B_0 field based on calculations made for each subject. This is typically done by mapping the static field throughout the scanner with the subject inside, and instructing the shimming coils to make the necessary adjustments [20].

2.3.3 Gradient Coils

As described in Section 2.2.1, in order to generate an image, the spatial location of each signal source must be uniquely known. In order to do this, a gradient is used in each orthogonal axis of the scanner. This is done using three additional arrangements of conducting wire coils constructed in concentric cylindrical layers in the scanner bore [21]. Conventionally, the slice select gradient in the z direction is provided by a Maxwell pair coil; two coils of the same radius, at a known separation carry currents in opposing directions to induce a uniform magnetic field gradient along the length of the bore, with the gradient being defined as zero at the isocentre of the magnet. There are now many possible ways of achieving transverse gradients in the bore of the scanner; ranging from simple to highly complex [18]. Commonly used is an arrangement of two pairs of saddle shaped wire coils, each pair of coils effectively produces a linear field gradient in each of the x and y directions. This arrangement is known as a Golay set [22].

Gradient coils necessarily have their own cooling system to minimise heating within the coil [21]. Additionally, the gradient coils are shielded to protect any adjacent conductive scanner components from experiencing eddy currents. As with the shielding applied to the main magnet, this can take the form of passive or active shielding components [23].

2.3.4 Radiofrequency transmit and receive coils

B_1 pulses are typically transmitted from a volume coil making up the innermost layer of the MRI scanner bore. The spectrometer generates a radiofrequency signal that is then convolved with a chosen pulse shape and passed through the amplifier. The RF coil transmits this as a highly uniform electromagnetic pulse, tuned to the appropriate resonant (Larmor) frequency, which excites the material in the volume coil. A simple single coil element (for example in a single element surface receive coil) consists of a loop of wire connected in parallel to a capacitor in a highly tuned resonant circuit specific to the resonant frequency of the material being imaged. The received

radiofrequency signal induces a current in the coil by virtue of Faraday's Law of induction, which is measured by the spectrometer and collated by the computer for preprocessing. It is advantageous for the receive coil to be as near as possible to the material under investigation. For this reason, specific removable volume coil arrangements are used that are customised to the shape of the body part being imaged. For example, neuroimaging coils, neurovascular (head and neck) coils, body (torso) coils, limb (knee) coils and neonatal (incubator) coils. Alternatively, surface coils can be placed on the area of interest. All data presented in this thesis is acquired using a neuroimaging (head only) receive coil.

2.3.5 Parallel imaging

The neuroimaging coils used to acquire the data presented in this thesis have 8 and 32 coil elements, arranged in a cylindrical geometry, working synchronously to acquire signal from the volume. Where there are multiple elements to a coil, scan time can be dramatically reduced by exploiting the way the receiver coil receives the RF signal. The design currently used on Philips scanners was pioneered in 1997 [24], later improved on in 1999 [25], and is now known as sensitivity encoding, or SENSE. In a coil in which the field of view of each element is overlapping, knowledge of the sensitivity map of each coil element is used to partially fill k-space so that some trajectories do not need to be sampled. The signal from regions detectable by two or more elements is under-sampled, without compromise to the spatial resolution. Alternatively, the field of view can be expanded without increase in scan duration. When the data is reconstructed to form an image, the sensitivity maps are used to calculate weighting values that are used to fill k-space without aliasing. Scan time is reduced by an acceleration factor, R. Scans acquired with higher values of R at the same spatial resolution inevitably lead to higher noise in the image.

2.3.6 Computer Interface

The scanning hardware is controlled by computer using an interface that enables the user to input parameters of the subject being scanned, such as identification information, and select the scans to be performed. The computer calculates the bandwidth of frequencies across which the radiofrequency pulse will emit, and also the power at which the gradients will be applied − this information is then sent to the waveform generator as a digital signal. The signal is converted to analogue and each of the RF and gradient waveforms is amplified before being sent to the coils for transmission. Once the signal of interest has been received, it is amplified and converted to a digital signal before being reconstructed into an image.

2.3.7 Pulse programming

The interface provides options for the user to enhance and optimise protocols before scanning, and to customise the sequence for a particular investigation. However, advancements in knowledge and understanding can be made by coding scanner sequences that are atypical or previously untried. It is possible to develop these sequences off-line using a scanner simulation package known as a pulse programming environment (PPE). This enables the user to make alterations to the code controlling, for example the wave form, and to observe the consequences of these changes without directly altering the way the scanner performs. Successful alterations can then be transferred to the scanner interface by means of a software patch. This method has been used in Chapters 5 and 6 of this thesis.

2.3.8 Data handling

Data can be stored in its raw format, before Fourier transform is performed, so that post-processing corrections can be performed. Alternatively, or additionally, transformed images can be exported from the scanner for pre-processing and analysis. Typically, data may require correction for subject motion and / or removal of artefacts before it can be analysed. This is done

off-line, after the data has been exported from the scanner and stored elsewhere.

2.3.9   Safety

As long as safety is taken into consideration, there are no known medical side effects of MRI, a marked difference when MRI is compared to other diagnostic imaging methods such as those requiring the use of x-rays or ionising radiation (gamma, positron emission). Patients must be carefully assessed for exclusion criteria such as the presence of a metal implant that would be detrimentally affected by the magnetic field, for example a pacemaker, aneurism clip or cochlear implant. For research scanning, criteria are more stringent, excluding subjects with any metal implant, as the risks of scanning have no clinical diagnostic benefit to the subject, and image quality may be poor due to the susceptibility imaging artefacts caused by such items. Any person moving in or around the magnetic field must first remove all loose metal objects, as these create a projectile risk if they are sharply attracted towards the bore of the magnet.

Conductive materials must not be allowed to form a current loop within the scanner during the application of gradients, as the gradient can induce a current in the loop, which may cause heating. It is advisable to remove any metal jewellery during scanning, even if it is not loose. Some tattoo ink can also contain metal particles, and heating can occur within the tattoo. In these cases, it is sufficient to warn the subject of the risks prior to the scan and, if necessary, immediately apply cooling to prevent or treat skin burn on removal from the scanner. The human body can also form a current loop within the scanner, so care must be taken to ensure that surfaces of bare skin are not allowed to touch, and if necessary, an insulating layer is placed between the subject's skin and the bore of the scanner to prevent any surface burns.

Specific absorption rate, or SAR, is a measure of the rate of absorption of radiofrequency electromagnetic radiation by the human body. It is defined as power absorbed per unit mass of tissue, and has units Watts per kilogram

(W/kg). Sequences with high SAR can cause heating of the subject. Gradient switching is the change in the total magnetic field per unit time (dB / dt), and is the property of a gradient that induces a coil in a current loop. By the same mechanism, it can cause peripheral nerve stimulation, which in most cases is merely unpleasant, but at a high enough gradient switching rate, could become dangerous to the subject by interfering with the cardiac electrical signal. Gradient switching causes small amounts of motion within the scanner hardware that happen very rapidly. The vibration produces high amplitude acoustic noise, and for this reason, subjects must wear ear protection in the form of ear plugs and ear defenders. Commercial scanners have in-built software intended to limit both SAR and gradient switching and prevent any harm coming to subjects undergoing an MRI scan. For gradient switching, regulatory agencies have imposed an absolute value of dB / dt to which human scanners must be limited.   To limit SAR, the scanner uses its own measurements of the subject to calculate the maximum power it can use for the excitation pulse.

Contrast agents used in MRI scanning are based on paramagnetic materials, such as gadolinium, and act to create or enhance the contrast of an image by significantly shortening the longitudinal relaxation time of tissue. Gadolinium is toxic, and must be delivered into the body in a chelated form so that it is chemically inert in the body and is removed from the blood with other waste products. For subjects with renal impairment, however, the disposal of the chemical is compromised, and it is best to avoid using gadolinium based contrasts in order to reduce the risk of nephritic problems.   As with the administration of any exogenous chemical to the body, any patient carries a small but still very real risk of anaphylactic reaction to the contrast agent.

Transient effects such as dizziness, nausea and magnetophosphenes (bright lights in the visual field) are less of a direct safety concern, but some people find them disturbing nonetheless. These effects can be reduced, if not avoided by taking care to move slowly through the static field.

Cryogens are the low temperature materials essential to maintaining the current in the superconducting magnet. When cooling gases are in their cold (cryogenic) state, the main risk from them is cold burns if they were to come into contact with skin. However, if cryogens are allowed to heat up, for example in the case of a leak, they rapidly expand, displacing any air from the area. This carries the risk of asphyxiation to anyone in the vicinity. Very occasionally, a large amount of cryogen can be released instantaneously, for example, in the event of a scanner quench, the entire helium supply is allowed to boil off in order to dissipate the heat from rapidly increasing the resistance in the superconducting wires that form the magnet. For this reason, every MRI scanner must be fitted with a quench pipe, which provides a safe escape route for the rapidly expanding gas. This prevents asphyxiation risk and also prevents the explosion risk of having a large amount of rapidly expanding material in an enclosed space.

2.3.10 Ethics

All experiments on humans, animals, or human tissue must have prior approval from a body of ethics governance. Most medical institutions and research institutions that are actively undertaking such experiments will have their own ethics committee overseeing all such experimentation and ensuring that ethical standards are maintained. All experiments reported in this thesis were carried out with prior approval from the University of Nottingham Medical School Ethics Committee.

2.3.11 Advantages and disadvantages of high field

Work in this thesis has been performed at 3 T and 7 T. At higher magnetic field, a higher proportion of the magnetic dipole moments will align parallel with the field. This results in higher signal to noise ratio. In addition, magnetic field strength influences the way the excited magnetic dipole moments interact with each other and with the surrounding lattice of the material. This results in longer T_1 relaxation times and shorter T_2 decay times of tissue at high field, theoretically increasing the contrast to noise ratio of the

weighted image. However, as the magnetic field strength increases, higher frequency RF pulses are required to excite the precession of the magnetic dipole moment into the transverse plane. This results in a higher specific absorption rate and acoustic noise. While high field offers the possibility of improved image quality, caution must be used to ensure the safety and comfort of human subjects. In addition, it is more difficult to create and maintain a homogeneous static field when the field strength is higher as it is more susceptible to inhomogeneities produced by introducing a subject into the field. Perturbations in the magnetic field (ΔB) are linearly dependent on the B_0 magnetic field, related proportionally by magnetic susceptibility (χ) as shown in Eqn. [2.40]. Magnetic susceptibility (χ) is constant for a given material.

$$\Delta B = \chi B_0 \hspace{4cm} \text{Eqn. [2.40]}$$

This makes the active shimming of the magnet for each scan at high field critically important.

References

1. Rabi, II, Zacharias, JR, Millman, S, Kusch, P. A New Method of Measuring Nuclear Magnetic Moment. Physical Review, 53 (4): 318 (1938).

2. Purcell, E. M., Torrey, H. C. and Pound, R. V. Resonance Absorption by Nuclear Magnetic Moments in a Solid. Physical Review, 69,37-38 (1946).

3. Webb, S. The Physics of Medical Imaging. Institute of Physics Publishing, Bristol, UK (1988).

4. Dirac, PAM. The quantum theory of the electron. Proceedings of the Royal Society of London. Series A, 117:610–624, (1928).

5. Levitt, MH. Spin Dynamics: Basics of Nuclear Magnetic Resonance. Wiley-Blackwell Publishing, New Jersey, USA (2008).

6. Huettel, SA, Song, AW, McCarthy, G. Functional Magnetic Resonance Imaging. Sinauer Associates, Sunderland, Massachusetts, U.S.A (2004).

7. Matlab version 2009b, The MathWorks Inc., Natick, MA.

8. Hennig, J, Friedburg, H. Clinical applications and methodological developments of the RARE technique. Magnetic Resonance Imaging, Volume 6, Issue 4, p391-395 (1988).

9. Wright PJ, Mougin OE, Totman JJ, Peters AM, Brookes MJ, Coxon R, Morris PE, Clemence M, Francis ST, Bowtell RW, Gowland PA. Water proton T1 measurements in brain tissue at 7, 3, and 1.5 T using IR-EPI, IR-TSE, and MPRAGE: results and optimization. MAGMA. 21(1-2):121-30 (2008).

10. Hahn, EL. Spin echoes. Phys. Rev., 80(4):580–594, (1950).

11. Carr, HY and Purcell, EM. Effects of diffusion on free precession in nuclear magnetic resonance. Physical Review, 94(3):630–638, (1954).

12. Mansfield, P, Howseman, AM, Ordidge, RJ. Volumar imaging using NMR spin echoes - echo volumar imaging (EVI) at 0.1 T. Journal of Physics E: Scientific Instruments, 22(5):324–330, (1989).

13. Bernstein, M, King, K, Zhou, X, Fong, W. Handbook of MRI pulse sequences, volume 32. Academic Press New York, (2005).

14. Garroway, AN, Grannell, PK, Mansfield, P. Image formation in NMR by a selective irradiative process. Journal of Physics C: Solid State Physics, 7(24):L457–L462 (1974).

15. Kumar, A, Welti, D, Ernst, RR. NMR Fourier zeugmatography. Journal of Magnetic Resonance 18:69–83 (1975).

16. Mansfield, P. Multi-planar image formation using NMR spin echoes. J. Phys. C: Solid State Phys., 10:L55-L58 (1977).

17. Philips Healthcare, N.V., Eindhoven, Netherlands.

18. Mansfield, P, Chapman, B. Active magnetic screening of coils for static and time-dependent magnetic field generation in NMR imaging. J. Phys. E: Sci. Instrum., 19:540-545 (1986).

19. McGinley, JVM, Srivastava, VC, DeMeester, GD. Passive shimming technique for MRI magnets. Mag. Res. Im., 15(3):XIX (1997).

20. Konzbul, P, Sveda, K, Srnka, A. Superconducting Shim System with High Purity Magnetic Field for NMR and MRI Solenoid Magnet MIDI - 200. IEEE Transactions on Magnetics, 32(4):2643-2646 (1996).

21. McRobbie, D, Moore, E, Graves, M, Prince, M. MRI From Picture to Proton. Cambridge University Press, (2007).

22. Turner, RT. Gradient coil design: a review of methods. Magnetic Resonance Imaging, 11:903–920 (1993).

23. Bowtell, R, Mansfield, P. Gradient coil design using active magnetic screening. Magn Reson Med, 17(1):15–9; discussion 19–21 (1991).

24. Sodickson, DK, Manning, WJ. Simultaneous acquisition of spatial harmonics (SMASH): fast imaging with radiofrequency coil arrays. Mag. Res. Med., 38(4):591-603 (1997).

25. Pruessmann KP, Weiger M, Scheidegger MB, Boesiger P. SENSE: sensitivity encoding for fast MRI. Magn Reson Med. 42(5):952-62 (1999).

3 Neuroimaging

3.1 Introduction to Neuroanatomy

Early insight into neuroanatomy came from sciences such as phrenology. This took the extreme view that every task has an anatomical region associated with it. At the opposite end of the spectrum were subscribers to the concept of equipotentiality, who believed that no brain function can be localised discretely, and that any given process in the brain depends on patterns of activity spread throughout the whole brain. Towards the middle of that spectrum lie the studies of cognitive neuropsychology and neurology, which have developed over a period of several decades. From these studies, scientists have deduced that while many mental functions are associated with a specific region or regions of the brain, others can be attributed to patterns of activity that span large-scale neurocognitive networks [1]. One of the most widely used atlases of the human brain was devised by the German anatomist Korbinian Brodmann, who divided the brain into 52 discrete areas, known as Brodmann Areas, BA [2], based on their histological features.

Magnetic resonance imaging can be used to gain information about the structure of the brain. As described in the previous chapter, pulse sequences can be designed to elicit different contrast between tissue types, for example, grey matter and white matter, or cerebrospinal fluid. Structural imaging of this kind is highly useful for the diagnosis of clinical conditions where the anatomy of the brain is altered, for example the detection of a brain tumour. In addition to structural imaging, magnetic resonance techniques can be used to interrogate functional processes that occur in the brain. Later chapters in this thesis report on experiments that investigate the cerebral blood flow and the vascular territories that make up the cerebral blood supply. Another chapter will report measurement of brain activity, exploiting the change in blood oxygenation level dependent (BOLD) contrast at the site of brain activity, and also the increase in perfusion observed in an active area of the brain. This chapter will discuss the mechanisms behind the processes that are investigated in this thesis.

3.1.1   The Brain

Within the human skull is the brain, consisting mainly of white matter and grey matter. The subarachnoid space and ventricles are filled with a protective liquid called cerebrospinal fluid (CSF). Grey matter contains the majority of the neurons in the brain, while white matter consists mainly of axons that are covered in a sheath of electrically insulating material, myelin. Both white matter and grey matter are supplied oxygenated blood by the cerebral vasculature, with grey matter being more highly perfused than white matter. The majority of grey matter is distributed across the surface of the cerebral cortex, and additionally deep grey matter structures exist in the cerebellum, deep cerebellar nuclei and brainstem. The neuronal cells in the grey matter are responsible for most of the brain function. Tracts of white matter connect areas of grey matter together, transmitting electrical signals in the form of an electrical current across an action potential.

The brain is supplied with oxygenated blood by the internal carotid arteries and the vertebrobasilar system, consisting of the two vertebral arteries and the basilar artery. The basilar artery and internal carotid arteries join the anterior and posterior cerebral arteries and anterior and posterior communicating arteries at the Circle of Willis, from which the cerebral arterial system is distributed. This is shown in a Time of Flight (TOF) contrast angiogram in Figure 3.1.
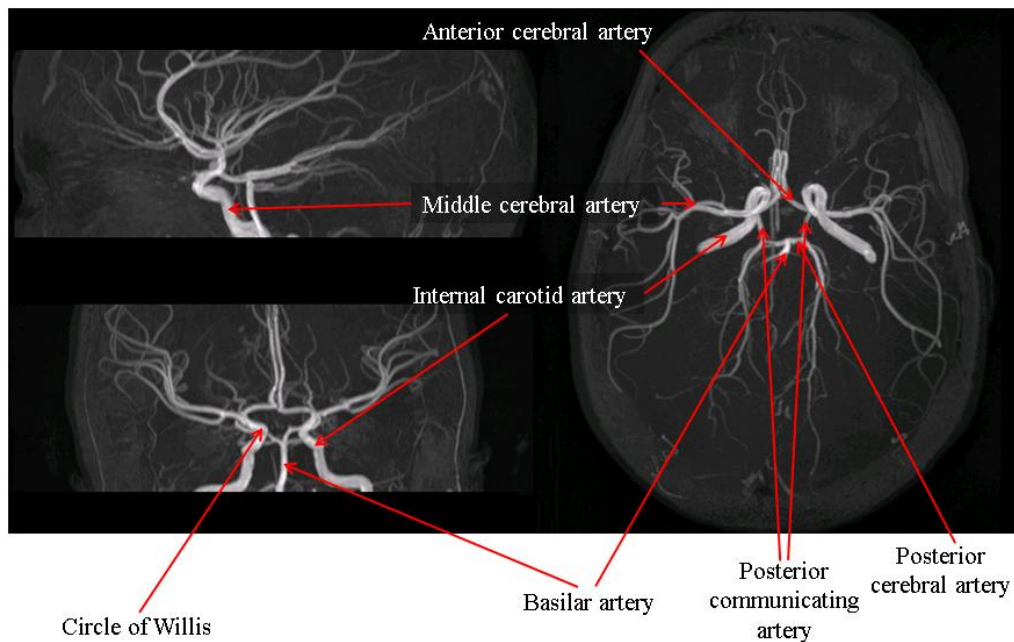
Figure 3.1: The cerebral vasculature with major arteries labelled, shown using a time of flight contrast angiogram.

3.1.2 Brain function

Neurons and axons exhibit an action potential caused by the flow of a current of electrically charged ions across membranes of the cell. Neurons receive signals through dendritic and somatic connections from other neurons, and then transmit these integrated signals to other neurons. The signal itself is a tiny ionic current passed through an ion channel in the cell membrane [2]. When several such cells are oriented similarly to each other and share synchronous activity, these action potentials become large enough to detect from outside the brain. This can be done using techniques such as electroencephalography (EEG), which detects the voltage fields of the action potential on the scalp, of the order 10 – 100 microvolts, or using magnetoencephalography (MEG), where the magnetic dipole fields, of the order 10 – 1000 femtotesla, associated with the action potentials are detected from outside the head.

We know that when a brain region is active, the neurons in that area generate an electromagnetic signal. Functional magnetic resonance imaging (fMRI) methods do not directly measure this neuronal signalling, but instead use

inferences from physiological changes that are correlated with neuronal activity, such as increased oxygen demand and blood flow.

Observing brain function requires fast image acquisition, so that images are acquired at a similar frequency to the haemodynamic changes that occur. There are different MR methods of imaging these short term changes that occur in the brain, with those used in this thesis being:

1. Blood-oxygen level dependent (BOLD) contrast or T_2* weighted fMRI. This is the most widely used fMRI method, which indirectly measures neuronal activity by using the relative change in blood oxygenation in an active area of the brain.

2. Arterial spin labelling (ASL). This is a non-invasive method of directly assessing blood flow by using an endogenous contrast in the form of magnetically labelled arterial water as it enters the brain.

This section will discuss the MR methods that are most useful for the study of pharmacological fMRI, i.e. assessing the modulation of these signals by an exogenous chemical, such as a drug.

3.2   Measuring brain function using BOLD

When Ogawa et al placed test tubes of deoxygenated blood in a container of saline, they found that the presence of the deoxygenated blood decreased the MR signal in the surrounding saline in a T_2* weighted image [3]. In-vivo, deoxygenated blood induces a field inhomogeneity in surrounding tissue in the form of microscopic magnetic field gradients surrounding the capillaries. These field gradients accelerate the dephasing of the transverse magnetisation of the magnetic dipole moments, decreasing T_2*. The magnetic properties of oxygenated and deoxygenated haemoglobin molecules are different. Oxygenated haemoglobin is diamagnetic; meaning that it has no magnetic moment and is weakly repelled by a magnetic field. Deoxygenated haemoglobin is paramagnetic; therefore, its non-zero magnetic moment causes it to have a weak attraction to a magnetic field. A T_2* weighted image shows high signal in areas where there is high blood oxygenation due to the higher

T_2^* of oxygenated blood. Neuronal activity modulates the relative amount of deoxyhaemoglobin present in immediately surrounding tissue. It is thought that there is an increase in the amount of oxygenated haemoglobin in active brain areas, as a result of increases in cerebral blood flow and blood volume that exceed the cerebral metabolic rate of oxygen ($CMRO_2$) consumption, leading to an excess of oxygenated blood. This is known as the functional Blood Oxygen Level Dependent (BOLD) signal [2], and is illustrated diagrammatically in Figure 3.2.
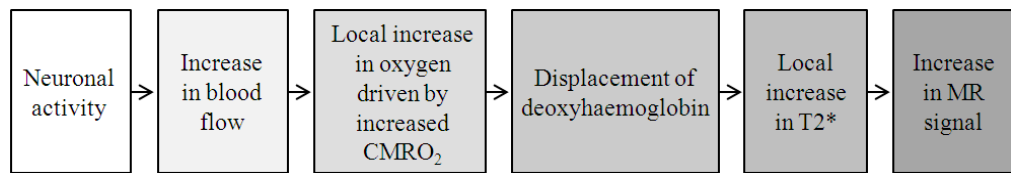
Figure 3.2: The mechanism behind the generation of BOLD contrast.

3.2.1 The Haemodynamic Response Function

The shape of the BOLD signal response to a short neuronal activation, termed an "event", is called the haemodynamic response function (HRF). Much research has involved modelling the shape of this haemodynamic response function [4, 5]. The shape of the HRF is shown in Figure 3.3 and has three key features; the initial dip (1), the positive overshoot (2) and the post-stimulus undershoot (3).
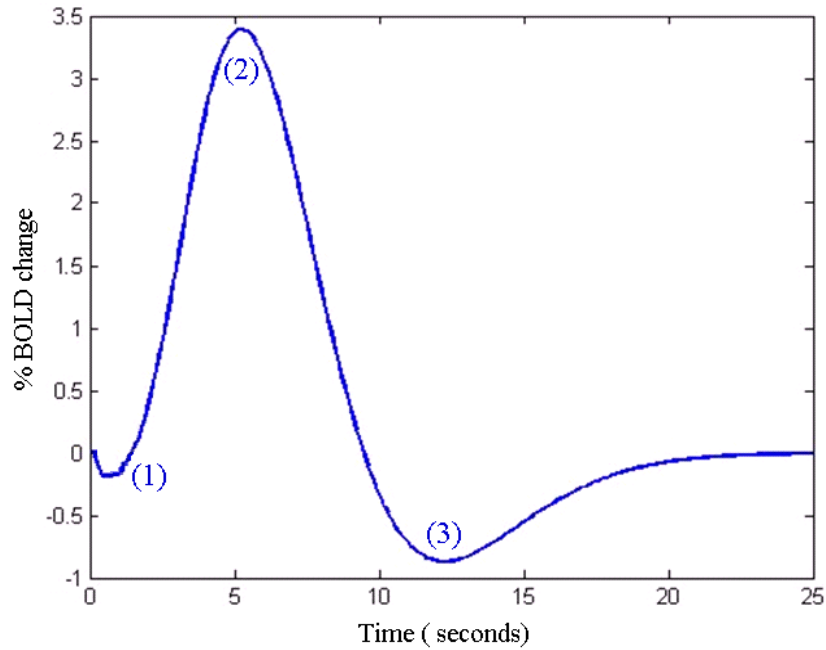
Figure 3.3: Haemodynamic response function (HRF) of a short stimulus, showing the initial dip (1), the positive overshoot (2) and the post-stimulus undershoot (3).

Some studies have suggested the existence of an "initial dip"; namely a decrease of up to 1% in the BOLD signal preceding the characteristic increase in MR signal, which is up to $3 - 5$ % at 3 T. It has been postulated that the initial dip is caused by an increase in the oxygen extraction to meet the increased metabolic demands before the compensatory increase in cerebral blood flow takes place [6]. The effect seems to be highly dependent on field strength (making it almost undetectable at low field strength) and continues to be controversially discussed as it is not consistently detectable, even at high field strength. As the "initial dip" may be due to oxygen extraction, it may provide a more accurate measure of the spatial location of neuronal activity than the subsequent higher amplitude peak in the haemodynamic response curve [7].

The peak of the BOLD signal occurs at the point of maximum oxygenated haemoglobin, approximately $5 - 6$ seconds after a short stimulus or event. After the BOLD signal has peaked, the signal then decreases to below the original baseline level, termed the "post-stimulus undershoot". The cause of this effect is still a hotly debated topic [8, 9, 10]. One potential mechanism is that the cerebral blood flow returns to its baseline level faster than the cerebral

blood volume, leading to a larger amount of deoxygenated haemoglobin being present, and the BOLD signal falls to a value below baseline. Then, as the blood volume slowly falls to its original level, the BOLD signal rises to return to its baseline level [10]. An alternative explanation is that cerebral blood flow (CBF) and cerebral blood volume (CBV) are coupled, whilst the cerebral metabolic rate of oxygen consumption ($CMRO_2$) is uncoupled from these quantities [8, 9].

The BOLD response to a stimulus event is assumed to follow a linear relationship with neuronal activity [11, 12]. This assumption is used in the application of General Linear Model (GLM) analysis methods. However, more realistically, repeated activation of the same region of the brain causes less change in the BOLD signal with each repetition. This is called the nonlinear or refractory effect, and describes the adaptation of brain tissue. The refractory effect appears to last as long as the neuronal activity, as shown in studies involving visual attention [13], and this has been shown to be approximately 6 seconds [11,14].

Images with BOLD contrast are optimally acquired using an echo time that is approximately equal to the T_2^* of the tissue being imaged, which is field strength dependent, with values of T_2^* decreasing for a given material as field strength increases. In grey matter, T_2^* takes a value of approximately 40 to 60 ms at 3 T and 25 to 33 ms at 7 T, dependent on the cortical area under investigation [15,16]. T_2^* weighted acquisitions typically use an echo time (TE) of approximately 35 to 50 ms at 3 T [16] and approximately 25 ms at 7 T [15, 16].

3.2.2 Acquisition of BOLD fMRI Data

The strength of the BOLD response increases significantly with the magnetic field strength [17], in terms of both the percentage signal change compared to baseline and the sensitivity to microvasculature. Thus, increases in the magnetic field strength can have a profound effect on the quality of the functional BOLD images. However, T_2^*-weighted images are highly prone to

susceptibility artefacts that are due to inhomogeneities in the magnetic field where there is an air-tissue boundary. These effects increase with magnetic field strength and with proximity to the air-tissue interface. This effect can be overcome, at least in part, by simultaneously acquiring data using multiple echo times, as use of a shorter echo time is less susceptible to signal dropout. In this case, a weighted summation image of the two images acquired at different echo times can be used. One disadvantage of using BOLD contrast is the indirect relationship between changes in BOLD signal and neuronal activity. Using BOLD fMRI, it is possible that a change in neurovascular state can result in the change in the brain activity observed. This makes interpretation of BOLD fMRI data highly complex and great care must be taken to avoid such inaccuracies.

The BOLD signal change in response to a task is defined as the difference in the signal in BOLD weighted images during that task compared to the BOLD weighted signal during some control, or baseline condition. Any areas in which the BOLD signal has increased during the task in comparison to baseline is deemed to be "more active" during the task. Conversely, "negative BOLD" signal refers to any regions that are less active during the task in comparison to baseline, i.e. the BOLD signal has decreased during the task in those areas. However, as activations are inferred based on signals that are being measured relative to other signals, great care must be taken when interpreting the "negative BOLD" signal.

Functional MRI is often enhanced by being used in conjunction with another technique, for example electroencephalography (EEG), in which electrical potentials in the brain are measured, magnetoencephalography (MEG), which measures the magnetic flux caused by neuronal activity, lesion (any abnormal tissue) study, or transcranial magnetic stimulation (TMS) using an electromagnetic coil.

3.2.3 BOLD Task-Driven Experimental Design

It is important to optimise the experimental design of any study to extract the maximum statistical power from the data. BOLD signal changes are very small; sometimes less than 1% of the static signal, and thus a drug induced modulation of this change is even smaller. Experimental designs that involve observing pharmacological modulation of known task induced activity usually fall into the categories of presenting subjects with either a block design task, or an event related task. These tasks can take a variety of forms, such as a visually or auditory cued motor task or cognitive task, or a passive visual, somatosensory or auditory stimulus. There are also mixed or semi-random designs, which combine aspects of both blocked and event related designs. The block based experiments (Figure 3.4A) are a good way of measuring state-related processes, i.e. processes that represent modes of brain function, like mood induction. They have good detection power but have limited use for estimation of the haemodynamic response function [2]. Event related designs are good at measuring stimulus-related processes (Figure 3.4B), i.e. the response function of a process caused by an individual event or stimulus. The advantage of this design is that it is good for estimating the shape of the haemodynamic response, but it provides weaker power when detecting changes in brain state during a task [2]. Mixed designs can occasionally prove to be a good compromise on detection and estimation power. Additional to this, the power for optimised detection and estimation can be increased by varying the inter-stimulus interval randomly, which is called jittering.
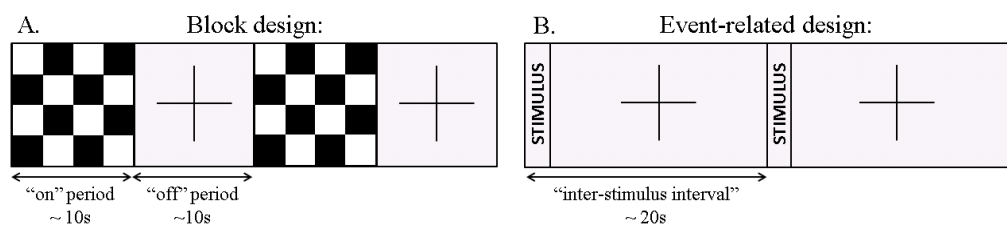
Figure 3.4: Two standard approaches to designing a functional MRI stimulus; (A) block design and (B) event related design.

Sample sizes are also critical in ensuring that the results of a study reach statistical significance. For fMRI research studies, such as the one reported in Chapter 4 of this thesis, it is advised that the sample size should be a minimum of 15 to 20, depending on the size of the effect being observed [18].

3.2.4 fMRI Data Preprocessing and Analysis

Once raw data has been reconstructed into images, preprocessing steps are typically applied before analysis can take place. These are often run using one of the widely available software packages, such as FMRIB Software Library [19] or Statistical Parametric Mapping [20]. Preprocessing steps typically include removal of physiological noise, motion correction, co-registration and smoothing. Physiological noise correction removes noise from subject heart beat and respiration, and additionally scanner drift. Work presented later in this thesis uses the RETROICOR method [21]. Motion correction uses a mathematical algorithm to calculate any gross head motion (either translation or rotation) and realign all the images by minimising the sum of the square of the residual signal. Typically, a 6 parameter rigid-body registration is used. It is necessary to exclude subjects from the analysis for whom their motion is so excessive that motion correction may introduce motion correlated artefacts into the data (defined to be motion greater than one voxel in this thesis). Following this, images can be normalised to a common template to allow group comparisons. This is often done using a standard brain template such as the MNI brain [22] or the Talairach atlas. Finally, in order to increase the signal-to-noise of an image, spatial smoothing is applied. The level of smoothing is defined by the full-width half-maximum (FWHM) of the curve used to convolve with the data. While increasing the signal-to-noise ratio, either temporally or spatially, this will in turn decrease the resolution, either temporally or spatially, therefore care must be taken in choosing the level of smoothing to apply. For the preprocessing of fMRI data collected in this thesis data have been smoothed across 1.5 to 2 voxels, which corresponds to a FWHM of between 5 and 8 mm.

Subsequent statistical analysis often takes the form of a univariate or multivariate approach to a General Linear Model (GLM), followed by the formation of parameter maps that are then interrogated using hypothesis testing. Typically, single subject analysis will take the form of a fixed effects analysis, which treats the variance of each scan as being identical, i.e. from a single subject or from an identical population, and that the variances are fixed. Analyses for larger groups will typically take the form of random effects analysis. Random effects analysis assumes that the sample of subjects was taken randomly from a population, and so the effect size in each subject will need to be greater than the variance between subjects [23]. Depending on the nature of the interrogation, i.e. the hypothesis being tested, higher level group statistical testing can be in the form of single group, two group or paired t tests or multi-way analysis of variance (ANOVA) tests. The latter are more flexible, particularly for analysis of data from pharmacological studies, as several levels of comparison are needed.

3.2.5   Applications / Uses of BOLD fMRI

There are numerous applications of fMRI that have been published over the years. These range from the study of basic neuroscience to understand simple sensory tasks such as the brain's response to motor, visual and somatosensory stimuli; to the study of attention – focussing the consciousness on a particular object or location; and the study of memory – the distribution of different parts of the brain associated with memory processes and studying the functional differences between memory encoding and memory retrieval. The main application of fMRI reported in this thesis is to study the physiological and functional effects of a pharmacological agent on the brain's response to an emotional visual stimulus. Notably, the changes in cerebral haemodynamics, neuronal response and functional connectivity are of particular interest.

3.2.6   Pharmacological Modulation of BOLD

Many studies have used BOLD as a measure of brain activity to assess how certain exogenous pharmacological agents modify the brain's response to a

given task [24, 25]. Commonly, addictive substances are studied, such as caffeine, amphetamine and nicotine, to investigate the behaviour of arousal or reinforcement associated with the drug. Also of interest are the effects of modulating the production and uptake of neurotransmitters, such as dopamine, on cognitive task performance and task related BOLD signals. This has been used to successfully demonstrate the mechanism behind the perceived and observed changes caused by that drug. In addition, the known effect of a drug can be exploited to enhance functional MRI studies. To give one example; caffeine is an adenosine receptor antagonist and thus a cerebral vasoconstrictor, which decreases the resting cerebral blood flow [26, 27, 28]. Some research has suggested that this property can be exploited as a BOLD contrast enhancer; as deoxyhaemoglobin levels are lower at baseline, but increase normally on activation, thus increasing the BOLD contrast. This increase in BOLD contrast was found to be between 22% and 37% for a visually cued motor task [26], suggesting that caffeine could be used as a contrast enhancement agent in BOLD fMRI studies. Caffeine has been shown to modulate the shape of the haemodynamic response to a stimulus through the comparison of parameters such as the time to peak, the full width half maximum, the maximum peak, and the amplitude of the initial dip. It is theorised that this is due to modulation of the cerebral blood flow and the rate of oxygen metabolism [27]. Caffeine has also been shown to significantly reduce the time to peak of the haemodynamic response [28], and the magnitude of the initial dip [29].

3.3   Pharmacological fMRI Study Design

A literature review on pharmacological fMRI (termed phMRI) in 2000 [24], suggests phMRI to be a relatively non-invasive way of mapping a pharmacological modulation of task related brain activity. The review predicts the increase and development of phMRI as an analytical tool in the area of drug research, and its use by monitoring the effect of pharmacological intervention on a neurological disorder or condition. There have been several studies published that use fMRI to quantitatively study the action of a pharmacological agent. For example recreational drugs such as ketamine [30],

or more widely used substances such as caffeine [26, 31] and prescribed medication [32] on the human brain [25].

There are two main questions that can be answered by pharmacological fMRI (phMRI) studies. One approach is to seek regional and / or global changes in BOLD or perfusion signal that are associated with the action of a pharmacological agent, but are not associated with any task-induced activity. An alternative approach is to test for a change in task-induced activity that is caused by the administration of the pharmacological agent. This can be done using any task that can usefully be observed using fMRI (Section 3.2). For best results, the modulation of the state of interest should be observed in their comparison to a control state. Depending on the experimental design and the exact research question being investigated, the control condition can take the form of a measurement made before the administration of the drug, a control group of healthy volunteers or a condition where a placebo is given, to eliminate any activity that is due to the subject anticipating the administration of the drug. To maximise the power of studies where repeated measurements are being taken, the crossover repetition of drug or stimulus should always be randomised to account for the effect of order on the two conditions. An example placebo controlled crossover study design is given in Figure 3.5. This design is used for the study of the effect of beta-blockers on task related brain activity, which is the focus of Chapter 4.
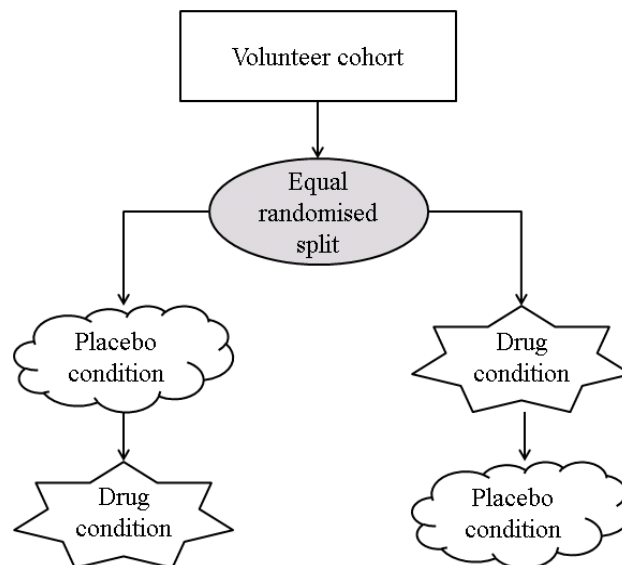
Figure 3.5: An example study design using a randomised placebo controlled crossover.

3.4   Functional connectivity

The previous section described task-driven BOLD responses. During the performance of a task or the processing of a stimulus, spatially disparate areas of the brain can also be observed to function synchronously (correlate) with each other as part of a network; this is termed functional connectivity (fc) [40]. Studying functional connectivity gives insight into which areas of the brain form networks and how these networks are modulated. Connectivity between brain areas is usually assessed by numerical correlation of the signal fluctuations in such brain areas over time, typically over the course of a few minutes. One standard method to assess such correlation is in terms of the Pearson correlation coefficient of signal timecourses from two spatially distinct areas [33], which can range from -1 to +1. Large positive values signify high correlation (i.e. signal is in synchrony between regions), while large negative values show an inverse correlation between two regions (i.e. as the signal goes down in one region, it goes up in the other). Values near zero signify absence of, or very little correlation. Correlation is also often referred to in terms of functional distance, which is given by the inverse of the magnitude of correlation (independent of the sign of the correlation). Therefore, pairs of voxels with a strong positive or negative correlation have a low functional distance between them, whilst pairs of voxels with little or no correlation are described as being separated by a very large functional distance.

Early task driven functional connectivity studies were performed by looking for brain regions exhibiting signal intensities with a high degree of temporal correlation. This was first done for simple tasks where the networks of inter-communicating brain regions are known (e.g. motor, visual, auditory networks). It was shown using BOLD fMRI that a significant amount of the noise in the measurement was not random in nature, but had a significant spatio-temporal correlation [34]. Functional connectivity can be assessed by applying temporal correlation analysis using an internal reference of a known activation pattern in the brain e.g. the signal timecourse of a known "seed" region of interest [35, 36, 1]. There is no absolute threshold above which

56

correlation coefficient values are considered significant, as this depends on the strength of correlation in the system being observed, and the duration over which the correlation is assessed. However, for data typically acquired over a period of 5 minutes, voxels with correlation coefficients of magnitude greater than 0.3 are generally considered to reflect a significant correlation [37].

3.4.1   Resting state functional connectivity

Functional connectivity can be used to characterise the temporal coherence of disparate brain regions while the subject is at rest [38] to provide information on the networks of interconnected brain regions. Many resting state networks have been identified; of the order of a dozen [37]. An example of a network of interconnected brain regions active during rest is the default mode network (DMN), shown in Figure 3.6. The default mode network consists of interconnected regions where activation correlates during rest. Typically, the default mode network comprises the posterior cingulate cortex and the inferior parietal lobules [39, 37]. Regions within the default mode network are usually active in the resting brain, therefore when comparing activity during a task to baseline; one might expect these regions to be less active during the task. This must not be interpreted as a negative BOLD signal associated with the task being performed, only with the deactivation of the default mode network.
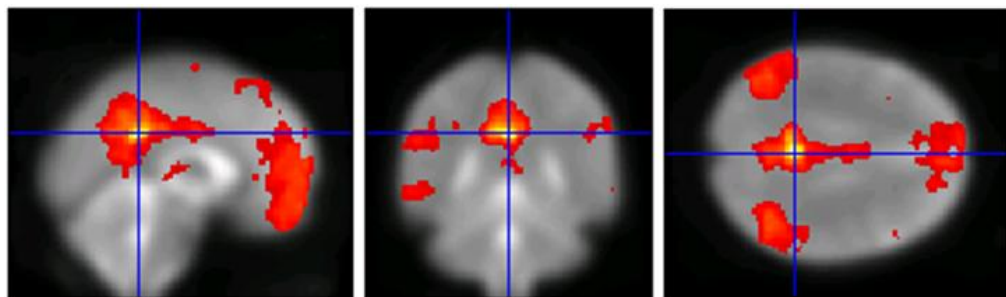
Figure 3.6: Correlation between disparate brain regions comprising the default mode network.

The salience network is of particular interest later in this thesis as it is concerned with the processing of emotional responses. The salience network mainly exhibits connectivity between the bilateral insulae and the anterior

cingulate cortex (shown in Figure 3.7). The primary sensory regions make up the sensory networks, such as the sensorimotor network (primary somatosensory and motor cortices) and the visuospatial network (primary visual cortex).
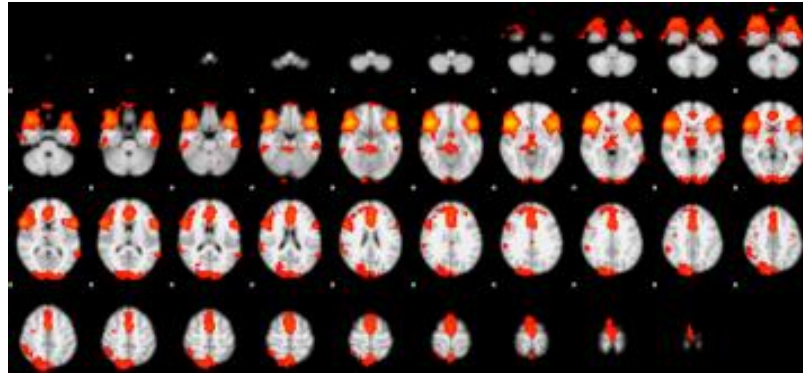
Figure 3.7: Correlation in the salience network showing coherence between the bilateral anterior insula and anterior cingulate cortex.

3.4.2   Functional connectivity: Acquisition and Analysis Methods

Acquisition methods used are largely very similar to those used in task-driven BOLD functional MRI; EPI acquisition with an echo time of approx 40 ms, however it is most important to maximise temporal resolution, thus limiting the TR, and typically a TR of 2 seconds is used.

Functional connectivity analysis can be approached in a number of ways. Seed based connectivity analysis, as described above, is often used to determine the pattern of a network and the strength of the correlation. The technique was pioneered in a study assessing correlations in the motor cortex during resting state [40]. This involves the selection of a seed of interest from an *a priori* hypothesis. For example, either from a known anatomical region, or alternatively, on the basis of areas identified from functional activation provided by general linear model analysis. The timecourse of the voxel, or the mean timecourse of the group of voxels from the seed, is then extracted from the data. Then, in a voxel to voxel method, the Pearson correlation coefficient is calculated for the timecourse of that voxel with the seed. This produces a map of Pearson correlation coefficients. These maps can be threshold and

quantitatively compared between subject groups, or drug conditions, by comparing the magnitude and extent of supra-threshold clusters. A recent study by Hale et al [37] used this method to demonstrate the presence of the default mode and sensorimotor networks during resting state and compared the strength of the functional connectivity between field strengths (3 T and 7 T). They used an anatomically defined seed in the posterior cingulate for definition of the default mode network. A motor task localiser was used to determine appropriate seed locations for the sensorimotor network. Their results showed that the use of a conservative threshold of Pearson correlation coefficient allowed robust definition of the both networks during resting state.

A further seed-based method of assessing functional connectivity is that of psychophysiological interaction (PPI), a concept introduced by Friston et al [41]. A region of interest for the seed must first be selected; the selection of the seed location should be based on an *a priori* hypothesis about the functional connectivity present in the data. The time course of the signal in that region is then extracted and the areas with correlating timecourses are identified using a general linear model, as typically used in task-driven fMRI. This provides statistical maps that can be compared between two conditions using mixed effects analysis, paired t-testing or factorial analysis, for example between two drug conditions [42, 43] between two subject groups [44]. This method is similar to the seed-based correlation coefficient method, but has the advantage that covariates of no interest can easily be appended to the model, for example to regress out the effect of motion. Also, rather than just identifying all brain regions whose activity is correlated with that of the seed, psychophysical interaction methods particularly look for areas where activity is correlated to both the task and to activity in the seed. While this latter point is highly relevant for assessing connectivity within task or stimulus induced brain activity, it is less relevant to resting state functional connectivity. McCabe et al used this method to assess changes in resting state functional connectivity in healthy volunteers between two different anti-depressant medications (citalopram and reboxetine) compared to placebo. They used timecourses from seeds in the default mode network in their psychophysiological interactions analysis. Their analysis found reduced

connectivity in the groups that had taken anti-depressants compared to the placebo group, with citalopram reducing connectivity between the amygdala and the ventral medial prefrontal cortex, whilst reboxetine reduced connectivity between the orbitofrontal cortex and both the amygdala and striatum. The study published by McCabe et al [45] is of a similar experimental design (placebo controlled pharmacological modulation of resting state functional connectivity) to the data presented later in Chapter 4 of this thesis.

Hypothesis-free methods such as independent component analysis (ICA) can be used to identify the components of interconnected networks within the brain. Once networks of interest have been identified, it is possible to further interrogate these networks by choosing a seed region and assessing temporal correlations with the seed region. Such analysis techniques currently in use are mostly derived from the singular value decomposition method applied to a time series from a voxel or a region of interest within the brain. This reduces complex timecourse data sets to lower dimensions in order to reveal underlying structures in the form of orthogonal components of voxel timecourses. From this, principal component analysis is derived, where one is able to specify an anatomical region with which to search for coherence. This is the method used in early functional connectivity studies [1, 34]. In a study published by Bullmore et al, subjects were given a complex visually stimulating cognitive task. The periodicity of the experimental design was used to identify individual voxels that were active during each stimulus in the task. From here, singular value decomposition was used to identify pairs and groups of regions within the brain that exhibited "positive" or "negative" connectivity. For example, the regions used for visual input analysis had a negative connectivity with all other regions [1]. The method of principal component analysis through singular value decomposition works well for hypothesis driven investigation of network connectivity; however where there is no clear hypothesis, independent component analysis is commonly used.

Biswal et al [34] demonstrated that it is possible to simultaneously measure activation using BOLD and ASL signal during resting state, and that the

temporal correlation found with the two methods was synchronous. Further discussion of arterial spin labelling (ASL) techniques, including FAIR, is given in Section 3.5.4. From their data, the group concluded that task driven activation correlated more with BOLD functional connectivity than it did with functional connectivity derived from perfusion weighted data. However, this technique, although advanced at the time, was not optimal for acquiring ASL signal as their echo time is too long and thus the resultant image is primarily BOLD weighted and much of the ASL signal will be lost. Later in this chapter, the methods section describes a similar technique to this, where instead two acquisitions are performed interleaved to provide almost simultaneous blood flow and BOLD data with a pseudo-continuous arterial spin labelling method. Notwithstanding, they hypothesised that the observed low frequency fluctuations that show high temporal correlation across multiple brain regions are, in fact, neuronal in origin.

More recent research published by De Luca et al [45] used ASL and BOLD data separately, analysed by a probabilistic ICA method to assess functional connectivity during resting state and during a bilateral finger tapping task. Their probabilistic ICA method was used in favour of a seed based approach that was deemed to introduce bias into the analysis associated with specifically searching for coherence with a given anatomical region. Employing a probabilistic independent component analysis over a model-free ICA gives the advantage that the results are possible to interpret with quantifiable statistical significance. Comparisons between independent components derived from BOLD and ASL data separately showed similar patterns in several components. Perfusion weighted signals generated from ASL data give the added, physiologically more meaningful dimension and thus inferences are not just based on the BOLD response. In their discussion, De Luca et al also postulate that the techniques outlined may be a helpful way of addressing the question of whether or not functional and resting state networks are altered by a pharmacological intervention.

3.4.3 Pharmacological Modulation of Functional Connectivity

A number of studies on pharmacological modulation of functional connectivity have been reported in animal models [48, 49]. However, such studies in human subjects are less prevalent. Recent studies have investigated the effect of a drug, such as the beta blocker propranolol or a direct modulation of neurotransmitter on functional connectivity in autism patients [50] and healthy subjects [51, 52, 53, 54, 55, 56], including smokers [47, 57].

3.5 Blood Flow and Perfusion MRI

Blood flow is the transit of blood through blood vessels and is conventionally measured in centimetres per second (cm/s), and can be measured non-invasively using Phase Contrast Angiography (PCA) and Time of Flight (TOF) contrast angiography. Perfusion MRI directly measures the delivery of blood to the tissue, termed cerebral blood flow (CBF). This is defined as the rate of delivery of arterial blood to a capillary bed and exchange with the tissue.   CBF has the units millimetres per 100 grams per minute (ml/100g/min), whilst CBV takes the units of millimetres per 100 grams (ml/100g), or is sometimes expressed as a percentage. Perfusion can be measured using exogenous contrast media such as gadolinium, or endogenous contrast as in the technique of Arterial Spin Labelling (ASL), to enhance and maximize the difference in signal detected between the inflowing blood and the surrounding tissue.

3.5.1 Flow

Blood flow can be measured non-invasively using the MR methods of Phase Contrast Angiography (PCA) and Time of Flight (TOF) contrast angiography. Both of these techniques are used in Chapters 5 and 6 of this thesis to locate major inflowing arteries in the neck.

Phase contrast angiography (PCA) uses a bipolar gradient following the excitation pulse, preceding the readout. Spins that stay stationary during the

application of the gradient have zero phase, and spins that travel during this time accrue a phase difference, $\Delta\phi$, proportional to their velocity in the direction parallel to the bipolar gradient [58], as shown in Figure 3.8. This produces an image contrast that is sensitive to the velocity of blood in the axis of the bipolar gradient, with fast moving spins producing higher signal intensity. This is shown as a projection image of the blood vessels in the volume of 60 mm slice in the sagittal plane, Figure 3.9 (A).
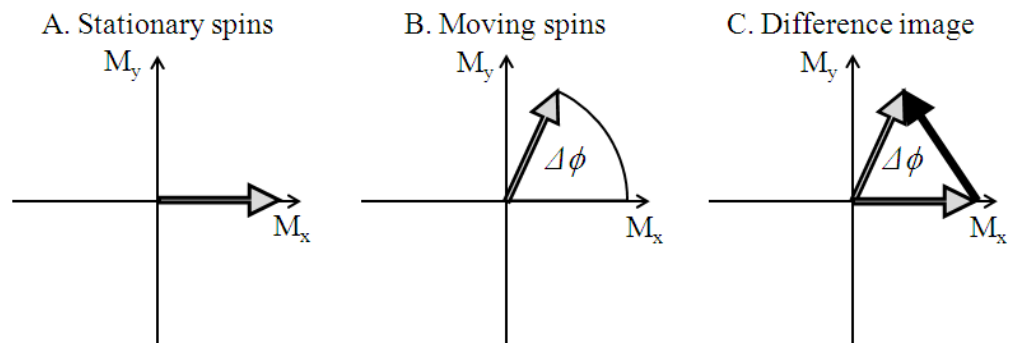
Figure 3.8: Diagram of phase accumulation in phase contrast angiography (PCA). Spins located in blood flowing through a bipolar gradient will accumulate a phase (B), whereas stationary spins will not (A). The vector difference (C) gives the contrast of the image.

Time of Flight (TOF) contrast uses multiple saturation pulses with short TR to saturate the longitudinal magnetisation of stationary tissue. Moving spins will not have received these pulses, so that their longitudinal magnetisation is still relaxed, producing higher signal intensity. This produces an image contrast that is sensitive to the flow velocity. This is acquired over many narrow slices that are perpendicular to the flow of blood to retain sensitivity to blood that is flowing slowly through the slice. These slices are then used to form a maximum intensity projection (MIP) across the entire volume, as in Figure 3.9 (B), where 100 slices of thickness 0.7 mm were acquired.
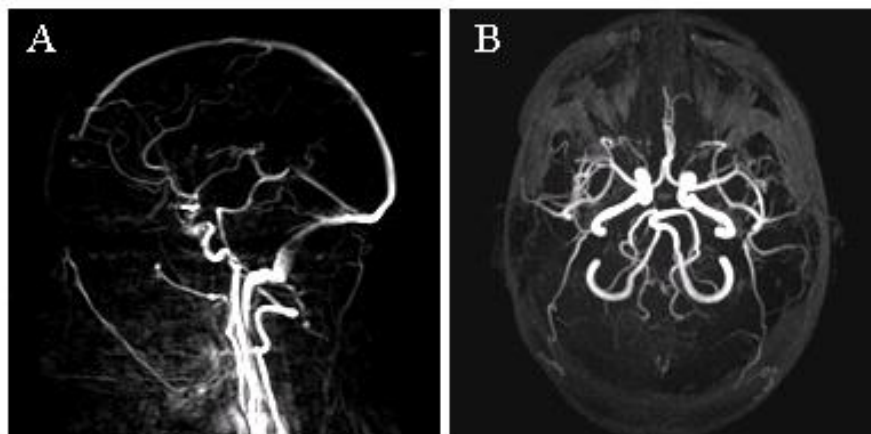
Figure 3.9: Non-invasive MR angiography in the form of (A) sagittal phase contrast angiogram (PCA) and Time of Flight (TOF) contrast angiogram (B).

3.5.2 Perfusion

Dynamic susceptibility contrast (DSC) and dynamic contrast enhanced (DCE) MRI measures perfusion using an exogenous contrast agent in the form of an injected bolus of paramagnetic material, such as gadolinium. By monitoring the contrast agent bolus over time, the cerebral blood flow (CBF) and cerebral blood volume (CBV) can be measured. This requires knowledge of the concentration of the contrast agent in the blood supply, also known as the arterial input function (AIF). Although DSC does give very spatially specific results within a specified region of interest (ROI), this technique is invasive, as gadolinium must be injected into the subject. Also, one is not able to control the transit delay of the bolus, which is not ideal, given that only one measurement of signal change can be obtained per bolus of contrast. Therefore in recent years, non-invasive perfusion methods are being investigated, one of which is Arterial Spin Labelling (ASL), which is a topic of research in Chapters 5 and 6 of this thesis.

3.5.3 Origin of Arterial Spin Labelling (ASL) signal

Arterial Spin Labelling (ASL) uses a magnetic label as an endogenous contrast used to measure perfusion MRI. Perfusion is the measurable quantity of the

flow of blood through the capillaries in tissue to deliver the oxygen and nutrients to the tissue, as demonstrated in Figure 3.10.
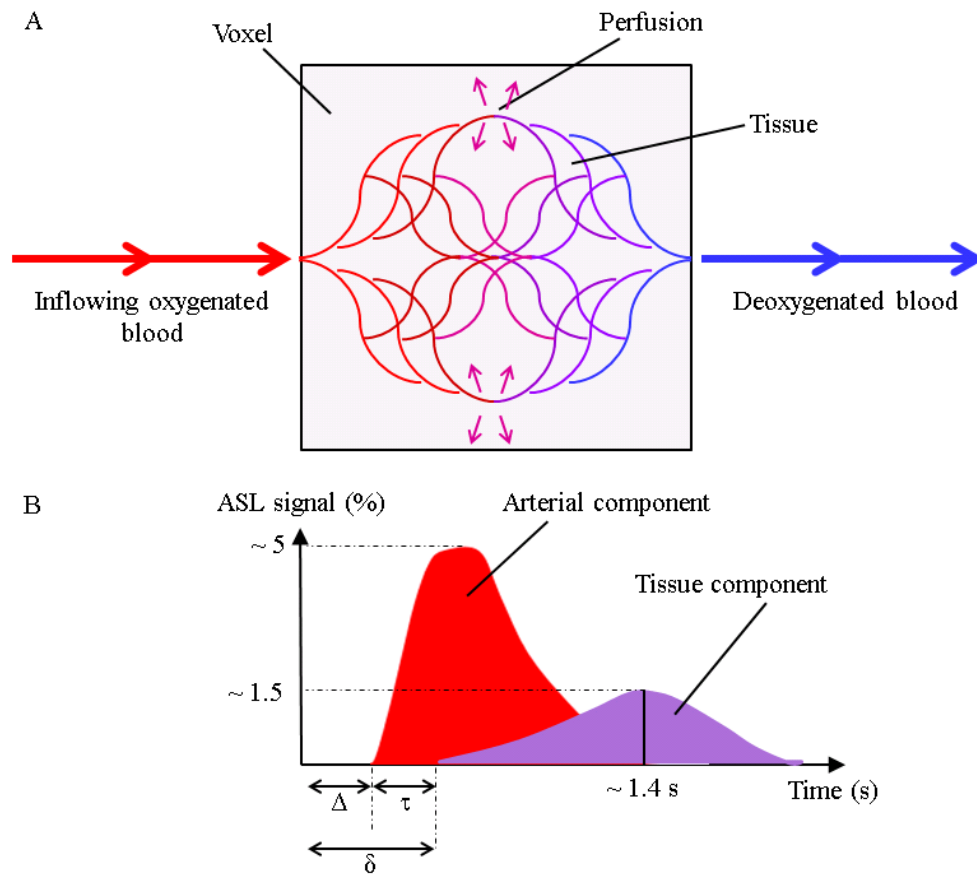
Figure 3.10: (A) Schematic of vasculature showing perfusion and (B) diagram outlining perfusion measurements in terms of arterial and tissue contributions to the ASL signal. The arterial transit time is given by Δ, and the capillary (tissue) transit time, δ. τ is the time taken for exchange between arterial and tissue compartments.

By manipulating the magnetisation of blood flowing into a region, ASL provides contrast in perfused tissue non-invasively. RF pulses are used to magnetically label hydrogen nuclei in blood water molecules, typically using hyperbolic secant or FOCI pulses to invert their longitudinal magnetisation. After a delay time for the labelled blood to enter the capillaries and perfuse the tissue (known as the inversion time or post-label delay, TI), the brain is imaged, resulting in a "label" image. A second, "control" image is then collected without this magnetic labelling. Subtracting the "label" image from the "control" image gives an ASL perfusion weighted difference signal, ΔM [59].

Using ASL to measure perfusion has several advantages. Primarily, ASL measures a physiologically meaningful quantifiable parameter, which leads to an unambiguous interpretation. In contrast to DSC, it is non-invasive and completely safe. This allows for repeated measurements to be taken and averaged, providing a robust, reproducible measure of cerebral perfusion. ASL does not interfere with or alter in any way the mechanism of brain activity and natural perfusion as labelling occurs completely undetected by the blood and surrounding tissue. For functional studies, ASL measures an absolute level of brain activity, rather than a change relative to baseline activity, an advantage over BOLD contrast. In this way it can be used not only to measure resting perfusion, but also to monitor changes associated with task activation [60] or with the administration of a pharmacological agent [61] or over a period of time [62], since ASL is not reliant on a T_2* weighted signal. This is important when measuring the effect of a drug on the CBF. ASL perfusion can also eliminate the problematic nature of low frequency scanner drift noise due to the fact that the ASL data are acquired by collecting and subtracting alternating label and control images [63].

Arterial Spin Labelling can be divided into two main types of labelling schemes: continuous (CASL) and pulsed (PASL), as depicted in Figure 3.11. In continuous ASL, the blood entering a narrow slice in the neck is continuously labelled for approximately 2 seconds using a low power radiofrequency pulse, to result in a steady state of flow driven inversion. This provides ASL images with a very high signal-to-noise ratio, but also requires a large amount of radio frequency energy resulting in a high specific absorption rate, SAR. CASL also typically requires the use of separate labelling and imaging coils, which are not usually available on commercially supplied machines. Conversely, pulsed ASL typically uses a short radiofrequency pulse, typically a hyperbolic secant pulse, lasting only a few milliseconds to label the blood entering a thick slab, with a much narrower label gap between the labelling region and the imaging region. In PASL, the same RF coil is used for both labelling and imaging. For both continuous and pulsed ASL schemes, an image is acquired after the post-label delay, TI.
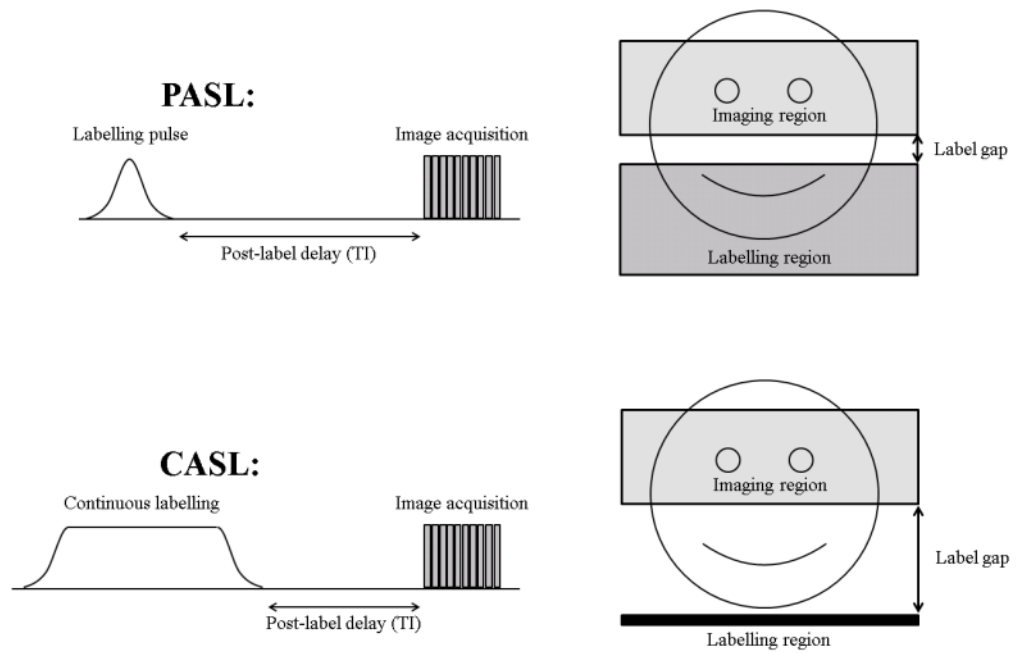
Figure 3.11: Diagram showing pulsed and continuous ASL; pulse sequence and relative placement of imaging and labelling regions.

The image encoding following the application of the label must be acquired rapidly before the label decays. Many different gradient echo and spin echo schemes are used, but most routine is Echo Planar Imaging (EPI), Gradient and Spin Echo (GRASE, [64]), true Fast Imaging with Steady-state Precession (FISP, [65]). All the work in this thesis uses a gradient echo – echo planar acquisition (GE-EPI) for the ASL acquisition. This is usually acquired using the shortest possible echo time (TE) for the sequence, often around 10 to 13 ms at 3 T, in order to minimise distortion due to magnetisation transfer effects. It is often desired to make different acquisitions at different echo times following the application of a single labelling pulse, in order to increase or decrease the sensitivity of the acquisition to the ASL inversion label.

The use of just one acquisition following an inversion pulse is known as single-phase (or single TI) ASL, and a post-label delay of approximately 1500 ms is often used at 3 T for the brain, as this time allows for the passage of the labelled arterial blood water into the tissue without the label decaying. However, the post-label delay required is dependent on the field strength as this alters the T_1 of the tissue being imaged. Above, single-TI ASL methods have been described; alternatively, one may vary the number of acquisitions

that follow a single inversion pulse. If measurement of arterial or tissue transit time is required, then a multi-phase method is used where images are acquired at intervals following labelling in order to follow the transit of blood through the brain for the duration of the T_1 of blood (approximately 1500 ms at 3T) [66], such as Look-Locker ASL [67] or QUASAR [68]. Timings can be varied to alter the sensitivity of the sequence to arterial or tissue signal, thus giving accurate measurement of either arterial blood volume (CBVa) and arterial transit time (Δ) or cerebral blood flow (CBF) and capillary transit time (δ). Signal readouts for each voxel can then be used to fit a curve of a hypothesised arterial input function for quantification of CBVa or CBF and the corresponding transit time [69, 70].

3.5.4   ASL Sequences

There are several different sequences available for pulsed ASL. Two of the most frequently used sequences are STAR (Signal Targeting Alternating Radiofrequency) [71] and FAIR (Flow-sensitive Alternating Inversion Recovery) [72]. Similar to FAIR is PICORE (Proximal Inversion with a Control for Off-Resonance Effects [73]). STAR, FAIR and PICORE use the application of a frequency selective adiabatic inversion pulse such as a hyperbolic secant or a FOCI (Frequency Offset Corrected Inversion) pulse. STAR has a user-specified labelling region in the neck, to which is applied a 180° inversion pulse in the labelling condition and two 180° pulses which sum to give a nominal 360° pulse in the control condition. FAIR and PICORE, on the other hand, work by using a selective inversion pulse with a slice select gradient for the labelling condition and a non-selective inversion in the absence of a slice select gradient for the control condition. FAIR and PICORE use a 180° flip angle for both label and control conditions, acquiring the control in the absence of a slice-selection gradient. Pulse sequences and positioning of selective inversion slabs with respect to labelling regions are shown for STAR, FAIR and PICORE in Figure 3.12.

A less frequently used technique is TILT (Transfer Insensitive Labelling Technique), also shown in Figure 3.12. TILT is based on the application of

two successive 90° pulses with a slice select gradient for both the label and control conditions. In the labelling condition, the pulses are in phase, causing accumulation of inversion, whereas in the labelling condition, the two pulses are equal and opposite, thus cancelling each other out.
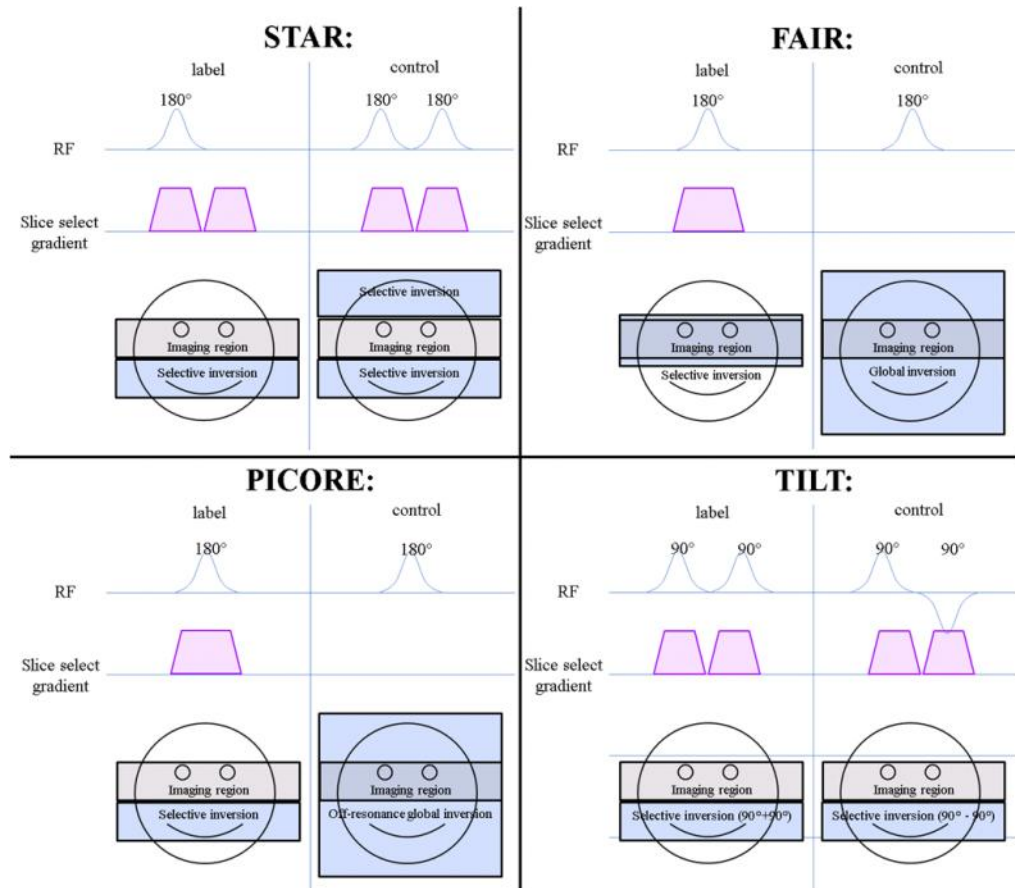
Figure 3.12: Pulse sequence diagrams for commonly used ASL sequences; STAR, FAIR, TILT and PICORE, showing RF pulses, gradients and position of inversion pulses with respect to the imaging region.

Another frequently used modification to pulsed ASL is QUantitative Imaging of Perfusion using a Single Subtraction (QUIPSS), and more recently, QUIPSS II. These involve the application of a saturation pulse either to the imaging slice (QUIPSS) or to the labelling region (QUIPSS II). This limits the duration for which labelled blood can continue to contribute to the MR signal (i.e. restricts the increase in cumulated signal to between two known time points), thus allowing quantitative CBF to be calculated using a single subtraction as opposed to multiple subtractions (LLEPI). QUIPSS and QUIPSS II are often used in functional perfusion experiments [74, 73].

A study in Chapter 4 of this thesis uses the recently developed pseudo-continuous ASL (PCASL) scheme. This labels a region in the neck below the imaging region, akin to continuous ASL, as shown in Figure 3.13. Typical label thicknesses used are of the order 100 mm, with a label gap of approximately 85 mm. Typically, a labelling duration of 1500 ms to 2000 ms is used, while post-label delay can vary from 900 ms to 1400 ms.
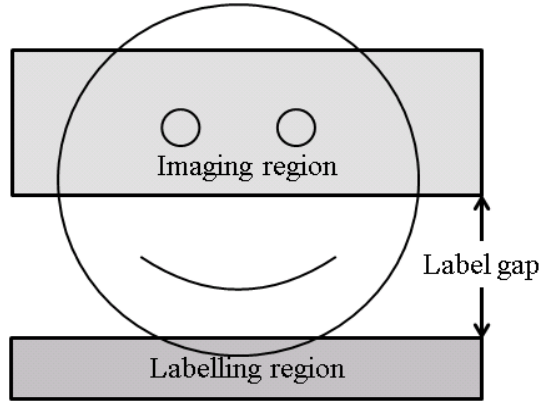
Figure 3.13: Schematic of PCASL, showing locations of labelling and imaging regions.

In PCASL, the repeated application of RF pulses produces a steady state in the absence of T_1 and T_2 decay [75]. If the rate of change of the direction of the steady state magnetisation is kept low, then the magnetisation can be considered to follow the steady state solution. The z component of the magnetisation in the steady state conditions is dependent on the flip angle of the RF pulse (α), and the phase shift experienced during the time between pulses (φ). It is therefore necessary to optimise the values α and φ to maintain the slowest rate of change of magnetisation vector. Eqn. [3.1] shows the steady state z component of the magnetisation, M_z, in terms of the RF flip angle, α, and the phase shift, φ [75].

$$M_z = \frac{\pm M_0 \sin \alpha \sin \frac{\varphi}{2}}{\sqrt{(1 - \cos \alpha)^2 + \sin^2 \alpha \sin^2 \frac{\varphi}{2}}} \qquad \text{Eqn. [3.1]}$$

The phase shift, φ, is described by a function of z position and flow velocity:

$$\Phi = \gamma \int_\delta Gzdt = \gamma \int_\delta G(z_0 + vt)dt = \varphi_0(z_0) + \varphi_1(v) \qquad \text{Eqn. [3.2]}$$

where, γ is the gyromagnetic ratio, G is the slice-select gradient, z_0 is the z distance from the labelling plane to the system isocentre, and v is the blood velocity through the labelling plane. For standard distances between the labelling plane and the imaging plane of approximately 100 cm, $\phi_0(z_0)$ (the zeroth order gradient moment) dominates over $\phi_1(v)$ (the first order gradient moment). Figure 3.14 shows the steady state solution of M_z for various values of the flip angle, α. The following plots show the effect of varying flip angle, α, on the z magnetisation as a function of phase shift, ϕ.
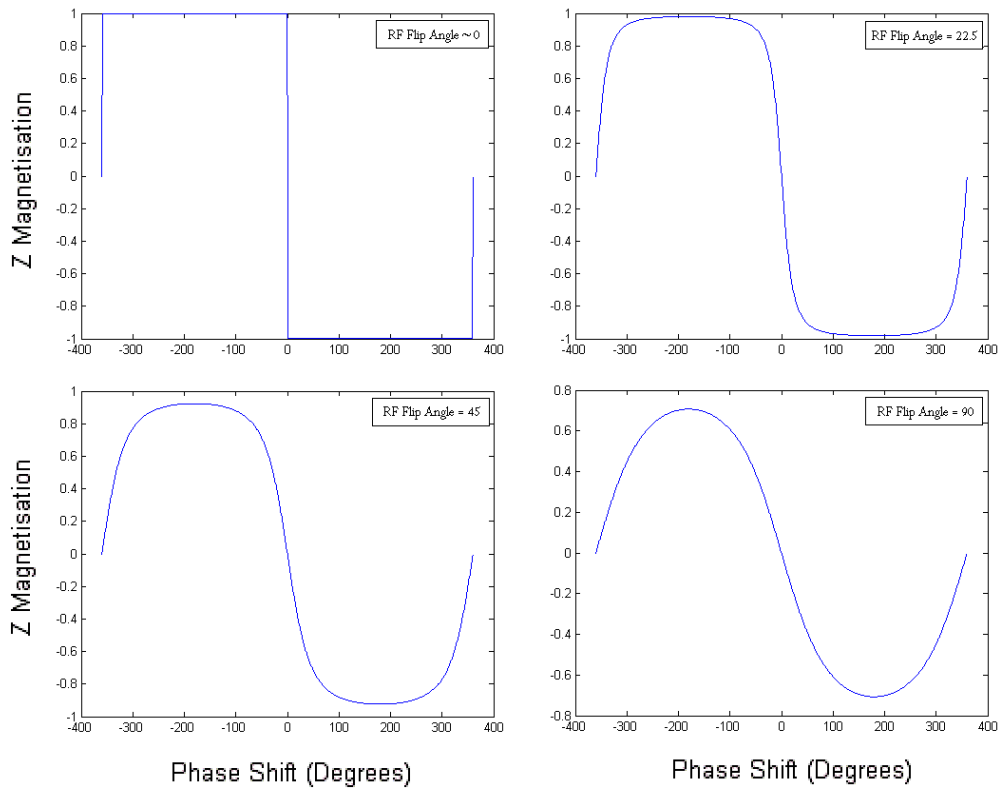
Figure 3.14: **Alsop model for the z component of the steady state magnetisation for four different values of α, the RF flip angle [75, 76, 77]. For slow changes in steady state angle, the magnetisation can be considered to follow the steady state solution.**

Wu et al [78] proposed two variants of the pseudo-continuous labelling schemes; balanced and unbalanced, as shown in Figure 3.15. Each scheme consists of a label and a control. For both schemes the polarity of the

71

radiofrequency pulse is constant during the labelling session, and alternates during the control session. The two schemes vary in their gradient properties; the balanced scheme uses a balanced non-zero zeroth gradient moment for both label and control, whereas the unbalanced scheme uses different gradients for the label and control conditions. The label condition has a non-zero balanced zeroth gradient moment whilst the control condition has nil zeroth gradient moment, and so no phase shift. Figure 3.15 shows a schematic of the pulse sequence for the balanced and unbalanced PCASL pulse sequences.
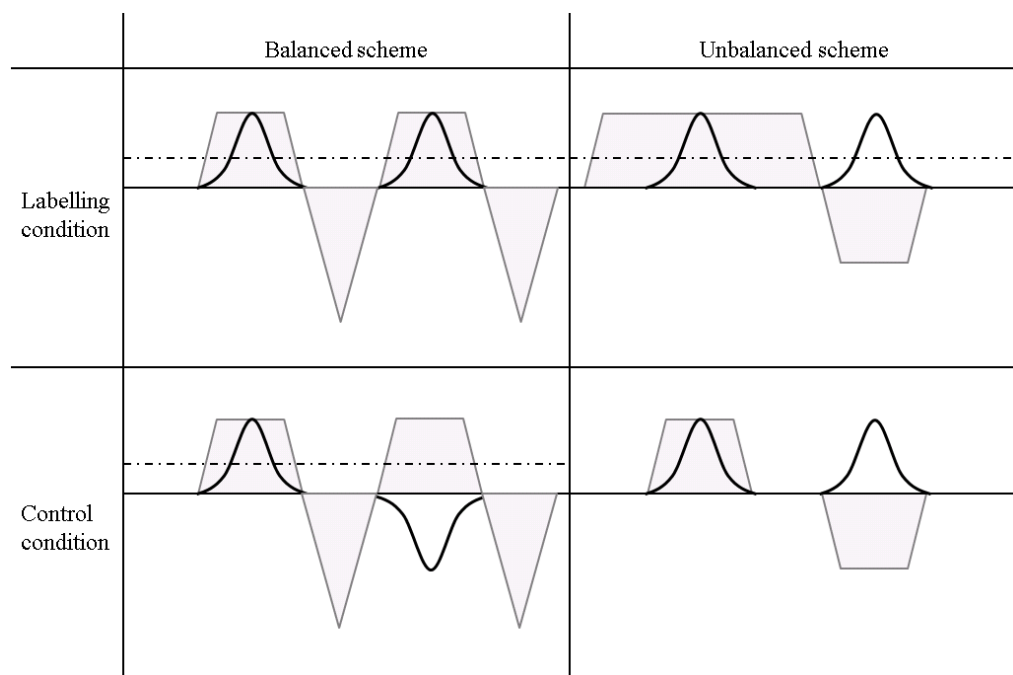
Figure 3.15: Balanced and unbalanced PCASL schemes; RF pulses and gradients shown for two consecutive pulses in the pulse train to demonstrate constant / alternating polarity of RF and gradients for each scheme.

The version of PCASL commercially available on the Philips MRI system uses an unbalanced PCASL scheme comprising repeated Hanning window RF pulses. These pulses have durations of approximately 0.5 ms and are repeated every 1 ms for a user-specified labelling duration.

Since development, PCASL has been widely used to demonstrate the measurement of steady state resting perfusion in grey matter and thus functional MRI [79] measurement of perfusion in white matter [80], and been

combined with multi-phase methods to quantitatively measure cerebral blood flow [81]. PCASL has been compared quantitatively with ^{15}O-water positron emission tomography (PET) for the reliability and accuracy of whole brain cerebral blood flow measurement and PCASL was found to reliably and accurately provide converging measurements in both white matter and grey matter regions of interest in healthy subjects and patients ranging in age from young to elderly [82].

3.5.5   CBF as a tool for measuring brain function

Regional perfusion changes provide a more direct method to assess neural activity than BOLD, as it only relies on the assumption that neuronal activation increases oxygen consumption in the cells, and therefore increased perfusion directly indicates the occurrence of brain activity. In contrast, the BOLD signal is dependent on a highly complex function of CBF, CBV and metabolic rate of oxygen consumption ($CMRO_2$), it cannot always be considered to directly reflect neuronal activity, and as described above can be confounded by differences in baseline vasculature (due to age, metabolic state, and the presence of disease or medication).

Arterial spin labelling presents the opportunity to detect regional perfusion changes with relatively high temporal resolution compared to positron emission tomography, which may correlate with the presentation of a task, the administration of a drug, or some other covariate of interest [72]. Studies have previously used ASL perfusion to isolate task related regional changes in perfusion. For example, ASL perfusion was used to localise activity associated with cue-induced nicotine craving in smokers [83]. 21 smokers underwent ASL fMRI while being shown smoking and non-smoking related cues. Smoking related cues were correlated with an increased level of perfusion as measured by ASL in the dorsolateral prefrontal cortex and the posterior cingulate cortex, both areas implicated in reward substrates, and drug conditioned reward substrates by *a priori* knowledge gained from humans and animals.

3.5.6 Pharmacological Modulation of ASL Perfusion

ASL can assess the effect of a drug on the brain in one of two ways; either to detect a global change in cerebral blood flow that correlates with drug administration [84, 26], or alternatively, to look for regional changes in the ASL signal, correlated with pharmacological interaction, which may signify the modulation of task related brain activity [31, 85]. In Chapter 4 of this thesis, both these methods are used to investigate the effects of the beta-blocker, propranolol.

In a study by Bendlin et al, the effect of caffeine was observed using BOLD contrast fMRI for its effect on the BOLD response to a word stem completion task, and on resting ASL perfusion [84]. 21 healthy volunteers were randomly divided into three groups: one group ingested a cup of coffee containing approximately 222 mg caffeine (n = 10), one group received decaffeinated coffee (n = 5), and one group water (n = 6). Subjects each had two scans, one at baseline, and one after receiving the coffee, decaffeinated coffee or water. In each scan, the subjects performed the word stem completion task while undergoing BOLD fMRI scanning. In addition, subjects were also scanned using ASL perfusion at rest. The ASL scan demonstrated, as expected, that caffeine significantly decreased the cerebral perfusion, whilst the two groups that were given decaffeinated coffee and water did not show any significant differences in perfusion, and so they were combined to form a single control group. Comparison between the first and second sessions showed that while the subjects that received caffeinated coffee exhibited a significant decrease in the extent of BOLD activation in the second scan, no significant change in extent of activation was found in the subjects in the control group. However, the signal intensity increased significantly in both the caffeinated coffee group and in the control group, with the control group having the greater rise in signal intensity, conflicting with previous findings [26]. Here, the use of ASL allowed the identification of a drug induced modulation of global perfusion that could explain the phenomenon detected using BOLD contrast fMRI.

The effect of caffeine on a visual and motor stimulus was assessed using simultaneous BOLD and ASL perfusion fMRI [31] using a PICORE Q2TIPS sequence [85]. This was performed before and after an intravenous infusion of either saline (placebo) or one of a number of caffeine doses. Both BOLD and ASL signal were compared before and after infusion. The maximum increased BOLD response was detected in the group that received an intermediate dose of intravenous caffeine, whereas the maximum CBF response as measured by ASL was detected in the group that received the highest caffeine dose. This decoupling of the two differently acquired observations of the haemodynamic response gives great insight into the mechanisms behind drug action and the dependence of BOLD signal on both neuronal activity and changes in baseline flow.

References

1.   Bullmore ET, Rabe-Hesketh S, Morris RG, Williams SC, Gregory L, Gray JA, Brammer MJ. Functional magnetic resonance image analysis of a large-scale neurocognitive network. NeuroImage. 4(1):16-33 (1996).

2.   Huettel, SA, Song, AW, McCarthy, G. Functional Magnetic Resonance Imaging. Sinauer Associates, Sunderland, Massachusetts, U.S.A (2004).

3.   Ogawa, S, Lee, T, Nayak, AS, Glynn, P. Oxygenation-Sensitive Contrast in Magnetic Resonance Image of Rodent Brain at High Magnetic Fields. Magnetic Resonance in Medicine, Volume 14, p68-78 (1990).

4.   Glover, GH. Deconvolution of Impulse Response in Event-Related BOLD fMRI. NeuroImage, Volume 9, p416-429 (1999).

5.   Friston KJ, Frith CD, Turner R, Frackowiak RS. Characterizing evoked hemodynamics with fMRI. NeuroImage. 2(2):157-65 (1995).

6.   Menon, RS, Ogawa, S, Hu, X, Strupp, JP, Anderson, P, Ugurbil, K. BOLD Based Functional MRI at 4 Tesla Includes a Capillary Bed Contribution: Echo-Planar Imaging Correlates with Previous Optical Imaging Using Intrinsic Signals. Magnetic Resonance in Medicine, Volume 33, p453-459 (1995).

7.   Kim, D, Duong, TQ, Kim, S. High-resolution mapping of iso-orientation columns by fMRI. Nature neuroscience, Volume 3, no 2, p164-169 (2000).

8.   Schroeter ML, Kupka T, Mildner T, Uludağ K, von Cramon DY. Investigating the post-stimulus undershoot of the BOLD signal - a simultaneous fMRI and fNIRS study. NeuroImage. 1;30(2):349-58 (2006).

9.   Lu H, Golay X, Pekar JJ, Van Zijl PC. Sustained poststimulus elevation in cerebral oxygen utilization after vascular recovery. J Cereb Blood Flow Metab. 24(7):764-70 (2004).

10.   Hua J, Stevens RD, Huang AJ, Pekar JJ, van Zijl PC. Physiological origin for the BOLD poststimulus undershoot in human brain: vascular

compliance versus oxygen metabolism. J Cereb Blood Flow Metab. 31(7):1599-611 (2011).

11.   Boynton, GM, Engel, SA, Glover, GH, Heeger, DJ. Linear systems analysis of functional magnetic resonance imaging in human V1. J. Neuroscience 16:4207–4221 (1996).

12.   Liu, Z, Rios, C, Zhang, N, Yang, L, Chen, W, He, B. Linear and Nonlinear Relationships between Visual Stimuli, EEG and BOLD fMRI Signals. Neuroimage 50(3):1054–1066 (2010).

13.   Huettel, SA, Güzeldere, G, McCarthy, G. Dissociating the neural mechanisms of visual attention in change detection using functional MRI. Journal of Cognitive Neuroscience, Volume 13, p1006-1018 (2001).

14.   Dale, AM, Buckner, RL. Selective averaging of rapidly presented individual trials using fMRI. Human Brain Mapping, Volume 5, p329-340 (1997).

15.   Yacoub, E, Shmuel, A, Pfeuffer, J, Van De Moortele, P, Adriany, G, Andersen, P, Vaughan, JT, Merkle, H, Ugurbil, K, Hu, X. Imaging brain function in humans at 7 Tesla. MRM 45:588 (2001).

16.   Peters, AM, Brookes, MJ, Hoogenraad, FG, Gowland, PA, Francis, ST, Morris, PG, Bowtell, R. $T2^*$ measurements in human brain at 1.5, 3 and 7 T. MRI, 25:748-753 (2007).

17.   van der Zwaag, W, Francis, S, Head, K, Peters, A, Gowland, P, Morris, P, Bowtell, R. fMRI at 1.5, 3 and 7 T: Characterising BOLD signal changes. Neuroimage 47:1425-34 (2009).

18.   Carter, CS, Heckers, S, Nichols, T, Pine, DS, Strother, S. Optimizing the Design and Analysis of Clinical Functional Magnetic Resonance Imaging Research Studies. Biol. Psychiatry. 64:842-849 (2008).

19.   FMRIB Software Library (FSL), version 4.1.6, Oxford Centre for Functional MRI of the Brain, UK (2008).

20.   Statistical Parametric Mapping, version 8 (SPM8), Wellcome Trust Centre for Neuroimaging, UCL, UK (2009).

21.   Glover GH, Li TQ, Ress D. Image-based method for retrospective correction of physiological motion effects in fMRI: RETROICOR. Mag Reson Med. 44:162–167 (2000).

22. Montreal Neurological Institute (MNI) Template. Montreal Neurological Institute, Montreal, Canada.

23. Friston, KJ, Ashburner, JT, Kiebel, SJ, Nichols, TE, Penny, WD. Statistical Parametric Mapping. Academic Press (2006).

24. Leslie, RA, James, MF. Pharmacological Magnetic Resonance Imaging: a new application for functional MRI. Trends in Pharmacological Sciences, 21:314-318 (2000).

25. Honey, G, Bullmore, E. Human pharmacological MRI. Trends in Pharmacological Sciences, 25(7):366-374 (2004).

26. Mulderink, TA, Gitelman, DR, Mesulam, MM, Parrish, TB. On the use of caffeine as a contrast booster for BOLD fMRI studies. NeuroImage, 15:37-44 (2001).

27. Perthen, JE, Lansing, AE, Liau, J, Liu, TT, Buxton, RB. Caffeine-induced uncoupling of cerebral blood flow and oxygen metabolism: A calibrated BOLD fMRI study. NeuroImage, 40:237-247 (2008).

28. Liu, TT, Behzadi, Y, Restom, K, Uludag, K, Lu, K, Buracas, GT, Dubowitz, DJ, Buxton, RB. Caffeine alters the temporal dynamics of the visual BOLD response. NeuroImage, 23:1402-1413 (2004).

29. Behzadi, Y, Liu, TT. Caffeine reduces the initial dip in the visual BOLD response at 3 T. NeuroImage, 32:9-15 (2006).

30. Abel, KM, Allin, MPG, Kucharska-Pietura, K, Andrew, C, Williams, S, David, AS, Phillips, ML. Ketamine and fMRI BOLD Signal: Distinguishing between Effects Mediated by Change in Blood Flow Versus Change in Cognitive State. Human Brain Mapping, 18:135-145 (2003).

31. Chen Y, Parrish TB. Caffeine dose effect on activation-induced BOLD and CBF responses. Neuroimage. 46(3):577-83 (2009).

32. McKie, S, Del-Ben, C, Elliott, R, Williams, S, del Vai, N, Anderson, I, Deakin, JFW. Neuronal effects of acute citalopram detected by pharmacoMRI. Psychopharmacology, 180:680-686 (2005).

33. Zhang H, Tian J, Zhen Z. Direct measure of local region functional connectivity by multivariate correlation technique. Conf Proc IEEE Eng Med Biol Soc. 2007:5231-4 (2007).

34. Biswal, BB, van Kylen, J, Hyde, JS. Simultaneous Assessment of Flow and BOLD Signals in Resting-State Functional Connectivity Maps. NMR In Biomedicine, 10:165–170 (1997).

35. Bandettini PA, Jesmanowicz A, Wong EC, Hyde JS. Processing strategies for time-course data sets in functional MRI of the human brain. Magn Reson Med. 30(2):161-73 (1993).

36. Kleinschmidt, A, Merboldt, K, Hanicke, W, Steinmetz, H, Frahm, J. Correlational Imaging of Thalamocortical Coupling in the Primary Visual Pathway of the Human Brain. Journal of Cerebral Blood Flow and Metabolism 14:952-957 (1994).

37. Hale, JR, Brookes, MJ, Hall, EL, Zumer, JM, Stevenson, CM, Francis, ST, Morris, PG. Comparison of functional connectivity in default mode and sensorimotor networks at 3 and 7T. Magn Reson Mater Phy 23:339–349 (2010).

38. Friston, KJ, Frith, CD, Liddle, PF, Frackowiak, RSJ. Functional Connectivity: The Principal-Component Analysis of Large (PET) Data Sets. Journal of Cerebral Blood Flow and Metabolism, 13:5-14 (1993).

39. Andrews-Hanna JR, Reidler JS, Sepulcre J, Poulin R, Buckner RL. Neuron. Functional-anatomic fractionation of the brain's default network. 65(4):550-62 (2010).

40. Biswal B, Yetkin FZ, Haughton VM, Hyde JS. Functional connectivity in the motor cortex of resting human brain using echo-planar MRI. Magn Reson Med. 34(4):537-41 (1995).

41. Friston, KJ, Buechel, C, Fink, GR, Morris, J, Rolls, E, Dolan, RJ. Psychophysiological and Modulatory Interactions in Neuroimaging. NeuroImage 6, 218–229 (1997).

42. McCabe, C, Mishor, Z. Antidepressant medications reduce subcortical–cortical resting-state functional connectivity in healthy volunteers. NeuroImage 57:1317–1323 (2011).

43. Dormal V, Dormal G, Joassin F, Pesenti M. A common right fronto-parietal network for numerosity and duration processing: An fMRI study. Hum Brain Mapp. [Epub ahead of print] (2011).

44. Minnebusch DA, Suchan B, Köster O, Daum I. A bilateral occipitotemporal network mediates face perception. Behav Brain Res. 198(1):179-85 (2009).

45. De Luca, M, Beckmann, CF, De Stefano, N, Matthews, PM, Smith, SM. fMRI resting state networks define distinct modes of long-distance interactions in the human brain. NeuroImage 29 1359 – 1367 (2006).

46. Filippini, N, MacIntosh, BJ, Hough, MG, Goodwin, GM, Frisoni, GB, Smith, SM, Matthews, PM, Beckmann, CF, Mackay, CE. Distinct patterns of brain activity in young carriers of the APOE-epsilon-4 allele. PNAS 106(17):7209–7214 (2009).

47. Cole DM, Beckmann CF, Long CJ, Matthews PM, Durcan MJ, Beaver JD. Nicotine replacement in abstinent smokers improves cognitive withdrawal symptoms with modulation of resting brain network dynamics. Neuroimage. 15;52(2):590-9 (2010).

48. Schwarz AJ, Gozzi A, Bifone A. Community structure in networks of functional connectivity: resolving functional organization in the rat brain with pharmacological MRI. Neuroimage. 1;47(1):302-11 (2009).

49. Bifone A, Gozzi A, Schwarz AJ. Functional connectivity in the rat brain: a complex network approach. Magn Reson Imaging. 28(8):1200-9 (2010).

50. Narayanan, A, White, CA, Saklayen, S, Scaduto, MJ, Carpenter, AL, Abduljalil, A, Schmalbrock, P, Beversdorf, DQ. Effect of Propranolol on Functional Connectivity in Autism Spectrum Disorder—A Pilot Study. Brain Imaging and Behavior 4:189–197 (2010).

51. Labus JS, Mayer EA, Jarcho J, Kilpatrick LA, Kilkens TO, Evers EA, Backes WH, Brummer RJ, van Nieuwenhoven MA. Acute tryptophan depletion alters the effective connectivity of emotional arousal circuitry during visceral stimuli in healthy women. Gut. 60(9):1196-203 (2011).

52. Khalili-Mahani N, Zoethout RM, Beckmann CF, Baerends E, de Kam ML, Soeter RP, Dahan A, van Buchem MA, van Gerven JM, Rombouts SA. Effects of morphine and alcohol on functional brain connectivity during "resting state":A placebo-controlled crossover

study in healthy young men. Hum Brain Mapp. [Epub ahead of print] (2011).

53. Rzepecki-Smith CI, Meda SA, Calhoun VD, Stevens MC, Jafri MJ, Astur RS, Pearlson GD. Disruptions in functional network connectivity during alcohol intoxicated driving. Alcohol Clin Exp Res. 34(3):479-87 (2010).

54. Tivarus, ME, Hillier, A, Schmalbrock, P, Beversdorf, DQ. Functional connectivity in an fMRI study of semantic and phonological processes and the effect of L-Dopa. Brain and Language 104:42–50 (2008).

55. Kelly, C, de Zubicaray, G, Di Martino, A, Copland, DA, Reiss, PT, Klein, DF, Castellanos, FX, Milham, WP, McMahon, K. L-Dopa Modulates Functional Connectivity in Striatal Cognitive and Motor Networks: A Double-Blind Placebo-Controlled Study. The Journal of Neuroscience 29(22):7364–7378 (2009).

56. Kunisato Y, Okamoto Y, Okada G, Aoyama S, Demoto Y, Munakata A, Nomura M, Onoda K, Yamawaki S. Modulation of default-mode network activity by acute tryptophan depletion is associated with mood change: a resting state functional magnetic resonance imaging study. Neurosci Res. 69(2):129-34 (2011).

57. Franklin TR, Wang Z, Sciortino N, Harper D, Li Y, Hakun J, Kildea S, Kampman K, Ehrman R, Detre JA, O'Brien CP, Childress AR. Modulation of resting brain cerebral blood flow by the GABA B agonist, baclofen: a longitudinal perfusion fMRI study. Drug Alcohol Depend. 1;117(2-3):176-83 (2011).

58. Bernstein, M, King, K, Zhou, X, Fong, W. Handbook of MRI pulse sequences, volume 32. Academic Press New York, (2005).

59. Wolf, RL, Detre, JA. Clinical Neuroimaging Using Arterial Spin-Labeled Perfusion MRI. Neurotheraputics, 4(3):346-359 (2007).

60. Boynton, GM, Engel, SA, Glover, GH, Heeger, DJ. Linear systems analysis of functional magnetic resonance imaging in human V1. Journal of Neuroscience, 16(13):4207-4221 (1996).

61. Petersen, ET, Zimine, I, Ho, YL, Golay, X. Non-invasive measurement of perfusion: a critical review of arterial spin labelling techniques. The British Journal of Radiology, 79:688-701 (2006).

62. Wang, J, Aguirre, GK, Kimberg, DY, Roc, AC, Li, L, Detre, JA. Arterial Spin Labelling Perfusion fMRI With Very Low Task Frequency. Magnetic Resonance in Medicine, 49:796-802 (2003).

63. Aguirre, GK, Detre, JA, Zarahn, E, Alsop, DC. Experimental Design and the Relative Sensitivity of BOLD and Perfusion fMRI. NeuroImage, 15:488-500 (2002).

64. MacIntosh BJ, Pattinson KT, Gallichan D, Ahmad I, Miller KL, Feinberg DA, Wise RG, Jezzard P. Measuring the effects of remifentanil on cerebral blood flow and arterial arrival time using 3D GRASE MRI with pulsed arterial spin labelling. J Cereb Blood Flow Metab. 28(8):1514-22 (2008).

65. Fenchel M, Martirosian P, Langanke J, Giersch J, Miller S, Stauder NI, Kramer U, Claussen CD, Schick F. Perfusion MR imaging with FAIR true FISP spin labeling in patients with and without renal artery stenosis: initial experience. Radiology. 238(3):1013-21 (2006).

66. Detre JA, Wang J. Technical aspects and utility of fMRI using BOLD and ASL. Clin Neurophysiol. 113(5):621-34 (2002).

67. Günther M, Bock M, Schad LR. Arterial spin labeling in combination with a look-locker sampling strategy: inflow turbo-sampling EPI-FAIR (ITS-FAIR). Magn Reson Med. 46(5):974-84 (2001).

68. Petersen ET, Lim T, Golay X. Model-free arterial spin labeling quantification approach for perfusion MRI. Magn Reson Med. 55(2):219-32 (2006).

69. Brookes, MJ, Morris, PG, Gowland, PA, Francis, ST. Noninvasive Measurement of Arterial Cerebral Blood Volume Using Look-Locker EPI and Arterial Spin Labeling. Magnetic Resonance in Medicine 58:41–54 (2007).

70. Francis, ST, Bowtell, R, Gowland, PA. Modeling and Optimization of Look-Locker Spin Labeling for Measuring Perfusion and Transit Time Changes in Activation Studies Taking into Account Arterial Blood Volume. Magnetic Resonance in Medicine 59:316–325 (2008).

71. Edelman RR, Siewert B, Adamis M, Gaa J, Laub G, Wielopolski P. Signal targeting with alternating radiofrequency (STAR) sequences:

application to MR angiography. Magn Reson Med. 31(2):233-8 (1994).

72.   Kim, SG. Quantification of relative cerebral blood flow change by flow-sensitive alternating inversion recovery (FAIR) technique: application to functional mapping. Magn. Reson. Med. 34, 293–301 (1995).

73.   Wong, EC, Buxton, RB, Frank, LR. Quantitative Imaging of Perfusion Using a Single Subtraction (QUIPSS and QUIPSS II). Magnetic Resonance in Medicine, 39:702-708 (1998).

74.   Iannetti, GD, Wise, RG. BOLD functional MRI in disease and pharmacological studies: room for improvement? Journal of Magnetic Resonance Imaging, 25:978-988 (2007).

75.   Dai, W, Garcia, D, de Bazelaire, C and Alsop, DC. Continuous Flow-Driven Inversion for Arterial Spin Labeling Using Pulsed Radio Frequency and Gradient Fields. Magn Reson Med. 60(6):1488-97 (2008).

76.   Garcia, DM, de Bazelaire, C, Alsop, D. Pseudo-continuous Flow Driven Adiabatic Inversion for Arterial Spin Labelling. Proc. Intl. Soc. Mag. Reson. Med. 13 (2005).

77.   Matlab. The MathWorks Inc., Natick, MA.

78.   Wu WC, Fernández-Seara M, Detre JA, Wehrli FW, Wang J. A Theoretical and Experimental Investigation of the Tagging Efficiency of Pseudocontinuous Arterial Spin Labeling. Magn Reson Med. 58(5):1020-7 (2007).

79.   Pfefferbaum, A, Chanraud, S, Pitel, A, Shankaranarayanan, A, Alsop, DC, Rohlfing, T, Sullivan, EV. Volumetric cerebral perfusion imaging in healthy adults: Regional distribution, laterality, and repeatability of pulsed continuous arterial spin labeling (PCASL). Psychiatry Research: Neuroimaging, 182(3):266-273 (2010).

80.   Lu, K, Liu, TT, Wong EC, and Jung, Y. Regional white matter perfusion measurement using an optimized pseudo-continuous ASL MRI. Proc. Intl. Soc. Mag. Reson. Med. 17 (2009).

81. Jung, Y, Wong, EC, and Liu, TT. Multiphase Pseudocontinuous Arterial Spin Labeling (MP-PCASL) for Robust Quantification of Cerebral Blood Flow. Magn Reson Med. 64(3):799-810 (2010).

82. Xu G, Rowley HA, Wu G, Alsop DC, Shankaranarayanan A, Dowling M, Christian BT, Oakes TR, Johnson SC. Reliability and precision of pseudo-continuous arterial spin labeling perfusion MRI on 3.0T and comparison with 15O-water PET in elderly subjects at risk of Alzheimer's disease. NMR Biomed. 23(3):286-93 (2010).

83. Franklin TR, Wang Z, Wang J, Sciortino N, Harper D, Li Y, Ehrman R, Kampman K, O'Brien CP, Detre JA, Childress AR. Limbic activation to cigarette smoking cues independent of nicotine withdrawal: a perfusion fMRI study. Neuropsychopharmacology. 32(11):2301-9 (2007).

84. Bendlin BB, Trouard TP, Ryan L. Caffeine attenuates practice effects in word stem completion as measured by fMRI BOLD signal. Hum Brain Mapp. 28(7):654-62 (2007).

85. Luh, WM, Wong, EC, Bandettini, PA, Hyde, JS. QUIPSS II with thin-slice TI1 periodic saturation: a method for improving accuracy of quantitative perfusion imaging using pulsed arterial spin labeling. Magn. Reson. Med. 41, 1246–1254 (1999).

4 Effect of beta-blocker on resting and task-driven brain activity

This chapter reports on a healthy volunteer study into the effect of the peripherally acting beta-blocker, nadolol on brain activity at rest and associated with the processing of an emotional visual stimulus. First, this chapter introduces the relevant literature on the processing of emotion and arousal stimuli. The measures that were taken to design the experiment, acquire and analyse the data are then described, followed by the results found.

4.1 Background

Several published experiments have led to the general understanding that there is a correlation between peripheral reactivity (such as changes in heart rate and blood pressure) during the processing of emotions and the underlying neuronal activity. The James-Lange theory of emotion, developed in the late 19th century but still commonly referred to [1], states that the experience of an emotion results from the perception (feeling) of an aroused bodily state (arousal). Subsequently, the two-factor theory of emotion [2] agrees that the perception of arousal is highly relevant, but states that the emotion experienced is due to a combination of the two factors of cognitive state and physiological arousal. Further, it suggests that awareness of physiological arousal causes enhanced emotional state, but the nature of arousal is the same for all emotions and that a subject will use emotionally relevant cues to interpret their feeling of arousal. Peripheral reactivity can be modulated by a pharmacological agent, such as a beta-adrenoceptor antagonist (beta-blocker), which causes a decrease in heart rate and blood pressure by blocking the uptake of adrenaline at the beta-adrenergic receptors.

4.1.1 Neural processing of emotion and arousal

The James-Lang theory of emotions is supported by many neuroimaging studies [3, 4, 5, 6], which demonstrate that peripheral autonomic nervous system responses to emotional stimuli, such as changes in heart rate and blood pressure, can be predicted by observing changes in the level of activity in

relevant brain regions, including the limbic system, comprising the amygdala, brainstem and the salience network (anterior insula and anterior cingulate). These regions have also been shown to be key areas implicated in mediating interoceptive awareness [7].

It is possible to describe states of mood and changes to those states in terms of two concepts when discussing the psychology and physiology of emotion and mood; *valence* and *arousal*. Valence is an emotional value that refers to the intrinsic attractiveness or aversiveness of a stimulus. Valence is scaled from highly aversive / highly unpleasant (corresponding to a low valence) to highly attractive / highly pleasant (high valence). Arousal is the state of being reactive to stimuli; being awake or alert. Stimuli can be described as ranging from soporific (low arousal) to highly stimulating (high arousal). These concepts are relevant when discussing peripheral autonomic reactivity as the degree of reaction induced in the autonomic nervous system by the presentation of a stimulus will be approximately correlated to the subjective arousal rating attributed to it [7]. While the valence and arousal of a given stimulus are generally independent, stimuli with extreme valences (very high or very low) are associated with higher arousal states than stimuli of neutral valence.

4.1.2   Functional neuroimaging studies of emotional processing

In the literature, there are many studies that report investigations into the brain's response to emotional visual stimuli. Here, some of these shall be outlined, and their findings reported.

Visual stimuli used in studies into emotional processing and mood induction often take the form of photographs of emotional faces, including happy, angry, sad, or disgusted facial expressions taken from the Standardized Face Database (The Karolinska Directed Emotional Faces – KDEF [8]) [3], or images combining emotionally arousing faces and scenes [9], as provided by the International Affective Picture System (IAPS [10]) [11, 12, 13]. The order

of presentation of stimuli of different valences is either randomised or fixed to ensure that any intensity carryover effects are minimised [14].

Neuroimaging in such studies is typically performed using fMRI [14] or Positron Emission Tomography (PET [11]). Electroencephalography (EEG) [12] and magnetoencephalography (MEG) [13] recording can also be used either alone, or EEG in combination with fMRI.

Subjective ratings of perceived mood are used to better understand neural processing of emotional stimuli. Participants in such studies are often asked to rate pleasantness and arousal of images during the imaging study, or outside the scanner using a system such as a self-assessment manikin (SAM, Bradley and Lang, 1994, Pollatos et al 2005). Conversely, in some studies, subjects are intentionally not asked to rate images, as this is viewed as a possible cause of alteration to brain activation patterns [16].

Critchley and co-authors assessed the link between peripheral processes and brain activity by identifying which regions of the brain exhibited activity that correlated with evoked changes in heart rate [3]. Subjects were presented with visual stimuli in the form of photographs of emotional faces during fMRI acquisition and the recording of heart rate. Critchley et al demonstrated that changes in heart rate in response to an emotional stimulus can be predicted by the level of activity within an emotion matrix of interconnected brain regions, including the amygdala, insula, anterior cingulate, and brainstem.

An article recently published in 2011 in the Journal of Addiction Biology by Kobiella et al [14] reports results from a pharmacological study similar in design to the one described in this chapter. Kobiella et al studied the effect of the stimulant Nicotine on the brain activity elicited by a mood induction task. This was a double-blinded, randomised crossover design, recruiting 35 healthy non-smoking participants. Subjects viewed emotional stimuli from the IAPS while undergoing fMRI. They used an event related design in which 40 images were used for each stimulus type (neutral, pleasant or unpleasant); each image was presented for two seconds, followed by a randomly varying

inter-stimulus interval of between 2.0 and 9.9 seconds (mean 6 seconds). Data were assessed for brain areas that showed greater activation in each of the emotional stimuli when compared to neutral stimuli.

Reviewing the literature, it has been shown that picture stimuli of both valence types (i.e. both pleasant and unpleasant images) are processed using a common subset of active brain regions, as shown in Table 4.1. Due to the use of visual stimuli, activations are always elicited in the visual cortex [17, 18]. For this reason, it is common to assess not only the areas of activation under emotional stimuli (i.e. the main effect), but also the areas that are more active during emotional stimuli *in comparison to* matched neutral stimuli (i.e. [pleasant > neutral], [unpleasant > neutral]). It is also possible to consider task-induced deactivation; areas that are less active during emotional stimuli during baseline, which can be further explored using contrasts such as [neutral > pleasant] or [neutral > unpleasant]. Few studies discuss this, and this thesis will focus on task-induced positive activation only. Table 4.2 shows brain regions that are reported as exhibiting activation in response to emotion and mood inducing visual stimuli, compared to neutral stimuli.

Emotional stimulus	Brain region	Papers
Fear	amygdala	[19]
Negative Emotion	dorsal cingulate cortex, dorsomedial prefrontal cortex	[12]
Pleasant / Unpleasant	insula	[20, 21]
Pleasant / Unpleasant	anterior cingulate cortex	[22, 18]
Pleasant / Unpleasant	medial prefrontal cortex	[23, 16, 24]
Pleasant / Unpleasant	ventromedial prefrontal cortex	[20]
Pleasant / Unpleasant	orbito-frontal cortex	[25]
Threat	amygdala	[26]

Table 4.1: Brain regions shown to exhibit activity in response to emotional and mood inducing visual stimuli as reported in the literature.

Stimulus comparison	Brain region	Papers
Pleasant > Neutral	amygdala	[15, 27, 18, 3, 14]
Pleasant > Neutral	hippocampus	[28, 29]
Pleasant > Neutral	precuneus	[11, 14]
Pleasant > Neutral	insula	[3]
Pleasant > Neutral	anterior cingulate cortex	[3, 14]
Pleasant > Neutral	brainstem	[3]
Pleasant > Neutral	right substantia innominata	[9]
Pleasant > Neutral	middle / inferior occipital gyrus, fusiform gyrus	[14]
Pleasant > Neutral	posterior cingulate cortex	[14]
Pleasant > Neutral	thalamus	[14]
Unpleasant > Neutral	amygdala	[15, 27, 18, 3, 14]
Unpleasant > Neutral	hippocampus	[28, 29, 14]
Unpleasant > Neutral	nucleus accumbens	[11]
Unpleasant > Neutral	precuneus	[11, 14]
Unpleasant > Neutral	insula	[3, 14]
Unpleasant > Neutral	brainstem	[3]
Unpleasant > Neutral	anterior cingulate cortex	[9, 3]
Unpleasant > Neutral	red nucleus, thalamus	[14]
Unpleasant > Neutral	fusiform gyrus, middle / inferior temporal gyrus, middle / inferior occipital gyrus	[14]

Table 4.2: Brain regions exhibiting greater response to emotional visual stimuli, compared to neutral visual stimuli as reported in the literature.

The salience network [27], comprising the bilateral insula and anterior cingulate cortex [30, 31], is believed to be involved in affective processes, such as emotional responses and interoceptive awareness [32, 33]. As shown in Table 4.1 and Table 4.2, these areas are widely reported as exhibiting increased activation in response to emotional visual stimuli, compared to neutral stimuli using a range of experimental designs. Additionally, the amygdala is reported in the processing of emotional stimuli, particularly those of a negative valence.

4.1.3 Modulation of emotional processing

It has been demonstrated that in patients with spinal cord injury that causes them to have a deficit in the peripheral feedback mechanism, there is a reduction in the level of brain activity in the interconnected emotion matrix of brain regions in response to an aversive fear conditioning task [6]. This difference was assessed using functional MRI in a study comparing brain activity in the spinal cord injury group with that of a healthy control group. The reduced activity in the task-related brain regions in the patient group was attributed to their reduction in feedback to emotional stimuli, thus supporting the hypothesis of the integration of emotion and bodily arousal.

The next question to investigate is whether a pharmacological manipulation of peripheral reactivity induced by drugs interacts with the experience of emotions and the central activation to the processing of emotional stimuli. This pertinent question gives a more practical controlled comparison, analogous to the spinal cord injury group described above. If a drug can replicate the disruption of the peripheral feedback mechanism found in patients with spinal cord injury, then it can be hypothesized that an experimentally induced decrease in peripheral reactivity should decrease both the experience of emotional intensity, as well as the accompanying brain activity during the processing of emotional stimuli.

The amygdala response to emotional verbal stimuli has been shown to be reduced by a single 40 mg dose of the centrally acting beta-blocker, propranolol [34]. In a placebo controlled fMRI study, it was demonstrated that the BOLD response to memory encoding in the amygdala and to memory recall in the hippocampus was reduced by propranolol compared to placebo, without any significant effect on recall ability.

Some behavioural studies have observed the effect of both peripherally and centrally acting beta-blockers on the memory of emotional material [35, 36]. Cahill et al [36] investigated the proposal that emotional memory of a stressful experience is associated with increased levels of the beta-adrenergic stress

hormone. 36 subjects were given a single dose of either 40 mg propranolol or placebo in a single-blinded design. One hour after tablet administration, subjects were presented with a sequence of slides showing a short story of either emotionally arousing or neutral matched content, with each slide being presented for 20 seconds. Memory assessment of the emotional story was carried out one week following the initial session. The study was designed to eliminate the confound that propranolol has been reported to affect alertness and concentration in patients. If this was the case, subjects would experience impaired memory of the neutral story in the propranolol condition compared to placebo, which was not found. Instead, the effect was selective impairment of the ability to recall the emotional story following propranolol compared to placebo; strongly supportive of the hypothesis that beta-blockade impairs the enhanced memory of emotional arousal.

In a later emotional memory recall experiment [35], the centrally acting beta-blocker, propranolol, the peripherally acting beta-blocker, nadolol, and a placebo were assessed. Subjects were randomly placed in one of the three drug groups and administered a single dose of either 40 mg propranolol, 40 mg nadolol or matched placebo. At the appropriate peak plasma concentration for the drug (a delay of 3 hours for nadolol, 1 hour for propranolol; the placebo group were divided equally between 1 hour and 3 hour delay), subjects were then shown emotionally arousing stimuli in the form of a slide show of an emotional story across 11 slides, each presented for 20 seconds, each with audio narration. This was almost identical to the slideshow described as the emotional stimulus in the study described prior to this one [36]. In this latter study, the slides that constituted the emotional story were grouped into neutral and emotive stimuli. A week later, subjects were examined on the detail they could recall. All subjects exhibited enhanced memory of the emotional stimuli compared to the neutral stimuli. However, this study reported no significant differences in memory recall ability between the drug groups. They concluded that the single 40 mg dose of each drug used in their study was insufficient to produce an effect.

4.1.4 Beta-blockers

Beta-blockers are a class of drugs that are widely prescribed as a treatment for a number of indications including hypertension, atrial fibrillation and prophylaxis of migraine. They act by inhibiting the stimulation caused by the uptake of epinephrine at the beta-receptors, thus having a negative chronotropic and inotropic effect on the heart, i.e. they decrease the heart's sympathetic actions of increasing the rate and strength of heart beat. Beta-1 receptors are located in the cardiac muscle, and a blockade of these receptors directly causes the observed decrease in heart rate and blood pressure. Beta-2 receptors are predominantly found in smooth muscles such as those that line the airways, (e.g. bronchial muscles). A blockade of beta-2 receptors causes airway constriction and for this reason, use of beta-blockers is contra-indicated in subjects with asthma, even if the subject is otherwise healthy. Some beta-blockers selectively block beta-1 or beta-2 receptors, whereas others termed "non-selective" will block all beta-receptors, although often there will be a preference for the blockade of one receptor type. The important distinction to be made in this study is that beta-blockers can be broadly divided into two subgroups; centrally acting and peripherally acting. This distinction refers to the extent to which beta-adrenergic transmission is blocked, i.e. whether the effect acts mainly on the central nervous system, the peripheral nervous system, or both. Centrally acting beta-blockers, such as propranolol, suppress autonomic responses from the central nervous system whilst peripherally acting beta-blockers, such as nadolol, suppress these signals from the peripheral nervous system. In the study presented in this chapter, the drug has carefully been chosen to be a peripherally acting beta-blocker, in order to modulate only the peripheral autonomic feedback, minimising modulation of central reactivity [35].

4.1.5 Summary of experimental design

Several studies have consistently demonstrated reduced amygdala responsiveness [34], and emotional memory encoding and retrieval under the influence of beta-blockade [35, 36, 38]. Much of this evidence has been the

product of research on post-traumatic stress disorder [39, 40]. For example, studies have reported that the administration of a beta-blocker to subjects who have recently experienced a trauma resulted in a significant reduction in their probability of later developing the disorder [39, 40]. The mechanism of action behind the effect reported in these studies however has a certain ambiguity as the beta-blocker used is the centrally acting beta-blocker, propranolol. A centrally acting beta-blocker causes a global modulatory effect on the autonomic nervous system, and is expected to result in decreased central reactivity, such as a reduction in CBF. When designing a study, care must be taken to eliminate the direct central effects of the chosen drug and disentangle the effects of reactions to emotional arousal compared to neutral stimuli. Since propranolol does not act selectively in the periphery, the modulatory effects that are reported in these papers may be direct central effects. To disentangle these possible effects, this chapter studies the influence of the peripherally acting beta-blocker, nadolol, on the fMRI response to neutral, pleasant and unpleasant visual stimuli. Nadolol crosses the blood brain barrier to a considerably lesser extent than a centrally acting beta-blocker. Emotional picture stimuli are expected to induce a change in mood, which will be reflected by changes in brain activity. This is further optimised by using a double blinded placebo controlled crossover study design.

It is currently not well understood whether modulation of the peripheral feedback mechanism will in turn modulate activity in the brain areas implicated in mediating interoceptive awareness. The idea of creating a pharmacological blockade of autonomous nervous responsiveness is an elegant way to test the James-Lange theory, and the more recent two-factor theory proposed by Schachter and Singer.

By collating current information in the literature, it is suggested that both stimuli of emotional faces and emotional scenes elicit the use of overlapping structures due to similarities in the underlying processes [3, 14]. On this basis, stimuli both of emotional faces and emotional scenes are used in this chapter. In this way, the study can observe drug modulation by the chosen drug, nadolol, on all picture stimulus types across the range of image valences.

Emotional images provide a stimulus which induces a mental state or "mood" in the subject. A block design is better suited to this type of stimulus, as it provides a longer period over which the stimulus acts, and a baseline period between stimuli of different valences allows the subject to return to baseline or switch "off" the mood, which will not happen as rapidly as for other visual stimuli [32]. Additionally, this design allows for comparison of each stimulus condition to a baseline, or "off" condition, assuming that its duration is long enough for the effect of the emotional stimulus to have worn off / dissipated. Further, this allows the comparison of each emotional state (pleasant, unpleasant) to the neutral state with respect to the baseline.

The number of repeated measurements should be maximised, whilst keeping the length of the entire study reasonable from the perspective of participant attention and comfort. Subjects' attention can be maintained by introducing a response task between stimulus blocks. In addition, information on subjective arousal rating can be useful in correlating intensity of activation with intensity of arousal perceived. Also, behavioural data can be used to identify or justify any outliers in the dataset.

The primary study aim of this chapter is to determine whether nadolol modulates activity in brain regions within the salience network during the presentation of emotional visual stimuli. Further secondary aims are:

- To determine whether any differences in activity are specific to the valence of the emotional stimulus (pleasant or unpleasant);
- To determine whether BOLD changes are associated with perfusion changes as measured using ASL;
- To determine whether nadolol modulates activity in regions not implicated in the salience network or the processing of emotional stimuli, indicative of a confound by direct central action of a beta-blocker;
- To determine whether there are changes in resting perfusion or resting functional connectivity in response to nadolol, which could explain the differences in response to stimuli, if found.

The hypothesis formed for the primary outcome measure is that a single 80 mg dose of nadolol reduces emotion-related bodily arousal, and in line with the James-Lange theory and the two-factor theory, consequently reduces the neural response to emotional stimuli. Despite contradictory previous results [35], nadolol is also expected to reduce subjective arousal and intensity of perceived emotional experience.

4.2 Materials and methods

4.2.1 Participants

The number of subjects required for statistical power can be calculated in terms of the effect size [41]. The effect size of previous studies with similar experimental designs have been adequate [42], and thus the recommendation of Carter et al is that an adequate sample size should be at least 15 to 20 subjects for comparison between subjects and stimuli. Therefore, this study design recruited 20 subjects, allowing for some subjects to be excluded later if necessary. For this reason, ethical approval was sought for the recruitment of 20 healthy volunteers for the pharmacological study; in addition 5 volunteers were recruited for the pilot study to optimise the scanning protocol and emotional stimuli. The study was approved by the University of Nottingham Medical School Research Ethics Committee in the form of an amendment to a previously approved pharmacological MRI study. Approval was also sought and obtained from the Nottingham University Hospitals Trust Research and Development department, also by amendment to a previously approved pharmacological MRI study. Approval from the Medicines and Healthcare products Regulatory Agency (MHRA) was not required, in compliance with the Clinical Trial Directive [43], as the effect under investigation is not related to the clinical action or efficacy of the drug.

Volunteers for the study were recruited *via* posters placed in academic and residential buildings on campus, in accordance with the Research Ethics Committee approval. The recruitment poster is given in Appendix A. All respondents to the advertisement were first screened for contra-indications to

MRI, including reporting negative for metal implants or prostheses, no metal objects in their bodies, and no history of claustrophobia, blackouts or seizures, and for contra-indications in their medical history against taking the beta-blocker, nadolol, for example a history of asthma or cardiac condition. The safety questionnaire used is included in Appendix B. Further, respondents underwent cardiac examination including 12-lead electrocardiogram, interrogated for cardiac output parameters and rhythm strips administered by a qualified cardiology nurse in Cardiology West, Queen's Medical Centre, Nottingham. Clinical assessment of healthy volunteers was undertaken by Dr A. A. Hosseini. Participants were English speaking and had normal vision or were able to use contact lenses to correct their vision to normal. Female participants were asked to confirm that they were not pregnant at the time of either scan. Volunteers gave fully informed written consent after the procedure was explained to them. Volunteers were asked to abstain from any psychoactive substances (including alcohol, caffeine, tea, chocolate, pain killers, energy drinks) on the day of each scan. All MRI scans took place between 4 pm and 8 pm.

Volunteers completed the following psychological questionnaires preceding their first MRI scan, for psychological assessment independent of drug effect:

- Hospital Anxiety and Depression Scale (HADS) [44]
- Emotion Reactivity Scale (ERS) [45]
- Toronto Alexithymia Scale (TAS) [46]
- Bermond-Vorst Alexithymia Questionnaire (BVAQ) [47]
- Interpersonal Reactivity Index (IRI) [48]
- Body Perception Questionnaire [49]

These questionnaires are provided in Appendix C.

4.2.2   Drug administration

Each volunteer attended two scan sessions, with a separation between sessions of 7 to 21 days. In each session, the participant was given a single tablet for

oral administration containing either 80 mg nadolol or placebo in a double-blinded, randomised, crossover design, as shown in Figure 4.1. Nadolol is a non-selective, peripherally acting beta-blocker, typically produced by Sanofi Aventis under the trade name Corgard [50] as an 80 mg tablet to be swallowed once a day, and is prescribed to patients for the treatment of hypertension, angina and migraine. The 20 tablets each of 80 mg nadolol and placebo were provided by the Pharmacy at the Queen's Medical Centre, Nottingham.
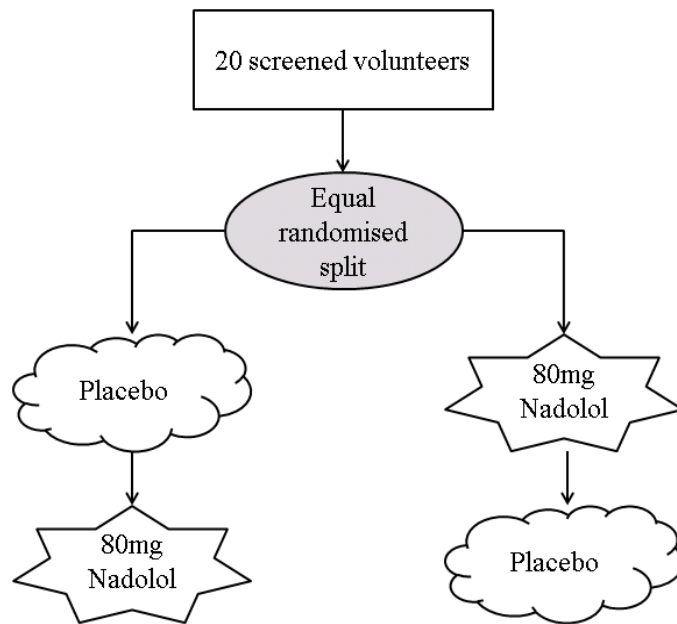
Figure 4.1: Schematic of randomised crossover pharmacological fMRI study design.

The peak plasma concentration of nadolol occurs approximately 3 hours after drug administration [38]. Therefore, after tablet administration, the volunteer waited 2 hours 30 min before commencing imaging to allow the peak plasma concentration of the drug to occur at the same point during each MRI scanning session. In each session, the volunteer spent approximately one hour in the MR scanner (with image acquisition time taking approximately 42 minutes).

4.2.3 Behavioural questionnaires

Directly before each MR scan, subjects underwent training for the functional task to be presented in the MR scanner. Following this, subjects completed two further behavioural questionnaires, devised by Professor Olga Pollatos:

- Pain empathy questionnaire: subjects were shown images of people in pain and not in pain and asked to rate the level of pain experienced, along with their rating of valence and arousal.

- Emotional faces questionnaire: subjects were asked to categorise the emotion depicted on the faces of the people in the photographs into the categories: neutral, happy, fearful, sad, angry and disgusted.

Copies of these questionnaires are given in Appendix D.

4.2.4 Physiological measurements

Blood pressure is a primary outcome measure of drug action. Blood pressure was measured at the beginning of the session, following a five minute rest period, to allow the blood pressure to settle after the subject arrived. This was followed immediately by tablet administration. Blood pressure was measured again at two hours following tablet administration, and a third time after leaving the MRI scanner, having allowed a further five minute rest period. Systolic and diastolic blood pressure readings were used to calculate mean arterial blood pressure (MABP). This is an estimate of the average blood pressure experienced throughout the cardiac cycle and is calculated from the systolic blood pressure (BP_{sys}) and diastolic blood pressure (BP_{dia}) using the following equation:

$$MABP = BP_{dia} + \frac{BP_{sys} - BP_{dia}}{3} \qquad \text{Eqn. [4.1]}$$

While systolic blood pressure and diastolic blood pressure are not described by a normal distribution in the population [51], mean arterial blood pressure in healthy adults can be approximated to a normal distribution, and thus normal distribution significance testing such as t-tests can be used [51, 52]. Therefore, MABP was compared across the three readings taken in each session, and between drug conditions using paired t-tests.

Vector cardiogram and breathing rate data were acquired during the entire scan duration (see Section 4.2.5). Vector cardiogram data from the resting state BOLD scan (duration 5 minutes) and from the emotion fMRI task (duration 14 minutes) were used for the calculation of the variance in cardiac cycle duration (peak-to-peak, or RR variance), and comparison of this effect between drug conditions. This time domain assessment of heart rate variance has been used previously as a surrogate for heart rate variability as calculated using frequency domain methods such as spectral analysis [53, 54], as there is a strong correlation between frequency domain variability and time domain variance [55]. Cardiac cycle length was calculated using in-house software written in Matlab, which read in the physiological log files produced by the MRI scanner and measured the separation of the cardiac markers. This was then used to calculate the variance in cardiac cycle across the duration of the scan. A paired t-test was used to make comparisons between drug sessions.

4.2.5   MRI scan protocol
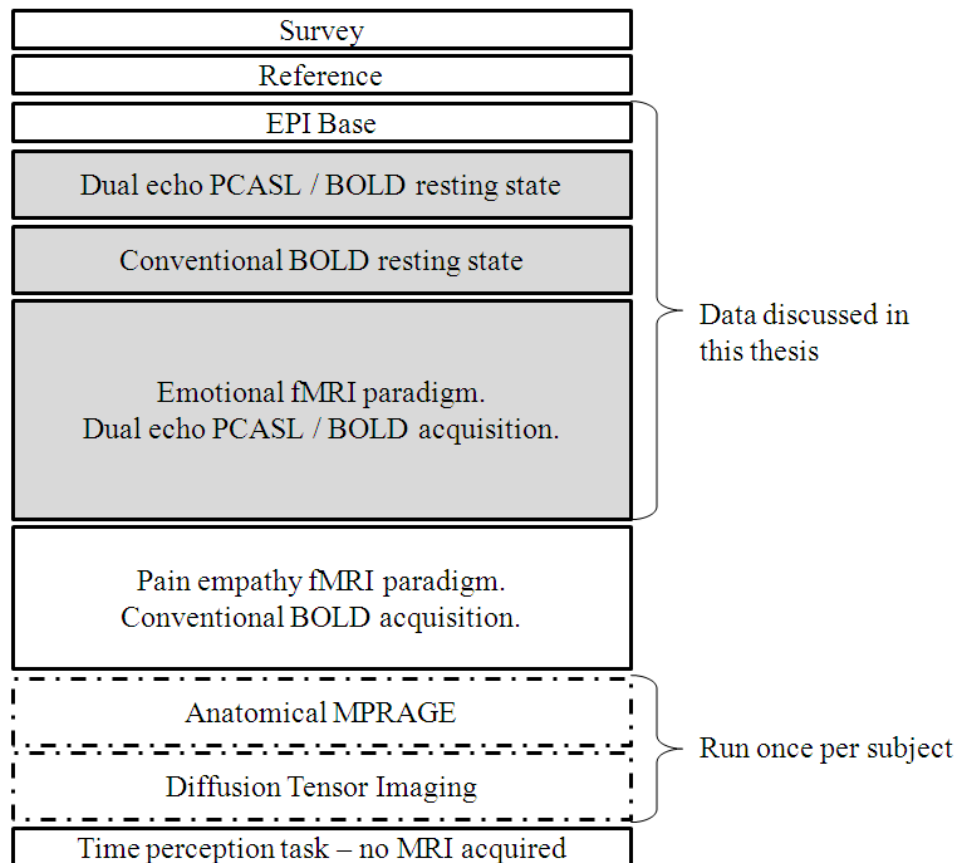
Figure 4.2: Complete scanning protocol for functional MRI study.

Figure 4.2 shows the complete scanning protocol performed. The focus of this chapter is on the results of the emotional fMRI paradigm. Resting BOLD and PCASL data were also acquired for baseline assessment of perfusion and resting state functional connectivity.

All MRI data were acquired on a Philips Achieva 3.0T MRI scanner with an 8-element SENSE head coil. Subjects were positioned comfortably in the MR scanner. Physiological data were acquired throughout scanning using respiratory bellows and a vector cardiogram provided by Philips Healthcare. A soft head restraint was used to limit head movement during image acquisition and for comfort. All stimuli were presented on a projector screen at the subjects' feet using the software Presentation [56]; subjects viewed the screen using a mirror attached to the RF coil placed approximately 10 cm from the face. Subjects were also given an 8-button response device [57], which was demonstrated to them. Following each task, the subject was asked if they were comfortable and happy to proceed, and the next task would be explained before proceeding. Before the tasks, subjects underwent a standard set-up protocol of survey and reference, and EPI test (two dynamic pairs of the dual echo EPI sequence with TE = 13 / 36.5 ms, at the same resolution as the other EPI scans, using a TR of 10 s). Further, 10 dynamic pairs of PCASL were acquired at the same parameters as the functional scan in order to test that the labelling scheme was working effectively. Next, the two resting state scans were performed (see Section 4.2.7 for full description), followed by the emotion visual stimulus fMRI paradigm (acquisition methods and task described in Section 4.2.8 and Section 4.2.9 respectively). After the emotion fMRI paradigm, subjects completed a pain empathy task, with a stimulus consisting of images of people in pain (to induce empathy in the subject) and control images of people not in pain. Images were matched for number of faces, limbs, motion, etc. Following this, subjects underwent a time perception task, during which no MR images were acquired. In this task, participants were asked to tap a response button at a rate that feels comfortable to them, for an undisclosed duration that was triggered on screen with "START" and "STOP" signals. The duration of the task was 60 seconds. During this time, subjects' breathing rate and cardiac output were recorded. It

is hypothesised that subjects will tend to press the button at a rate that is related to their heart rate, and that as nadolol lowers the heart rate, their responses will be slower under this condition. Anatomical MPRAGE and DTI scans were acquired once per subject, as they were considered to be independent of drug effect.

Scans were acquired in the same order on both scanning sessions for each participant. The scanning duration was approximately 47 minutes for the scan session that included the anatomical scans and 37 minutes without the anatomical scans. One hour was allowed for each scanning session as the subjects were MRI scanner naive, and additionally would need to be reminded of how to perform each upcoming task.

4.2.6 Optimisation of PCASL acquisition method

4.2.6.1   Background

In using MRI to optimally determine the brain regions that are active during the presentation of emotional stimuli, and further to detect modulation of this pattern of activity, it is essential to use a pulse sequence that provides good signal-to-noise ratio and contrast-to-noise ratio. As outlined in Chapter 3 of this thesis, the PCASL scheme uses a steady state technique, and as such, provides the optimal ASL sensitivity (contrast-to-noise) of all the schemes commercially available. I started to develop an unbalanced pseudo continuous arterial spin labelling (PCASL) pulse sequence using the pulse programming environment for use on the Philips 3 T Achieva MRI scanner. However, during this time, an unbalanced PCASL sequence was developed within Philips Healthcare, and included in the new version of the software release. Therefore, this commercial version of PCASL was used for the study presented in this chapter. Given that the study was to be performed in a clinical setting, this also had the additional advantage in PCASL being available in the commercial package of the MRI scanner, and this circumvented the need to apply and subsequently remove a software patch each scanning session.

A dual EPI acquisition method using two different TE values was chosen for the image readout, as this permits the simultaneous acquisition of two sets of images with different image contrasts. Perfusion weighted contrast was obtained using PCASL acquired at a short echo time (TE = 13 ms) and subtraction of the ASL label from control images. BOLD weighted contrast was subsequently acquired using the second echo of the dual echo EPI data collected at an echo time of 36.5 ms. A diagram showing the dual EPI acquisition to simultaneously acquire BOLD and ASL weighted images is shown in Figure 4.3.
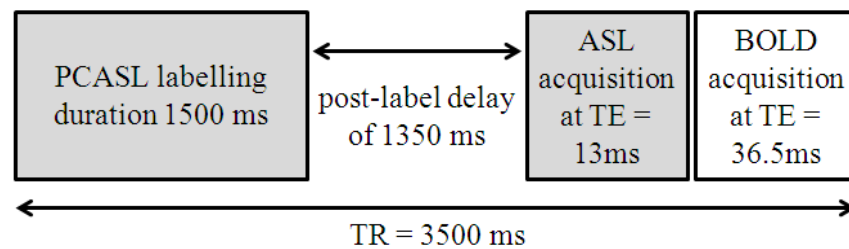
Figure 4.3: Sequence diagram showing simultaneous dual acquisition of BOLD and ASL images using the PCASL scheme.

4.2.6.2   Optimisation of PCASL for use in pharmacological fMRI studies

PCASL was tested on a healthy volunteer to optimise its use for the study. This involved finding optimum values of the flip angle, α, label gap, labelling duration and post label delay. In addition, the acquisition needed to be optimised for coverage and temporal resolution by determining the most appropriate values of echo time (TE), repetition time (TR), number of slices and spatial resolution. Published literature on the optimisation of PCASL for use in human neuroimaging was consulted. An example PCASL pulse sequence diagram is shown in Figure 4.4, showing the label as a series of several hundred RF pulses of flip angle, α, lasting approximately 0.5 ms, with a time between the start of two consecutive pulses of 1 ms. Labelling is followed by the post-label delay and the subsequent image acquisition. Figure 4.5 shows the geometric placement of the labelling and imaging regions, and the label gap.
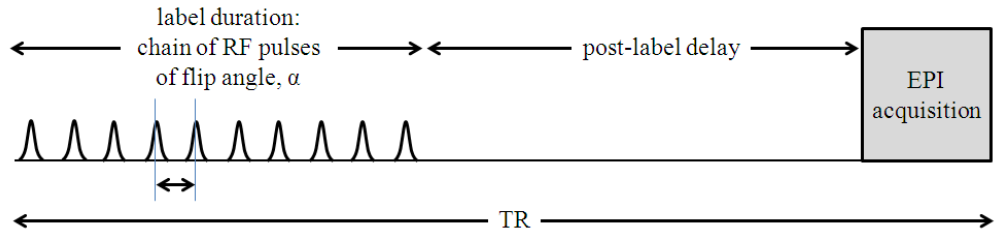
Figure 4.4: PCASL pulse sequence diagram for the labelling condition. The sequence used in this chapter has 1500 RF pulses, each lasting 0.5 ms.
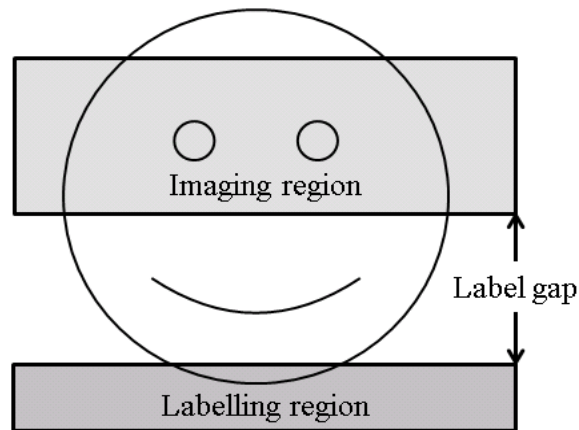
Figure 4.5: Diagram showing the label gap with respect to the positioning of labelling and imaging regions.

The optimum value of RF flip angle, α, labelling duration and post-label delay were determined from the published literature on experimental optimisation of PCASL [58, 59, 60, 61]. Typically, a labelling duration of 1500 ms to 2000 ms is used, while the post-label delay ranges from 900 ms to 1400 ms [58, 60]. Flip angles used in previous studies (α) can be seen to vary from 18° to 45° [58, 59, 60]. In the PCASL sequence used in this chapter, a labelling duration of 1500 ms was used, consisting of 1500 RF pulses, each lasting 0.5 ms, repeated every 1 ms, with a post-label delay of 1350 ms and a flip angle of 18°. For the image readout, the shortest possible echo time (TE) of 13 ms was chosen to provide optimal signal-to-noise of EPI images, with a readout flip angle of 90° and a TR of 3500 ms. Coverage had to be traded off against temporal resolution. For this study, it was decided that at a standard fMRI EPI resolution of 3mm × 3mm × 5mm, 13 axial slices would be sufficient. It is possible to determine the label gap experimentally [58], where the label gap is defined as the distance from the bottom of the imaging region to the top of the

selective inversion slab (Figure 4.5). For the purpose of this experiment, the base of the imaging slab was aligned with the Anterior Commissure – Posterior Commissure (ACPC), such that the imaging region would cover the amygdala and insula, and extend to cover the anterior cingulate cortex, which are the main anatomical regions of interest in this study. With the above values of label duration and post-label delay, the TR could be no shorter than 3500 ms. This is a compromise between the need for both temporal resolution and spatial resolution.

Optimum label gap was verified by assessing the ASL signal on a single healthy volunteer for a range of label gaps (50 mm, 60 mm, 75 mm, 85 mm, 95 mm, 120 mm and 150 mm), as shown in Figure 4.6 and Figure 4.7. Perfusion weighted signal intensity is proportional to the rate of perfusion. To assess the efficiency of the perfusion weighted image, mean signal intensity was calculated over a 15 mm diameter spherical region of interest placed in the grey matter of the primary visual cortex (GM ROI), and compared to the mean signal intensities for similar regions of interest in the posterior white matter (WM ROI). Figure 4.6 shows the perfusion weighted image obtained by labelling at each of the label gaps. As shown in Figure 4.7, the highest perfusion weighted signal for grey matter and white matter was achieved at a label gap of 85 mm, in agreement with published literature [58]. This value was therefore used in future experiments.
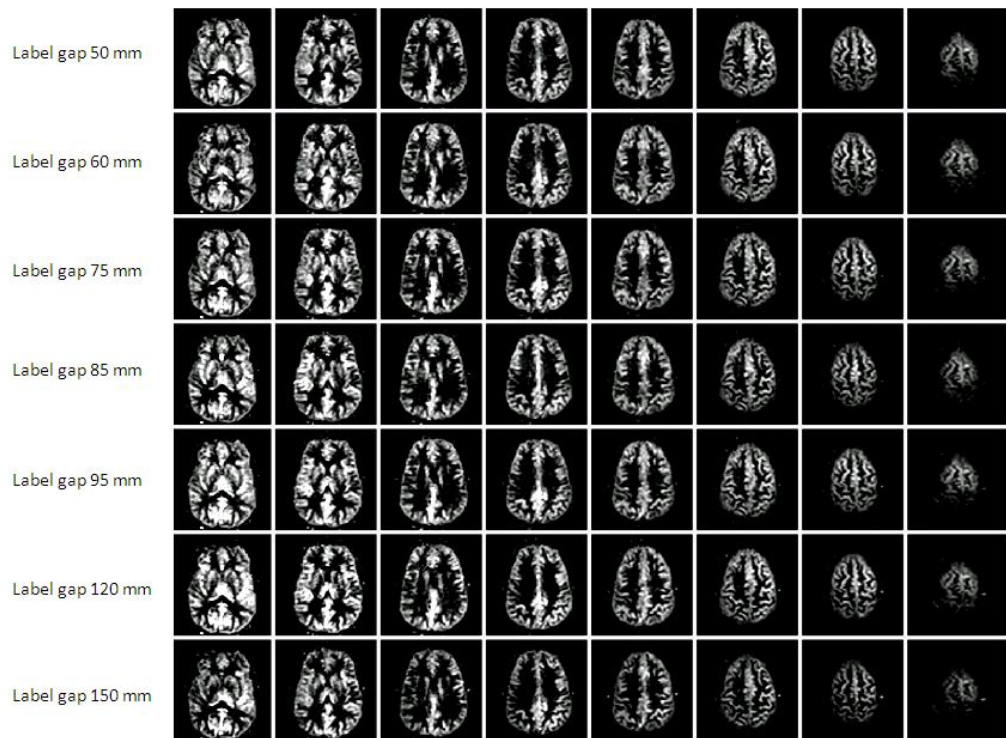
Figure 4.6: Perfusion weighted images produced at differing label gaps, to determine the optimal label gap for maximised signal intensity.
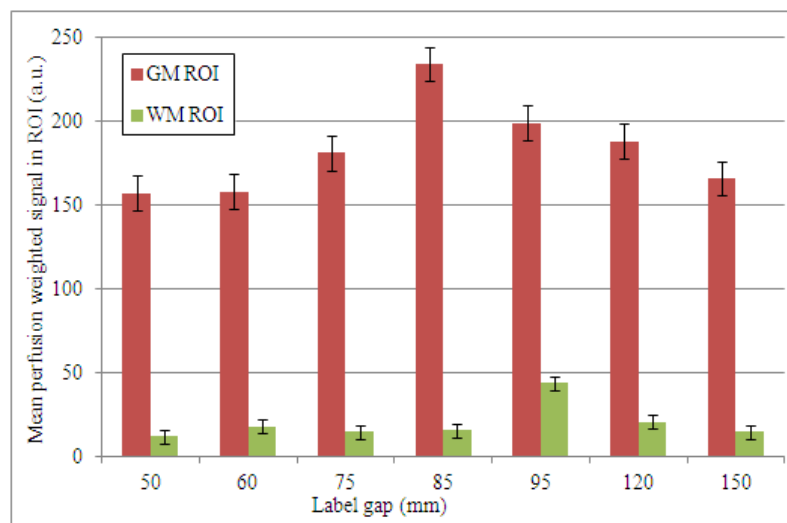
Figure 4.7: Mean perfusion weighted signal intensities (arbitrary units) for regions of interest in the grey matter (GM ROI) and white matter (WM ROI) as a function of label gap. A label gap of 85 mm is shown to provide optimal signal change.

4.2.7 Resting state data acquisition methods

Two resting state scans were acquired in this study; the first using PCASL to derive quantitative resting CBF measurement; 40 dynamic ASL pairs were

collected, using the same image parameters and coverage as described above and used for the emotion stimulus task. A total of 40 dynamic pairs resulted in a scan duration of 4 minutes 40 seconds. The second resting state scan was performed to assess functional connectivity. This used a conventional single echo EPI BOLD sequence with wider brain coverage than for the PCASL acquisition. BOLD images were acquired with a TE of 40 ms, flip angle 80°, 30 slices at 3 mm isotropic resolution. 150 dynamics were acquired at a TR of 2 s, making the scan duration 5 minutes. Immediately prior to both resting state acquisitions, four "dummy" dynamics were performed in order to induce a steady state to allow stabilisation of longitudinal relaxation. For both resting state scans, subjects viewed a grey screen with a central fixation cross. This was presented using Presentation software, version 14 [57]. Subjects were instructed to fixate on the cross and not to let their attention wander from it.

The resting state BOLD data was also used to assess for EPI data quality. This is important as the BOLD effect we are trying to extract from the EPI data is very small in magnitude, with subtle changes in this signal being less than 1%. Quality assessment was performed on the single echo BOLD data, as there are fewer confounds introduced by stimulation during the task. Data were analysed using the EPI stability tool (Philips Healthcare, [62]) to assess a large region of interest covering the central slice of each scan for radius of decorrelation (a measure of the spatial correlation of the noise in the MR signal), scanner drift, signal-to-noise ratio and signal-to-fluctuation noise ratio. Signal-to-fluctuation noise ratio is the ratio between the signal and the temporal fluctuation in the noise, and is analogous to temporal signal-to-noise ratio, not accounting for low frequency drift.

4.2.8   Emotion stimulus data acquisition methods

Double echo pseudo-continuous ASL – BOLD gradient echo, echo planar images were acquired using echo times of 13 ms for the ASL data and 36.5 ms for the BOLD data. As described above, PCASL was applied for a labelling duration of 1500 ms followed by a post-label delay of 1350 ms. The distance from the top of the labelling region to the start of the imaging region (i.e. the

label gap) was fixed to 85 mm [58]. Images were acquired using a TR of 3500 ms, a flip angle of 90° and a sense factor of 3. 13 axial slices of thickness 5 mm were acquired with an in-plane resolution of 3 mm. Two "dummy" dynamic pairs were performed at the beginning of the scan in order to induce a steady state, thereby reducing signal fluctuations caused by T_1 saturation effects.

4.2.9   Emotion stimulus task

The emotional stimulus consisted of neutral, pleasant and unpleasant photographic images from the International Affective Picture System (IAPS) test battery [10]. The 40 image numbers chosen for each condition are shown in Table 4.3. A pictorial representation of the fMRI task paradigm is shown in Figure 4.8. Each image was displayed for 3.5 s. This duration was chosen to match the TR of the acquisition of one ASL image. Images were grouped into blocks of 4 images of the same valence, making an "on" period of 14 s, after which there was an "off" period (fixation cross) of 14 s, during which the volunteer was prompted to rate arousal on a scale of 1 to 9, as previously trained outside the MRI scanner. Images chosen were standardised with respect to valence, arousal and dominance. Block composition was standardised with respect to arousal and number of faces. Images and blocks were ordered randomly, and the order differed between the two sessions to avoid habituation effects. Every image was shown once per session and no images were repeated within a session. This design was decided on in discussion with Professor Olga Pollatos from the University of Potsdam, based on the original study concept by Professor Dorothee Auer. Stimuli were presented, and behavioural responses were collected using Presentation software, version 14 [57].

	Valence		
	Neutral	Pleasant	Unpleasant
Image numbers from IAPS test battery [10].	2190, 2200, 2210, 2270, 2480, 2500, 2514, 2850, 5020, 5030, 5120, 5200, 5500, 5510, 5520, 5530, 5534, 6150, 7004, 7009, 7020, 7031, 7035, 7040, 7050, 7060, 7080, 7090, 7096, 7100, 7130, 7140, 7150, 7160, 7170, 7175, 7190, 7233, 7235, 7490	1560, 1590, 1601, 1603, 1710, 2000, 2040, 2050, 2070, 2080, 2150, 2165, 2303, 2311, 2340, 2341, 4599, 4601, 4603, 4610, 4653, 4689, 4700, 5600, 5830, 7230, 7260, 7325, 7330, 7350, 8041, 8080, 8120, 8185, 8190, 8200, 8420, 8461, 8490, 8510	1050, 1090, 1110, 1120, 1200, 1220, 1300, 1302, 1930, 2682, 2752, 2900, 3030, 3100, 3140, 3180, 3280, 3300, 3530, 6200, 6230, 6241, 6244, 6250, 6314, 6350, 6510, 6530, 6540, 6571, 6610, 9000, 9010, 9041, 9050, 9160, 9190, 9220, 9280, 9421

Table 4.3: Numbers of photographic images in the IAPS test battery used in the emotional visual stimulus fMRI paradigm.
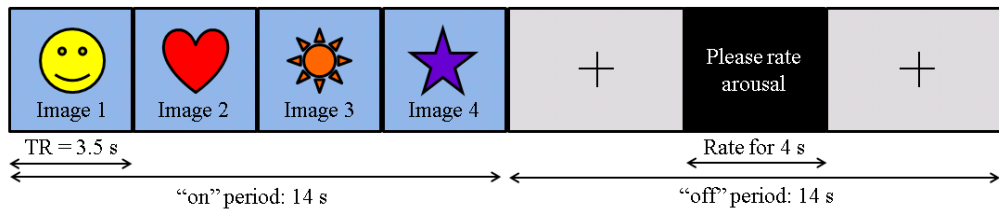
Figure 4.8: Diagrammatic representation of the fMRI task paradigm. This depicts one block of the "on" and "off" periods. This was repeated ten times for each stimulus of neutral, pleasant and unpleasant valence. Total duration = 14 minutes.

4.2.10 Analysis of all MRI data

Data were quality assessed, and any dataset that exhibited excessive motion (greater than 2 mm translation between dynamics) was excluded from further analysis. All data were corrected for physiological noise caused by breathing and heart rate using software written by Emma Hall based on RETROICOR [63], then motion corrected and co-registered to MNI space [64] using an affine registration transformation to a voxel size of 2 mm isotropic. Resting BOLD data were acquired at an original resolution of 3 mm isotropic and were smoothed with a Gaussian kernel of FWHM 5 mm. Data from the emotion stimulus task were acquired using a slice thickness of 5 mm and thus a broader

smoothing was used, with a FWHM of 8 mm. Motion correction, realignment and smoothing preprocessing steps were performed using SPM8 [65].

4.2.11 Analysis of resting ASL data

Following preprocessing, the voxel-by-voxel average percentage change in ASL signal over the scan duration was calculated. These images were then divided through by the EPI base image to normalise the ASL signal to the base EPI signal. Mean and standard deviation values in a grey matter mask were calculated for each subject, under each drug condition. Further, using SPM8, a paired t-test was carried out between resting perfusion weighted data for the two drug conditions. Group maps were threshold to a significance level of $p < 0.001$ uncorrected, with a cluster threshold of 20 voxels.

4.2.12 Analysis of resting state BOLD data

Initial probabilistic independent component analysis (ICA) was carried out using Multivariate Exploratory Linear Optimised Decomposition into Independent Components (MELODIC) from FSL [66]. High pass temporal filtering was applied at 300 s. No low pass temporal filtering was applied. Data were temporally concatenated across subjects and the group analysis was performed on this single concatenated 4D data set. There was no limit given on the number of independent components to generate. Independent component maps produced by the analysis were thresholded at $p > 0.5$, so that the voxels reported in each component have a greater probability of contributing to that component than to the background noise [66]. Independent component analysis allows preliminary hypothesis-free analysis to confirm the presence of networks of interest, and identify appropriate seed regions for further hypothesis-driven analysis techniques.

Psychophysiological interaction analysis was used to assess the presence of both the default mode network and the salience network and to determine whether these networks were modulated by the drug nadolol. This analysis requires the selection of a seed, based on *a priori* knowledge of the networks

concerned. Seeds for both networks were 9 mm diameter spheres placed on co-ordinates from the literature. For the default mode network (DMN), a seed was placed at MNI co-ordinates [0 -45 30] in the posterior cingulate cortex (PCC) [67, 68]. For the salience network, a seed in the anterior cingulate cortex, MNI co-ordinates [0 18 42], was used [69]. The average BOLD signal was extracted for the volume of the seed for each of the 150 time points. Next, functional connectivity analysis was performed in SPM8 [65] using a general linear model. The timecourse of the network seed was used as a regressor, and the motion parameters were included as covariates of no interest. Higher level group comparisons were then performed in a random effects analysis in the form of single group t-tests of each drug condition and paired t-tests between the two drug conditions. Clusters of significance $p < 0.001$ uncorrected were considered.

4.2.13 Analysis of BOLD fMRI Data from emotion task

Random effects analysis was performed using Statistical Parametric Mapping, version 8 (SPM8), and software toolboxes coded in Matlab [70]. First level analysis used a general linear model of the stimulus duration convolved with a canonical haemodynamic response function to calculate the effect of the three stimulus conditions (neutral, pleasant and unpleasant). The six motion parameters and button press for arousal rating were included in the model as covariates of no interest.

Second level random effects analysis with a one sample t-test was used to assess the main effect of the task and a paired t-test to assess differences between the two drug conditions. A flexible factorial design of repeated-measures ANOVA was used to assess within-subject comparisons between the three stimuli (neutral, pleasant, unpleasant) and drug conditions (nadolol, placebo). Subjects, stimulus valence and drug conditions were input as three independent factors in the design. This allowed the interrogation of the interaction between the factors of drug condition and stimulus valence. The difference effects between stimulus conditions ([pleasant > neutral], [unpleasant > neutral]) were then assessed between drug conditions; [pleasant

> neutral for placebo] greater than [pleasant > neutral for nadolol] and *vice versa*. At this point, a binary mask of the main effects was applied to the data such that stimulus correlated changes could confidently be interpreted as increases or decreases in "positive BOLD" activation, and not "negative BOLD" deactivation. Significance was reported for differences between drug conditions at $p < 0.001$ uncorrected.

There may be detectable differences between the way that male and female subjects process emotional stimuli, and thus differences in drug modulation of this effect between the two gender groups were explored using a flexible factorial design for each gender group, to a significance level $p < 0.001$. Due to the small number of subjects ($n < 10$) in each gender group, this subgroup analysis is clearly underpowered and thus exploratory only.

Finally, anatomically defined regions of interest were defined using an anatomical atlas (WFU Pick Atlas toolbox from SPM8) [65] based on areas reported in the literature to be instrumental in emotional processing. Regions of interest in the anterior insula, anterior cingulate cortex and amygdala were chosen [9, 18, 3, 14]. In addition, a control region was used in the form of a 7 mm sphere in the primary visual cortex as this region is active during the task, but not implicated in emotional processing. These regions of interest were used to interrogate the parameter estimates for BOLD changes (beta values) for each subject in the group and each drug condition. Parameter maps were also interrogated using regions of interest defined from areas exhibiting notable differences in activity between the two drug conditions, while still avoiding circularity [71].

4.2.14 Analysis of PCASL fMRI Data from Emotion Task

After subtraction and linear interpolation of ASL label and control pairs, the resulting perfusion weighted images were preprocessed as described in Section 4.2.10.

First level analysis was performed using Statistical Parametric Mapping, version 5 (SPM5, [65]), as described for the BOLD data, using a general linear model to model the effect of the three stimulus conditions (neutral, pleasant and unpleasant) and including the button press rating and motion parameters as covariates of no interest. Higher level analysis used a flexible factorial design that interrogated the differences between two conditions ([pleasant > neutral] and [unpleasant > neutral]) for each pair of drug conditions ([nadolol > placebo] and [placebo > nadolol]). As with the BOLD data, parameter maps were masked using a binary mask of main effects, and significance was reported at a level of $p < 0.001$. Region of interest (ROI) analysis was performed as described in Section 4.2.13.

4.3 Results

Twenty ($n = 10$ male, $n = 10$ female) healthy, non-smoking volunteers, with a mean age $= 22 \pm 2$ years took part in the study. All participants had a body mass index (BMI) in the healthy range, with a group mean of 22 ± 2. All 20 subjects attended both scan sessions (drug and placebo); with a mean $\pm$ standard deviation of 13 ± 5 days between visits. All subjects accepted both tablets without adverse side effects, and were compliant with the performance of the task and with the MRI scan and physiological monitoring.

4.3.1 EPI stability data

Mean, range and standard deviation of the values of radius of decorrelation, scanner drift, image signal-to-noise ratio and temporal signal-to-noise ratio define the image quality of the resting BOLD data. Radius of decorrelation is a measure of the spatial auto-correlation of the noise in the signal across the image [62]. These values are shown in Table 4.4. Literature shows that acceptable values for the radius of decorrelation cover a range between 4.4 and 16.6 pixels [62]. Scanner drift measurements should be low. Values of image signal-to-noise ratio (SNR) and temporal signal-to-fluctuation-noise ratio (SFNR) should be similar and as high as possible [62].

	Mean	Standard Deviation	Minimum	Maximum
RDC [pixel]	7.82	2.73	5.09	10.55
Drift [%]	0.03	0.59	-0.56	0.62
SNR mean across ROI	73.99	12.49	61.50	86.48
SFNR mean across ROI	70.47	10.62	59.84	81.09

Table 4.4: Quality assessment of resting state EPI data showing the radius of decorrelation (RDC), scanner drift, signal-to-noise ratio (SNR) and signal-to-fluctuation noise ratio (SFNR) as calculated using EPI Tool (Philips Healthcare, [62]).

4.3.2 Physiological data

Blood pressure measurements for readings before tablet administration, 2 hours following tablet administration and following MRI scan are shown in Table 4.5. All subjects experienced a reduction in blood pressure after 2 hours. All subjects were deemed to exhibit a high enough blood pressure to be safe to leave the centre after the final blood pressure measurement.

	80 mg nadolol	**placebo**
On arrival	110/73 ($\pm$8/6)	108/69 ($\pm$8/8)
After 2 hours	99/65 ($\pm$8/7)	104/68 ($\pm$9/8)
After MRI scan	108/72 ($\pm$13/9)	115/74 ($\pm$10/11)

Table 4.5: Mean ($\pm$ standard deviation) values of blood pressure (systolic / diastolic) across the group (n = 20).

Nadolol caused a drop in blood pressure of 11/8 mmHg compared to a drop of 4/1 mmHg in the placebo group. Individual subjects' mean arterial blood pressure (MABP), are shown in Figure 4.9, and were interrogated with a paired t-test; MABP (mean $\pm$ standard deviation) dropped from 85.1 $\pm$ 6.3 mmHg to 76.7 $\pm$ 6.0 mmHg, a significant reduction of $p < 5 \times 10^{-7}$ correlated with drug administration, while MABP dropped only slightly from 82.1 $\pm$ 6.7 mmHg to 79.6 $\pm$ 6.8 mmHg in the placebo condition, which is not significant (Figure 4.10). The difference between drug conditions was significant to $p < 0.002$, corrected for multiple comparisons.
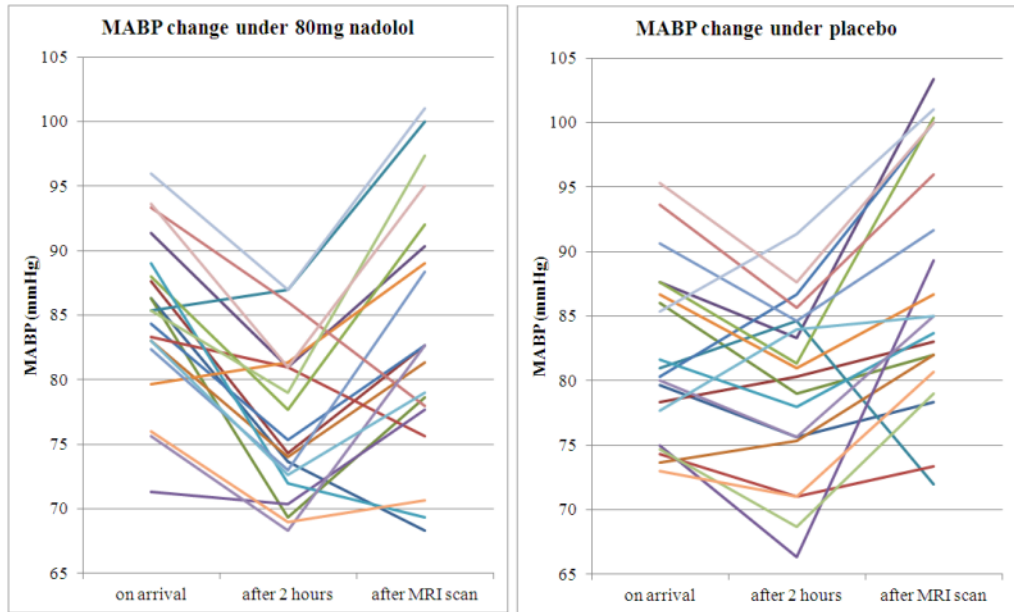
Figure 4.9: Mean arterial blood pressure (MABP) measurements for all subjects (n = 20), under both drug conditions.
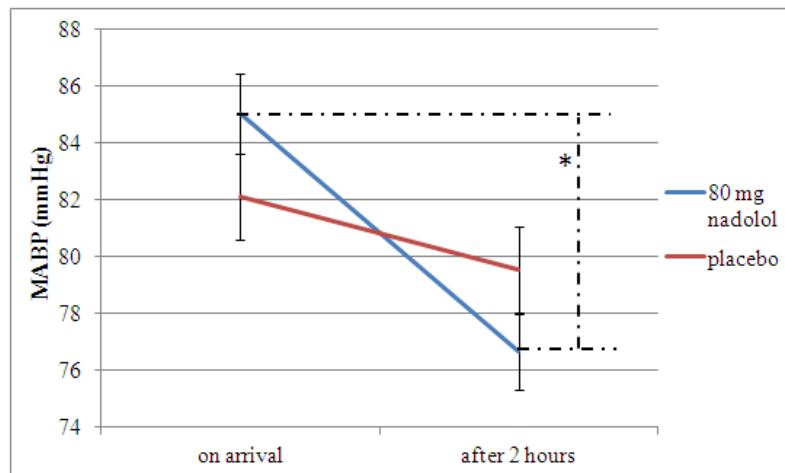
Figure 4.10: Group (n = 20) average (± standard error) effect of nadolol and placebo on mean arterial blood pressure (MABP). Asterisk represents a significant reduction in MAPB 2 hours after drug administration (p < 0.002, multiple comparisons corrected).

Nadolol reduced heart rate with significantly greater effect than placebo, as expected. A mean reduction of 17 beats per minute was found for nadolol compared to 10 beats per minute for placebo (significance of p < 0.01), as shown in Figure 4.11.
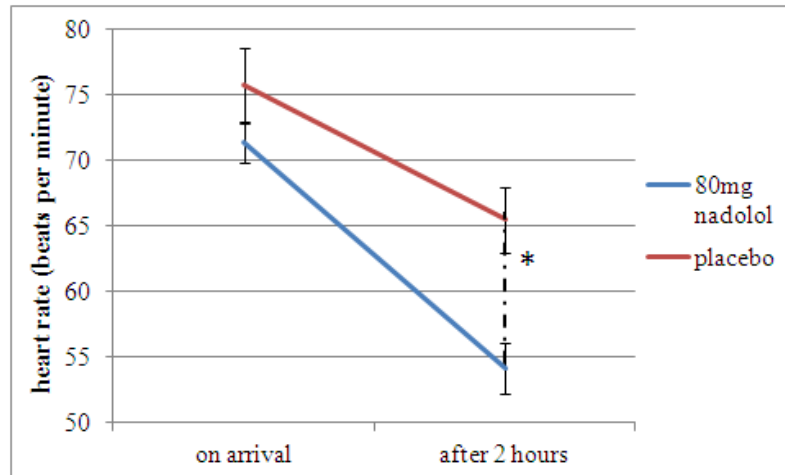
Figure 4.11: Group (n = 20) average (± standard error) effect of nadolol and placebo on heart rate. Asterisks represent a significant decrease in heart rate (p < 0.0001).

Heart rate was assessed during the resting state BOLD scan (duration 5 minutes) and during the emotion task (duration 14 minutes) using the physiological log files from the MRI scanner. During the resting state BOLD scan, the decrease in heart rate due to nadolol was significant to $p < 1 \times 10^{-5}$, whereas during the emotional stimulus, the decrease in heart rate due to nadolol was significant to $p < 5 \times 10^{5}$. In both drug conditions, the mean heart rate was higher during the emotional fMRI task than during the resting state BOLD scan, since the task increases the arousal of the subject by providing a visual stimulus and a small motor demand from the button response. For subjects taking nadolol, this difference was significant to $p < 0.005$, whereas for subjects taking placebo this significance was only $p < 0.05$.

The variance in the length of cardiac cycle (peak-to-peak, or RR variance) was compared between 80 mg nadolol and placebo using physiological data acquired during the emotional fMRI paradigm and the resting state BOLD scan. There was no significant difference between the variance in cardiac cycle length between the two drug conditions during the resting state BOLD scan. However, there was a significantly higher variance in individuals' cardiac cycle length under nadolol compared to placebo during the emotional stimulus task ($p < 0.02$). Mean cardiac cycle length and variance in peak-to-peak duration are given in Table 4.6 for each drug condition.

	Peak-to-peak duration (ms)	Peak-to-peak variance (ms^2)
Resting state (80 mg nadolol)	1122 ± 28 *	4993 ± 571
Resting state (placebo)	967 ± 34 *	4165 ± 562
Emotion task (80 mg nadolol)	1096 ± 24 **	6588 ± 846 ***
Emotion task (placebo)	948 ± 33 **	4437 ± 623 ***

Table 4.6: Mean (± standard error) cardiac cycle length (peak-to-peak duration) and variance in cardiac cycle length (peak-to-peak variance) in the group (n = 20) both at rest (duration 5 minutes) and during the emotional stimulus task (duration 14 minutes) for each drug condition. Asterisks represent significant drug induced effect; (* p < 0.00005, ** p < 0.00005, *** p < 0.02).

4.3.3 ASL resting perfusion

Mean ASL perfusion weighted images for the placebo and 80 mg nadolol groups are shown in Figure 4.12. The mean grey matter perfusion weighted signal change across the group is shown in Figure 4.13. There was no significant difference found between the two drug conditions. Paired t-test in SPM8 showed no significant differences between the two drug conditions at a significance level of p < 0.001, and cluster threshold of 20 voxels.
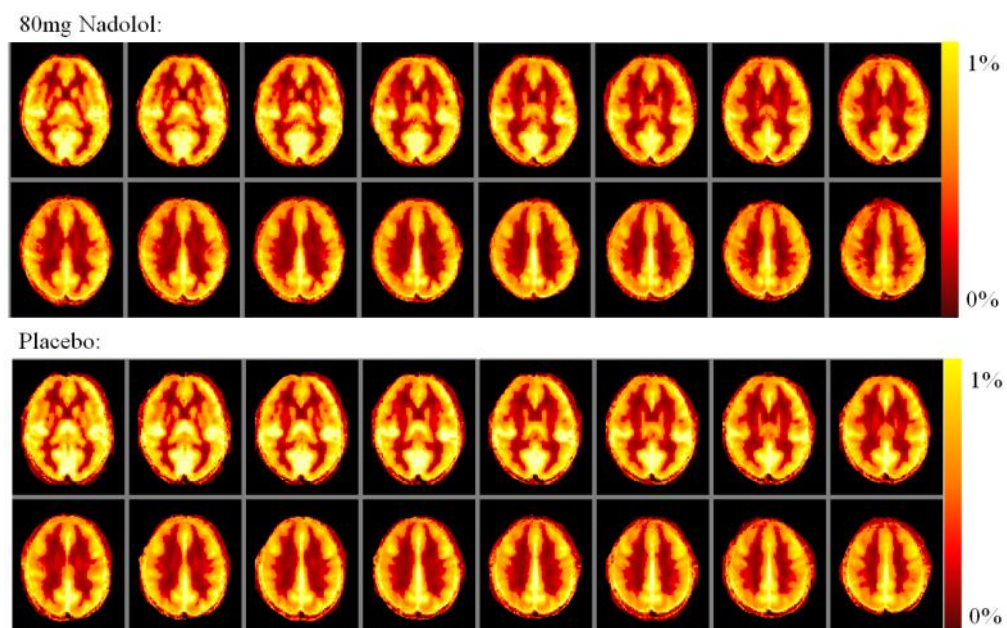
Figure 4.12: Group (n = 20) mean perfusion weighted signal in the nadolol condition (above), placebo condition (below). Colour bars represent normalised ASL signal change.
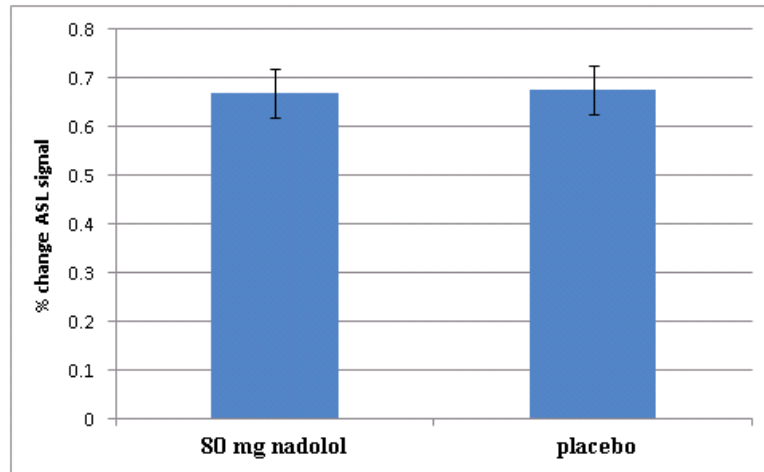
Figure 4.13: Comparison of mean ASL signal change between 80mg nadolol and placebo measured within a grey matter mask.

4.3.4   Functional MRI data: main effects of task

No significant difference in the degree of head motion was found between the two drug conditions. Three subjects exhibited head motion of greater than 2 mm displacement between consecutive dynamics in at least one drug condition, and thus were excluded from the data analysis. The magnitude of peak relative motion between consecutive dynamics was 11 mm translation and 0.1° rotation for the entire group, and 2 mm translation and 0.08° rotation with 3 subjects excluded. First level analyses showed that stimuli of all three valences elicited strong BOLD responses in the visual cortex and surrounding areas of the occipital lobe.

Figure 4.14 shows the one sample t-tests for BOLD response in each drug group and stimulus valence at significance $p < 0.05$, corrected for false discovery rate (FDR), with a cluster threshold of 20 voxels. Tabulated peak t-statistics for regions exhibiting BOLD responses along with cluster size and MNI co-ordinates are given in Appendix E.

Similar results were obtained for the simultaneously acquired perfusion weighted timeseries, but with a smaller effect size due to the lower contrast-to-noise ratio of ASL. Therefore, a lower threshold of uncorrected significance

of p < 0.001 and a cluster threshold of 20 voxels was used to interrogate the data (Figure 4.15).
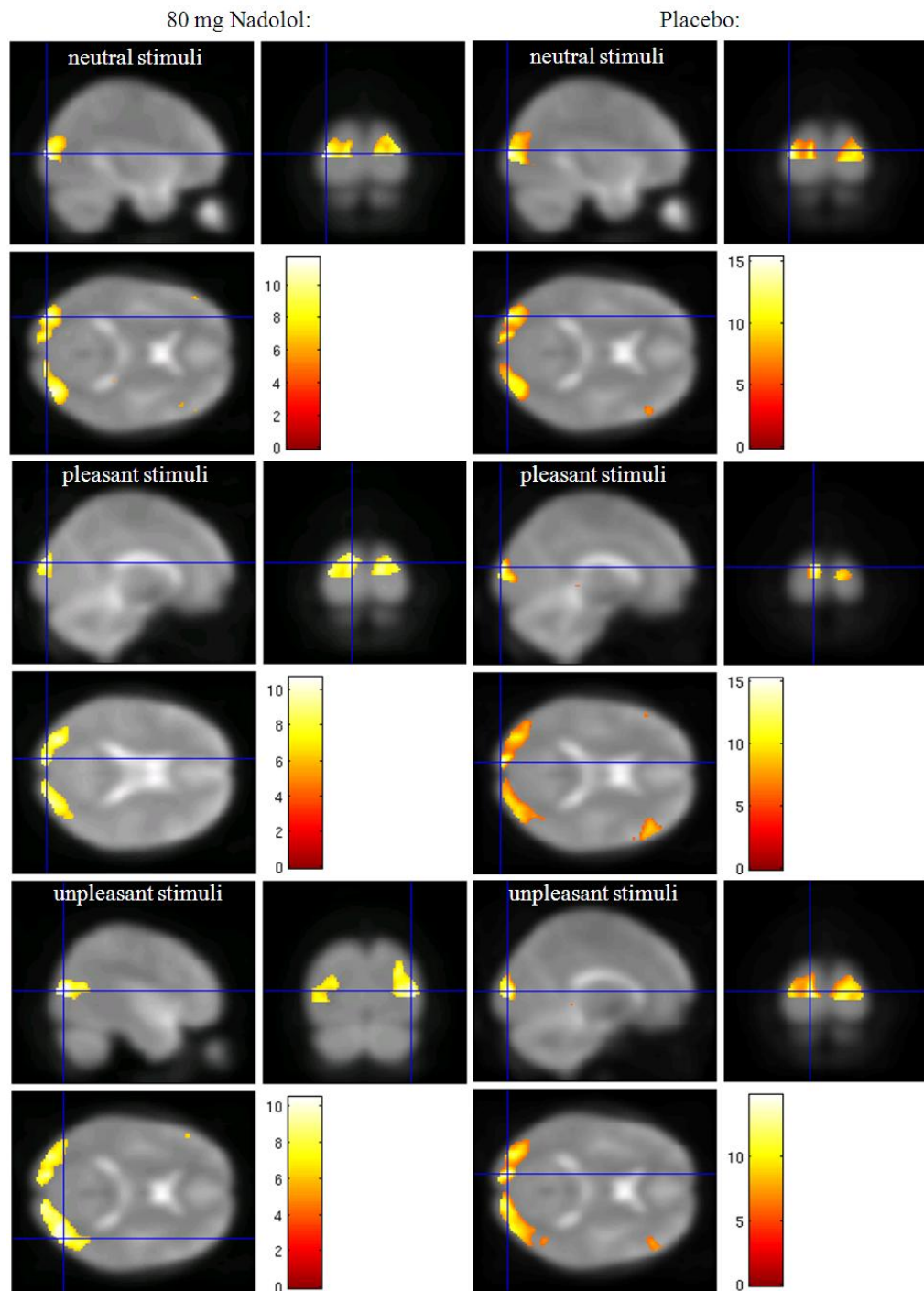
Figure 4.14: Group (n = 17) random effects analyses (using SPM8) showing areas of BOLD response to neutral, pleasant and unpleasant stimuli compared to baseline. P < 0.05 (FDR corrected), cluster threshold = 20 voxels. Colour bars show T statistics.
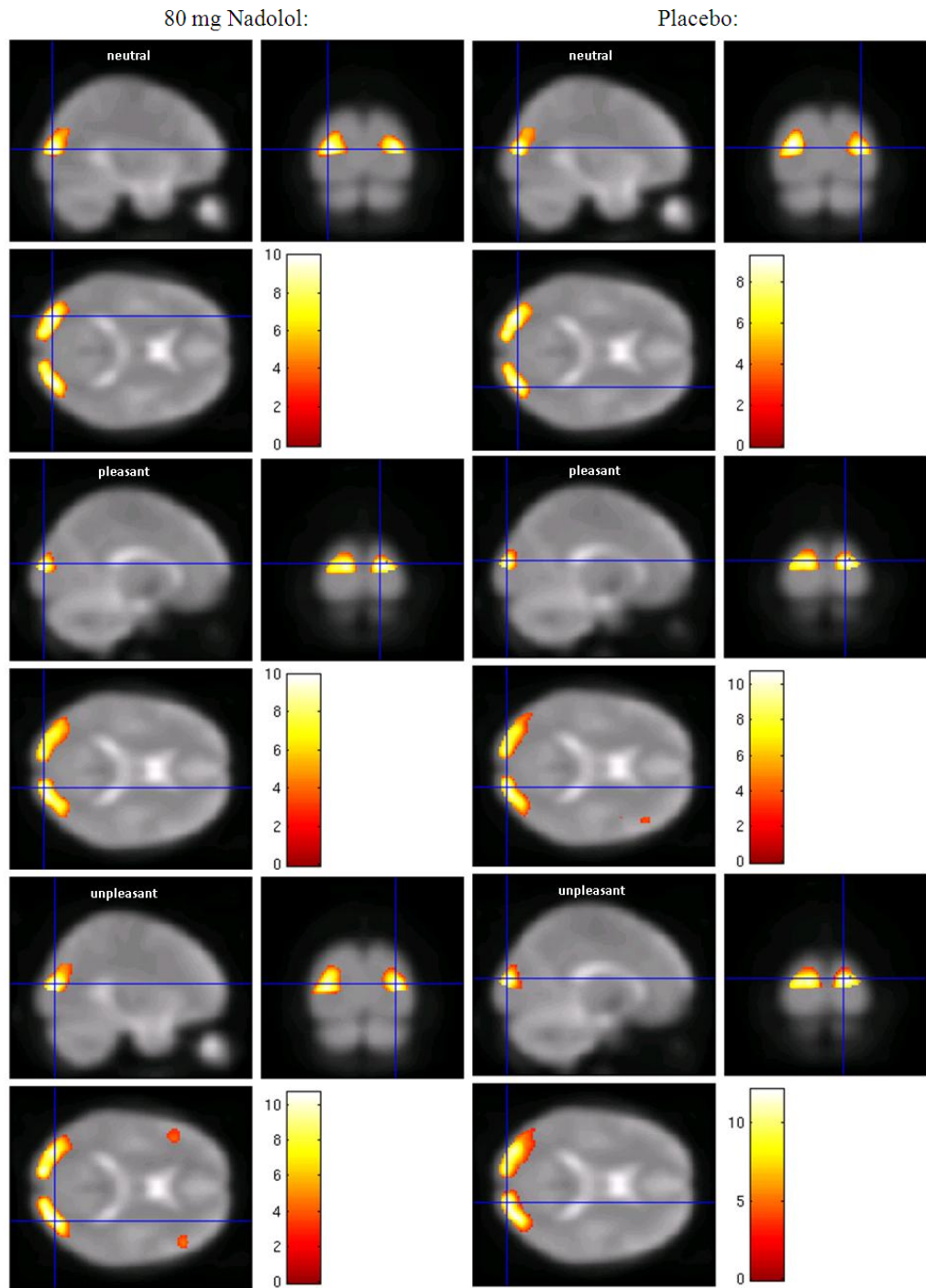
Figure 4.15: Single group (n = 17) higher level analyses (using SPM8) showing areas of greater perfusion in response to neutral, pleasant and unpleasant stimuli compared to baseline. P < 0.001, cluster threshold = 20 voxels. Colour bars show values of T statistic.
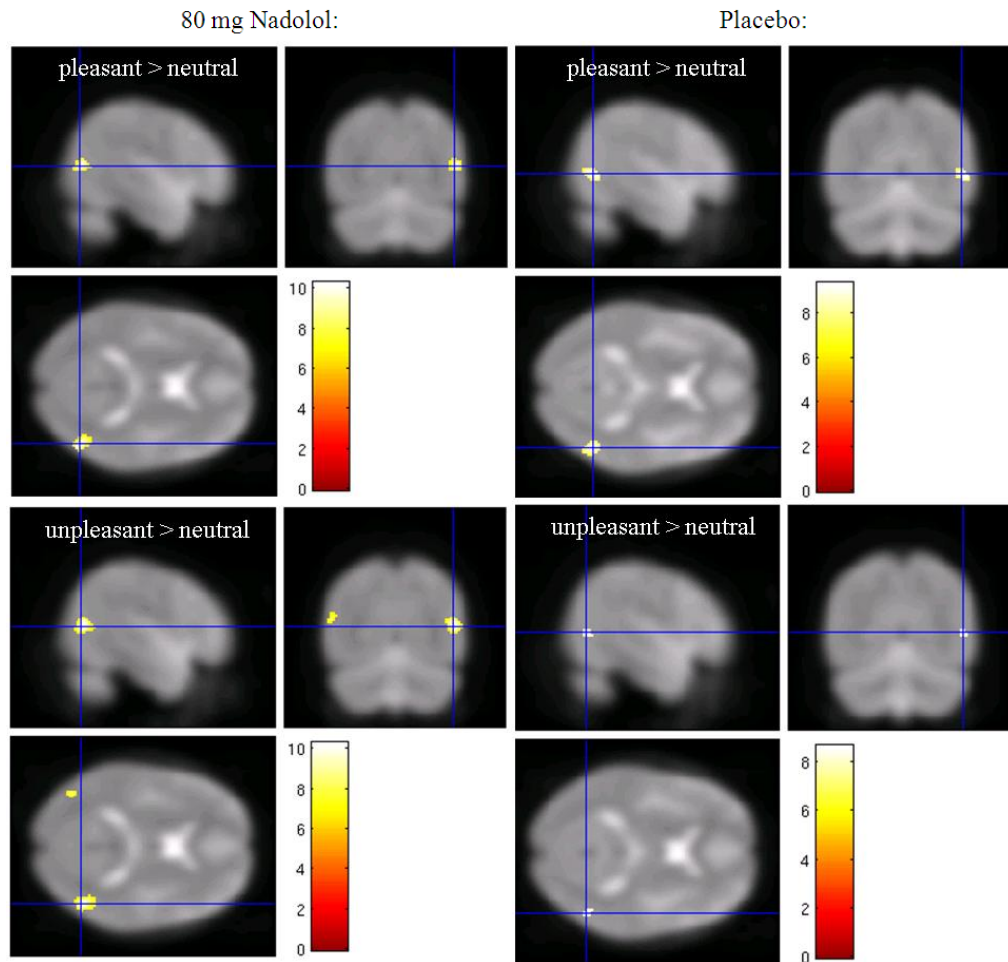
Figure 4.16: Single group (n = 17) higher level analyses (using SPM8) showing areas that exhibited greater BOLD response under emotional stimuli compared to neutral stimuli, masked with a binary mask of all areas more active during task than baseline. P < 0.05 (FDR corrected), cluster threshold = 20. Colour bars show values of T statistic.

Figure 4.16 shows that compared to the neutral stimuli, pleasant and unpleasant stimuli elicited significantly greater activation in the middle/inferior occipital and temporal gyri, fusiform gyrus and amygdala as well as (but with lower significance) in the superior medial frontal cortex and anterior cingulate cortex. BOLD responses for these comparisons are masked using a binary mask of areas more active during stimuli than baseline. Regions shown at a false detection rate (FDR) corrected significance of p < 0.05, cluster threshold of 20 voxels. Peak t-statistics for regions exhibiting BOLD responses along with cluster size and MNI co-ordinates are tabulated in Appendix E. A similar pattern of activity is seen for perfusion weighted changes as for BOLD. Perfusion responses for the same comparisons are

shown in Figure 4.17; at uncorrected significance level of p < 0.001, cluster threshold of 20 voxels.
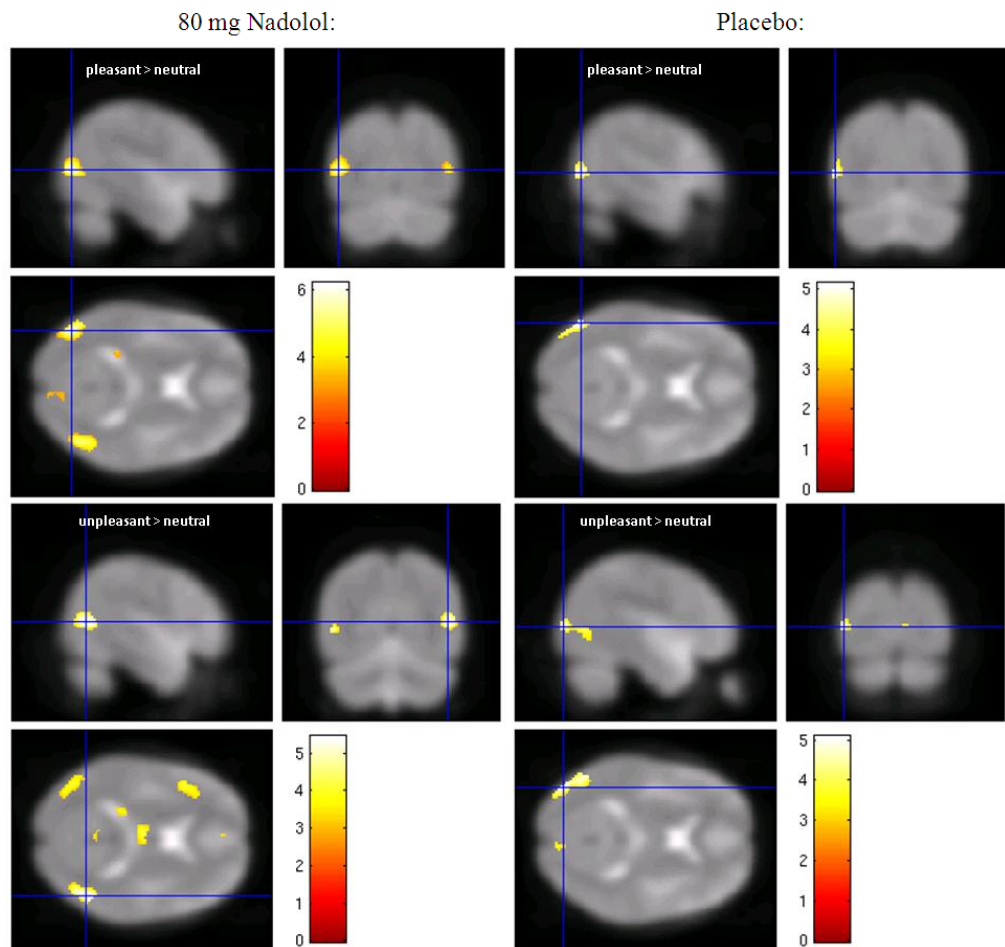
Figure 4.17: Single group (n = 17) higher level analyses (using SPM8) showing areas of greater perfusion in response to pleasant and unpleasant stimuli compared to neutral responses, masked with a binary mask of all areas more active during stimuli than during baseline. P < 0.001, cluster threshold = 20 voxels. Colour bars show T statistics.

There were no areas of the brain that were significantly more active during presentation of the neutral stimuli than either of the emotional stimuli, under either drug condition.

4.3.5   Functional MRI data: comparison between drug conditions

Comparing the activation maps shown above for differences in response between drug conditions, there are areas of task related activity that exhibit a drug correlated modulation significant at p < 0.001, with a cluster threshold of

20 voxels. Comparison of the conditions [pleasant > neutral] and [unpleasant > neutral] between drug conditions showed the right anterior insula, MNI co-ordinates [46 20 -8] to be more active under placebo than nadolol. Figure 4.18 shows this for the [pleasant > neutral] condition, with a peak T statistic of 3.95 and z_{max} = 3.9. The anterior insula cortex forms part of the salience network and thus drug modulation of task related activity is of interest.

[placebo > 80 mg nadolol]
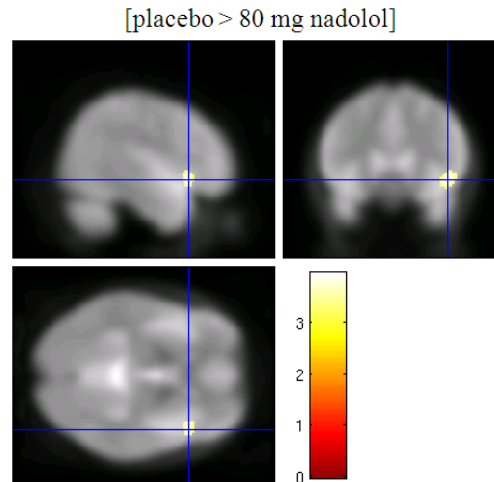
Figure 4.18: Group random effects map of reduced activation under nadolol compared to placebo for [pleasant > neutral] (n = 17), using SPM8. T_{max} = 3.95, z_{max} = 3.9, p < 0.001, cluster threshold = 20 voxels. Colour bar shows values of T statistic.

Anatomically defined left and right anterior insula cortex regions were interrogated using region of interest (ROI) analysis for BOLD signal changes. In addition, a region in the anterior cingulate cortex (ACC) was assessed, which also forms part of the salience network. The region of interest in the anterior cingulate was selected from a paper by Machulda et al [69] for its functional connectivity with the salience network. Figure 4.19 shows mean ($\pm$ standard error) BOLD intensity changes in these regions in response to neutral, pleasant and unpleasant stimuli compared to "off" periods, under the two drug conditions of nadolol and placebo. This reflects the random effects analysis, showing a significant drug induced decrease in the BOLD response to unpleasant stimuli in the right anterior insula. The ACC shows a significant drug induced decrease in BOLD response to pleasant stimuli. The same three ROIs were then used to interrogate the simultaneously acquired perfusion weighted ASL signal changes for each stimulus compared to "off", as shown

in Figure 4.20. The perfusion response to pleasant stimuli in the ACC is significantly reduced by 80 mg nadolol.
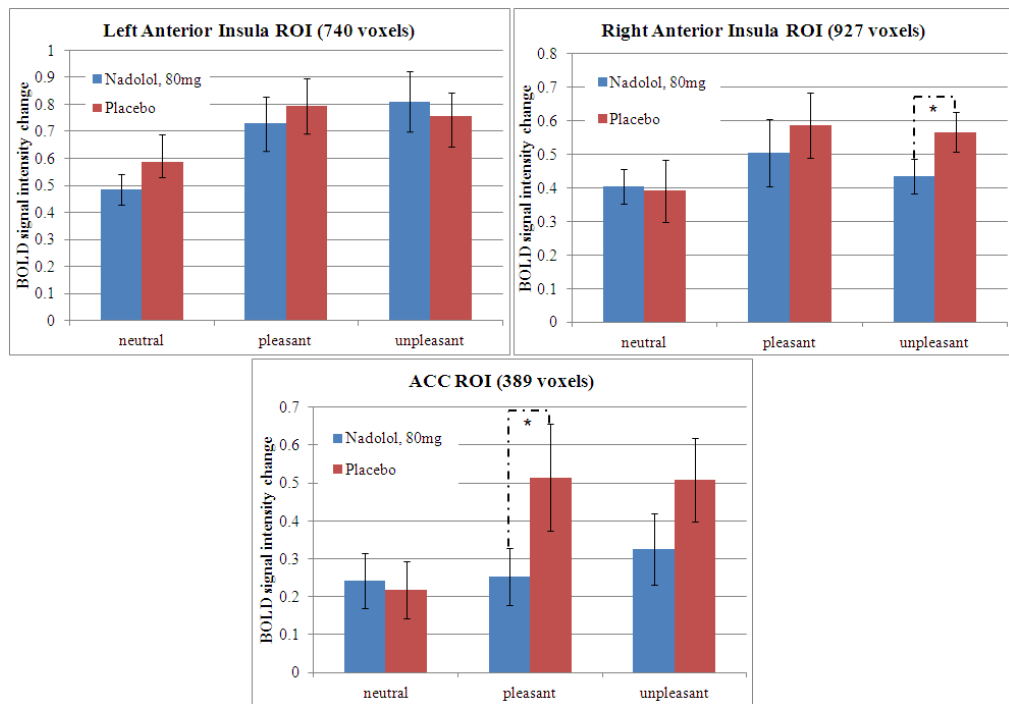
Figure 4.19: Group (n = 17) values for mean ± standard error BOLD intensity changes in anatomically defined left and right anterior insula ROIs, ACC ROI from literature [69]. Asterisks represent significance p < 0.05 using a paired t-test.
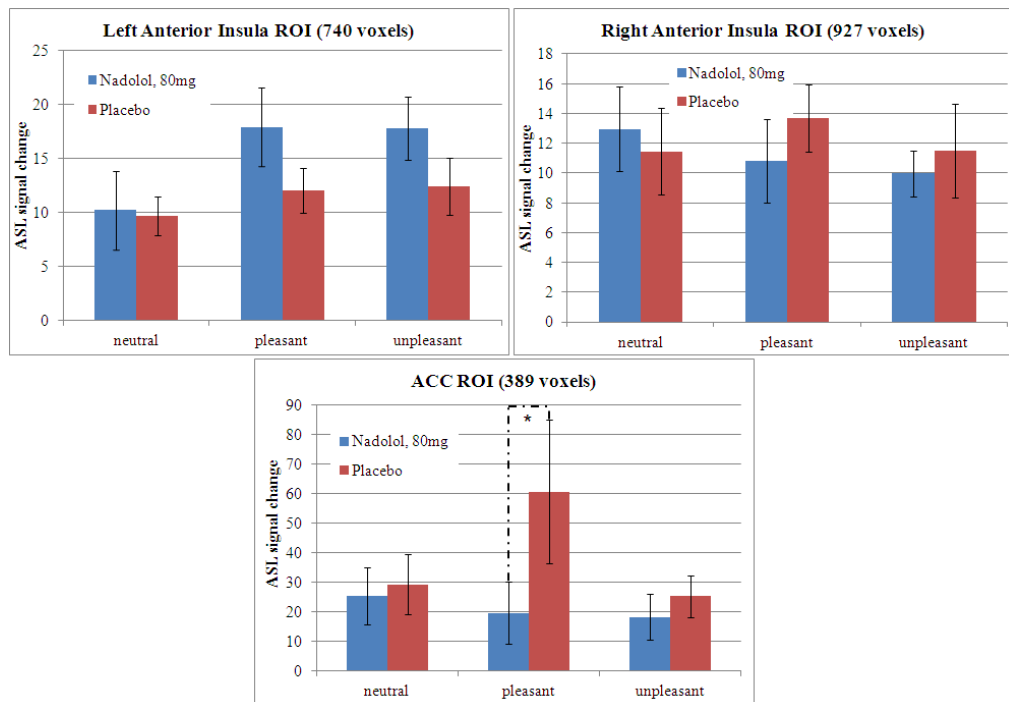
Figure 4.20: Group (n = 17) values for mean ± standard error perfusion weighted changes in anatomical left and right anterior insula ROIs, ACC ROI from literature [69]. Asterisks represent significance p < 0.05 using a paired t-test.

Analysis of resting ASL data was used to investigate whether the drug induced differences elicited above arise in part from baseline changes in perfusion. The three ROIs were used to interrogate the resting PCASL data for drug induced changes in resting perfusion, by calculating the mean regional ASL signal in each ROI for each subject. Group mean (± standard error) values are given in Figure 4.21. None of these three ROIs elicited a statistically significant difference between the two drug conditions.
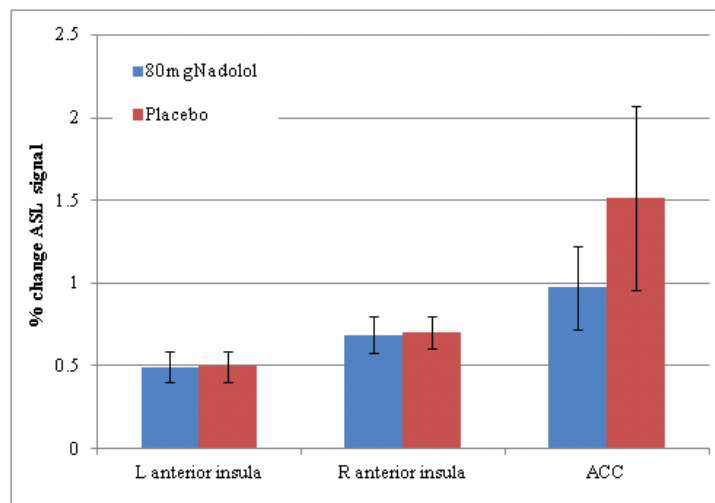
Figure 4.21: ROI analysis of resting perfusion: group (n = 20) values for mean ± standard error % change ASL signal in anatomical ROIs in the left and right anterior insula, and in the ACC ROI from literature [69].

It was hypothesised that due to the involvement of the amygdala in emotional processing and the limbic system, particularly in the processing of unpleasant stimuli, amygdala activation may be modulated by nadolol. Anatomically defined ROIs in the amygdalae were interrogated for differences between the two drug conditions in BOLD and perfusion weighted response for the whole group. Interestingly, both amygdalae exhibited significant increases in BOLD activity under nadolol, compared to placebo, Figure 4.22. These differences were not seen in the simultaneously acquired ASL signal, Figure 4.23.
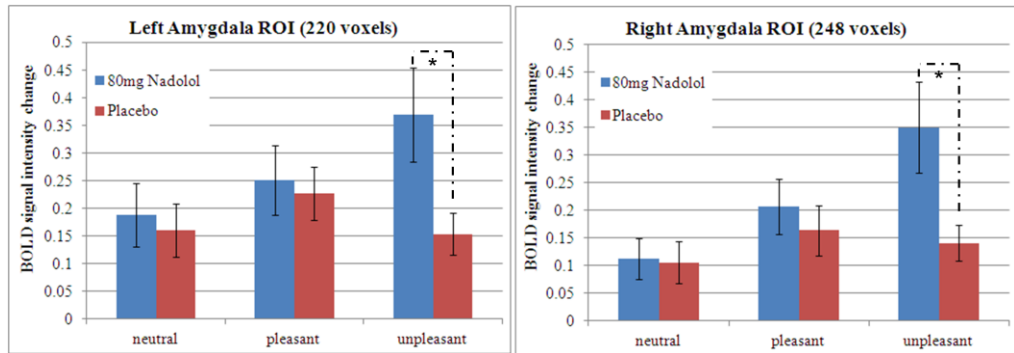
Figure 4.22: Group (n=17) mean and standard error BOLD intensity changes in anatomical ROIs in the amygdalae in response to stimuli of each valence, under each drug condition. Asterisks represent significance p < 0.04 using paired t-test.
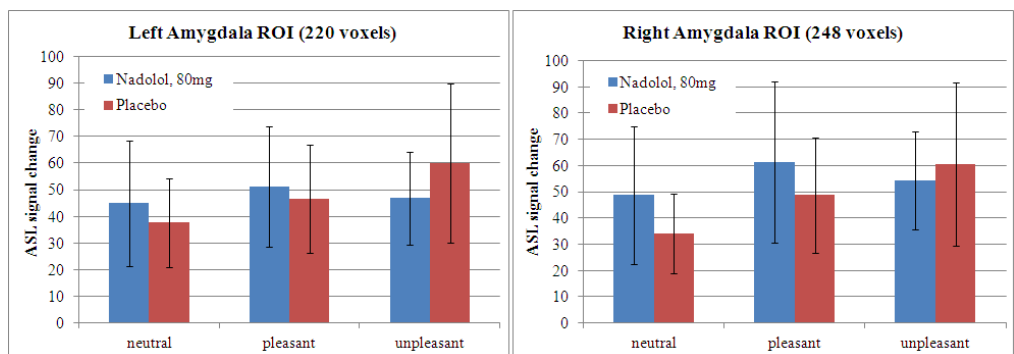
Figure 4.23: Group (n = 17) values for mean ± standard error absolute ASL signal changes in anatomical amygdala ROIs, in response to each stimulus, under nadolol and placebo. No significant differences found using a paired t-test.

Resting perfusion data was used to investigate whether the drug induced BOLD differences elicited in the amygdala were present in baseline perfusion. There were no statistically significant differences between drug conditions, Figure 4.24, showing group mean values for ASL signal (± standard error).
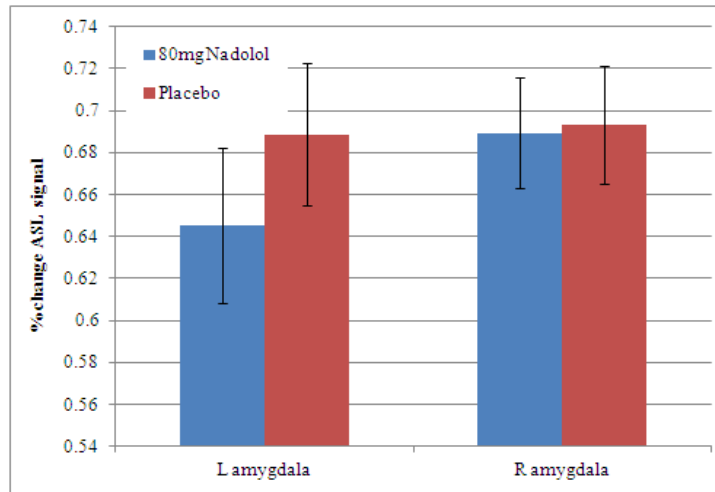
Figure 4.24: ROI analysis of resting perfusion: group (n = 20) values of mean ± standard error % change ASL signal in anatomically defined ROIs in the amygdalae (left and right amygdalae ROIs contain 220 and 248 voxels respectively).

To act as a control against potential confounds, ROI analysis was performed on an anatomically defined region in the primary visual cortex, chosen on the basis of it being hypothesised to exhibit task related activity that is not modulated by a peripherally acting beta-blocker. A 7 mm diameter spherical ROI was placed in the primary visual cortex, at MNI co-ordinates [8 -80 4]. No significance was found between the drug conditions in the primary visual cortex response to stimuli of any valence using paired t-tests, Figure 4.25.
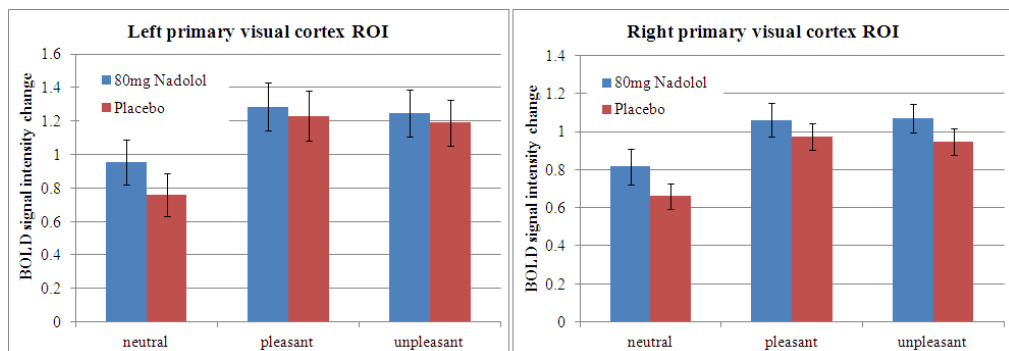
Figure 4.25: Group (n = 17) values of mean ± standard error absolute BOLD intensity changes in ROIs in the primary visual cortex in response to each stimulus, under 80 mg nadolol and placebo. Each 7 mm diameter spherical ROI contained 179 voxels. No significance found using paired t-test.

4.3.6   Functional MRI data: gender differences

There were also small areas of significantly different activation between the two gender groups (females n = 9, males n = 8). For placebo greater than nadolol, for both [pleasant > neutral] and [unpleasant > neutral] conditions, females exhibited areas of activation in the right insula that were not significantly present in males, shown in Figure 4.26. This suggests that the main effects described above in Section 4.3.5 are driven by the female subjects. In [pleasant > neutral], this was centred at MNI co-ordinate [40 20 - 10] with a peak T = 4.18, z_{max} = 4.07 and was significant to p < 0.001. In [unpleasant > neutral], the effect was located at MNI co-ordinate [38 14 -8], with peak T = 4.69, z_{max} = 4.53 and was significant to p < 0.001. ROI analysis used 7 mm diameter spherical regions of interest centred on the MNI co-ordinates of peak activation from the comparison [pleasant > neutral for placebo] greater than [pleasant > neutral for nadolol] and [unpleasant > neutral for placebo] greater than [unpleasant > neutral for nadolol]. BOLD signal changes in regions centred at [-47 24 0] and [39 17 -9] are shown in Figure 4.27.
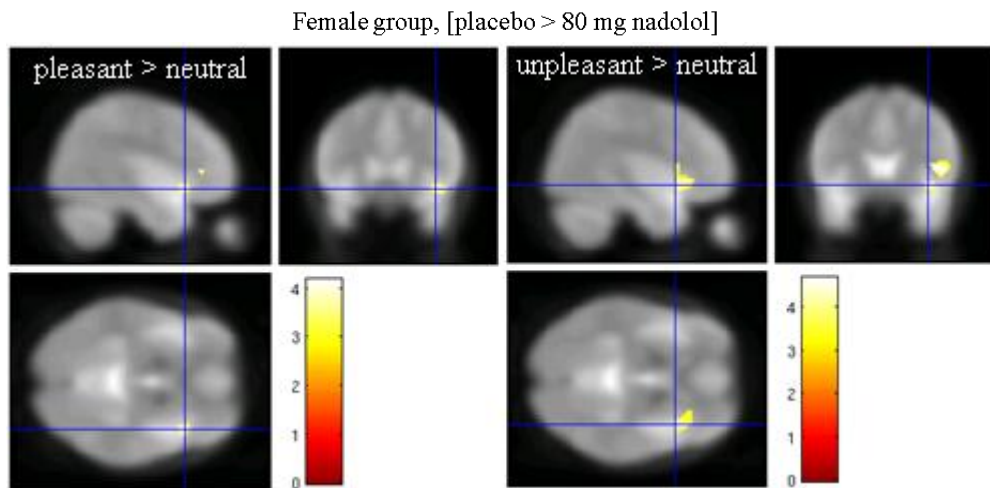
Figure 4.26: Differences in activation (using SPM8) in the female group only (n = 9). [Pleasant > neutral]: T_{max} = 4.18, z_{max} = 4.07. [Unpleasant > neutral]: T_{max} = 4.69, z_{max} = 4.53. P < 0.001, cluster threshold = 20 voxels. Colour bars show T statistics.
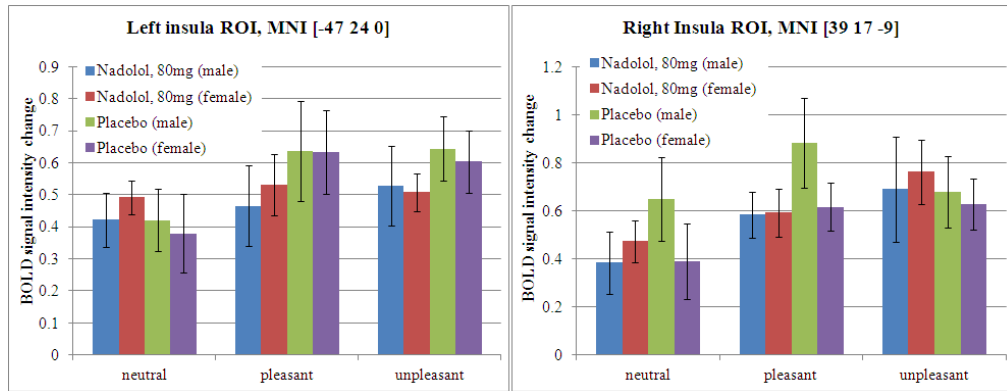
Figure 4.27: Mean ± standard error BOLD intensity changes for male (n = 8) and female (n = 9) subjects separately, for each stimulus, under 80 mg nadolol and placebo. 7 mm diameter insula ROIs (each 179 voxels) placed at sites of peak difference in activation in the insula as defined from whole group analysis.

In the male subjects there was a region of greater activation in the condition [unpleasant > neutral] not seen in females, for the nadolol group compared to the placebo group. This was located in the bilateral amygdala / thalamus region and was stronger in the right cortex than left (peak T statistic of 4.75, $z_{max} = 4.56$, $p < 0.001$) at MNI co-ordinates [32 -28 -6], Figure 4.28.
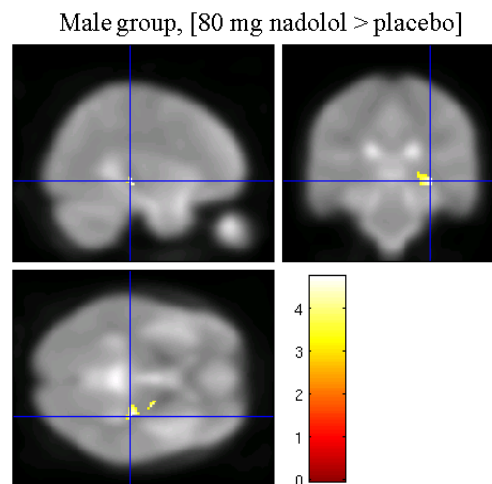
Figure 4.28: Region of greater activation seen (using SPM8) in the condition [unpleasant > neutral] in the male (n = 8) group only. $T_{max} = 4.75$, $z_{max} = 4.56$, $p < 0.001$, cluster threshold = 20 voxels. Colour bar shows values of T statistic.

This region was interrogated using ROI analysis using a 7 mm diameter sphere centred at the peak difference in activation at MNI co-ordinates [-14 -10 -10] and [32 -28 -6] for the left and right amygdala / thalamus activation regions

respectively. BOLD signal intensity changes for these regions are shown in Figure 4.29.
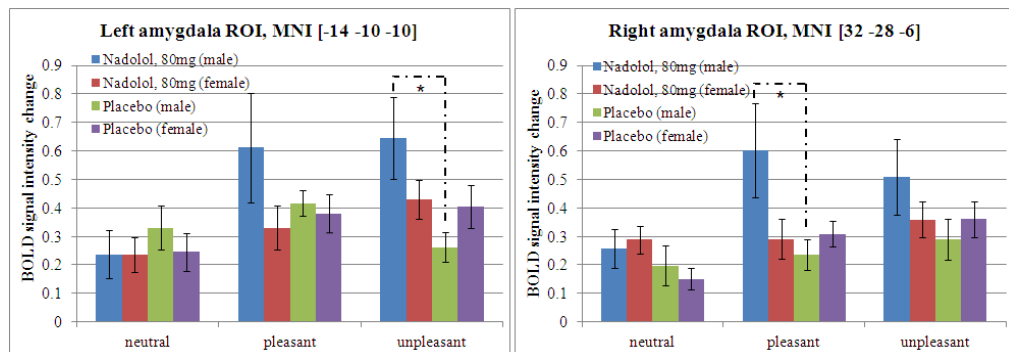
Figure 4.29: Mean ± standard error BOLD intensity changes for male (n=8) and female (n=9) subjects separately. 7 mm diameter ROIs (each 179 voxels) placed at sites of peak difference in activation in the amygdala / thalamus region. Asterisks represent significance calculated by paired t-test at p < 0.05.

4.3.7 Resting state BOLD data: Independent Component Analysis

No subjects exhibited head motion of greater than 2 mm displacement between consecutive dynamics in either drug condition, and thus all 20 subjects' datasets were included in the resting state BOLD data analysis. The magnitude of maximum relative motion between consecutive dynamics was 1.8 mm translation and 0.075° rotation for the entire group. No significant differences were found in the degree of motion between the two drug conditions.

Group analysis of all 40 scans together produced 27 components. Candidate components were found for networks of interest; the default mode network (DMN, Figure 4.30) and the salience network (SN, Figure 4.31).
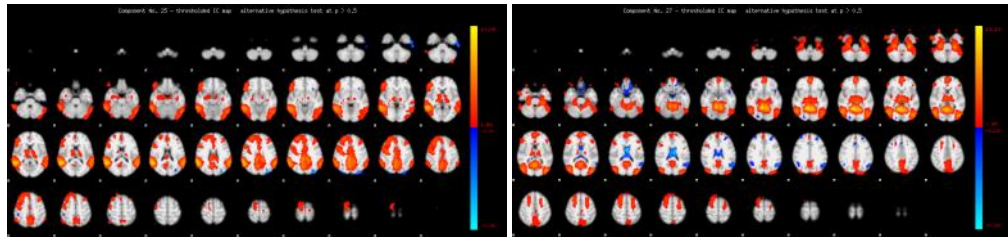
Figure 4.30: Default mode network components for the group (n = 20) using FSL MELODIC. Maps show correlation between inferior parietal lobules and anterior and posterior cingulate cortices.
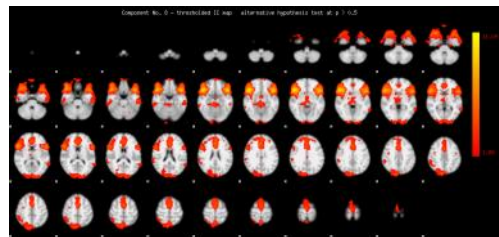
Figure 4.31: Salience network component for the group (n = 20) using FSL MELODIC, exhibiting correlation between bilateral insula and anterior cingulate cortex.

Group independent component analysis on the nadolol condition alone extracted 26 independent components, while analysis on the placebo condition alone identified 28 independent components. As the design of the analysis did not restrict the number of components resolved, it is possible for the same set of correlations to be resolved into different components each time the comparison is run. As these components do not directly correspond between drug conditions, the statistics produced cannot be compared quantitatively, and the definition of networks through independent component analysis is not optimal for further quantitative techniques such as dual linear regression. Therefore, psychophysiological interactions analysis was used to determine if there was an effect of 80 mg nadolol on resting state functional connectivity.

4.3.8 Resting state BOLD data: Psychophysiological Interaction Analysis

First level analysis was run on each subject and each drug condition individually. All subjects showed clear correlation in the default mode network between all four known nodes. First level analysis for an example subject is shown in Figure 4.32, with suprathreshold voxels of correlation

shown in red, significant to p < 0.005, corrected for family wise error rate (FWE).
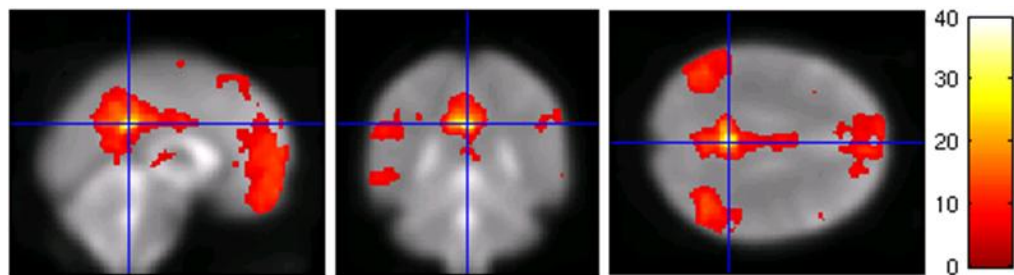
Figure 4.32: First level analysis for one subject in the placebo condition demonstrating default mode network correlation, using a seed in the posterior cingulate cortex, SPM8. Significance p < 0.05 FWE, cluster threshold = 20 voxels.

Single group t-tests for each drug condition are shown in Figure 4.33, at significance level p < 0.05 FWE corrected. These demonstrate the consistency across subjects for locations of activity correlated with the posterior cingulate cortex. Paired t-tests between drug conditions showed few supra-threshold voxels with small cluster sizes. No supra-threshold voxels survived FWE correction.
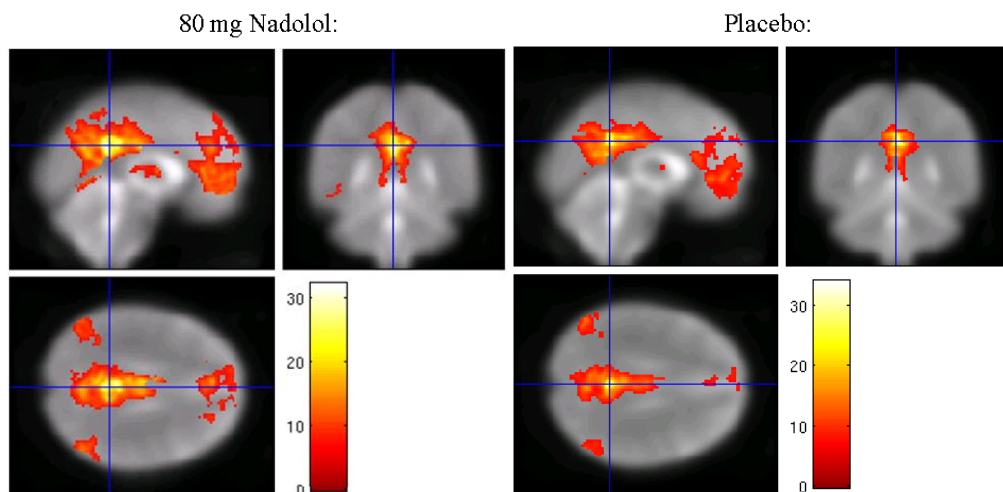
Figure 4.33: Group (n = 20) random effects analysis: t-tests using SPM8 for 80 mg nadolol and placebo show correlation in the default mode network using a seed in the posterior cingulate cortex. Significant to p < 0.05 FWE, cluster threshold = 20 voxels.

First level analysis using a seed in the anterior cingulate cortex elicited connectivities with the bilateral insula and superior frontal regions, in

agreement with the published findings of Machulda et al [69]. Single group t-tests for nadolol and placebo are shown in Figure 4.34 at significance p < 0.05 FWE. Paired t-tests between drug conditions again showed no significant differences.
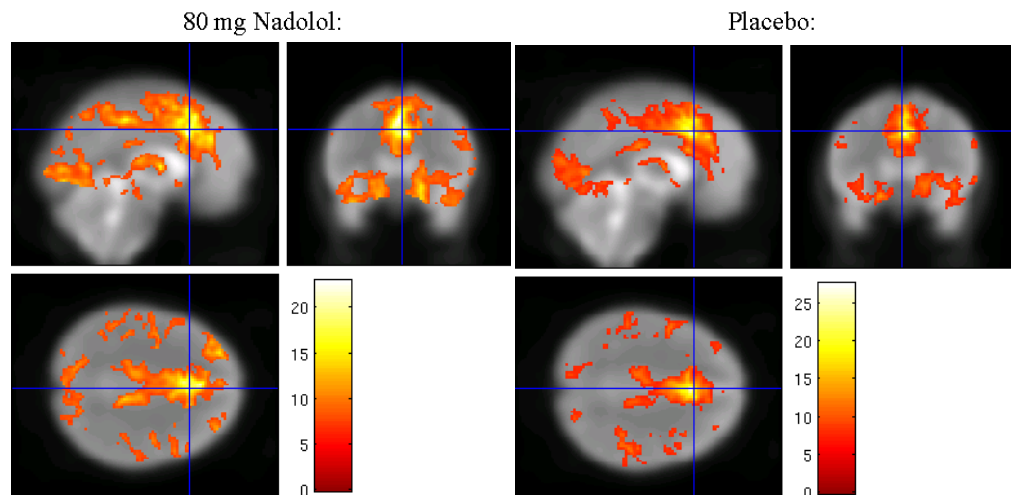
Figure 4.34: Group (n = 20) random effects analysis: t-tests using SPM8 for 80 mg nadolol and placebo show correlation in the salience network using a seed in the anterior cingulate cortex [69]. Significant to p < 0.05 FWE, cluster threshold = 20 voxels.

4.4   Discussion

4.4.1   Summary of findings

A single dose of 80 mg of the peripherally acting beta-blocker, nadolol, significantly reduced mean arterial blood pressure and heart rate but did not significantly affect resting cerebral blood flow, as assessed by the ASL signal in grey matter cortical regions. Nadolol increased the variance in the peak-to-peak cardiac cycle duration during the emotional stimulus task, but not during rest. Assessment of BOLD and perfusion responses to neutral, pleasant and unpleasant visual stimuli showed robust widespread activations in the visual cortex. Pleasant and unpleasant visual stimuli elicited significantly greater BOLD and perfusion responses in the fusiform gyrus, middle / inferior temporal gyrus and middle / inferior occipital gyrus regions, compared to responses to neutral visual stimuli.

On comparison of the group (n = 17) response to emotional stimuli between drug conditions, nadolol was shown to significantly reduce responses to [pleasant > neutral] stimuli in the right insula (p < 0.001 uncorrected). The anterior insula and anterior cingulate are believed to contribute to the processing of emotions through involvement in the salience network. Regions of interest placed in the bilateral anterior insula and anterior cingulate cortex showed that nadolol caused a significant reduction in both BOLD response and perfusion response to [pleasant > neutral] stimuli in the anterior cingulate cortex (p < 0.05). Resting perfusion was also assessed in the anterior insula and ACC and showed no significant drug dependent effect. Further region of interest analysis elicited a significant increase due to nadolol of BOLD signal in the amygdala in response to [unpleasant > neutral] stimuli. There was no significant difference in the perfusion signal in these regions either in response to stimuli or at rest. Region of interest analysis was used in a primary visual area to control for possible confounds of nadolol modulating task driven activity outside the areas associated with the processing of emotional stimuli. No significant differences were found between the two drug conditions in BOLD signal intensity changes in the primary visual cortex for stimuli of any valence.

Data were interrogated for differences representing drug modulation of brain activity between male and female subject groups. Reduction in insula activity demonstrated in the group (n = 17) was significant in the female group (n = 9, p < 0.001) for [pleasant > neutral] and [unpleasant > neutral] stimuli, but was not seen in the male group (n = 8). The male group exhibited a significant drug correlated increase in task related activity in the amygdala (p < 0.001 uncorrected). Region of interest analysis showed this was significant in the left amygdala for [unpleasant > neutral] stimuli and in the right amygdala for [pleasant > neutral] stimuli. This was confirmed by paired t-test (p < 0.05).

Resting state BOLD data were investigated for differences in the functional connectivity of the DMN and salience network between drug conditions. No drug correlated modulation was found using psychophysiological interaction analysis. The analysis took account of motion parameters as covariates of no

interest, but did not control for white matter or cerebrospinal fluid nuisance regressors.

4.4.2   Discussion of findings

Nadolol is widely known to reduce heart rate and blood pressure. The reduction measured in heart rate and blood pressure in 20 healthy volunteers was significant to $p < 0.01$ and $p < 0.002$ respectively. Cardiac cycle length variance has been shown to be used as a surrogate for heart rate variability as it provides a strong correlation with outcomes from spectrum analysis methods, but can be achieved using much simpler analysis methods [55]. Cardiac cycle length variance is negatively correlated with age [54, 72], and the values in the placebo condition of 4165 ± 562 ms^2 and 4437 ± 623 ms^2 during the resting state BOLD scan and the emotional stimulus task respectively fall within the range of previously published values [72]. Nadolol increased variance in cardiac cycle length during the resting state BOLD scan and emotional stimulus task to 4933 ± 571 ms^2 and 6588 ± 846 ms^2 respectively. This was significant during the emotion stimulus task ($p < 0.02$). Beta-blockers are hypothesised to increase heart rate variability through a central effect on the parasympathetic drive [73]; however, nadolol is not expected to have a central effect. The assessment of blood pressure, heart rate and cycle length variance demonstrate that adequate sympathetic blockade has been induced by 80 mg nadolol [74].

Percentage change in ASL signal as measured using PCASL can be assumed to be linearly related to CBF using a two compartment model [75] if blood transit time does not change. In the absence of measurement of blood transit time, as there is no significant difference between percentage change in ASL signal between nadolol and placebo, there will be no significant difference in estimated blood flow between the two conditions, provided that transit time does not change between conditions. In addition, region of interest analysis of BOLD responses in the primary visual cortex supports the assumption that 80 mg nadolol has not modulated any activity not associated with the processing of emotional stimuli. These two measures can be used to conclude that

nadolol has acted in the periphery only and that further assessment of modulation of task related activity is not confounded by central effects.

Patterns of task correlated activity elicited by visual emotional stimuli concur with previous studies using similar stimuli. Broadly, emotional stimuli cause increased BOLD and perfusion responses in the fusiform gyrus, middle / inferior temporal gyrus and middle / inferior occipital gyrus regions in comparison to neutral stimuli [14]. The insula and anterior cingulate cortex have been found to also exhibit increased response to emotional stimuli [14, 3, 20, 21]. This study reports that activity in the insula has been shown to be significantly reduced by the administration of nadolol in comparison to placebo. The insula is implicated in the processing of emotions and acts within the salience network. Previous studies produce conflicting evidence as to whether beta-blockers (either peripherally acting or centrally acting) modulate the processing of emotion, or the activity within regions of the brain associated with the processing of emotions, such as the salience network and the amygdalae. This has previously been investigated by examining the ability to recall emotional stimuli compared to neutral stimuli). Propranolol has been reported to impair memory of the emotional stimuli compared to placebo [36]; supporting the hypothesis that blockade of the peripheral reactivity will impair emotional arousal. Contradictory to this, neither propranolol nor nadolol were found to impair memory recall of emotional stimuli in a later study by the same group [35]. Similarly, the centrally acting beta-blocker, propranolol, has been shown to reduce activity in the amygdala associated with the encoding and retrieval of emotional verbal stimuli, without significantly affecting behavioural responses [34].

Region of interest analysis on the anterior cingulate cortex, a component of the salience network, showed a reduction in BOLD response to pleasant and unpleasant stimuli under nadolol compared to placebo, with the reduction in response to pleasant stimuli being significant ($p < 0.05$). A corresponding significant reduction in perfusion response to pleasant and unpleasant stimuli under nadolol compared to placebo was also found. There was no significant decrease in perfusion in the same region during rest, but the standard error of

the perfusion measurements in that region during rest were substantially greater than in other regions of the brain, likely due to the proximity of the region to inflowing arteries.

Activity in the amygdala is associated with arousal and the processing of fear and threat, as well as emotional stimuli [19, 26, 15, 27, 3, 14]. Strange et al [34] showed that the centrally acting beta-blocker, propranolol, significantly reduced the activity in the amygdala in response to emotional verbal stimuli, without reduction of memory recall ability. This thesis reports that there was a significant increase in the activity in both amygdalae in response to negative emotional stimuli, after the administration of nadolol compared to placebo. This finding contradicts previous studies using centrally acting beta-blockers that reported reduced amygdala response to verbal emotional stimuli [34]. Impaired amygdala response in those studies may have been mediated by a central beta-adrenergic mechanism rather than a consequence of reduced bodily arousal. However, the increased responsiveness of the amygdala after peripheral beta-blockade is difficult to explain. One speculative theory is that this is due to an imbalance of central and peripheral beta-adrenergic arousal resulting in some form of 'sensitisation' of central beta-adrenergic amygdala arousal. It is logical to investigate the possibility of an associated reduction in perfusion in the same region in response to emotional visual stimuli or at rest, however no such difference in either task response or resting perfusion was found.

It is intuitive to understand that there may be a difference in the way males and females process emotional stimuli, and thus it is interesting to explore this possibility. However, analysis performed on gender subgroups of this study is purely exploratory due to the small size of gender subgroups (n = 8 male, n = 9 female). Female subjects (n = 9) exhibited a significant drug correlated reduction of activity in the insula in response to both [pleasant > neutral] and [unpleasant > neutral] stimulus comparisons. This reduction was not significant in the male group (n = 8). This could be due to a greater response in the insula in female subjects, which was reduced by nadolol, or alternatively that the insula response to emotional stimuli in male subjects was not

modulated to the same degree as in female subjects. This was investigated using region of interest analysis on the gender subgroups, which was inconclusive as no statistically significant differences were found.

Male subjects (n = 8) exhibited a significant drug correlated increase of activity in the amygdala in response to [unpleasant > neutral] stimuli. While this increase was also detected significantly at the whole group level (n = 17), it was not significant in the female subgroup (n = 9). Region of interest analysis was used to explore levels of BOLD signal intensity in the gender subgroups separately, and this showed that the male subjects taking nadolol exhibited higher activation in the amygdala in response to [emotional > neutral] stimuli than did the males taking placebo, or the females in either drug condition. Therefore, nadolol caused an increase in amygdala response to emotional stimuli, with no differences being found in any other group. The explanation for this is not clear.

Independent component analysis is a hypothesis free method of exploring connectivity in the brain. Using a temporal concatenation of all subjects' data, 27 components were identified, including the default mode network and salience network. Due to the randomised nature of component identification, direct comparisons cannot be made between drug conditions, even qualitatively, as analysis of each drug condition produced a different arrangement of components. Quantitative comparisons between drug conditions cannot be made without further methods such as dual linear regression, which was not appropriate in this case due to suboptimal definition of the resting state networks from independent component analysis.

Psychophysiological interaction analysis was used to successfully define the default mode network and the salience network based on the hypothesis that these networks can be defined from known seed regions within the brain. The default mode network has been defined using a seed region of interest in the posterior cingulate cortex [68]. A prior study using this method has shown that the sedative propofol increases the connectivity of the posterior cingulate cortex with non default mode regions of the brain such as sensorimotor areas,

anterior thalamic nuclei and the reticular formation [76]. The technique has also previously been defined using a seed in the anterior cingulate cortex [69] to assess changes in salience network functional connectivity. The psychophysiological interaction analysis reported in this thesis defined group resting state networks that closely resemble those in previously published studies for both the default mode network [68] and the salience network [69]. There was no significant difference in the amount of subject head motion detected between the two drug conditions, shown using a paired t-test. The analysis used motion parameters as regressors of no interest, but did not control for covariates of no interest in the white matter or cerebrospinal fluid noise parameters. Also, global demeaning can be used to further reduce detection of spurious correlations [77]. While the effect of these noise elements is not large, there is no evidence to suggest that they are not affected by the administration of a beta-blocker, and thus lack of control for them may have either introduced the possibility of detecting spurious correlations, or masked a small drug dependent effect on functional connectivity within the networks investigated. Having said this, even by lowering the significance level of the paired t-tests between drug conditions, there was no discernable pattern to the suprathreshold voxels showing differences between the two drug conditions.

4.4.3 Strengths of the study

A single 80 mg dose of the peripherally acting beta-blocker, nadolol reduces sympathetic activity, as evident by the primary outcomes of significant reduction in heart rate and blood pressure. However, reassuringly, perfusion weighted data measured using ASL does not suggest any significant global difference in the resting perfusion between the two drug conditions. Further, there was no significant modulation of task-induced activity not associated with the processing of emotions, as evident in analysis of the region of interest in the visual cortex during the processing of visual emotional stimuli. This would imply that the choice of a peripherally acting beta-blocker was correct and any direct central effects were avoided. This fact alone separates the work presented in this thesis from previous work published that uses the centrally

acting beta-blocker, propranolol [34, 35, 36] as any differences in brain function are confounded by the central action of the drug.

The sample size of 20 used here is larger than sample sizes used previously [34], and allowed contingency for subjects to be excluded from data analysis. Inevitably, three subjects were excluded from analysis of the emotional stimulus task, reducing the sample size to 17. A minimum sample size of 15 to 20 is considered acceptable for studies of this type [41]. Additionally, the placebo controlled randomised crossover design of drug administration provides greater statistical power for a given effect size.

The additional information provided by simultaneously acquired BOLD and ASL data allows interrogation of task related response through both BOLD signal intensity changes and perfusion responses. The use of dual echo ASL BOLD sequences for functional MRI is still not commonplace and certainly the use of ASL contrast for pharmacological functional MRI is in its infancy. Additionally, the steady state pseudo continuous ASL (PCASL) acquisition gives further insight into tissue perfusion responses to emotional stimuli with good contrast-to-noise ratio, and the assessment of potential modulation as caused by the beta-blocker nadolol. Given the additional information that these two techniques provide when used in combination, further development and use is encouraged.

4.4.4   Weaknesses of the study

The PCASL sequence used for the assessment of drug induced changes in resting perfusion and response to the emotional task used a single inversion time (TI). Care was taken to image and label in the same position between the two scanning sessions, and differences in signal intensity are accounted for by normalising the ASL signal images to a base EPI. This provides a good assessment of any drug modulation of the PCASL signal, which can be assumed to have a linear relationship with CBF [75], but assuming blood transit time does not change between drug conditions. A multiphase ASL acquisition using a pulsed ASL labelling scheme would give a quantifiable

measure of CBF and blood transit time, and thus drug induced modulation of these two quantities could be assessed. However, the spatial coverage of such a scheme is limited.

To improve the sensitivity of resting state network detection in BOLD data, more rigorous measures could be taken to regress out nuisance signal. While drug correlated change in subject head motion was not shown to be statistically significant, no assessment was made of white matter or cerebrospinal fluid noise levels. If these were substantial, or if they changed significantly after the administration of nadolol, they may introduce spurious correlations, or mask genuine correlations of low magnitude [77].

To be critical of the methods chosen for acquisition in this study, it is necessary to mention that the PCASL scheme results in reduced brain coverage and temporal resolution compared to a standard BOLD EPI acquisition. The PCASL sequence was optimised prior to the study to maximise the coverage for a given temporal resolution, and care was taken to ensure that this would include the main areas of interest, from the amygdala to the anterior cingulate cortex. In functional MRI studies the temporal resolution is important so this could not be sacrificed too greatly, and a repetition time (TR) of around 2000 ms is typical for a standard BOLD acquisition. This had to be increased due to the requirement of the labelling duration and post label delay for the PCASL sequence, and a TR of 3500 ms was considered acceptable. The stimulus paradigm was adapted accordingly to ensure that each "on" period and "off" period lasted for 14s, thus including two dynamic pairs of image acquisition. However, this still resulted in reduced statistical power due to the fact that fewer images are acquired in each stimulus condition (neutral, pleasant and unpleasant) for a given total task duration (14 minutes).

Emotional images were chosen with a variety of compositions, including animals, objects, faces and scenes. Emotional faces are known to elicit enhanced processing in the limbic system [78]. Previous studies have tended to use emotional images of either faces or scenes. In the design, it was

intentional to use a mixture of both emotional faces and emotional scenes in order to provide a broad subject matter for the emotional stimulus, as well as to elicit activation from all relevant brain regions and networks, and minimise any gender bias in the subjective arousal induced by the stimuli. However, this meant that the set of images did not have a predominance of emotional faces, which may have limited the limbic task involvement.

While the sample size was deemed to be acceptable for the study [41], despite the necessary exclusion of three subjects due to motion (resulting in n = 17), single gender subgroup sizes were not adequate for robust statistical analysis. Results from gender subgroups are based on group sizes of n = 8 male and n = 9 female. Therefore, any results reported here from gender subgroup analysis are exploratory only and do not carry the same statistical power as whole group (n = 17) analysis.

4.4.5   Impact of the study, future directions

Drug correlated differences have highlighted regions of the brain that are implicated in the salience network and in the processing of emotions, such as the insula and amygdala. This goes some way towards addressing the initial hypothesis that the peripherally acting beta-blocker modulates emotion related brain function. While some results presented here support the hypothesis, such as the reduction of task related activity in the insula, increased activity in the amygdala is counter-intuitive and contradictory to the hypothesis. These results promote interesting discussion of the mechanisms behind emotion processing and its modulation by nadolol.

A working theory could be as follows; it is possible that the blockade of the peripheral nervous system responses could cause the amygdala and its associated network of brain areas to "work harder" to compensate for the lack of peripheral information. Alternatively, it could be suggested that the peripheral blockade may sensitize central receptors in the amygdala, and thus emotional stimuli cause greater activity while the amygdala is in this enhanced state. An alternative speculative explanation for the paradoxical modulation

of amygdala response is that nadolol suppresses the processes that rationalise the emotional visual stimuli as merely non-threatening images, thus leaving the processing of threat and fear stimuli unsuppressed in the amygdala. However, there is no evidence that any of this speculation is correct and thus the topic is open for discussion and may require further analysis of behavioural and physiological data acquired for this study, or further experimentation may be needed.

The suggestion of drug induced modulation of brain function that differs in the two gender groups would imply that emotional visual stimuli are processed differently by males and females. If this were shown to be the case, a gender specific modulation of neural emotional processing could be exploited by future studies to provide more information on the mechanisms behind the processing of different stimuli that elicit activations in separate areas of the brain. It may be possible to suppress one set of processes in males and compare patterns of responses to emotional stimuli with those in females, for example. Such a study would require a larger number of subjects for comparisons between gender groups. In line with the effect size of this study, group sizes of 20 males and 20 females should be performed.

References

1. Fehr, FS, Stern, JA. Peripheral physiological variables and emotion: the James-Lange theory revisited. Psychol Bull, 74(6):411-24 (1970).

2. Schachter, S. and Singer, J. E. Cognitive, social and physiological determinants of emotional states, Psychological Review, 69, 379-399 (1962).

3. Critchley, HD, Rotshtein, P, Nagai, Y, O'Doherty, J, Mathias, CJ, Dolana, RJ. Activity in the human brain predicting differential heart rate responses to emotional facial expressions. NeuroImage 24:751-762 (2005).

4. Critchley, HD, Ellipt, R, Mathias, CJ, Dolan, RJ. Neural activity relating to generation and representation of galvanic skin conductance responses: a functional magnetic resonance imaging study. J Neurosci. 20:3033:3040 (2000).

5. Critchley, HD et al. Neuroanatomical basis for first- and second-order representations of bodily states. Nat Neurosci 4:207-212 (2001).

6. Nicotra, A, Critchley, HD, Mathias, CJ, Dolan, RJ. Emotional and autonomic consequences of spinal cord injury explored using functional brain imaging. Brain, 129, 718–728 (2006).

7. Pollatos O, Herbert BM, Matthias E, Schandry R. Heart rate response after emotional picture presentation is modulated by interoceptive awareness. Int J Psychophysiol 63:117-124 (2007).

8. Lundqvist, D., Litton, J. E. The Averaged Karolinska Directed Emotional Faces - AKDEF, CD ROM from Department of Clinical Neuroscience, Psychology section, Karolinska Institutet, ISBN 91-630-7164-9 (1998).

9. Viinikainen, M, Jääskeläinen, IP, Alexandrov, Y, Balk, MH, Autti, T, Sams, M. Nonlinear Relationship between Emotional Valence and Brain Activity: Evidence of Separate Negative and Positive Valence Dimensions. Human Brain Mapping 31:1030–1040 (2010).

10. Lang, PJ, Bradley, MM, Cuthbert, BN. International Affective Picture system (IAPS): Instruction manual and affective ratings. Technical

Report A4, Center for Research in Psychophysiology, University of Florida (1999).

11. Paradiso S, Johnson DL, Andreasen NC, O'Leary DS, Watkins GL, Ponto LL, Hichwa RD. Cerebral blood flow changes associated with attribution of emotional valence to pleasant, unpleasant, and neutral visual stimuli in a PET study of normal subjects. Am J Psychiatry. 156(10):1618-29 (1999).

12. Pollatos, O, Kirsch, W, Schandry, R. On the relationship between interoceptive awareness, emotional experience, and brain processes. Cognitive Brain Research 25 948 – 962 (2005).

13. Moratti S, Keil A, Stolarova M. Motivated attention in emotional picture processing is reflected by activity modulation in cortical attention networks. NeuroImage. 21(3):954-64 (2004).

14. Kobiella, A, Ulshofer, DE, Vollmert, C, Vollstadt-Klein, S, Buhler, M, Esslinger, C and Smolka, MN. Nicotine increases neural response to unpleasant stimuli and anxiety in non-smokers. Addiction Biology 16:285-295 (2011).

15. Breiter HC, Etcoff NL, Whalen PJ, Kennedy WA, Rauch SL, Buckner RL, Strauss MM, Hyman SE, Rosen BR. Response and habituation of the human amygdala during visual processing of facial expression. Neuron. 17(5):875-87 (1996).

16. Taylor, SF, Phan, KL, Decker, LR, Lizberon, I. Subjective rating of emotionally salient stimuli modulates neural activity. Neuroimage 18:650-659 (2003).

17. Liberzon, I, Taylor, SF, Fig, LM, Decker, LR, Koeppe, RA, Minoshima, S. Limbic Activation and Psychophysiologic Responses to Aversive Visual Stimuli: Interaction with Cognitive Task. Neuropsychopharmacology 23(5):208 - 516 (2000).

18. Morris JS, Ohman A, Dolan RJ. Conscious and unconscious emotional learning in the human amygdala. Nature. 4;393(6684):467-70 (1998).

19. Wilensky AE, Schafe GE, LeDoux JE. The amygdala modulates memory consolidation of fear-motivated inhibitory avoidance learning

but not classical fear conditioning. J Neurosci. 15;20(18):7059-66 (2000).

20. Phan KL, Fitzgerald DA, Gao K, Moore GJ, Tancer ME, Posse S. Real-time fMRI of cortico-limbic brain activity during emotional processing. Neuroreport. 1;15(3):527-32 (2004).

21. Phillips ML, Young AW, Senior C, Brammer M, Andrew C, Calder AJ, Bullmore ET, Perrett DI, Rowland D, Williams SC, Gray JA, David AS. A specific neural substrate for perceiving facial expressions of disgust. Nature. 2;389(6650):495-8 (1997).

22. Killgore WD, Yurgelun-Todd DA. Activation of the amygdala and anterior cingulate during nonconscious processing of sad versus happy faces. Neuroimage. 21(4):1215-23 (2004).

23. Kim H, Somerville LH, Johnstone T, Alexander AL, Whalen PJ. Inverse amygdala and medial prefrontal cortex responses to surprised faces. Neuroreport. 19;14(18):2317-22 (2003).

24. Winston, JS, O'Doherty, J, Dolan, RJ. Common and distinct neural responses during direct and incidental processing of multiple facial emotions. NeuroImage 20:84–97 (2003).

25. Blair RJ, Morris JS, Frith CD, Perrett DI, Dolan RJ. Dissociable neural responses to facial expressions of sadness and anger. Brain. 122 (Pt 5):883-93 (1999).

26. Hariri AR, Mattay VS, Tessitore A, Fera F, Weinberger DR. Neocortical modulation of the amygdala response to fearful stimuli. Biol Psychiatry. 15;53(6):494-501 (2003).

27. Liberzon, I, Phan, KL, Decker, LR and Taylor, SF. Extended Amygdala and Emotional Salience: A PET Activation Study of Positive and Negative Affect. Neuropsychopharmacology, 28, 726–733 (2003).

28. Gur RC, Schroeder L, Turner T, McGrath C, Chan RM, Turetsky BI, Alsop D, Maldjian J, Gur RE. Brain activation during facial emotion processing. Neuroimage. 16(3 Pt 1):651-62 (2002).

29. Lane RD, Reiman EM, Bradley MM, Lang PJ, Ahern GL, Davidson RJ, Schwartz GE. Neuroanatomical correlates of pleasant and unpleasant emotion. Neuropsychologia 35(11):1437-44 (1997).

30. Seeley WW, Menon V, Schatzberg AF, Keller J, Glover GH, Kenna H, Reiss AL, Greicius MD. Dissociable intrinsic connectivity networks for salience processing and executive control. J Neurosci. 28;27(9):2349-56 (2007).

31. White TP, Joseph V, Francis ST, Liddle PF. Aberrant salience network (bilateral insula and anterior cingulate cortex) connectivity during information processing in schizophrenia. Schizophr Res. 123(2-3):105-15 (2010).

32. Menon V, Uddin LQ. Saliency, switching, attention and control: a network model of insula function. Brain Struct Funct. 214(5-6):655-67 (2010).

33. Palaniyappan L, Liddle PF. Does the salience network play a cardinal role in psychosis? An emerging hypothesis of insular dysfunction. J Psychiatry Neurosci. 1;36(4):100176 (2011).

34. Strange, BA, Dolan, RJ. β-Adrenergic modulation of emotional memory-evoked human amygdala and hippocampal responses. PNAS, 101(31) 11454-11458 (2004).

35. O'Carroll, RE, Drysdale, E, Cahill, L, Shajahan, P and Ebmeier, KP. Memory for emotional material: a comparison of central versus peripheral beta blockade. Journal of Psychopharmacology 13(1):32-39 (1999).

36. Cahill L, Prins B, Weber M, McGaugh JL. Beta-adrenergic activation and memory for emotional events. Nature 371:702-704 (1994).

37. Cahill L, Haier RJ, Fallon J, Alkire MT, Tang C, Keator D, Wu J, McGaugh JL. Amygdala activity at encoding correlated with long term, free recall of emotional information. Proc Natl Acad Sci USA 93:8016-8021 (1996).

38. van Stegeren AH, Everaerd W, Cahill L, McGaugh JL, Gooren LJ. Memory for emotional events: differential effects of centrally versus peripherally acting beta-blocking agents. Psychopharmacology 138:305-310 (1998).

39. Pitman, RK et al. Pilot study of secondary prevention of posttraumatic stress disorder with propranolol. Biol psychiatry 51:289-192 (2002).

40. Vaiva, G et al. Immediate treatment with propranolol decreases posttraumatic stress disorder two months after trauma. Biol psychiatry 54:947-949 (2003).

41. Carter, CS, Heckers, S, Nichols, T, Pine, DS, Strother, S. Optimizing the Design and Analysis of Clinical Functional Magnetic Resonance Imaging Research Studies. Biol. Psychiatry. 64:842-849 (2008).

42. Cohen, J. Statistical power analysis for the behavioral sciences (2nd ed.). Hillsdale, NJ: Erlbaum (1988).

43. The rules governing medicinal products in the European Union, Volume 10; Notice to Applicants, Questions & Answers, Clinical Trial Documents. European Commission Enterprise and Industry Directorate - General, Brussels, F2/BL D (2006).

44. Zigmond, AS and Snaith, RP. The hospital anxiety and depression scale. Acta Psychiatr Scand, 67:361–370 (1983).

45. Nock, MK, Wedig, MM, Holmberg, EB, Hooley, JM. The Emotion Reactivity Scale: Development, Evaluation, and Relation to Self-Injurious Thoughts and Behaviors. Behavior Therapy 39:107–116 (2008).

46. Taylor GJ, Ryan D, Bagby RM. Toward the development of a new self-report alexithymia scale. Psychother Psychosom. 44(4):191-9 (1985).

47. Vorst, HCM, Bermond, B. Validity and reliability of the Bermond–Vorst Alexithymia Questionnaire. Personality and Individual Differences, 30, 413-434 (2001).

48. Davis, M. Measuring individual differences in empathy: evidence for a multidimensional approach. J. Pers. Soc. Psychol. 44, 113–126 (1983).

49. Porges, SW. Body perception questionnaire. Laboratory of Developmental Assessment, University of Maryland, Baltimore, MD (1993).

50. Sanofi-Aventis, 1 Onslow Street, Guildford, Surrey, GU1 4YS, UK.

51. Pater C. The Blood Pressure "Uncertainty Range" - a pragmatic approach to overcome current diagnostic uncertainties (II). Curr Control Trials Cardiovasc Med. 6;6(1):5 (2005).

52. McCluskey, A, Lalkhen, AG. Statistics II: Central tendency and spread of data. Continuing Education in Anaesthesia, Critical Care and Pain, 7 (4): 127-130 (2007).

53. Dixon EM, Kamath MV, McCartney N, Fallen EL. Neural regulation of heart rate variability in endurance athletes and sedentary controls. Cardiovasc Res, 26 (7): 713-719 (1992).

54. Pagani M, Lombardi F, Guzzetti S, Rimoldi O, Furlan R, Pizzinelli P, Sandrone G, Malfatto G, Dell'Orto S, Piccaluga E, et al. Power spectral analysis of heart rate and arterial pressure variabilities as a marker of sympatho-vagal interaction in man and conscious dog. Circulation Research, 59: 178-193 (1986).

55. Stein, PK, Bosner, MS, Kleiger, RE, Conger BM. Heart rate variability: A measure of cardiac autonomic tone. American Heart Journal, 127(5):1376-1381 (1994).

56. Presentation Software, Version 14. Neurobehavioural Systems Inc., Albany, CA.

57. 8 button fibre optic response pad, Current Designs, Inc. 3950 Haverford Ave, PA.

58. Aslan, S, Xu, F, Wang, Pl, Uh, J, Yezhuvath, US, van Osch, M and Lu, H. Estimation of Labeling Efficiency in Pseudocontinuous Arterial Spin Labelling. Magnetic Resonance in Medicine 63:765-771 (2010).

59. Silva AC, Kim SG. Pseudo-Continuous Arterial Spin Labeling Technique for Measuring CBF Dynamics With High Temporal Resolution. Magn Reson Med. 42(3):425-9 (1999).

60. Wu WC, Fernández-Seara M, Detre JA, Wehrli FW, Wang J. A Theoretical and Experimental Investigation of the Tagging Efficiency of Pseudocontinuous Arterial Spin Labeling. Magn Reson Med. 58(5):1020-7 (2007).

61. Nezamzadeh M, Matson GB, Young K, Weiner MW, Schuff N. Improved Pseudo-Continuous Arterial Spin Labeling for Mapping Brain Perfusion. J Magn Reson Imaging. 31(6):1419-27 (2010).

62. Friedman L. Glover G.H. Report on a Multicenter fMRI Quality Assurance Protocol. J. of Magn. Res. Img. 23:827-839 (2006).

63. Glover GH, Li TQ, Ress D. Image-based method for retrospective correction of physiological motion effects in fMRI: RETROICOR. Mag Reson Med. 44:162–167 (2000).

64. Montreal Neurological Institute (MNI) Template. Montreal Neurological Institute, Montreal, Canada.

65. Statistitcal Parametric Mapping, Wellcome Trust Centre for Neuroimaging, UCL, UK (2009).

66. MELODIC (Multivariate Exploratory Linear Optimised Decomposition into Independent Components), FMRIB Software Library (FSL), version 4.1.6, Oxford Centre for Functional MRI of the Brain, UK (2008).

67. Andrews-Hanna JR, Reidler JS, Sepulcre J, Poulin R, Buckner RL. Neuron. Functional-anatomic fractionation of the brain's default network. 25;65(4):550-62 (2010).

68. Hale, JR, Brookes, MJ, Hall, EL, Zumer, JM, Stevenson, CM, Francis, ST, Morris, PG. Comparison of functional connectivity in default mode and sensorimotor networks at 3 and 7T. Magn Reson Mater Phy 23:339–349 (2010).

69. Machulda MM, Jones DT, Vemuri P, McDade E, Avula R, Przybelski S, Boeve BF, Knopman DS, Petersen RC, Jack CR Jr. Effect of APOE ε4 status on intrinsic network connectivity in cognitively normal elderly subjects. Arch Neurol. 68(9):1131-6 (2011).

70. Matlab version 2009b, The MathWorks Inc., Natick, MA.

71. Kriegeskorte N, Simmons WK, Bellgowan PS, Baker CI. Circular analysis in systems neuroscience: the dangers of double dipping. Nat Neurosci. 12(5):535-40 (2009).

72. Pagani, M, Malfatto, G, Pierini, S, Casati, R, Masu, AM, Poli, M, Guzzetti, S, Lombardi, F, Cerutti, S, Malliani, A Spectral analysis of heart rate variability in the assessment of autonomic diabetic neuropathy. Journal of the Autonomic Nervous System, 23(2):143-153 (1988).

73. Coker R, Koziell A, Oliver C, Smith SE. Does the sympathetic nervous system influence sinus arrhythmia in man?: evidence from combined autonomic blockade. J Physiol 356:459-64 (1984).

74. Cook, JR, Bigger Jr, JT, Kleiger, RE, Fleiss, JL, Steinman, RC, Rolnitzky, LM. Effect of atenolol and diltiazem on heart period variability in normal persons. Journal of the American College of Cardiology. 17(2)480-484 (1991).

75. Pfefferbaum, A, Chanraud, S, Pitel, A, Shankaranarayanan, A, Alsop, DC, Rohlfing, T, Sullivan, EV. Volumetric cerebral perfusion imaging in healthy adults: Regional distribution, laterality, and repeatability of pulsed continuous arterial spin labeling (PCASL). Psychiatry Research: Neuroimaging, 182(3):266-273 (2010).

76. Stamatakis EA, Adapa RM, Absalom AR, Menon DK. Changes in resting neural connectivity during propofol sedation. PLoS One. 2;5(12):e14224 (2010).

77. Auer, DP. Spontaneous low-frequency blood oxygenation level-dependent fluctuations and functional connectivity analysis of the 'resting' brain. Magnetic Resonance Imaging 26 1055–1064 (2008).

78. Ball TM, Sullivan S, Flagan T, Hitchcock CA, Simmons A, Paulus MP, Stein MB. Selective effects of social anxiety, anxiety sensitivity, and negative affectivity on the neural bases of emotional face processing. Neuroimage. [Epub ahead of print] (2011).

5 ASL at 3 T in healthy volunteers: combined use of Territorial ASL and multi-phase ASL

5.1 Introduction

The objectives of this chapter are to implement a technique known as Territorial Arterial Spin Labelling (TASL) at 3 T, not previously performed at Nottingham, and use this in combination with quantitative assessment of perfusion and blood transit times provided by multi-phase ASL in a healthy volunteer study to assess and verify the cerebral haemodynamics, in particular the watershed regions.

Arterial Spin Labelling (ASL) provides quantitative endogenous perfusion contrast that allows repeated image acquisition with rapid washout, as outlined in Chapter 3. To date, ASL is still not widely used in the clinical setting, with gadolinium dynamic contrast-enhanced (DCE) perfusion imaging being favoured [1]. Due to the fact that DCE perfusion uses an intravenously administered contrast agent that will fill any and all blood vessels in the body, it is not possible to determine the exact arterial route by which blood arrives to the brain; only that it has arrived there. In ASL, the inversion slab used to label inflowing blood is most typically applied to all inflowing vessels simultaneously. However, ASL offers a unique opportunity to selectively label inflowing blood by careful placement of a selective inversion slab. Using this method, it is possible to determine which tissue regions are supplied by a particular artery or arteries. This technique is known as Territorial Arterial Spin Labelling (TASL) [1, 2, 3]. TASL provides the potential to determine the relative contributions of different feeding arteries to the total blood supply, in order to map the vascular perfusion territories in the brain. The technique was first demonstrated by Eastwood et al using spatially selective inversion pulses at 1.5 T for the purpose of labelling the left and right cerebral blood supplies (internal carotid and vertebral arteries) separately [4].

A study by Hendrikse et al [2] first termed the technique TASL, and used a TILT labelling scheme (see Section 3.5.4) at 1.5 T to delineate the flow

territories of the left and right internal carotid arteries and the posterior supply, thus providing territory maps. Their work showed that by selectively labelling the internal carotid artery, labelled blood flowed into the ipsilateral anterior cerebral artery and middle cerebral arteries. Further, labelling of the basilar artery resulted in labelled blood flowing through both posterior cerebral arteries [2]. In regular ASL, blood water in all inflowing arteries is labelled simultaneously, thus the inversion slab is positioned below, and parallel to, the imaging slab so that the two regions do not overlap. However in TASL, the inversion slab is positioned as a "free" slab, as shown in Figure 5.1 and often overlaps the imaging region. To prevent the appearance of a high intensity band that would otherwise appear over the intersecting regions of the image volume and label slab on the perfusion weighted images, in-plane pre- and post- saturation pulses are used [5].

Coronal view	Sagittal view	Axial view	
	Front vessels only		LICA
	Front vessels only		RICA
	Back vessels only		BA
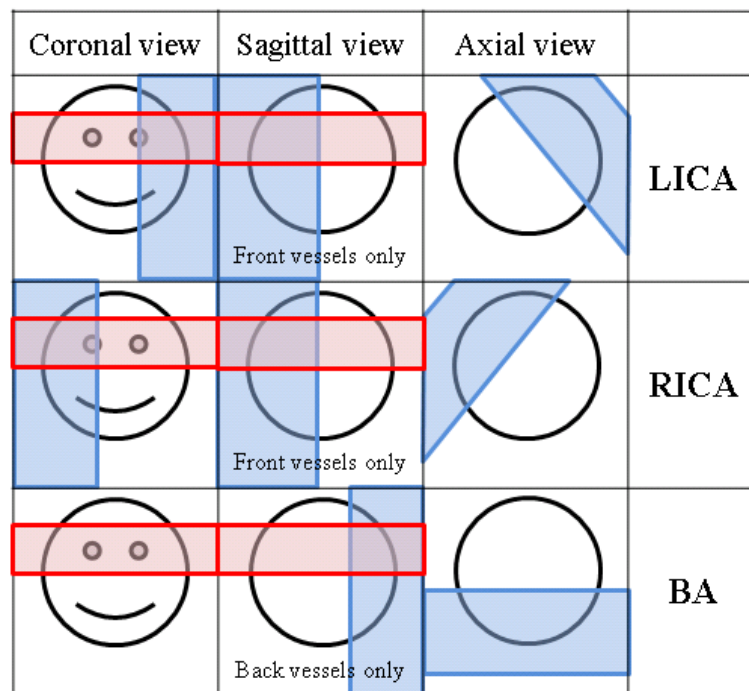
Figure 5.1: Schematic showing locations of labelling slabs for territorial ASL. Imaging region is shown in pink and can be seen to overlap the labelling region in all positions.

Territorial ASL has previously been demonstrated in both healthy subjects and in a patient with asymptomatic high-grade artery stenosis to provide maps of the vascular territories of the left and right internal carotid arteries (L / R ICA) and of the basilar artery (BA) using a pseudo-continuous arterial spin labelling

(PCASL) scheme [6]. In addition, this study used TASL to quantify the supply fraction provided by each artery in regions of mixed territorial supply.

Territorial ASL has been compared to the gold standard of digital subtraction angiography (DSA) in a cohort of patients with extra- or intra-cranial steno-occlusive disease [1], for the purpose of identifying occluded cerebral arteries. DSA requires the injection of gadolinium contrast, whereas TASL is entirely non-invasive. While TASL did not provide the same accuracy of vessel identification as DSA (TASL provided 89% success rate compared to 98% with DSA, as assessed using statistical contingency tests to measure agreement between methods), this was attributed to motion related artefacts incurred using TASL [1]. To date, there are still a strikingly small number of studies published in the literature that use the technique of territorial ASL.

An alternative ASL method is that of a multi-phase (also termed multi-TI) ASL scheme. Variants of this include inflow turbo-sampling EPI-FAIR (ITS-FAIR) [7], Look-Locker ASL [8, 9], or quantitative STAR labelling of arterial regions (QUASAR) [10]. The multi-phase technique was previously outlined in Section 3.5.4. In this method, an inversion label is applied to label inflowing blood from all arteries. Rapid repeated imaging of the brain following a single label can then be used to determine information on both the label arrival time and perfusion rate of the tissue. A pulse sequence for this method is shown schematically in Figure 5.2. This method involves applying a single label and subsequently imaging several times in close succession allowing the entire arrival and washout / relaxation of the labelled blood to be modelled. The first image is acquired at an inversion time with a post-label delay, TI, after the application of the labelling pulse. Subsequent images are acquired at a separation time, TA, after the initial image. A mathematical model of the label signal can then be used to create a fit of the response curve for each voxel, using the ASL signal measured at each time point [9]. This model accounts for inflow and exchange time, as well as the suppression by RF pulses, and relaxation time effects. In comparison to single TI pulsed ASL, multi-phase ASL provides additional information about the transit time to the tissue, allowing improved perfusion estimation. Given that multi-phase

data collects the perfusion weighted signal at additional time points, it is possible to calculate blood transit time and quantitative perfusion values. The number, separation (TA) and flip angle of the multiple image acquisitions, shown in Figure 5.3, can be varied so that the sequence is more sensitive to either arterial transit time (Δ) and arterial blood volume (CBVa) or capillary transit time (δ) and cerebral blood flow (CBF) [9]. For example, at 3 T, maximum sensitivity to CBF can be achieved (at a flip angle of 35° - 45°) using an initial TI of 300 ms, with 7 readout phases at a TA of 300 ms [9], and applying a vascular crushing gradient to suppress the signal originating from arterial blood that is flowing with a velocity greater than the specified vascular crushing velocity. Vascular crushing can be achieved using a bipolar gradient, described in terms of the velocity of blood flow above which signal will be crushed (V_{enc}) and is given in cms^{-1}. Sensitivity to CBVa requires a larger flip angle (for example, 50°), with more readout phases (up to 21) at a shorter TA (around 100 ms) thus suppressing signal from the tissue compartment [9]. Alternatively two sets of multi-phase ASL can be acquired with the same timings and flip angles with and without crushing gradients. Data acquired with crushing gradients can be used to suppress the arterial component and sensitise to tissue signal, whilst the subtraction of the two data sets provides sensitivity to the arterial signal (Figure 5.3), [10].
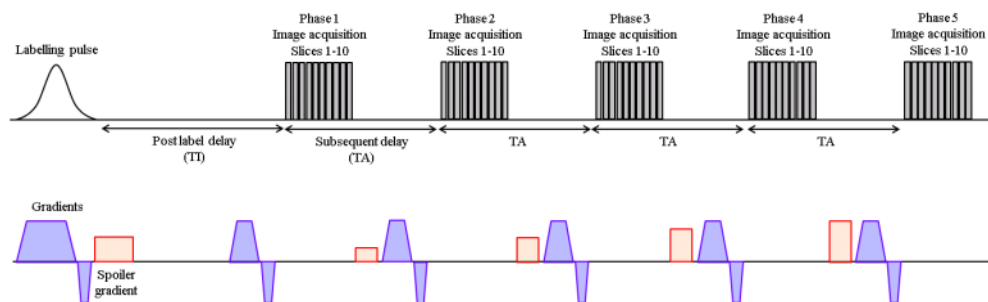
Figure 5.2: Pulse sequence diagram for multi-phase ASL acquisition [8], showing timings of image acquisitions and slice select gradients (spoiler gradients shown in red).
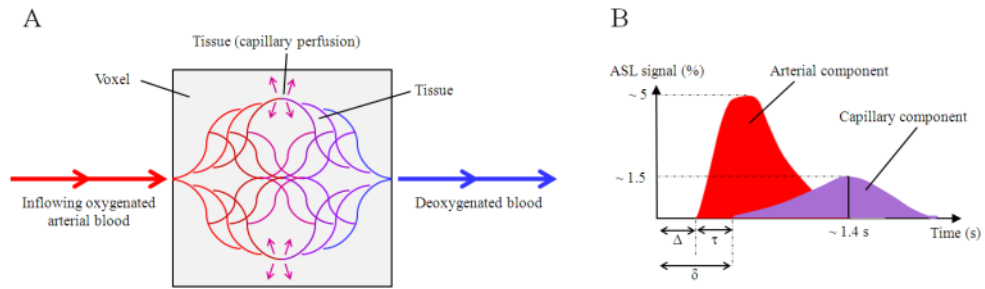
Figure 5.3: (A) Diagram of vasculature showing relative contributions of arterial (red) and capillary (purple) components to the ASL signal. (B) Schematic of the ASL signal changes expected in each compartment (ignoring effects of repeated suppression by the multi-phase acquisition). This shows the arterial (Δ) and capillary (δ) transit times, and τ which is the time taken for exchange between arterial and capillary compartments.

The cerebral watershed areas are the cortical grey matter areas supplied by the most distal branches of the arterial territories, defining the border zone between two arterial territories. A paper by Hendrikse et al describes the cerebral border zones as the regions extending from the frontal and occipital horns of the lateral ventricle to the fronto and parieto-occipital cortices [3]. In a study of healthy volunteers, it was shown that tissue in these regions exhibit significantly lengthened arterial transit time of blood [3]. These areas are considered to be at high risk of haemodynamic stroke and have possible involvement in thrombo-embolic stroke as a result of the reduced washout capacity [11, 12]. Hendrikse et al assessed global cerebral blood flow in patients with internal carotid artery occlusion and healthy controls. Images were acquired using a TILT labelling scheme at 1.5 T at post-label delay times of 200 ms, 400 ms, 600 ms, 800 ms, 1200 ms and 1600 ms, where each TI was acquired following a single inversion pulse (i.e. a single TI method). A general kinetic model [14] of the ASL signal was then used to calculate quantified CBF values within regions of interest in the grey matter of the bilateral middle cerebral arterial territories. The group found a significant decrease in cerebral blood flow in the region of interest in the hemisphere with occlusion compared to the contralateral region of interest, and compared to healthy control subjects [15]. It is possible to locate regions of the brain with lengthened transit times using a technique similar to the multi-phase ASL described above.

The precise location and extent of watershed regions is not easily derived [16] from brain atlases due to a high degree of inter-individual variation. Additionally, watershed regions may be shifted in subjects with cerebrovascular disease [15]. For these reasons, there is interest in physiologically defining the location and variation in the cerebral watershed regions. The primary aims of this chapter are as follows:

- To acquire territorial ASL – selective maps of the vascular territories of the internal carotid arteries and posterior circulation, and to separate the vascular territories of the middle cerebral and anterior cerebral arteries.

- To compare the locations and boundaries of the watershed regions at a group averaged level using Territorial ASL, with maps of lengthened arterial and capillary transit times (Δ and δ respectively) from multi-phase ASL data, indicative of watershed areas.

A secondary aim is to assess transit time variance across a range of cortical areas. This would provide useful information for planning future ASL studies and for functional MRI studies using perfusion weighted contrast.

5.2   Methods

The study was approved by the University of Nottingham Medical School Research Ethics Committee. All subjects gave fully informed, written consent after having the procedure explained to them, and confirmed that they had no past cerebrovascular medical history, and considered themselves to be healthy. This chapter reports a study in which ten subjects (age 27 ± 3 years, n = 5 male) were scanned on a Philips Achieva 3.0 T MRI scanner with an 8 element SENSE head coil in a single session. A total of 21 healthy subjects were scanned during the development of the protocol and the period in which the scanner operators were familiarising themselves with the technique, and the study. The scanning protocol run in ten subjects for the complete assessment is shown in Figure 5.4. To overview this protocol, subjects first underwent a standard set-up protocol of a survey and reference, followed by

an EPI base scan. The EPI base scan (two dynamics of the EPI acquisition, at the same resolution / bandwidth as the EPI scans used for the TASL and multi-phase CBVa readout, with a TE of 13 ms and a TR of 10 s) was used for the registration of the datasets to standard MNI space and to provide a measure of the equilibrium magnetisation, M_0. Coronal and sagittal phase contrast angiograms (PCA) and a time of flight (TOF) contrast angiogram, each taking approximately 3 minutes to collect, were used for locating inflowing arteries and thus for positioning selective inversion slabs for TASL. Standard ASL labelling all inflowing vessels was first acquired with a single TI, for assessment of total perfusion and validation of labelling. Territorial ASL was acquired for the four vascular territories of the left and right internal carotid arteries (LICA and RICA), posterior blood supply of the basilar and vertebral arteries (BA) and anterior cerebral artery (ACA). Multi-phase ASL was acquired labelling all inflowing vessels, both without and subsequently with vascular crushing to provide maps of arterial blood volume and transit time (CBVa and Δ) and cerebral blood flow and capillary transit time (CBF and δ) respectively. Each of the five single-TI ASL scans and each multi-phase ASL scan took approximately 4 minutes. The total scan time for the entire scan card was approximately 40 minutes; however the time in the scanner was slightly longer when accounting for planning time.

| Survey (1 min) |
| Reference (1 min) |
| Coronal PCA (2 min 30 s) |
| Sagittal PCA (2 min 30 s) |
| Time of Flight (2 min 30 s) |
| 10 slice EPI Base (30 s) |
| ASL – labelling all inflowing vessels (4 min) |
| TASL – RICA (4 min) |
| TASL – LICA (4 min) |
| TASL – BA (4 min) |
| TASL – ACA (4min) |
| Multi-phase ASL without vascular crushing (CBVa and Δ) (4 min) |
| Multi-phase ASL with vascular crushing (CBF and δ) (4 min) |

Planning location of selective inversion slab for TASL

Assessment of cerebral vascular territories

Assessment of haemodynamic flow and transit time parameters

Figure 5.4: Scanning protocol for combined assessment of territorial ASL and multi-phase ASL for haemodynamic parameter maps.

5.2.1   Territorial Arterial Spin Labelling (TASL)

In order to selectively label the arteries in the neck region for TASL, a fast, non-invasive method of determining the positions of the feeding arteries must first be used. This was performed using phase contrast (PCA) and time of flight contrast angiography (TOF), as shown in Figure 5.5 (see Section 3.5.1).
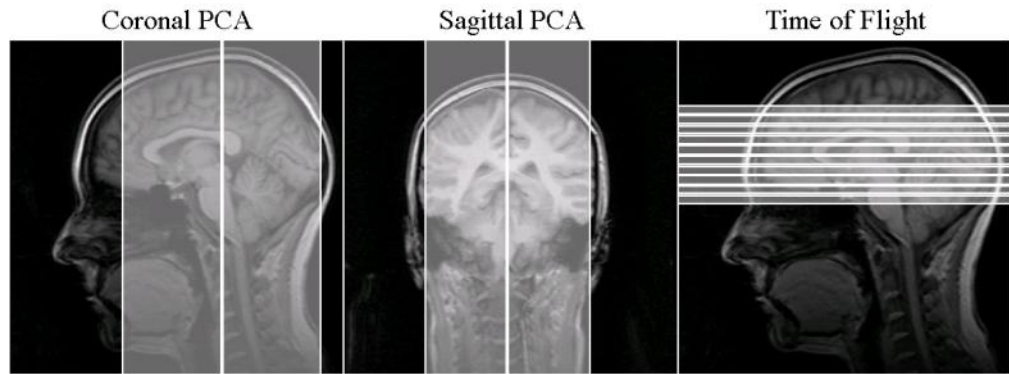
Figure 5.5: Locations of planning slabs for phase contrast angiograms (PCAs) and time of flight (TOF) angiogram, shown superimposed on to sagittal and coronal survey images.

Phase contrast angiography (PCA) was collected in coronal and sagittal planes to aid planning of TASL and comprised two thick slices in each direction. The coronal slices were positioned such that the anterior vessels (internal carotid arteries, middle cerebral artery) could be separated from the posterior vessels (basilar artery, posterior cerebral artery) by placing the two coronal slices symmetrically about the brainstem. The coronal PCA was acquired using a TE / TR of 7.6 ms / 14 ms, flip angle of 20°, and a SENSE factor of 2. An in-plane resolution of 0.72 mm by 1.2 mm was used for two 60 mm slices, with a field of view of 250 mm × 250 mm × 110 mm. A phase contrast velocity encoding of 30 cms^{-1} was used so that arterial blood flowing at this velocity will exhibit a maximum phase difference and thus maximum signal intensity. The sagittal slices were positioned such that the left and right internal carotid arteries could be clearly seen, i.e. that the two slices were positioned symmetrically about the interhemispheric fissure. The sagittal PCA was acquired using a TE / TR of 7.6 ms / 20 ms, flip angle of 15° and a SENSE factor of 2. An in-plane resolution of 0.72 mm by 1.2 mm was used for two 50 mm sagittal slices with a field of view of 230 mm × 230 mm × 95 mm. The phase contrast velocity encoding was again 30 cms^{-1}.

In the axial direction, a Time of Flight (TOF) contrast angiogram was collected. This was positioned to show the Internal Carotid Arteries (ICAs) and the Circle of Willis. The TOF was acquired using a TE / TR of 2.3 ms / 23 ms, 18° flip angle, SENSE factor 2, in plane resolution of 0.543 mm ×

0.82 mm with one hundred 0.7 mm slices and 200 mm × 200 mm × 70 mm field of view. From this, a maximum intensity projection (MIP) was formed. The PCAs and TOF MIPs were used for the subsequent planning of the selective TASL slabs [2].

Prior to TASL, single TI ASL data was acquired labelling all inflowing vessels (termed "all") using a 100 mm thickness slab positioned in the neck, parallel to the imaging slab, and a post-label delay of 1200 ms. In-plane saturation was applied to the imaging slab pre- and post-labelling (and is described in further detail below). This "all" single TI scan also provided a check as to whether the labelling was working efficiently, as the image subtraction tool, which is available as part of the scanner software, was used to check the image quality of the perfusion weighted images at the scanner.
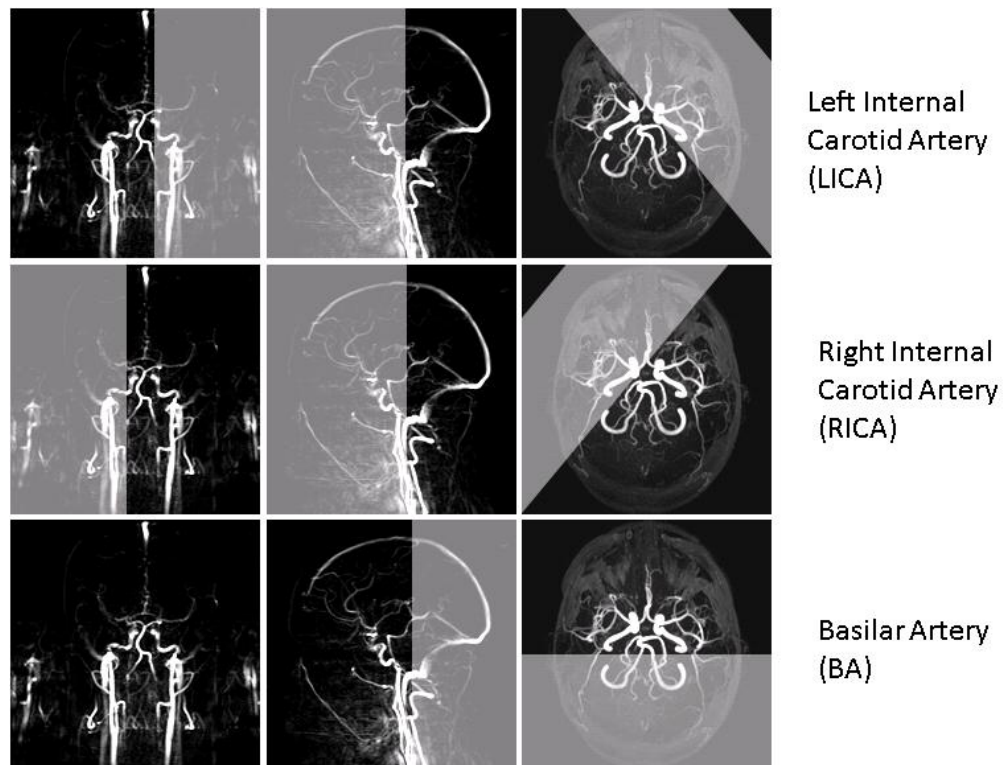
Figure 5.6: Locations of selective inversion labelling slabs used for TASL superimposed on to coronal and sagittal PCAs and axial TOF angiogram.

For TASL, slabs of an approximate thickness of 50 mm were positioned to label the anterior blood supply in the left and right internal carotid arteries (ICAs) and middle cerebral arteries, and to label the posterior blood supply

160

including the basilar artery (BA), vertebral artery and posterior cerebral artery, as described in previous work [2], and shown in Figure 5.6. In addition, the anterior cerebral arteries (ACA) were selectively labelled using a narrow inversion labelling slab of approximate thickness 20 mm, applied in the sagittal plane, as shown in Figure 5.7. All TASL data were also collected with a post-label delay of 1200 ms.
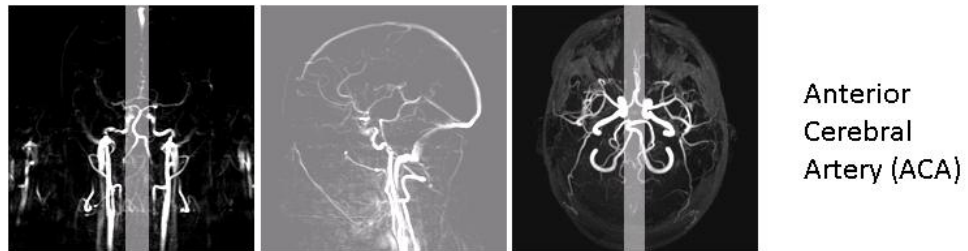
Figure 5.7: Location of the selective inversion slab used to label the anterior cerebral arteries, superimposed on coronal and sagittal PCAs and axial TOF angiograms.

All labelling was performed using a STAR (Signal Targeting with Alternating Radiofrequency) ASL sequence. This sequence uses alternately acquired label and control images followed by a single shot multi-slice EPI acquisition method. The STAR labelling scheme comprised two successive inversion pulses using hyperbolic secant adiabatic inversion pulses to form the control condition ($180° + 180° = 360°$). For the label condition, an adiabatic inversion pulse with nominal 360° degree power was used. In this way, the offset frequency and power used were identical for label and control STAR conditions, thus controlling for magnetisation transfer (MT) effects.

In-plane saturation was applied to the imaging plane for all ASL schemes using a pre-saturation and post-saturation scheme. Use of in-plane saturation is critical for TASL, as the label overlaps the imaging plane. The in-plane pre-saturation scheme comprised a WET (Water suppression Enhanced through T1 effects) scheme of four selective pulses (of flip angle 89.17°, 98.37°, 82.31° and 156.77°) applied prior to the labelling pulse, following labelling the post-saturation scheme comprised a single sinc pulse. Pre- and post-saturation pulses were applied to the imaging region, with additional coverage of 45 mm above the imaging region to prevent signal contributing from

inverted blood in vessels above the imaging region flowing downwards into the imaging region, and also 10 mm below the imaging region. The positions of the imaging slices and the pre- and post- saturation slab thickness are shown in Figure 5.8.
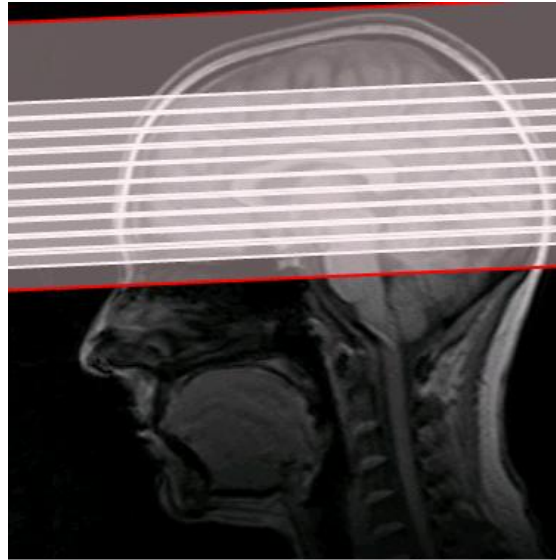
Figure 5.8: Location of imaging slab (slices shown in white) and the in-plane saturation pre- and post- saturation slabs (highlighted in red). The in-plane saturation had an additional thickness of 45 mm above and 10 mm below the imaging region.

For each labelled territory, 40 pairs of label and control images were acquired at a post-label delay (TI) of 1200 ms to maximise ASL signal whilst minimising arterial contribution to the signal [2, 17], and a TR per label / control pair of 6 s. As vessels could be difficult to selectively label, the location of the labelling slab was first tested by acquiring 5 dynamic pairs per territory, and subtraction of label and control images was performed on-line using the image subtraction tool. If necessary the labelling slab was repositioned at this stage, before repeating the process until satisfactory labelling of the territory was achieved. All single-TI ASL data were acquired with gradient echo EPI readout with 3 mm in plane resolution and a slice thickness of 8 mm with a 212 mm × 212 mm field of view. A 10 slice dataset was acquired in ascending order, positioned as shown in Figure 5.8.

Prior to the study, 11 subjects were scanned using the TASL protocol only, to give the scanner operators experience in using the technique and reduce the

effect of user dependence on planning the selective labelling. The success rate of labelling individual vascular territories in these 11 subjects is listed in Table 5.1, with complete success termed as good clear individual territories for each. Subsequently ten subjects were scanned for the complete protocol outlined in Figure 5.4.

Pilot subject	BA	LICA	RICA	Complete success?
1	✗	✗	✗	✗
2	✗	✗	✗	✗
3	✗	✗	✗	✗
4	✗	✗	✓	✗
5	✗	weak	✓	✗
6	✓	✓	weak	✗
7	✓	✓	✓	✓
8	✓	✓	✓	✓
9	✓	✓	✓	✓
10	weak	✓	✓	✗
11	✓	✗	weak	✗

Table 5.1: Success rate of labelling of vascular territories for the 11 subjects scanned during learning phase prior to the start of the study.

It is clear that as the learning progressed, success improved, but inevitably, there were still occasional failures due to proximity of other vessels to target vessels, thus causing additional labelling in the adjacent territory, or due to subject motion between the planning scans and the TASL acquisition.

5.2.2 Multi-phase ASL

Multi-phase ASL data were collected using the STAR labelling scheme, as described above for TASL, but with the labelling applied to all inflowing vessels. Following labelling, a multi-phase EPI readout sequence with an initial delay (TI) of 300 ms, and a total of 7 equally spaced acquisitions at an inter-phase interval (TA) of 300 ms was acquired. These timings ensure that the sequence was optimised to calculate cerebral blood flow (CBF) and

capillary transit time (δ) [9], when vascular crushing is applied. In the first instance, data were acquired without vascular crushing ensuring a large arterial component to the signal, providing an estimate of arterial transit time (Δ) and CBVa maps. Second, the scan was repeated with the addition of a bipolar vascular crushing gradient applied following each excitation, thus suppressing the signal from fast flowing spins [18]. A bipolar gradient of V_{enc} = 5 cms^{-1} was used to suppress the signal from fast flowing blood, thus weighting the sensitivity towards blood in the capillary compartment. This was applied using a 4 ms bipolar gradient with gradient amplitude 11 mT / m in the foot-head axis only. The velocity encoding of the bipolar gradient can be calculated from:

$$V_{enc} = (2\gamma A \delta^2)^{-1}$$ Eqn. [5.1]

where γ is the proton gyromagnetic ratio, A is the gradient lobe amplitude and δ is the gradient lobe duration plus half the sum of the rise and fall times. The bipolar gradients will cause an attenuation of the signal from moving protons, such that there will be a distribution of attenuation values across flow velocities, and the b factor can also be estimated from:

$$b = \frac{2}{3}\delta^3(2\pi\gamma A)^2$$ Eqn. [5.2]

which for this bipolar gradient was found to be equivalent to 0.37 smm^{-2}. Vascular crushed ASL data were used to produce maps of capillary transit time (δ) and perfusion (CBF).

All multi-phase data were acquired using a TE / TR of 14 ms / 3200 ms and a flip angle of 45°. The field of view and spatial resolution was identical to that used for the single TI data outlined above. However, since the multi-phase technique does not allow for as wide coverage as single-TI methods, due to the time constraints of acquiring several readouts in the interval between the phases, only 6 slices could be acquired. Slices were acquired in ascending order, with the centre of the stack for the multi-phase data positioned to match

the centre of the single-TI ASL stack. 40 dynamic pairs of label and control images were acquired for each of the two multi-phase ASL datasets.

5.2.3   Processing and Analysis

To inspect the quality of the data during scanning, data sets were viewed using the on-line image subtraction program available on the scanner, subsequently data were then processed and analysed off-line as outlined below. Single-phase ASL label and control images were subtracted for each dynamic to form perfusion weighted difference images. These individual difference images were then visually inspected for motion with a view to discarding degraded dynamics, however this was not necessary. The data were then averaged across the 40 dynamics. This was performed using software written in MATLAB [19]. Single-TI ASL data with all inflowing vessels labelled was used to calculate perfusion weighted difference images of the entire blood supply. TASL label and control images were subtracted to form perfusion weighted difference images of vascular territories (right and left ICAs, BA and ACA). All single-TI data were spatially smoothed to a FWHM of 8 mm.

Multi-phase ASL label and control images were also subtracted to give a perfusion weighted image for each readout phase and slice. Non-vascular crushed multi-phase data was then fitted on a voxel-by-voxel basis to form arterial transit time (Δ) and CBVa maps. Vascular crushed data was fitted to form capillary transit time (δ) and perfusion (CBF) maps. This was performed using in-house software developed and written in c by Dr Susan Francis. that used a three compartmental model of the multi-phase ASL sequence of perfusion measurements [9]. The model takes account of the arterial transit time of the blood (compartment 1) before making temporally stepwise calculations of the transit of blood through the arteriolar and capillary compartment (compartments 2 and 3 respectively). This is to avoid discontinuity as the blood makes transitions from one component to the next. Data were fitted by entering the perfusion weighted images and EPI base data, and assuming a T_1tissue of 1300 ms and T_1blood of 1600 ms.

To form group maps of the vascular territories, arterial and capillary transit times, CBF and CBVa, the 10 slice EPI base images were first transformed into MNI space [20] using the FLIRT linear registration tool in FSL [21]. The transforms created by this process were then applied to all ASL data.

Each vascular territory perfusion weighted image was threshold at a level that suppressed noise (approximately 0.5%) and averaged across the group. To further evaluate the data a number of quantitative analyses were then performed:

(i) Binary masks were formed of each territory (LICA, RICA, BA and ACA) from the thresholded TASL data formed above. These masks were then summed across subjects to create group probability maps showing the coincidence of the location of each territory across the group. Overlap of territorial labelling was assessed for each subject by calculating the number of voxels that appear in two adjacent territories as a proportion of each territory, as shown in Figure 5.9.
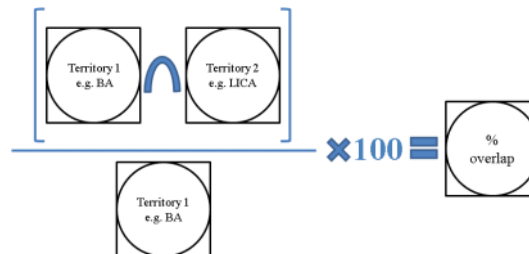
Figure 5.9: Method of calculating overlap between territories. Example shown is for the overlap of the LICA onto the BA.

(ii) Binary masks for the left and right ICA and BA territories were summed for each subject. This summed mask was then multiplied by a binary grey matter (GM) mask created using the FSL standard grey matter atlas, threshold at a probability of 0.5 [21]. A TASL watershed GM mask was then formed by subtracting the summed mask of vascular territories from the GM binary mask, as shown pictorially in Figure 5.10. This TASL watershed GM mask was then used as a surrogate for an objective definition of the watershed regions to

interrogate arterial and capillary transit time maps and for correspondence with watershed regions from multi-phase ASL data.
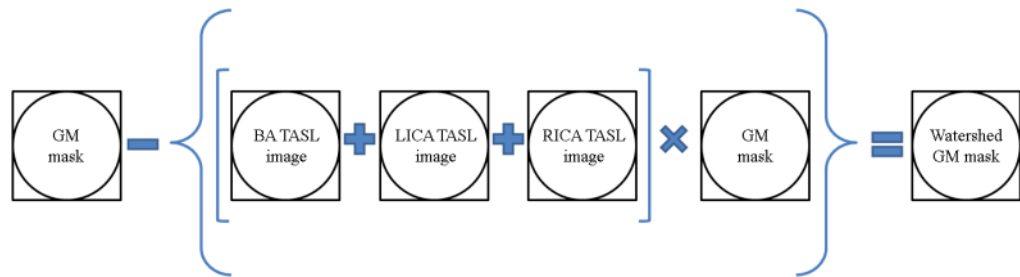
Figure 5.10: Method for producing a mask of watershed GM regions from the TASL data. Grey matter voxels that did not appear in any of the vascular territory maps were used to define the watershed region.

(iii)   Multi-phase ASL data were used to compute group haemodynamic parameter group maps of CBVa, Δ, CBF and δ, and the average and standard deviation of these values calculated across subjects. Watershed areas were manually defined from the multi-phase data as those regions displaying lengthened transit times, typically with arterial or capillary transit times greater than 900 ms, and classified as anterior, posterior and internal watersheds. To form objective grey matter watershed regions of interest (ROIs), the capillary transit time maps were threshold at 900 ms, and a binary mask formed. These multi-phase watershed masks were then multiplied by the standard GM mask described above to form a multi-phase watershed GM mask.

(iv)   Correspondence between TASL vascular territory maps and the watershed areas were calculated as percentage overlap. This was first performed by finding the number of voxels that appear in both the manually defined watershed region and the vascular territory and calculating this as a percentage of the number of voxels in the watershed region, as shown in Figure 5.11 (A). The hypothesis is that this percentage would be low if both methods are defining the watershed regions. Secondly, the percentage of common voxels that appear in both the TASL watershed GM mask and the multi-phase watershed GM mask was assessed, as shown in Figure 5.11 (B). The

hypothesis is that this value should be high if both methods define the watershed areas.
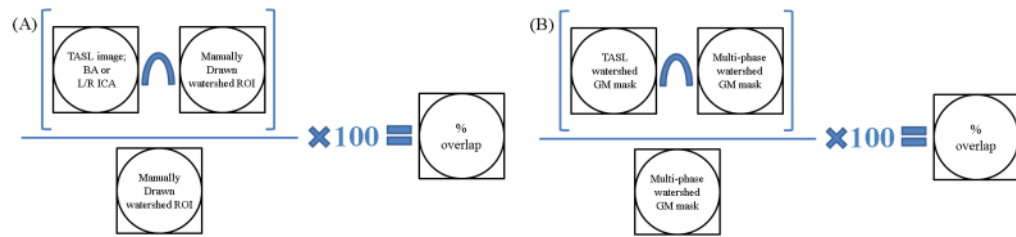
Figure 5.11: (A) Procedure for calculating correspondence between vascular territories and watershed areas as percentage overlap. (B) Procedure for calculating correspondence between methods of creating grey matter watershed masks.

Mean and standard deviation CBVa, Δ, CBF and δ values were computed for each vascular territory (left and right ICA, BA and ACA). These values were also computed for each of the manually drawn watershed regions (anterior, posterior and internal), as well as GM watershed areas calculated from the TASL and multi-phase data and the watershed area formed from the conjunction of the two GM watershed areas.

In addition, as a secondary aim, the parameters CBVa, Δ, CBF and δ were assessed for their mean value within anatomically defined regions of interest, the location and shape of which were found using the anatomical atlas (WFU Pick Atlas toolbox) from SPM [22]. Regions were chosen in the caudate, putamen, thalamus, primary somatosensory and motor cortices, insula, cingulate, inferior occipital cortex and occipital pole (including the primary visual cortex).

5.3 Results

5.3.1 Territorial ASL

Single phase "all" ASL data provided good quality perfusion weighted images, with the blood supply from all inflowing vessels labelled in all ten subjects scanned for the complete protocol. Group averaged images ($n = 10$) are shown in Figure 5.12. The increased perfusion weighted signal apparent in

the posterior region of the brain (visual cortex and occipital pole) at this TI is indicative of the lengthened arterial transit time of blood to that region and hence a contribution from arterial blood, whereas anterior and temporal grey matter regions that are also highly perfused exhibit a lower perfusion weighted signal due to the shorter arrival time.
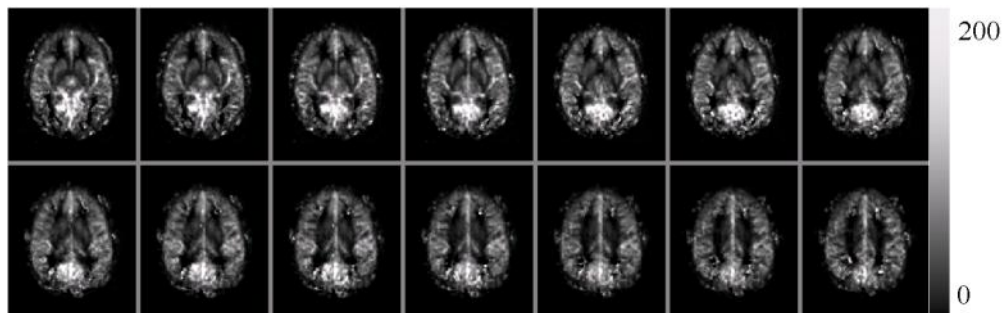
Figure 5.12: Group (n = 10) perfusion weighted (single-TI) images with all inflowing vessels labelled. Colour bar shows ASL signal intensity scale (arbitrary units).

Efficiency of selective labelling for territorial ASL was qualitatively assessed by assessing the vascular territory maps for each subject, as outlined in Table 5.2. Selective labelling of the ACA was unsuccessful in most subjects, with the primary reason for this being the additional labelling of the BA territory. Labelling was found to be highly successful for all three of the LICA, RICA and BA territories in only 5 out of 10 subjects. In the remaining subjects, only one or two territories were successfully labelled, with some territories receiving insufficient labelling and in other territories the labelling was not selective enough, thus labelling extra vessels additional to those intended. Failure was attributed to difficulty of placing labelling slabs over tortuous vessels and due to proximity of adjacent vessels limiting the ability to label only one vessel. There is also the possibility of subject motion occurring between the acquisition of the planning angiography and the territorial ASL so that labelling slabs no longer efficiently covered the required vessel. Figure 5.13 and Figure 5.14 show examples of this, where the labelling slab covering the anterior blood vessels (particularly the LICA) has also labelled the BA, and where the labelling slab covering the ACA has also inadvertently covered the posterior cerebral artery.

Study subject	BA	LICA	RICA	ACA		Complete success?
1	✓	weak	✓	also BA*		✗
2	✓	weak	weak	weak		✗
3	"all"*	weak	✓	also BA*		✗
4	✓	✓	✓	also BA*		✓
5	✓	✓	✓	also BA*		✓
6	✓	✓	✓	also BA*		✓
7	✓	✓	✓	✗		✓
8	weak	✓	weak	✗		✗
9	✓	✓	✓	weak		✓
10	weak	weak	✓	✗		✗

Table 5.2: Success of labelling the three vascular territories for each subject. Asterisks represent cases where adjacent territories were labelled in addition to the target territory.
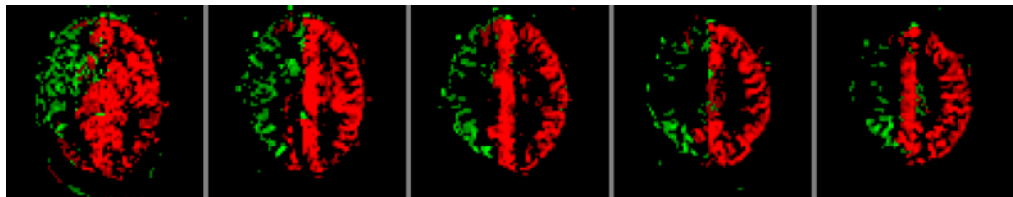
Figure 5.13: LICA (red) and RICA (green), shown in a subject where both anterior territories can be seen to overlap the territory of the BA (not shown). This is due to the labelling slab labelling posterior vessels in addition to anterior vessels.
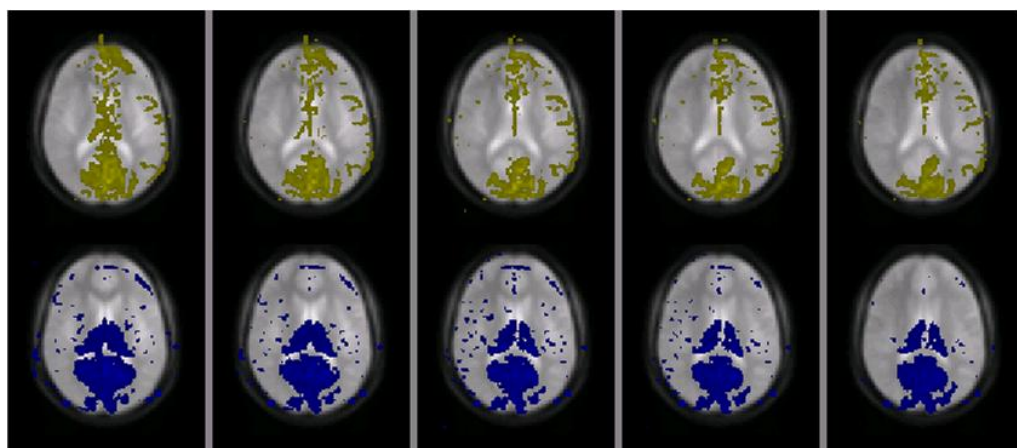
Figure 5.14: ACA (yellow) and BA (blue) shown in a subject where labelling of the ACA resulted in additional labelling of the posterior cerebral artery, and thus partial coverage of the posterior (BA) territory.

The binarised average map for the group of 10 subjects is shown in Figure 5.15, where each of the territories are colour coded using the standard labelling of using green, red and blue to represent the RICA, LICA and BA territories respectively, in addition the ACA is shown in yellow. It is clear that there is a correspondence throughout the group; all healthy volunteers in the group displayed similar borders of vascular territories. Probabilities of voxels appearing in each vascular territory across subjects scaled from 0 to 1 are shown in Figure 5.16 (A, B and C) for the posterior territory (BA), and left and right anterior territories (LICA and RICA) respectively. Table 5.3 shows how each territory overlaps onto each of the other territories as a mean percentage across the group. The left and right ICA territories show very little overlap, as expected from their geometric location. The greatest overlap seen is of the BA onto the ACA, where in some subjects, the entire BA territory labelled was contained within the labelling of the ACA territory. Conversely, the overlap of the ACA onto the BA is smaller, as in the ACA territory of every subject, there was at least some labelling additional to that of the BA territory.
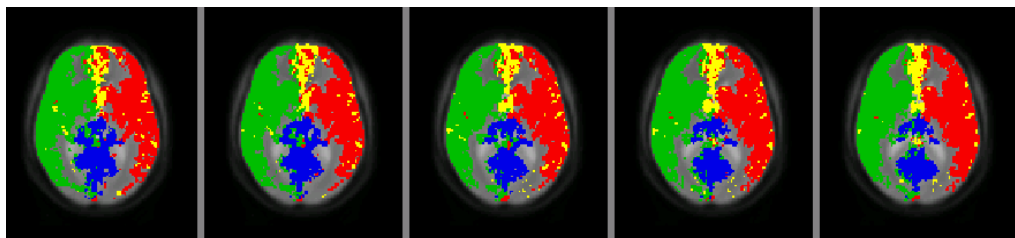
Figure 5.15: Group (n = 10) averaged maps of (A) vascular territory binary masks (green, yellow, red and blue represent RICA, ACA, LICA and BA respectively). Data shown are for five slices of MNI co-ordinates z = 2 to z = 10.
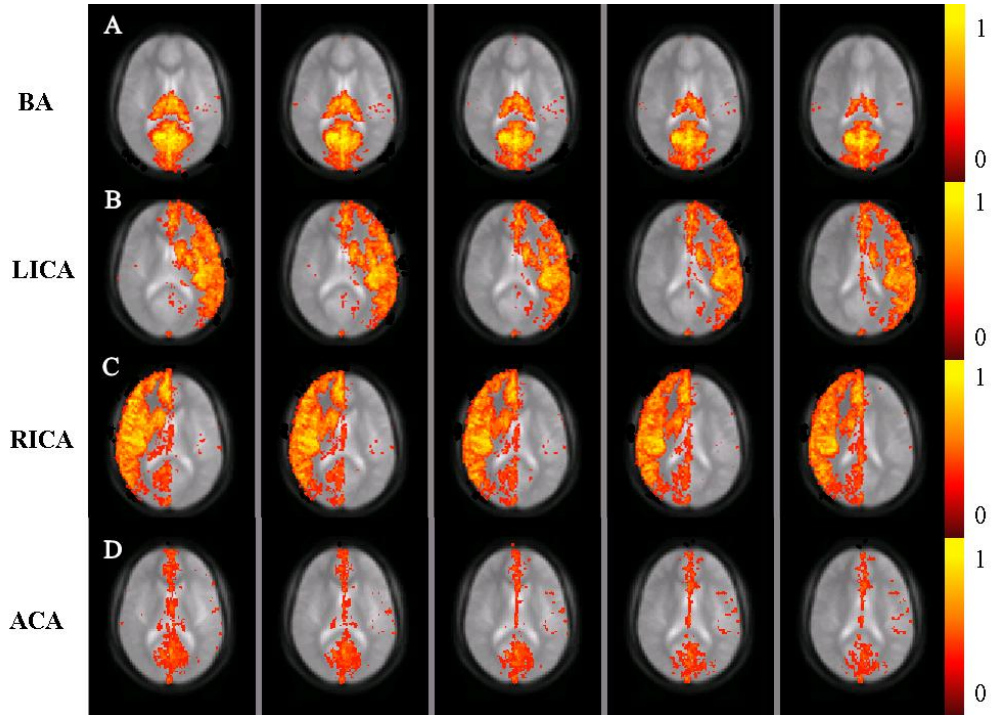
Figure 5.16: Group (n = 10) probability maps of the (A) BA, (B) LICA, (C) RICA and (D) ACA territories individually. Data shown are for five slices of MNI co-ordinates z = 2 to z = 10. Colour bar shows the probability of co-incidence across the group.

Overlap of territory	Onto territory	% overlap ($\pm$ st.err.)
LICA	RICA	3.9 $\pm$ 0.7
	BA	10.5 $\pm$ 2.7
	ACA	15.5 $\pm$ 3.7
RICA	LICA	5.7 $\pm$ 1.4
	BA	13.5 $\pm$ 2.6
	ACA	19.8 $\pm$ 4.3
BA	LICA	17.7 $\pm$ 6.6
	RICA	17.1 $\pm$ 6.4
	ACA	24.9 $\pm$ 7.1
ACA	LICA	16.0 $\pm$ 4.3
	RICA	12.7 $\pm$ 3.3
	BA	16.3 $\pm$ 4.1

Table 5.3: Overlap of each vascular territory onto the other vascular territories, shown as mean percentage ($\pm$ standard error) across the group.

5.3.2 Multi-phase ASL

Subtraction of label and control multi-phase data, and subsequent averaging across 40 dynamics gives perfusion weighted signal for the 7 phases (TIs) across each of the 6 slices, as shown in Figure 5.17 for the multi-phase ASL data acquired without vascular crushing, which is used for the calculation of CBVa and arterial transit time (Δ) maps.
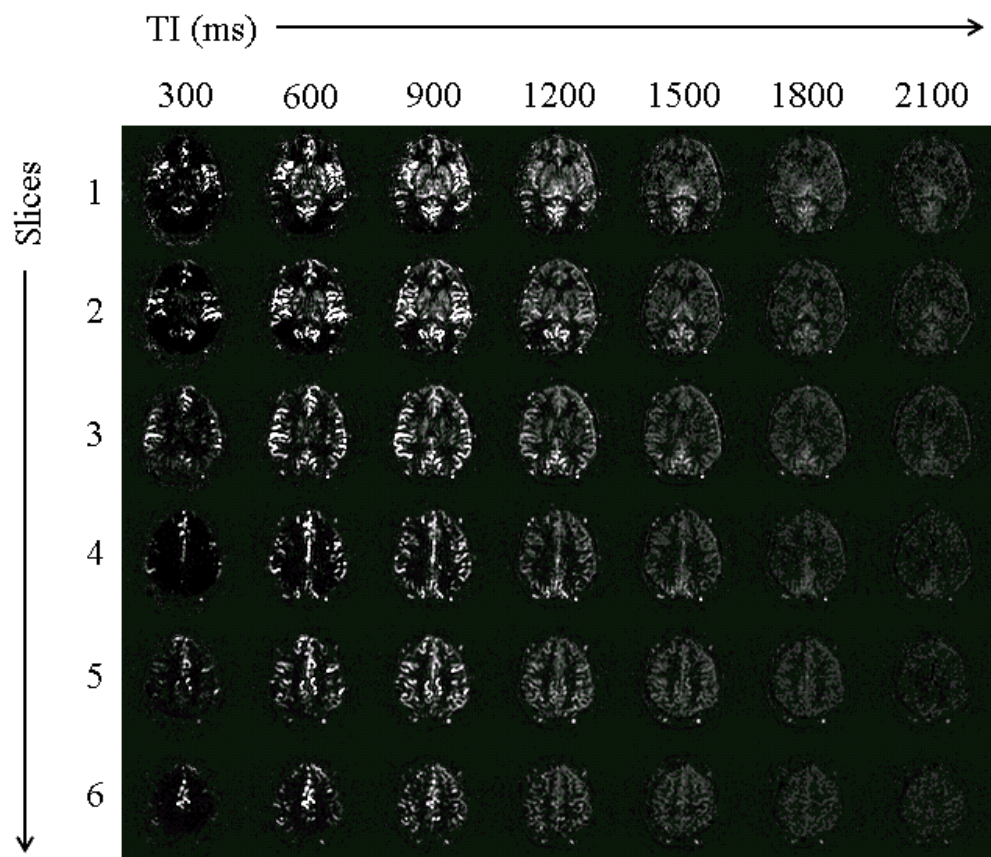
Figure 5.17: Multi-phase perfusion weighted acquired without vascular crushing for a representative subject, showing images at each inversion time (TI), averaged across 40 dynamics.

Figure 5.18 shows group maps of (A) mean arterial blood volume, CBVa, (B) arterial transit time, Δ, (D) estimated cerebral blood flow, CBF, and (E) mean capillary transit time, δ. Figure 5.18 (C) and (F) show thresholded transit time maps, at thresholds of $\Delta = 900$ ms and $\delta = 900$ ms respectively. Capillary transit time maps show a smaller spatial extent of lengthened transit times, improving delineation of the anterior, posterior and interior border zones in

comparison to the arterial transit maps. Thus the capillary transit time maps were used for definition of the watershed areas. This allowed for manual definition of the watershed regions by thresholding of the capillary transit time maps, as shown in Figure 5.19. The regions that were defined from these data correspond closely with the anatomical location of the watershed regions [23].
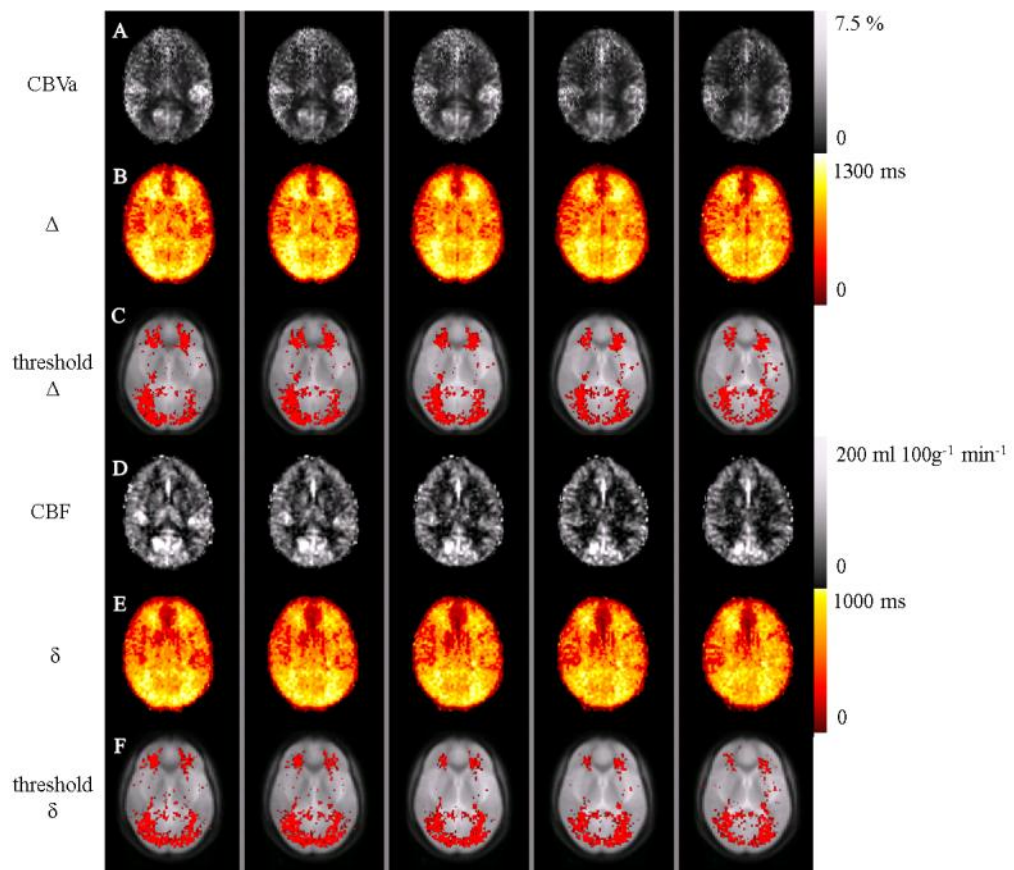
Figure 5.18: Group (n = 10) averaged maps of (A) arterial blood volume (CBVa), (B) arterial transit time (Δ), and (C) Δ threshold at 900 ms for the delineation of watershed regions. (D) Cerebral blood flow (CBF), (E) capillary transit time (δ), and (F) δ threshold at 900 ms for more precise delineation of watershed regions. Data shown are for five slices of MNI co-ordinates z = -6 to z = 2.
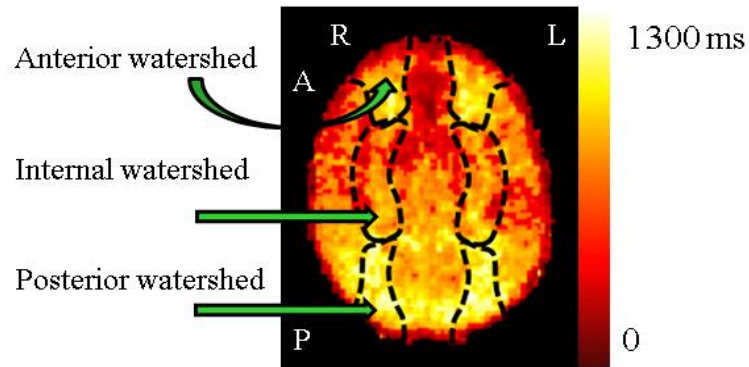
Figure 5.19: The locations of the three watershed regions (anterior, internal and posterior), as defined by inspection of capillary transit time maps.

5.3.3   Combined analysis of TASL and multi-phase ASL

Comparison of locations of territories and manually defined watershed regions can be seen in Table 5.4 demonstrated as a percentage of each arterial territory that overlaps onto each manually defined watershed region.

Watershed	Territory	% Overlap
Anterior	(L + R) ICA	20.4
Anterior	ACA	0.5
Interior	(L + R) ICA	65.9
Interior	ACA	0.3
Posterior	(L + R) ICA	19.8
Posterior	BA	1.2

Table 5.4: Percentage overlap of arterial territories onto each of the three manually drawn watershed regions.

Quantitative values for group haemodynamic parameters (mean ± standard error) calculated over territory regions and manually drawn watershed regions are shown in Figure 5.20 for arterial transit time (Δ), capillary transit time (δ) and perfusion (CBF). The posterior (BA) territory was found to have a significantly lengthened transit time compared to anterior / internal carotid artery territories (LICA / RICA and ACA), with the anterior cerebral artery exhibiting the shortest transit times.

175
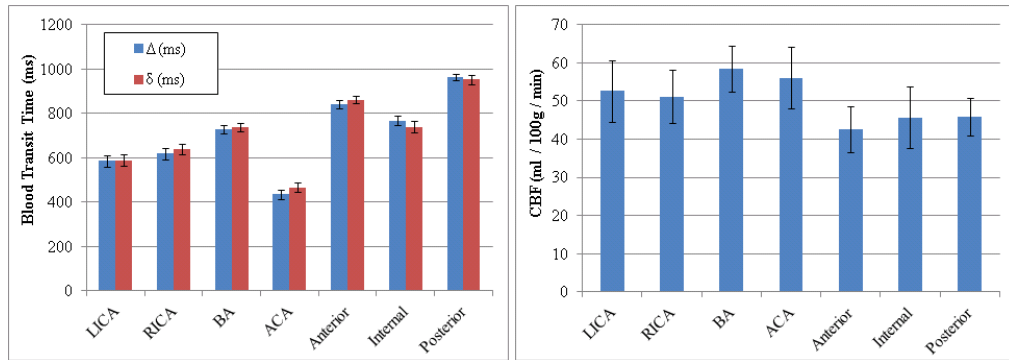
Figure 5.20: Mean (± standard error) values for the group; haemodynamic parameters of arterial transit time (Δ), capillary transit time (δ) and perfusion (CBF), measured in territories and watershed regions.

Perfusion rates in the watershed areas were reduced compared to mean values for the vascular territories, as would be expected for areas with decreased perfusion and delayed transit times [3].

The mask of grey matter watershed areas from the TASL scheme was used to interrogate blood transit time maps as a surrogate for objectively defined watershed regions. The mask of GM watershed regions formed by thresholding capillary transit time maps was also considered, as was the conjunction of these two masks. Figure 5.21 shows these three binary GM masks in a representative subject. In general across the subjects, the posterior watershed regions were better represented than the anterior or interior watershed regions using either method. The conjunction of the grey matter watershed masks derived from TASL and from thresholded multi-phase ASL maps of capillary transit time was calculated as a percentage overlap with each mask. The conjunction of the two GM masks overlaps the TASL derived GM watershed mask by an average (± standard error) of 19 ± 4 %, and the thresholded capillary transit time GM watershed mask by an average (± standard error) of 25 ± 6 %. Figure 5.22 shows the mean (± standard error) capillary transit times (δ) across each GM mask, averaged across the group of 10 subjects, and Figure 5.23 shows the corresponding mean (± standard error) CBF values within the three masks.
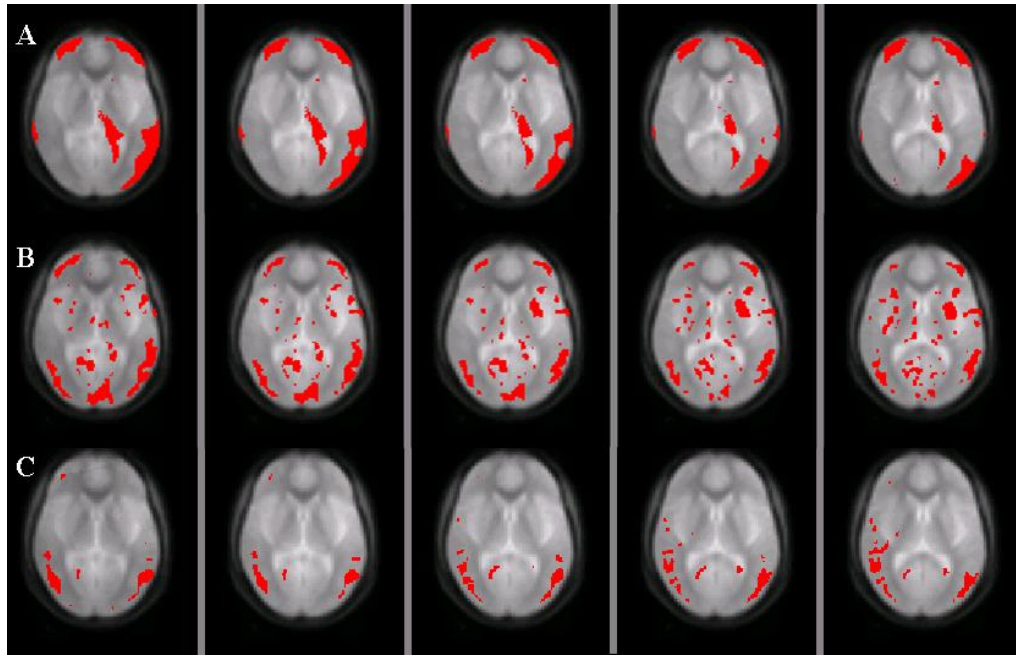
Figure 5.21: Binary grey matter masks estimating watershed regions from (A) voxels that do not appear in any vascular territory (B) voxels with capillary transit time > 900 ms and (C) the conjunction of (A) and (B) in a single representative subject. Masks shown for MNI co-ordinates z = -6 to z = 2.
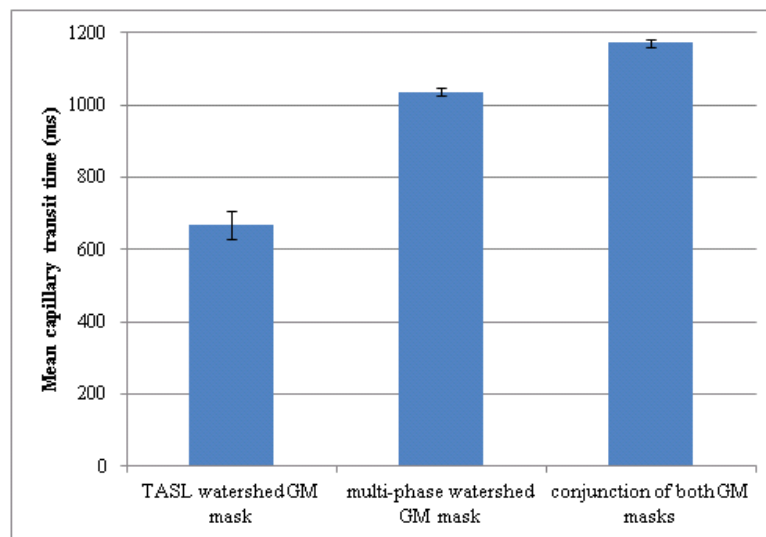
Figure 5.22: Mean capillary transit time (δ) within GM watershed masks derived from TASL, multi-phase ASL and the conjunction of both masks. Group (n = 10) values of mean ± standard error are shown.
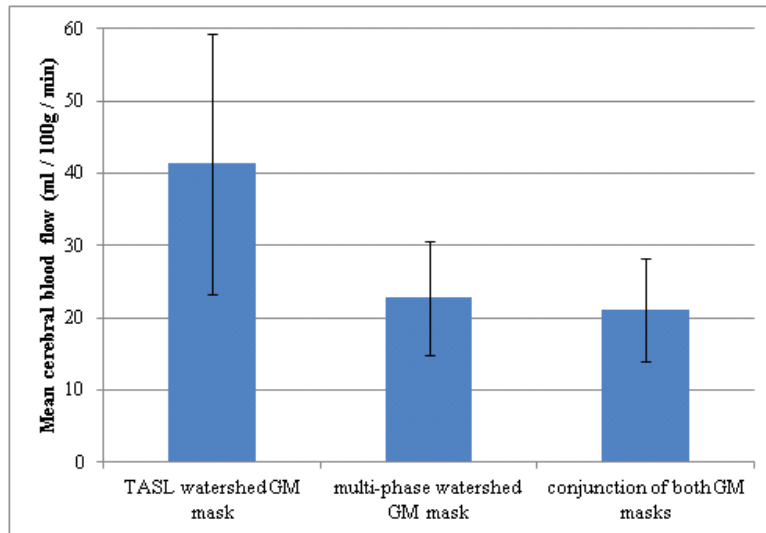
Figure 5.23: Mean cerebral blood flow (CBF) within GM watershed masks derived from TASL, multi-phase ASL and the conjunction of both masks. Group (n = 10) values of mean ± standard error are shown.

Cerebral blood flow and transit times were assessed for specified anatomical regions, namely the caudate, putamen, thalamus, primary motor and somatosensory cortices, insula, cingulate, inferior occipital cortex and primary visual cortex / occipital pole. The caudate and putamen we found to have the shortest transit time, with the occipital lobe showing the longest. CBF and transit time values for these regions are shown in Figure 5.24 and Figure 5.25.
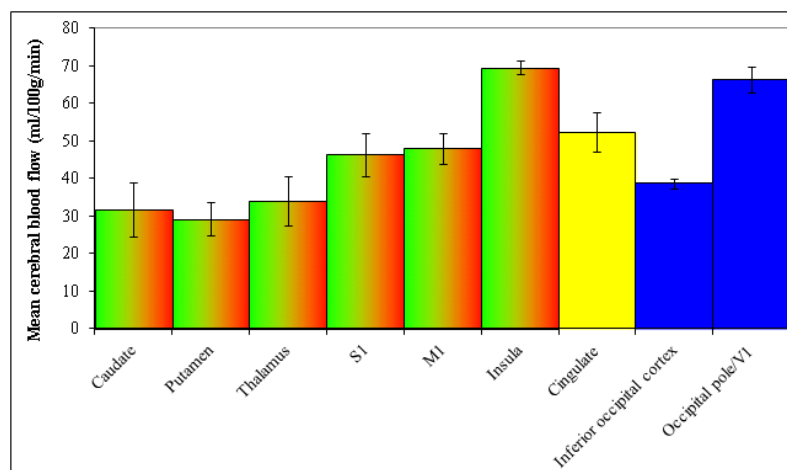
Figure 5.24: Mean cerebral blood flow values for selected anatomical brain areas; colour of bar indicates the corresponding territory in which the region falls.
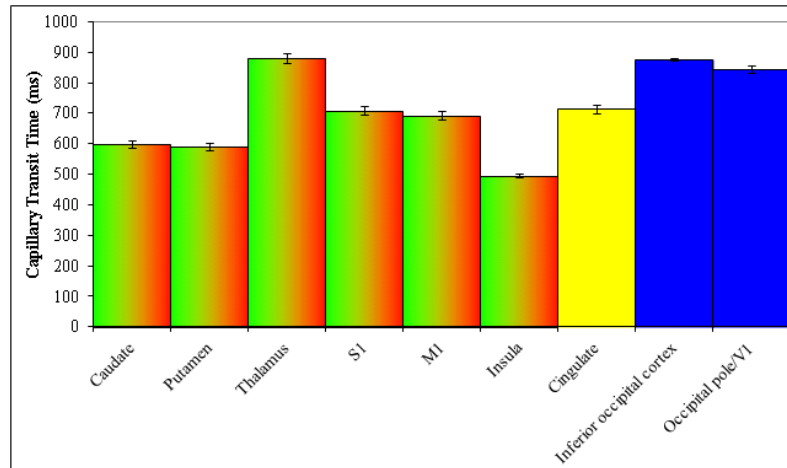
Figure 5.25: Mean capillary transit time (δ) values for selected anatomical brain regions; colour of bar indicates the corresponding vascular territory.

5.4 Discussion

5.4.1 Summary of findings

A scanner protocol has been developed that provides combined territorial ASL and quantitative multi-phase ASL in a 40 minute scan session to determine the cerebral vascular territories and haemodynamic parameters of cerebral blood volume (CBVa), cerebral blood flow (CBF) and arterial and capillary transit times (Δ and δ respectively). Using these methods, the location of the cerebral watershed regions in a cohort of healthy volunteers was investigated. Three different methods were used to define the location and size of watershed regions:

(i)   Forming a grey matter mask for each subject of voxels that do not appear in any TASL vascular territory map;

(ii)   Manually drawing around regions of lengthened blood transit time using group maps of capillary transit time (δ);

(iii)   Thresholding capillary transit time (δ) maps on individual subjects to a threshold of $\delta = 900$ ms and forming a grey matter (GM) mask.

(iv)   The common area between the masks formed by (i) and (iii) was assessed using the conjunction of the two masks.

Delineation of vascular territory maps showed agreement across the sample (n = 10). Masks of grey matter voxels that were not present in any vascular territory map provided a surrogate for an objectively defined watershed region. Watershed masks formed by finding voxels within a grey matter mask that were not present in any TASL map showed lengthened transit times and reduced CBF compared to other cortical regions. These masks showed that watershed regions corresponded highly with the distal branches of vascular territories.

From the multi-phase data, capillary transit time maps showed sharper definition of areas exhibiting lengthened transit times in comparison to arterial transit time maps. Watershed regions as defined using manually drawn regions of longer transit time corresponded to the distal branches of vascular territories. Masks of watershed regions were formed by thresholding capillary transit time maps to $\delta = 900$ ms. These watershed regions also corresponded to the distal branches of territories, and to watershed masks formed by subtracting vascular territory maps from a grey matter mask. The mask formed by the conjunction of the two objective methods for creating GM watershed masks showed further specific delineation of the watershed regions, exhibiting even longer mean transit times and lower mean CBF values, as shown in Figure 5.22 and Figure 5.23.

From inspection of anatomical ROI analysis on multi-phase data, mean values of capillary transit time (δ) were shown to be significantly lengthened in ROIs in the posterior of the brain, namely the inferior occipital cortex and the occipital pole / primary visual cortex (Figure 5.25).

5.4.2   Discussion of findings

The results presented in this chapter demonstrate the implementation of territorial ASL at 3 T and improvements made in the use of TASL in comparison to previous studies [24]. Territorial ASL has the potential for being a useful tool for clinical applications, as it provides a means of determining the route by which blood reaches certain areas of the brain.

However, the efficiency of this technique is highly user dependent as its success is reliant selective labelling of inflowing vessels. Scanner operators were practiced in using the technique prior to the start of the study, as shown in the pilot group of 11 subjects scanned (Table 5.1). However, in a group of 10 healthy human subjects studied here, only 5 were shown to exhibit highly successful labelling of the three core vascular territories; posterior (BA) and left and right anterior (LICA / RICA), as shown in Table 5.2. In the remaining 5 subjects, definition of one or more territories was not highly successful due to insufficient labelling of the inflowing vessel or due to extraneous labelling of additional vessels. In these cases, failure was attributed to difficulty in selectively labelling tortuous or closely adjacent vessels or due to subject motion following the planning angiography scans, resulting in the vessel leaving the labelling slab.

Combining the techniques of multi-phase and territorial ASL provides the ability to construct informative individual vascular and haemodynamic parameter maps that can in turn be combined to build a reference atlas of region-specific perfusion levels. From capillary transit time maps, the position and functional properties of watershed areas can easily be determined, either by manual definition of areas exhibiting lengthened transit time, or by the objective thresholding of capillary transit time maps. Combining TASL with the technique of multi-phase ASL adds extra information to the technique for assessing the location of watershed regions, providing a means by which to verify TASL data, as shown by the mask formed by the subtraction of vascular territory GM masks from a whole brain GM mask, and further by the conjunction of the two masks formed by these two objective assessments of watershed regions. Regions in this conjunction mask exhibited lengthened transit times and decreased perfusion as would be expected in watershed regions. Further, perfusion values were lower and transit times lengthened in comparison to the GM mask formed by the use of either method in isolation (Figure 5.22 and Figure 5.23). The methods outlined in this chapter provide a useful basis from which to study the haemodynamic effects of cerebrovascular disease, the physiological effects of healthy aging, blood pressure changes or

drugs that affect cerebrovascular dynamics through mechanisms such as autoregulation.

A post-label delay (TI) of 1200 ms was used, as in prior studies, to minimise arterial contribution to the signal, as demonstrated in previous studies [2, 17]. In patient groups and in older subjects, blood transit times are lengthened, suggesting the use of a longer TI for single-TI ASL. Alternatively, it would be useful to combine the territorial ASL technique with a multi-phase readout to form territorial maps of blood flow and transit time, thus allowing for the quantification of the component of perfusion from each of the supplying vessels to each of the territories. Then, in cases where vascular territories are seen to overlap, the quantified perfusion maps provided by the multi-phase readout could be compared with the "all" maps provided by standard ASL in order to determine the proportion of perfusion delivered by each of the feeding vessels.

5.4.3   Future work and clinical applications

This chapter has demonstrated that delineation of watershed areas can be assessed from the perimeter of vascular territories and from studying transit time maps for regions that display increased transit times. It may be interesting in future studies to further assess the length of vascular paths in combination with MR angiograms in order to draw a comparison between vessel length, vessel tortuosity and capillary transit time.

This healthy volunteer study has highlighted many of the positive elements to the use of ASL and uncovered potential clinical applications of the technique. However, ASL unfortunately has limitations that prevent it from being used in a widespread clinical setting. As ASL contrast is provided by a subtraction of the label image from the control image, it provides lower contrast to noise than other techniques, such as digital subtraction angiography (DSA) or dynamic contrast enhanced (DCE) perfusion. This is somewhat overcome by repeating a single ASL measurement many times and averaging across these dynamic scans. This can sometimes be very time consuming and introduce

prohibitively large motion artefacts. If motion correction is used either prior to or following subtraction of the label and control images, this may also introduce artefacts correlated to the motion of the subject. Motion is an even greater problem factor in patient groups than it is in healthy volunteer groups and so would need to be addressed before the technique can be used in clinical practice.

This chapter demonstrates the potential of the technique, but also highlights that the use of territorial ASL alone is not robust enough for clinical use. However, the use of territorial ASL in combination with multi-phase ASL provides some verification. Prior to clinical use, the technique of TASL would need to be demonstrated to have a significantly greater success rate, in line with techniques such as the gold standard, digital subtraction angiography (DSA), which boasts success rates as high as 98% [1].

This work could further be enhanced by acquiring comparable data using the above protocol an older healthy volunteer cohort, where transit times are expected to be lengthened and CBF to be reduced [28]. Other known factors affecting transit time include gender [29]. It would be very plausible to study the effect age or gender on blood transit times and perfusion rates using the methods described above; however this would require a larger cohort of subjects than has been studied here. These comparisons would provide information about changes in perfusion during the process of healthy aging with a view to identifying differences in the haemodynamic properties of brain tissue that are displayed in patients from clinical groups, such as working age dementia.

In some cases the blood arrival time can be delayed so significantly that the inversion applied to label the blood can have completely relaxed back by the time the blood has entered the imaging slab (i.e. if arterial transit time $> T_1$ of blood). This problem is exasperated when using techniques with multiple acquisitions per inversion, as the later acquisitions will not detect any labelled blood [30]. This would impact on the efficiency of the technique in the diagnosis and observation of conditions such as occlusive carotid artery

disease. One solution to this would be to use the technique at higher magnetic field strength, where T_1 times are longer [31], as discussed in Chapter 6 of this thesis.

There are asymptomatic variations in the physiological manifestation of the cerebral blood supply, for example, variations in the architecture of the Circle of Willis [25, 26] and harmless abnormalities in the arrangement of feeding arteries [23]. These may account for some of the cases in which territories are seen to overlap in healthy subjects, and it would be of interest in future studies to additionally interrogate the TOF data to assess for altered vasculature in the healthy subjects scanned here. An interesting enhancement to this study could be to examine the completeness of the Circle of Willis based on Time of Flight (TOF) data, to determine whether there is a haemodynamic consequence of this as measured using territorial ASL or multi-phase ASL. If these variations in the cerebral vasculature can be identified in asymptomatic subjects, then the information can be used to help the clinician make a better informed decision regarding treatment in the case that such a subject was to suffer a vascular event. In a clinical setting, it may be possible to use this information to assess the consequences of interventional surgery as a risk-free alternative to the angiographic balloon test occlusion assessment [27].

In patients with carotid artery stenosis and occlusion, Territorial ASL can be used to assess the vascular territories before and after medical or surgical intervention or other treatment of arterial stenosis or occlusion. In addition, multi-phase ASL can be used to measure quantitative perfusion before and after intervention. These techniques in combination would determine the success level of the surgery by ascertaining which areas of the brain, if any, were now receiving an increased blood supply, by which route that blood is being supplied, and whether the blood supply has been elevated / returned to an acceptable or normal level. Territorial ASL could also be used to assess collateral blood supply in such subjects as often the cerebral vascular supply system will respond to a trauma or an occlusion, maintaining blood supply to a poorly perfused brain region by increasing the blood flow through alternative routes. Territorial ASL therefore provides unique information that is not

deliverable using contrast enhanced perfusion methods as there is no capacity to be selective to only labelling one feeding artery at a time.

Since the research presented in this chapter was carried out, super-selective TASL has been developed [32], and further, super-selective territorial angiography [33]. These build upon the methods described in this chapter, with the augmentation of further gradients applied perpendicular to either the artery, or to the labelling plane following the application of each label. These gradients introduce a phase shift into the labelled blood, providing spatial information in the label. The level of selectivity is manipulated by changing the strength of the gradient. These methods allow territorial ASL with less dependence on the ability to plan the locations of the selective labelling slabs. Alternatively, velocity selective techniques [34] can be explored. In velocity-selective ASL, blood flowing below a specified velocity is labelled and thus slow and collateral CBF can be quantitatively measured. As the label used is velocity selective, rather than spatially selective, these techniques completely remove the reliance on planning of scans.

References

1. Chng SM, Petersen ET, Zimine I, Sitoh YY, Lim CC, Golay X. Territorial arterial spin labeling in the assessment of collateral circulation: comparison with digital subtraction angiography. Stroke. 39(12):3248-54 (2008).

2. Hendrikse, J, van der Grond, J, Lu, H, van Zijl, PCM, Golay, X. Flow Territory Mapping of the Cerebral Arteries With Regional Perfusion MRI. Stroke 35:882-887 (2004).

3. Hendrikse J, Petersen ET, van Laar PJ, Golay X. Cerebral border zones between distal end branches of intracranial arteries: MR imaging. Radiology. 246(2):572-80 (2008).

4. Eastwood JD, Holder CA, Hudgins PA, Song AW. Magnetic resonance imaging with lateralized arterial spin labeling. Magn Reson Imaging. 20(8):583-6 (2002).

5. van Laar PJ, Hendrikse J, Golay X, Lu H, van Osch MJ, van der Grond J. In vivo flow territory mapping of major brain feeding arteries. Neuroimage. 29(1):136-44 (2006).

6. Kansagra AP, Wong EC. Quantitative assessment of mixed cerebral vascular territory supply with vessel encoded arterial spin labeling MRI. Stroke. 39(11):2980-5 (2008).

7. Günther M, Bock M, Schad LR. Arterial spin labeling in combination with a look-locker sampling strategy: inflow turbo-sampling EPI-FAIR (ITS-FAIR). Magn Reson Med. 46(5):974-84 (2001).

8. Brookes, MJ, Morris, PG, Gowland, PA, Francis, ST. Noninvasive Measurement of Arterial Cerebral Blood Volume Using Look-Locker EPI and Arterial Spin Labeling. Magnetic Resonance in Medicine 58:41–54 (2007).

9. Francis, ST, Bowtell, R, Gowland, PA. Modeling and Optimization of Look-Locker Spin Labeling for Measuring Perfusion and Transit Time Changes in Activation Studies Taking into Account Arterial Blood Volume. Magnetic Resonance in Medicine 59:316–325 (2008).

10. Petersen ET, Lim T, Golay X. Model-free arterial spin labeling quantification approach for perfusion MRI. Magn Reson Med. 55(2):219-32 (2006).

11. Ringelstein EB, Zeumer H, Angelou D. The pathogenesis of strokes from internal carotid artery occlusion. Diagnostic and therapeutical implications. Stroke. 14(6):867-75 (1983).

12. Goode, SD, Ojango, C, Auer, D. BOLD fMRI Response in the Motor Cortex Is Strongly Linked with CO_2 Reactivity in Patients with Carotid Artery Disease. Proc. Intl. Soc. Magn. Reson. Med (2007).

13. Goode, SD, Altaf, N, MacSweeney, S, Auer, D. Assessing CO_2 Reactivity in Patients with Carotid Artery Disease Using BOLD fMRI. Proc. Intl. Soc. Magn. Reson. Med, (2007).

14. Buxton RB, Frank LR, Wong EC, Siewert B, Warach S, Edelman RR. A general kinetic model for quantitative perfusion imaging with arterial spin labeling. Magn Reson Med. 40(3):383-96 (1998).

15. Hendrikse J, van Osch MJ, Rutgers DR, Bakker CJ, Kappelle LJ, Golay X, van der Grond J. Internal carotid artery occlusion assessed at pulsed arterial spin-labeling perfusion MR imaging at multiple delay times. Radiology. 233(3):899-904 (2004).

16. Mull M. [Hemodynamically induced cerebral infarcts. Clinical significance of infarct pattern and angiomorphology]. [Article in German]. Radiologe. 37(11):871-7 (1997).

17. Pruessmann KP, Golay X, Stuber M, Scheidegger MB, Boesiger P. RF pulse concatenation for spatially selective inversion. J Magn Reson. 146:58–65 (2000).

18. Schepers, J, van Osch, MJP, Nicolay, K. Effect of Vascular Crushing on FAIR Perfusion Kinetics, Using a BIR-4 Pulse in a Magnetization Prepared FLASH Sequence. Magnetic Resonance in Medicine 50:608–613 (2003).

19. Matlab version 2009b, The MathWorks Inc., Natick, MA.

20. Montreal Neurological Institute (MNI) Template. Montreal Neurological Institute, Montreal, Canada.

21. FMRIB Software Library (FSL), version 4.1.6, Oxford Centre for Functional MRI of the Brain, UK (2008).

22. Statistitcal Parametric Mapping, version 8 (SPM8), Wellcome Trust Centre for Neuroimaging, UCL, UK (2009).

23. Blumenfeld, H. Neuroanatomy through Clinical Cases, p. 379. Sinauer Associates Inc.,U.S. (2002).

24. Golay X, Petersen ET, Zimine I, Lim TC. Arterial Spin Labeling: a one-stop-shop for measurement of brain perfusion in the clinical settings. Conf Proc IEEE Eng Med Biol Soc. 4320-3 (2007).

25. Rothberg M, Mattey WE, Bastidas J. Anomalous internal carotid-posterior cerebral artery circulation: one form of congenital incomplete circle of Willis. AJR Am J Roentgenol. 128(1):153-5 (1977).

26. Kim GE, Cho YP, Lim SM. The anatomy of the circle of Willis as a predictive factor for intra-operative cerebral ischemia (shunt need) during carotid endarterectomy. Neurol Res. 24(3):237-40 (2002).

27. Gevers S, Heijtel D, Ferns SP, van Ooij P, van Rooij WJ, van Osch MJ, van den Berg R, Nederveen AJ, Majoie CB. Cerebral Perfusion Long Term after Therapeutic Occlusion of the Internal Carotid Artery in Patients Who Tolerated Angiographic Balloon Test Occlusion. AJNR Am J Neuroradiol. [Epub ahead of print] (2011).

28. Parkes LM, Rashid W, Chard DT, Tofts PS. Normal cerebral perfusion measurements using arterial spin labeling: reproducibility, stability, and age and gender effects. Magn Reson Med. 51(4):736-43 (2004).

29. Shin W, Horowitz S, Ragin A, Chen Y, Walker M, Carroll TJ. Quantitative cerebral perfusion using dynamic susceptibility contrast MRI: evaluation of reproducibility and age- and gender-dependence with fully automatic image postprocessing algorithm. Magn Reson Med. 58(6):1232-41 (2007).

30. Detre JA, Wang J. Technical aspects and utility of fMRI using BOLD and ASL. Clin Neurophysiol. 113(5):621-34 (2002).

31. Gardener AG, Gowland PA, Francis ST. Implementation of quantitative perfusion imaging using pulsed arterial spin labeling at ultra-high field. Magn Reson Med. 61(4):874-82 (2009).

32. Helle M, Norris DG, Rüfer S, Alfke K, Jansen O, van Osch MJ. Superselective pseudocontinuous arterial spin labeling. Magn Reson Med. 64(3):777-86 (2010).

33. Helle, M, Rüfer, S, Teeuwisse, W, Jansen, O, Norris, DG, van Osch, M. Superselective MR-angiography based on pseudo-continuous arterial spin labeling and first applications in AVM patients. Proc. Intl. Soc. Mag. Reson. Med. 19 (2011).

34. Wong EC, Cronin M, Wu WC, Inglis B, Frank LR, Liu TT. Velocity-selective arterial spin labeling. Magn Reson Med. 55(6):1334-41 (2006).

6   Territorial ASL at 7 T in healthy volunteers

6.1   Background

Territorial Arterial Spin Labelling (TASL) has been developed and implemented at field strengths of 1.5 T and 3 T and shown to have the potential to non-invasively provide unique information on the cerebral vascular territories using selective labelling of inflowing blood vessels [1, 2], as outlined and demonstrated in Chapter 5 of this thesis. This could prove clinically useful; however, it is not yet used in the clinical setting. One reason for this is that ASL delivers a low contrast-to-noise ratio (CNR) and thus data is collected at reasonably poor spatial resolution and requires a number of averages, making the typical scan duration around 5 minutes. One major hindrance to the use of TASL, in addition to the CNR, is partial volume effects that limit the definition of, for example, the watershed areas. One way of reducing partial volume effects is to increase the spatial resolution of the images acquired. At 3 T, this would result in a significant reduction in the SNR of the image, requiring a significant increase in the length of the scan to collect a greater number of dynamics to match the SNR to that available at coarser resolution. Increasing the scan duration can be potentially problematic as this can lead to excessive motion, especially in patient groups. A potential solution may be found by collecting Territorial ASL at ultra-high field strength (7 T).

In recent years, many MR manufacturers have introduced ultra-high field (7 T) MR systems into their portfolio. The potential benefits of higher field strength to ASL are at least threefold:

(i)   There is an inherent increase in image signal-to-noise ratio (SNR) at higher field strength;

(ii)   Ultra-high field provides an increase in the longitudinal relaxation time (T_1) of both blood and tissue (the T_1 of blood is around 2 s at 7 T [4] compared to 1.5 s at 3 T [5], whilst grey matter T_1 increases from 1.3 s [6] to 1.85 s [7]). This results in a theoretical increase in the perfusion weighted signal change and perfusion contrast-to-noise ratio [8] and

allows for longer post-label delay times. This enables sensitivity to tissue that exhibits longer transit times, potentially advantageous for clinical patients where transit time are likely to be lengthened, which can lead to reduction of label detection at lower field strengths. Figure 6.1 shows an idealised model of the percentage perfusion weighted signal at 3 T compared to 7 T, using the parameters modelled in [8]. The continuous line shows this for the arrival of a theoretically continuous bolus (duration > 2200 ms) of labelled blood, whereas the dashed line represents the decrease in perfusion weighted signal after the arrival of a finite bolus of duration 1400 ms;
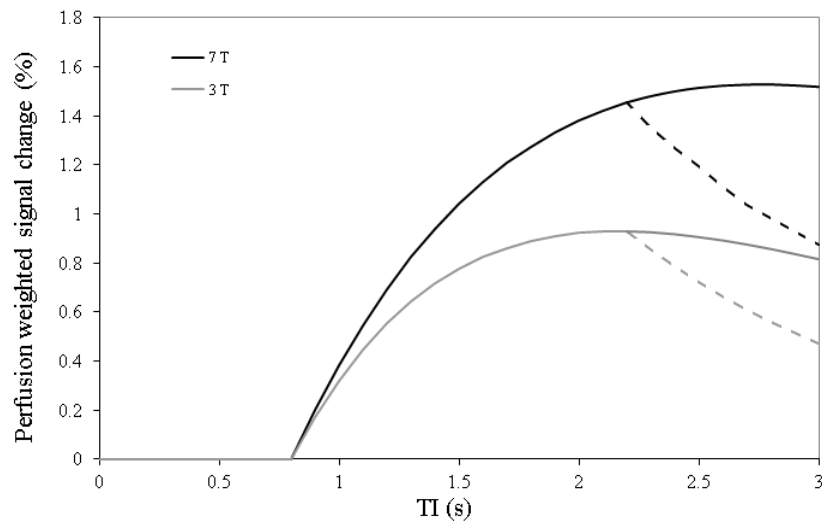
Figure 6.1: Idealised perfusion weighted signal, dependent on post-label delay (TI) at 3 T and 7 T. Modelled for CBF = 90 ml 100g^{-1}min^{-1}, capillary transit time = 800 ms, T$_1$blood = 1300 ms at 3 T and 1850 ms at 7 T, T$_1$tissue = 1600 ms at 3 T, 2100 ms at 7 T [8].

(iii)   Higher-field MRI and parallel imaging work synergistically, creating possibilities for increasing robustness of high SENSE factors, enabling faster read-out strategies at higher spatial resolution [9].

However, ultra-high field strength introduces additional challenges for ASL, and initial experiments with ASL at ultra-high field show that the implementation of ASL to obtain the expected gains at 7 T is not trivial [10]. Firstly, there is a fivefold increase in the specific absorption rate (SAR) of a given sequence at 7 T compared to 3 T, which is an important challenge. This can potentially limit the label duration or increase the required repetition time

of SAR-intensive ASL-methods, which is particularly problematic for techniques such as CASL and PCASL, resulting in a lower SNR per unit time. Alternatively, the increased SAR of the labelling can reduce the slice coverage available. SAR can be a problem even for PASL methods at 7 T, particularly when using labelling with a combination of additional background suppression pulses, or in–plane presaturation schemes. Secondly, the increased B_0 magnetic field inhomogeneities at ultra-high field pose problems for labelling, especially because these effects are most pronounced lower in the brain, in the region where labelling takes place. A third challenge is the B_1 inhomogeneity at 7 T due to the decreased electromagnetic wavelength in tissue, making the design and use of a body coil challenging at 7 T. Thus the common setup for 7 T MRI scanners is to use a head RF coil for transmission, further limiting the potential of providing a good labelling slab in the neck region. Together this results in limited B_1 efficiency at the level of the brain-feeding arteries causing inefficiencies in the application of the selective inversion pulse, limiting the width, sharpness of profile and position of the labelling region, all effecting the labelling efficiency which can result in an underestimation of perfusion signal [11]. Additionally, due to the potentially poor label profile, the applied inversion label can be observed to "bleed" into the imaging region, causing partial inversion of static tissue, evident as an artefact on the image. This can often be at least partially overcome with the use of in-plane saturation techniques, as explained later in this chapter [11]. One possible solution is to label higher in the brain, but this will immediately lead to a sacrifice of whole brain coverage, a significant disadvantage compared to current practice at 3 T, and also a limit of the application of TASL.

Pulsed ASL schemes typically used for TASL at lower field strength include TILT (transfer insensitive labelling technique) and STAR (Spin Targeting with Alternating Radiofrequencies) schemes (see Section 3.5.4). Both these schemes employ concatenated RF pulses, to eliminate magnetization transfer (MT) effects from the ASL signal. The inversion in TILT is achieved using two concatenated slice-selective 90° RF pulses with the second 90° RF pulse inverted in time and the second slice-selective gradient having opposite sign compared to the first. For the control, the second RF pulse has a 180° phase

shift. With this RF concatenation scheme, the magnetisation transfer (MT) signals from the static tissue in imaging slices are cancelled out between control and label sessions. However, even at low field TILT can suffer from potentially large slice profile artifacts and poor efficiency due to using 90° pulses which are non-adiabatic, efficiency is made worse at ultra-high field where the B_1 will vary across the labelling region, making this scheme unsuitable for ultra-high field. The STAR sequence for multi-slice acquisition uses a single 180° adiabatic pulse for the label experiment and two 180° + 180° pulses of half the power for the control experiment at the same proximal location. The use of adiabatic radiofrequency pulses for labelling at 7 T has the advantage of reducing the sensitivity to B_1 inhomogeneity. This scheme relies on the two 180° pulses to achieve a control condition; this can be limited at 7 T due to the effects of T_2 relaxation between the consecutive pulses. Further, SAR is increased due to the need for a nominal 360° pulse for the label and two 180° pulses for the control.

Other limiting factors of ultra-high field are the increased sensitivity to physiological noise at 7 T [12]. To overcome these effects, at 7 T, ASL data is collected with background suppression to minimise physiological noise contributions by nulling the static signal in ASL images at the post-label delay time [19], reducing physiological noise, as well as variance introduced by effects such as head motion and system instabilities. Finally, increased field strength leads to a reduction in the transverse relaxation time (T_2 and T_2^*), which in turn can lead to signal dropout in the ASL images, and can also effect the quantification of perfusion [13].

To date, TASL has not yet been performed at 7 T, likely due to the challenges described above in its implementation. The aim of this chapter is to develop a technique to implement Territorial ASL at ultra-high field strength (7 T) for the assessment of vascular territories in healthy adults.

6.2 Optimisation of TASL

6.2.1 Optimisation of the Selective Labelling Scheme for use at 7 T

6.2.1.1 Initial subject studies

Prior to this study, the ASL scheme that had been implemented and routinely used on the 7 T system was that of FAIR (Flow Alternating Inversion Recovery), in which all blood flowing in to the slice is labelled. This scheme had been shown to be more efficient for standard ASL than STAR [8], which uses an alternating label and control proximal and distal to the image slice. However, a selective label is required for TASL, making FAIR unsuitable for this purpose. Therefore the optimal labelling scheme for selective labelling required investigation. Further the efficiency of placing labelling slabs at oblique angles to the imaging plane needed to be assessed. Initially, the multi-slice STAR (Signal Targeting with Alternating Radiofrequency) scheme, which was implemented in Chapter 5 for Territorial ASL at 3 T, was assessed at 7 T. This uses a 180° inversion pulse to form a label (adiabatic 180° pulse with nominal 360° power to control for magnetisation transfer effects) and two consecutive inversion pulses for the control (180° + 180° = 360°), as shown in Figure 6.2.
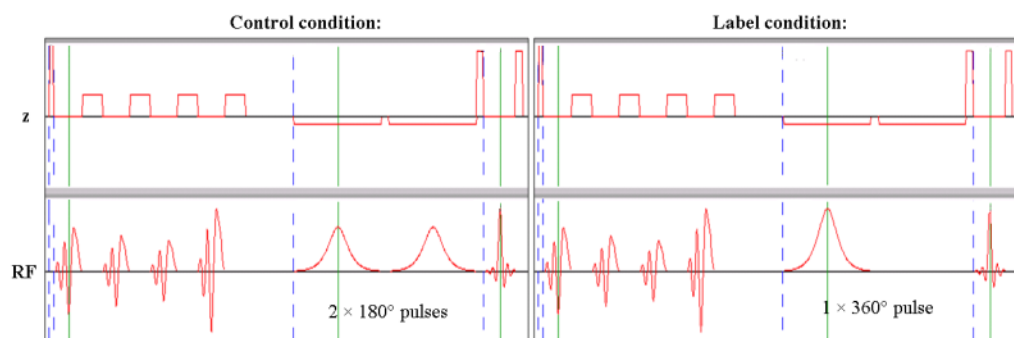
Figure 6.2: STAR pulse sequence showing slice select gradients in the z axis and RF pulses for label and control conditions, as a screen capture from Philips Graphical Viewer [14].

Pilot data was collected using STAR in a similar manner to that described in Chapter 5 for 3 T, with the addition of background suppression pulses at 7 T

(see Method for further details). STAR was initially assessed in 3 subjects to label all the inflowing blood in comparison to the standard FAIR acquisition routinely used at 7 T. However, STAR resulted in poor perfusion weighted images in all 3 subjects when compared to the standard FAIR scheme, as illustrated in Figure 6.3.
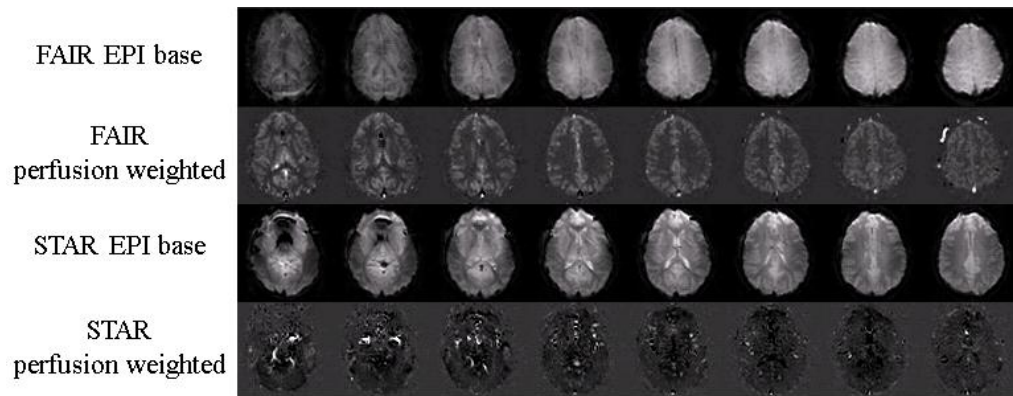
Figure 6.3: Use of the STAR labelling scheme results in poor perfusion weighted signal at 7 T in comparison to the standard FAIR scheme. Perfusion weighted images shown with EPI base.

6.2.1.2   Phantom studies

To understand the limitations of the STAR scheme, the efficiency of the label and control were assessed on an oblate ellipsoid agar gel gadolinium doped phantom of 20 cm diameter. The phantom comprised a saline solution containing 2 % wt / wt agar and 0.038 % v / v gadolinium (0.5 M Magnevist [15]) resulting in a longitudinal relaxation time, T_1, of approximately 1750 ms (with an inversion recovery curve null point of approximately 1200 ms) and T_2 of approximately 80 ms. It became apparent that the two consecutive 180° pulses in the STAR scheme resulted in a very poor control condition; however the single adiabatic pulse with nominal 360° flip angle led to an efficient label, as shown in Figure 6.4.

Label image: Control image:
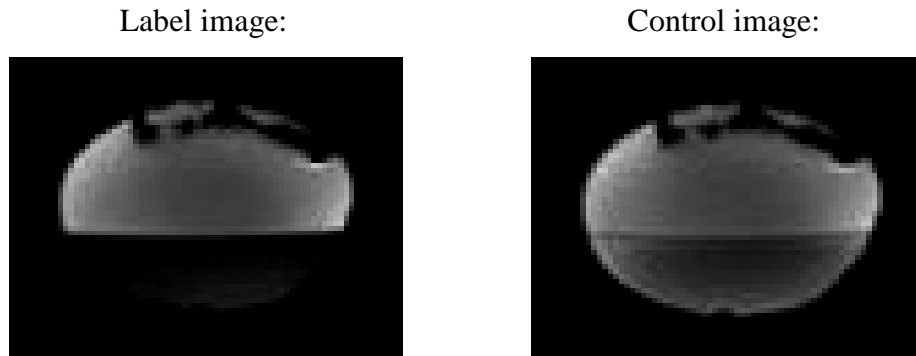
Figure 6.4: Coronal slice (level of cerebellum) through agar-doped phantom showing STAR label and control profiles. Images shown at phantom inversion recovery null point.

Therefore, alternative selective labelling schemes were considered, in particular, the PICORE (Proximal Inversion with a Control for Off-Resonance Effects – [16]) scheme. PICORE uses a single 180° adiabatic pulse for both label and control conditions, as shown in Figure 6.5. The label is applied using a selective inversion slab just below the imaging slice. In the control condition, an off-resonance inversion pulse without any slice-select gradient is utilized. This creates the same MT effect in the imaging slice for the control condition as for the label condition, as the frequency offset of the pulse used for each is matched. A further advantage of PICORE is that the labelling pulse can be applied at 180° power, thus producing much lower SAR compared to the STAR implementation. The PICORE scheme was therefore coded into the Philips 7 T pulse programming environment.
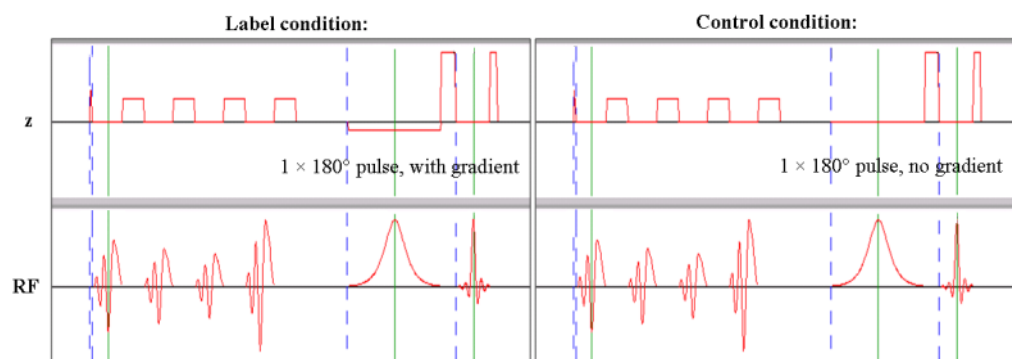
Figure 6.5: PICORE pulse sequence for label (left) and control (right) conditions, as a screen capture from Philips Graphical Viewer [14].

196

STAR and PICORE schemes were assessed on the agar phantom to compare the efficiency for three adiabatic pulse shapes, each of length 13 ms:

- A hyperbolic secant (HSC) pulse, the standard pulse used in the Philips software;

- C-shaped FOCI (Frequency Offset Corrected Inversion) pulses, with higher pulse frequency bandwidths, which have previously been found to give sharper profiles than a hyperbolic secant [17, 18]. These pulses can be described using the radiofrequency amplitude range, G_{min} to G_{max}, the pulse length parameter, β, and the side to width parameter, μ [19]. Two FOCI pulses were assessed:

    - FOCI1: using Philips default settings for (G_{min}, G_{max}, β and μ): (0, 1, 8, 9), BW 981 Hz;

    - FOCI2: optimised for the field strength of 7 T using values of (G_{min}, G_{max}, β and μ): (0, 4.42, 4.33, 7.75), BW 2870 Hz.

To assess the efficiency, images were collected at the null point of the inversion recovery curve (approximately 1200 ms for the agar phantom) to visualise the degree of inversion efficiency and the profile of the selective inversion slabs. The selective label was placed below the image slice to imitate the label used in standard ASL to label all inflowing blood.

Figure 6.6 shows example label and control profiles for STAR and PICORE labelling schemes, for each of the three inversion pulses, collected using sagittal profiles through the imaging volume. As shown above, it is clear the use of two consecutive 180° pulses for the STAR control does not provide a good control condition. In contrast, for this slab placement, PICORE provides a good control condition with fully recovered magnetisation. STAR had significantly (P < 0.001) reduced label efficiency (α) compared to PICORE (α ~94 % PICORE / α ~77 % STAR) from region of interest (ROI) analysis. In addition, STAR increased SAR, limiting the number of slices that could be acquired. Further, it was evident the FOCI2 inversion pulse provided an improved pulse profile over that of the HSC and FOCI1 pulses. A sharp profile is advantageous for territorial ASL to accurately label individual

feeding arteries and prevent labelling of multiple territories. The PICORE scheme with FOCI2 pulses was therefore the chosen scheme for TASL at 7 T.
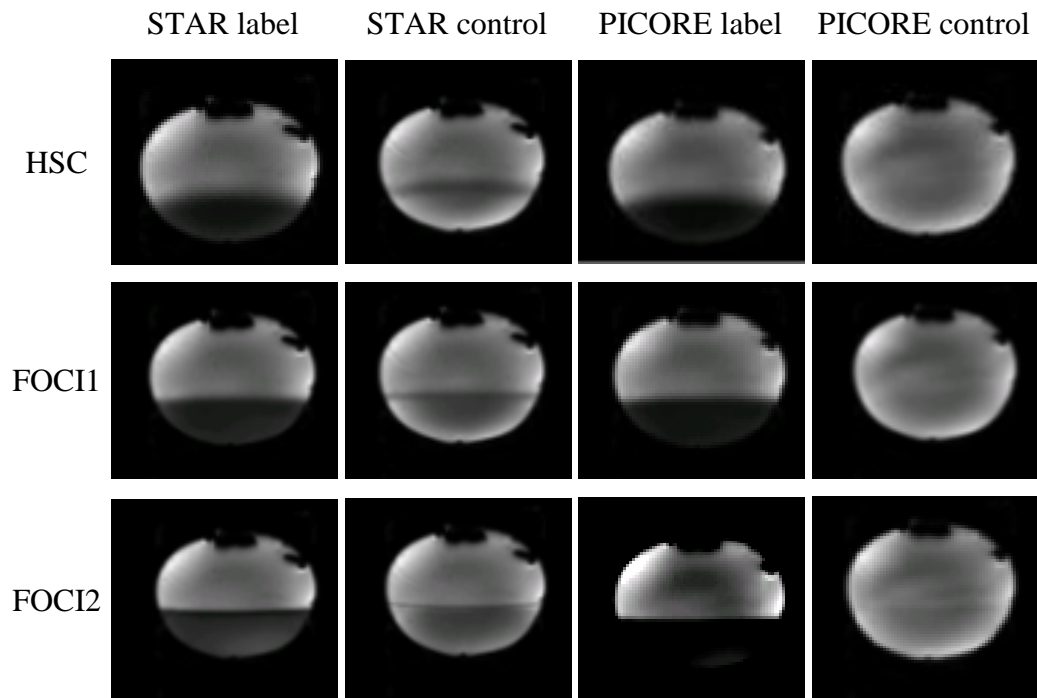
Figure 6.6: Coronal slice through phantom showing PICORE and STAR label and control profiles for three different pulses, acquired at inversion recovery null point.

6.2.1.3 Evaluating PICORE for standard ASL *in-vivo*

All *in vivo* imaging performed in this study was approved by the University of Nottingham Medical School Ethics Committee, and all subjects that participated in the investigation gave written, fully informed consent. Participants disclosed no past cerebrovascular medical history, and were considered healthy. All data are collected on the 7 T Philips Achieva system with a 32 channel SENSE receive coil, which was installed at Nottingham during the initial phase of this study. The 32 channel coil provided improved coil coverage in the neck region compared to the 16 channel coil.

The PICORE scheme was first evaluated for the condition of labelling all inflowing blood as performed in standard ASL. Single-TI STAR and PICORE data were first acquired with the label proximal to the imaging slice (thus labelling all inflowing blood) for each of the three adiabatic inversion pulses.

For each, a label thickness of 120 mm was used with a post-label delay (TI) of 1550 ms. ASL images were collected using a gradient echo (GE) EPI acquisition with a TE of 10 ms, and a spatial resolution of 3 mm in-plane and 5 mm slice thickness, with 10 slices being acquired with minimal spacing. The repetition time (TR) per ASL label / control was 3500 ms. In-plane saturation was applied to the image volume using the WET (Water suppression Enhanced through T_1 effects) scheme for presaturation (comprising four selective pulses of flip angles 106.8°, 86.8°, 76° and 153.6°) and a sinc pulse for post-saturation. In addition, all sequences performed at 7 T were implemented with background suppression. The background suppression scheme comprised two non-selective inversion pulses at inversion times TI_1 / TI_2 = 402 ms / 639 ms to suppress the static signal and reduce physiological noise and system variance. 50 dynamic ASL pairs were acquired labelling all arteries flowing into the head. Figure 6.7 and Figure 6.8 show the average subtraction perfusion weighted images for the STAR and PICORE schemes respectively for each of the adiabatic inversion pulses. Although absolute quantification is not performed, the signal intensities are proportional to perfusion and can be used for a qualitative assessment.
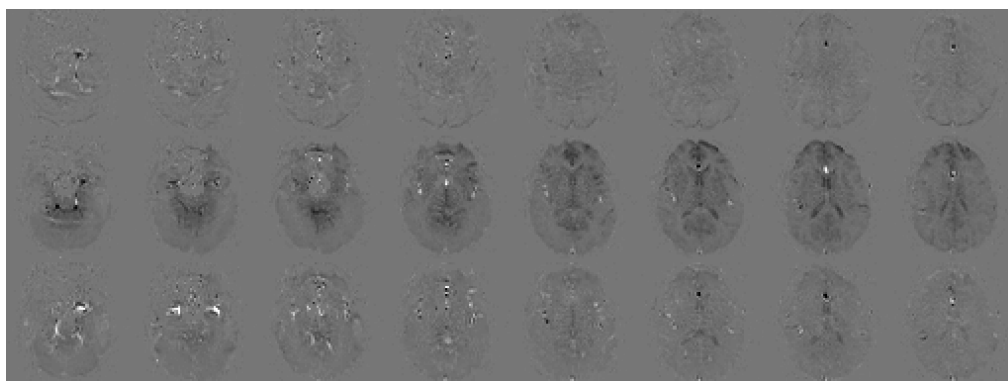
Figure 6.7: ASL perfusion weighted image using STAR for each pulse shape described above - row 1: HSC, row 2: FOCI1, row 3: FOCI2.
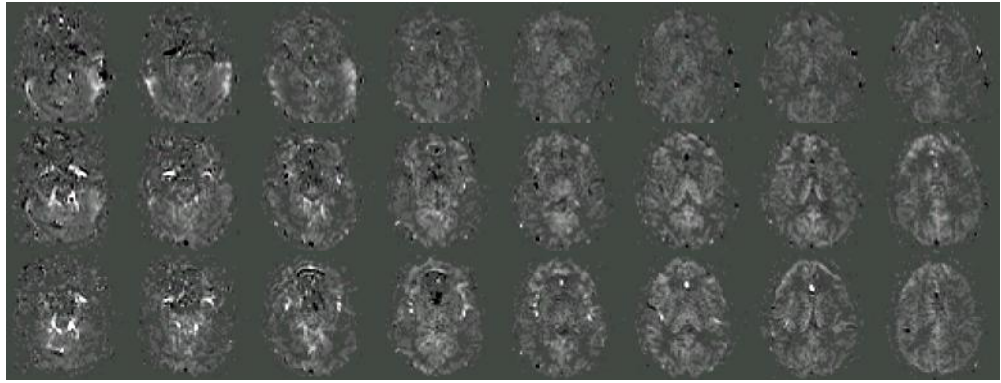
Figure 6.8: ASL perfusion weighted image using PICORE for each pulse shape described above – row 1: HSC, row 2: FOCI1, row 3: FOCI2.

Poor perfusion weighted images are seen for the STAR scheme due to the inefficiency of the control condition. The PICORE scheme can be seen to provide optimal labelling. These images were quantitatively assessed using region of interest (ROI) analysis for a 5 mm cube placed in the posterior grey matter. As shown in Figure 6.9, the PICORE scheme using FOCI2, gives marginally greater perfusion weighted signal than FOCI1, a substantial improvement on the hyperbolic secant pulse.
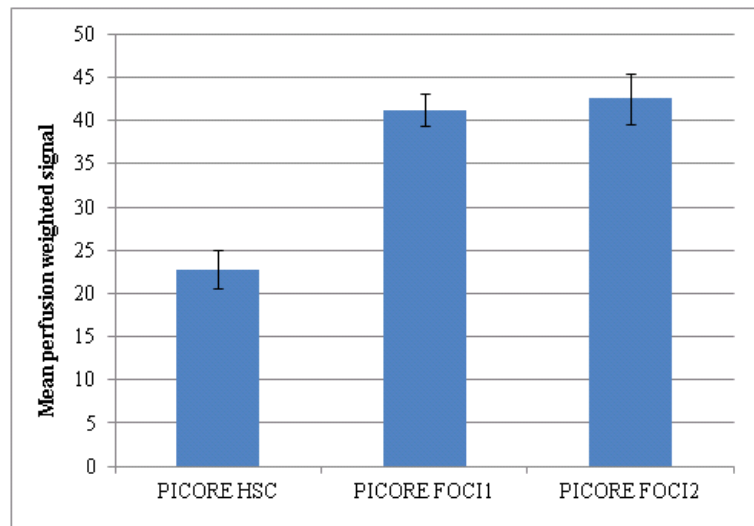
Figure 6.9: Mean (± standard error) perfusion weighted signal calculated in a grey matter region of interest for each pulse shape using the PICORE scheme given in Figure 6.8.

6.2.2 Using PICORE for TASL at 7 T

6.2.2.1 Theory

Having demonstrated the advantage of PICORE to label a slab proximal to the imaging plane, the next step was to evaluate the use of PICORE (with the FOCI2 pulse) as a 'free' selective label slab for territorial ASL, in which the slab can be placed at any geometry in order to label the blood flowing through a single artery *en route* to the brain. As described in Chapter 5, in TASL, inversion slabs are positioned to selectively label inflowing blood through the left and right ICA and BA [20], also shown in Figure 6.10.
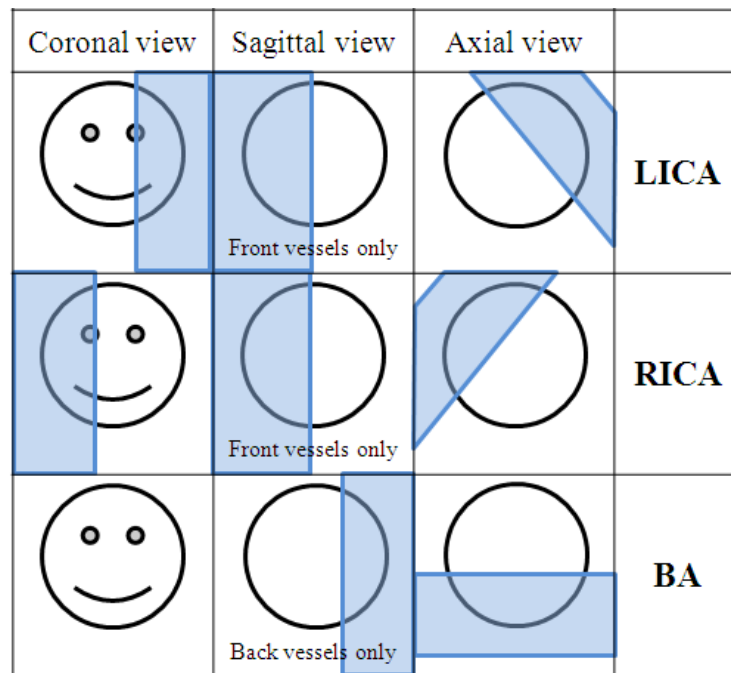
Figure 6.10: Schematic showing the posterior locations of labelling slabs used for territorial ASL.

The profile and efficiency of PICORE was assessed *in-vivo* for each position of the labelling slab. This was qualitatively performed by removing the in-plane saturation pulse from the ASL sequence, and acquiring data at the null point of the inversion recovery curve. However, on viewing the images, when the selective label was moved from its conventional position used for standard ASL (in the neck parallel to the imaging region to label all inflowing blood), a

dramatic loss of efficiency was observed in the control condition for certain orientations. This lack of efficiency in the control condition was observed more frequently for the hyperbolic secant pulse than for the higher bandwidth FOCI pulse.

To understand the origin of this effect, it is necessary to further consider how the PICORE scheme works, and the issues that arise at 7 T that can limit the efficiency of the scheme. As described above, PICORE uses a 180° adiabatic pulse for the label and control conditions. For the control condition, the same off-resonance inversion pulse is applied as for the label, but without any slice-select gradient, thus ensuring the same magnetisation transfer effect in the imaging slice but no inversion. However, this requires that the pulse is far enough off-resonance for this to be true. This may not be the case at ultra-high magnetic field strength.

The off-resonant frequency of the label pulse is determined by several factors; the geometric separation of the centre of the labelling slab from the imaging slab, herein known as the label offset distance (d), the thickness of the labelling slab (Δz), and the bandwidth of the radiofrequency pulse ($\Delta\omega$). As described in Chapter 2, the application of a gradient, G, at a position, r, modulates the Larmor frequency, ω, of the spins:

$$\omega_L = \gamma(B_0 + Gr)$$
Eqn. [6.1]

Thus, applying an inversion pulse containing a range of frequencies of bandwidth, $\Delta\omega$, centred at ω will invert a slab in the presence of a gradient. This range of frequencies corresponds to a label slab thickness (Δz) given by:

$$\Delta z = \frac{\Delta\omega}{\gamma G_z}$$
Eqn. [6.2]

If this is centred at a label offset distance d from the centre of the imaging plane, then d is given Eqn. [6.3].

$$d = \frac{(\omega - \omega_0)}{\gamma G_z} = \frac{\omega_{offset}}{\gamma G_z} \qquad \text{Eqn. [6.3]}$$

Combining these two expressions it can be seen that the frequency offset of the inversion pulse is given by:

$$\omega_{offset} = \frac{\Delta\omega \times d}{\Delta z} \qquad \text{Eqn. [6.4]}$$

For effective use of PICORE, the offset frequency must be large, such that the inversion pulse is off-resonance in the control condition. This is particularly an issue at 7 T, where there is a larger range of off-resonance frequencies, for example due to poor shimming. If this condition is not met, then the control condition will not be off-resonance and will effectively invert the spins. Eqn. [6.4] demonstrates that the off-resonance condition can be improved by (i) increasing the bandwidth of the pulse ($\Delta\omega$) (ii) maximising the label offset distance between the centre of the label and image slice (d), however this can limit the label efficiency, or (iii) reducing the slab thickness (Δz), but again this reduces the label duration and thus the perfusion weighted signal.

In general, FOCI pulses have a higher bandwidth than hyperbolic secant pulses (here, a bandwidth 981 Hz for the hyperbolic secant pulse compared to 2870 Hz for FOCI2), suggesting that the FOCI2 pulse will be more optimal for the implementation of TASL using PICORE.

For conventional ASL where the label is proximal and parallel to the image slice, and all inflowing arteries are being labelled, the arrangement is similar to that shown in Figure 6.11 (A), and the label offset distance, d, is large, resulting in a large ω_{offset}. However, TASL requires the labelling region to be applied oblique to the image plane, in order to selectively label individual inflowing arteries, as shown in Figure 6.11 (B). In this case, care must be taken to ensure that the label offset distance is maximised to result in the maximal frequency offset, ω_{offset}. As the distance between the label slab and the imaging slab is not constant (i.e. the imaging volume and label slabs are not parallel), it is also of importance over which axis the separation, d, is

measured, given by the orientation of the labelling slab as defined on the scanner. For example, if the label slab has transverse orientation, then the separation between the labelling and imaging slabs will be taken from the geometric offset in the foot-head direction. Whilst if the label slab is coronally oriented, then the anterior-posterior separation will be used, and if the label slab is sagittal, then the left-right offset distance will be of importance.

(A) Standard ASL   (B) Territorial ASL
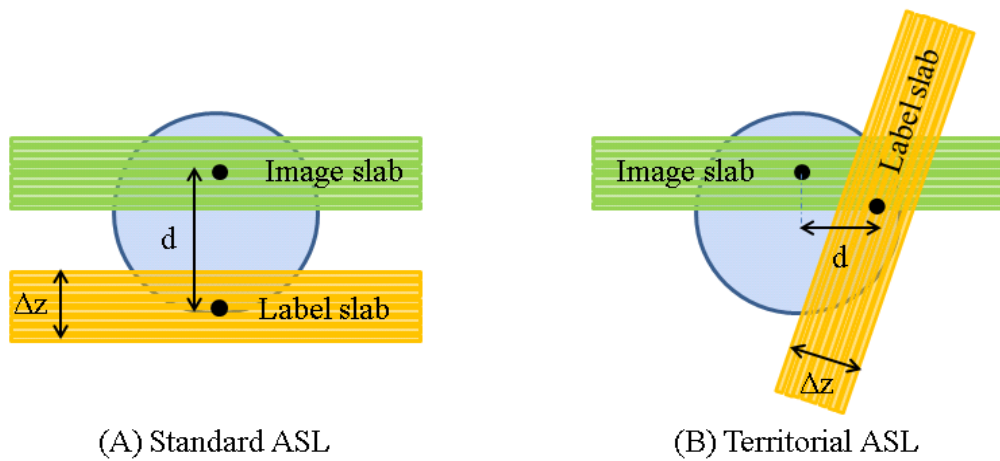
Figure 6.11: Label offset distance, *d*, between the image and label slabs on a spherical phantom. (A): Image and label slabs are oriented parallel and so the label offset distance (*d*) is the perpendicular separation. (B): Selective label applied oblique to the image slab and so the offset distance, *d*, is the separation along the axis corresponding to the orientation of the label slab (in this case sagittal, so *d* is in the left-right direction).

6.2.2.2   Phantom Verification

Having identified this geometric dependence for PICORE, this theory was then tested on the agar gel phantom by (i) changing the label offset distance (*d*) while keeping the slab thickness (Δz) and orientation constant, (ii) varying the label slab thickness (Δz) while keeping the label offset distance (*d*) and orientation of the labelling slab constant. By performing these experiments on the phantom, it was possible to confirm the theory of the correlation of control efficiency with the off-resonance frequency (ω_{offset}) of the inversion pulse.

For a sagittal label orientation with an axial orientation of the imaging slab, analogous to a LICA or RICA TASL scan, as shown in Figure 6.11 (B), and a

constant label thickness (Δz) of 20 mm, PICORE control condition efficiency was assessed for left-right label offset distances (d) ranging from 0 mm to 50 mm in 10 mm steps. For a sagittal label orientation at a fixed left-right label offset distance (d) of 10 mm, PICORE was assessed for label thicknesses (Δz) ranging from 20 mm to 100 mm in 20 mm steps. For each of the above geometries, the off-resonance frequency (ω_{offset}) of the FOCI2 pulse was calculated using Eqn. [6.4]. For a FOCI2 pulse with a bandwidth of 2870 Hz, these labelling geometries correspond to offset frequencies shown in Table 6.1. Inefficiency of control condition was often immediately apparent through visual inspection of data showing that there was still substantial inversion remaining in the control condition.

(i) Constant slab thickness Δz = 20 mm		(ii) Constant label offset distance d = 10 mm	
d (mm)	ω_{offset} (Hz)	Δz (mm)	ω_{offset} (Hz)
0	0	20	1435
10	1435	40	717.5
20	2870	60	478.3
30	4305	80	358.75
40	5740	100	287
50	7175		

Table 6.1: Off resonance frequencies of FOCI2 pulses calculated using Eqn. [6.4] for a variety of label offset distances (d) and label thicknesses (Δz).

Figure 6.12 shows an example case of when the left-right label offset distance of a sagittally placed label slab (d) is compared between 10 mm and 50 mm for a label thickness (Δz) of 20 mm. At a left-right label offset distance, d = 10 mm, corresponding to a ω_{offset} of 1.435 kHz, labelling is inefficient as significant inversion is exhibited in the control condition, whereas increasing the left-right offset distance to d = 50 mm, no inversion is present in the control condition, and thus optimal labelling is achieved.
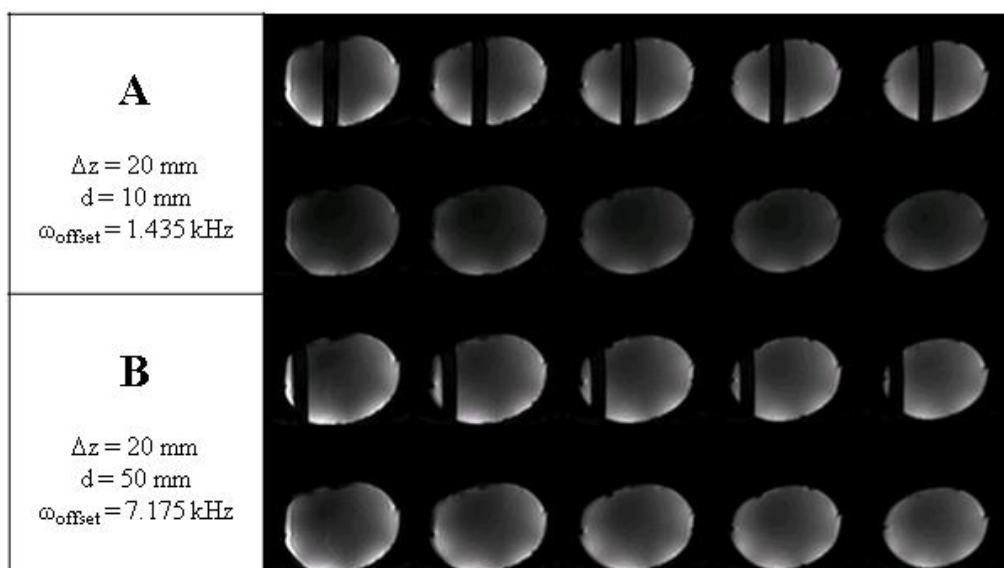
Figure 6.12: Effect of varying the left-right label offset distance (*d*) for constant thickness of the imaging slab (*Δz*). (A) Inefficient labelling and (B) improved, efficient labelling. This was demonstrated with a TI at the null point of the phantom (TI = 1200 ms).

A further example is shown in Figure 6.13, where here a constant left-right label offset distance (*d* = 10 mm) is used and the label thickness is compared between *Δz* = 50 mm and *Δz* = 10 mm, with the label placed in the sagittal orientation.
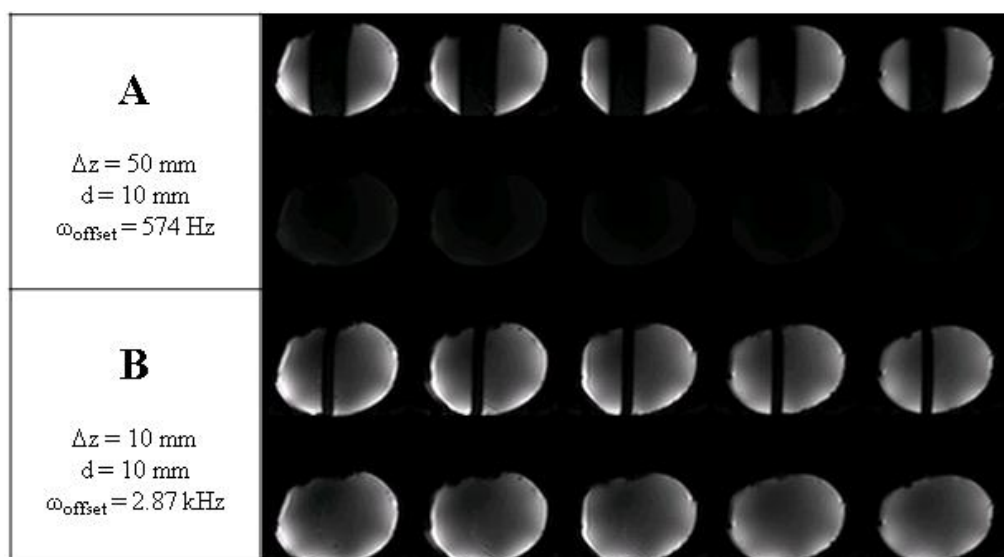
Figure 6.13: Comparison of different thicknesses of label slab (*Δz*) for a constant left-right distance between the label slab and the imaging slab (*d*), demonstrated using TI = 1200ms. (A) shows inefficient labelling due to inversion present in the control condition and (B) shows improved labelling efficiency.

It was found by visual inspection of data that geometries of label slabs using the FOCI2 pulse corresponding to an off-resonance frequency of below approximately 1.5 kHz resulted in poor control condition efficiency for PICORE, while geometries that provided off resonance frequencies of greater than 1.5 kHz were successful in providing a good control condition in the phantom. This was confirmed by quantitative interrogation of control images using a 50 mm cube region of interest in the phantom. Figure 6.14 shows measured mean signal intensities in the control condition as a function of label offset frequency, ω_{offset}. For low values of ω_{offset}, the signal intensity can be seen to improve up to a frequency offset of approximately 1.5 kHz, after which the control signal intensity does not improve further.
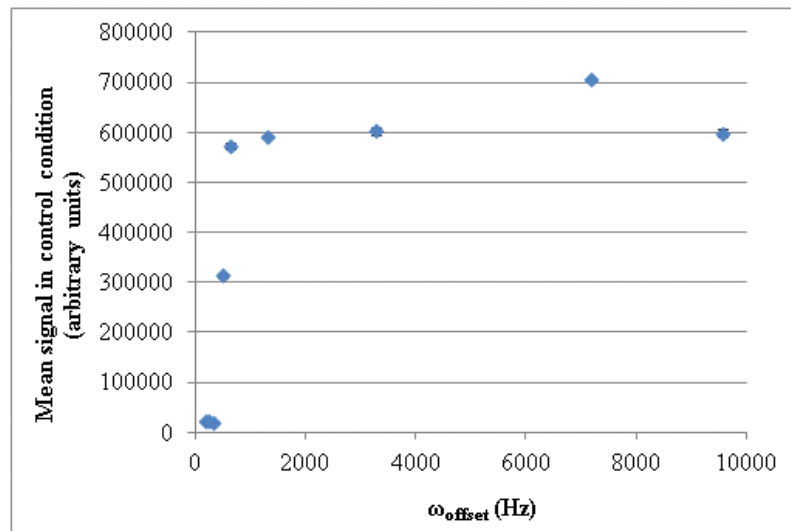
Figure 6.14: Measured mean signal intensity in the control condition as a function of the frequency offset of the pulse (ω_{offset}).

Effect of labelling slab orientation was also investigated by changing the orientation of the label slab, while keeping the imaging slab axially orientated for constant labelling slab thickness and label offset distance. Efficiency was found to be independent of label slab orientation (i.e. axial, coronal or sagittal), provided that the label offset distance along the corresponding axis was taken into account (as shown in Figure 6.11).

As further verification, the above procedure was also performed using PICORE with a hyperbolic secant pulse, which has a lower bandwidth. The

same principle was found to hold true, but the efficiency of the labelling broke down much more quickly (i.e. required greater label offset distances, d, and narrower slab thicknesses, Δz) than for the FOCI2 pulse due to the comparatively lower bandwidth of the hyperbolic secant pulse.

6.2.2.3 *In-vivo* verification

PICORE was then was then assessed on a healthy human subject using TASL. *In-vivo*, it must be considered there is a greater degree of inhomogeneity, and thus a greater range of offset frequencies due to magnetic susceptibility variations. It was therefore expected that in order to achieve efficiency of labelling, the threshold for off-resonance frequency would be higher *in vivo* than in the phantom. For TASL with oblique placement of label slabs, in-plane saturation pulses are applied before and after the inversion to cancel out the remaining static inversion signal in the tissue. However, in order to observe the location, profile and efficiency of the label slab on the brain, these pre- and post-saturation pulses were removed, and the brain imaged as normal, thus allowing inversion to be visible in the tissue. Figure 6.15 shows the label (lines 1, 3 and 5) and control (lines 2, 4 and 6) for PICORE when labelling inflowing blood in the basilar artery (BA), which provides the posterior blood supply to the brain and left / right internal carotid arteries (L / R ICA), provide the left and right sides respectively of the anterior blood supply. It is clear that PICORE is efficient at inverting the slab i.e. the labelling condition exhibits inversion and the edges of the slab are sharply defined. Also it is clear that there is no visible inversion in the control condition. Both of these factors demonstrate the adequate overall labelling efficiency provided by the PICORE sequence.
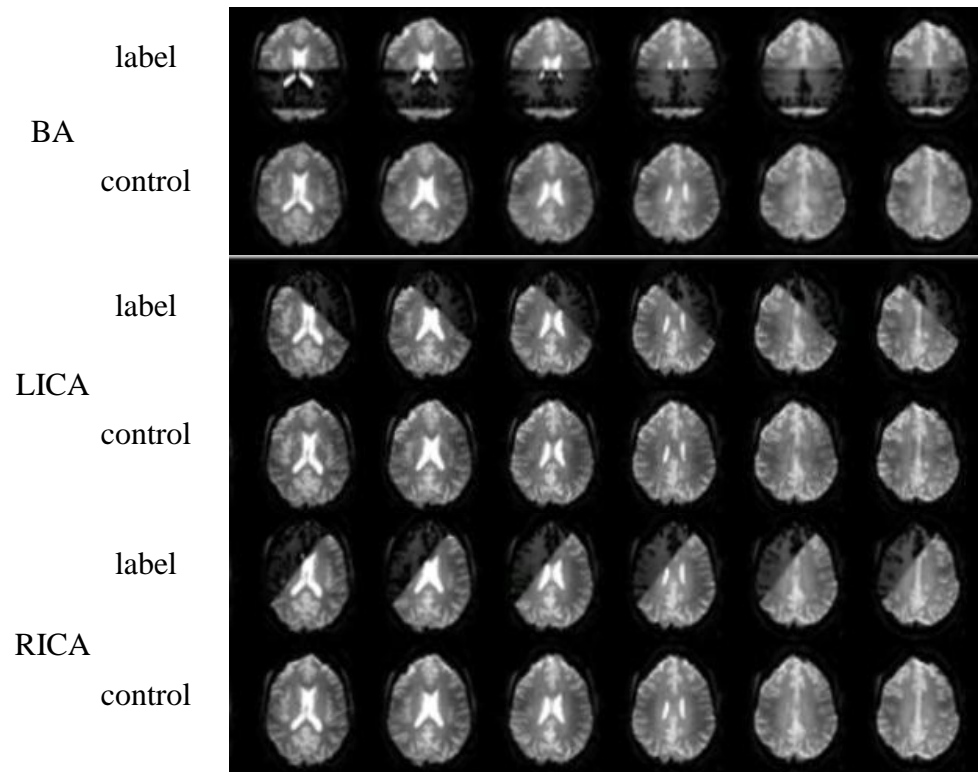
Figure 6.15: Label / control profiles for PICORE for the BA, RICA and LICA achieved by imaging without the application of in-plane saturation.

6.3 Optimised TASL in healthy volunteers

6.3.1 Participants

This study was approved by the University of Nottingham Medical School Ethics Committee, and all subjects that participated in the investigation gave written, fully informed consent. Participants disclosed no past cerebrovascular medical history, and considered themselves to be healthy.

6.3.2 TASL assessment

The complete series of TASL acquisitions was performed on 3 healthy human subjects using the PICORE ASL scheme with the FOCI2 pulse, as described in Section 6.2.2. Subjects were scanned on a Philips Achieva 7.0 T MRI scanner with a 32 element SENSE head coil for a single session lasting approximately 30 minutes. The complete protocol is outlined in Figure 6.16.
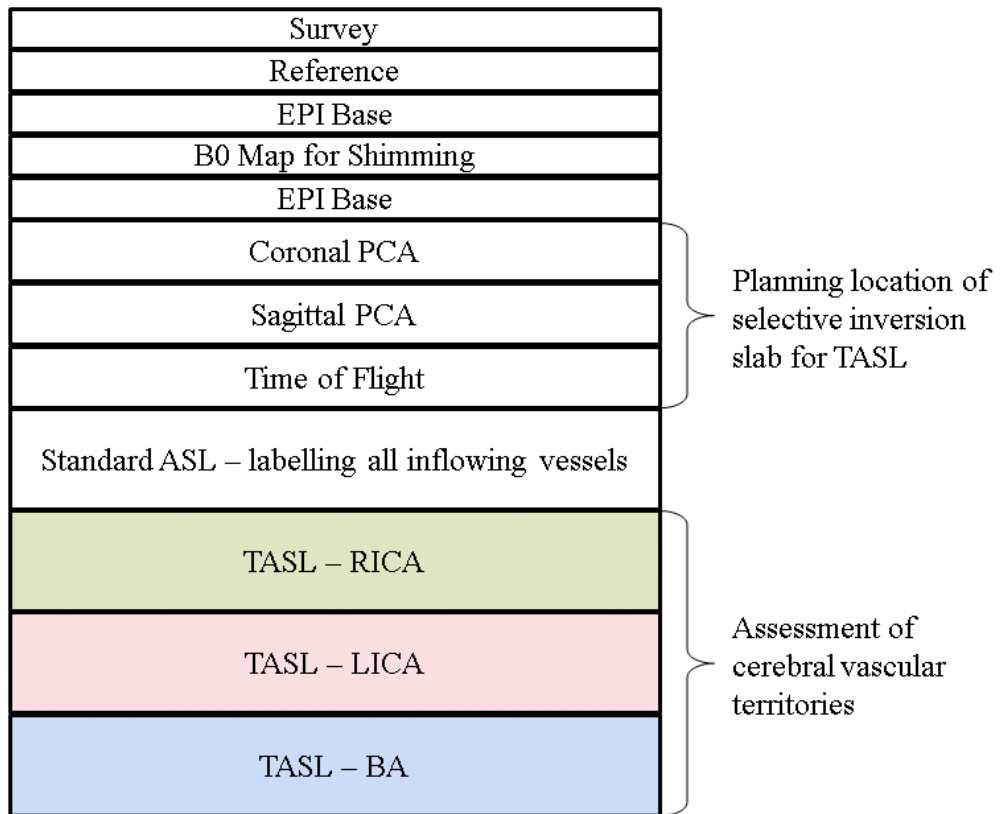
Figure 6.16: Scanning protocol for complete assessment of TASL at 7 T.

Subjects first underwent a standard set-up protocol of a survey, reference and EPI base scan (two dynamic pairs of basic EPI at 3 mm × 3 mm × 5 mm resolution and the same bandwidth as the TASL readout, using a TE / TR of 10 ms / 10 s) for the registration of datasets to MNI space. An image-based shimming technique with third-order shims was used to correct field inhomogeneities and minimize geometric distortions. The shim box was large to encompass the image volume and the labelling plane. Shimming was calculated using in-house software written in MATLAB [21] and data acquired from a B_0 map. Following this, the EPI base was again acquired to confirm success of shimming. As described in Chapter 5, coronal and sagittal phase contrast angiograms (PCAs) and a time of flight (TOF) contrast angiogram are required to locate the feeding arteries and thus to plan positioning of the selective label slabs for territorial ASL. PCAs were collected with an in-plane resolution of 0.72 mm × 1.2 mm, TE / TR of 7.6 ms / 20 ms, 20° flip angle, phase contrast velocity of 30 cms^{-1}, and SENSE factor 2. Two 50 mm PCA slices were acquired to visualize anterior and posterior feeding arteries (coronal) and left and right ICAs (sagittal), using the slice

positioning as described in Chapter 5. The TOF was performed using TE / TR = 3.5 ms / 41 ms, 20° flip angle, SENSE factor 1.5, in plane resolution of 0.62 mm, 60 slices of thickness 0.9 mm and $240 \times 240 \times 54$ field of view. The TOF was used to form a maximum intensity projection (MIP). Positioning of selective labelling slabs using PCAs and TOF is shown in Figure 6.17.
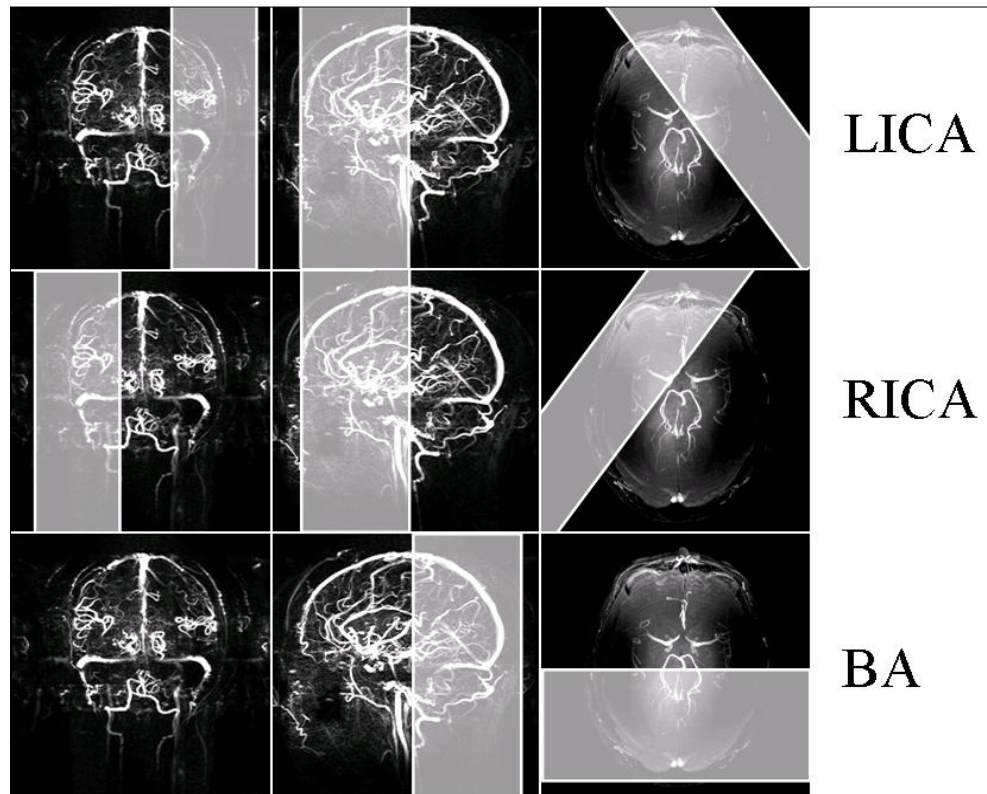
Figure 6.17: Locations of selective label slabs used for labelling TASL superimposed on to coronal and sagittal PCAs and axial TOF angiograms acquired at 7 T.

ASL data (standard ASL and TASL) were collected using a gradient echo (GE) EPI acquisition with SENSE factor 2 and TE of 10 ms, the data was collected with resolution of 3 mm $\times$ 3 mm $\times$ 5 mm, and 10 slices acquired with minimal temporal spacing. ASL data was collected with a post-label delay of 1550 ms, ASL time per label / control of $TR_{ASL} = 3500$ ms. In TASL, the label slab inevitably overlaps the imaging region on the labelling condition, as shown in Figure 6.18. Therefore it is essential that the effect of the inversion within the imaging slice itself is suppressed to prevent static offset signal not related to perfusion. To achieve this, in-plane saturation pulses must be applied to the imaging region immediately preceding (pre-

saturation) and following (post-saturation) the inversion pulse [11]. Four selective pulses known as the WET (Water suppression Enhanced through T_1 effects) scheme were used for in-plane saturation. As described in Chapter 5, the pre- and post- saturation region covered the entire imaging region and extended upwards by 45 mm to prevent signal contributing from inverted blood in vessels above the imaging region flowing downwards into the imaging region, and also 10 mm below the imaging region.
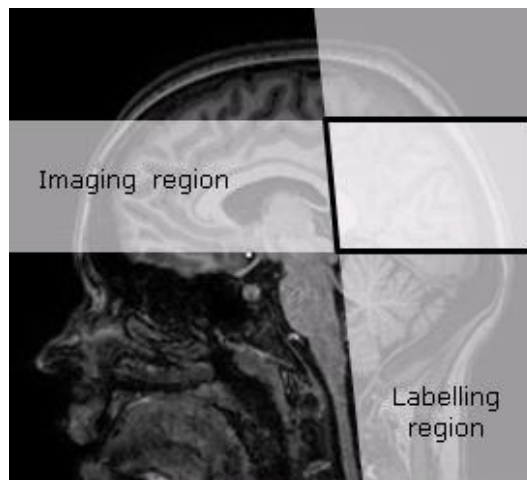
Figure 6.18: Overlap of labelling region on to imaging region, demonstrating the need for in-plane saturation.

Background suppression pulses were applied with inversion times TI_1 / TI_2 = 402 ms / 639 ms, these had previously been optimised to null the static signal at TI = 1550 ms. 50 dynamic ASL pairs were collected for each of the following arterial territories; left and right internal carotid arteries (LICA and RICA) and posterior blood supply of the basilar and vertebral arteries (BA) [20].

6.3.3   Data analysis

To inspect the quality of the data during scanning, data sets were viewed using the on-line image subtraction program available on the scanner, subsequently data were then processed and analysed off-line as outlined below.

Single-phase ASL label and control images were subtracted for each dynamic to form perfusion weighted difference images. These individual difference images were then visually inspected for motion with a view to discarding any dynamics displaying excessive motion (greater than one voxel). Territorial ASL label and control images were subtracted to form maps of each of the three vascular territories; posterior territory (BA) and left and right anterior territories (LICA and RICA). This was performed for each subject individually. EPI base images were transformed into standard MNI space [22] using the FLIRT linear registration tool from the FSL Software suite [23]. Registration transforms were then further applied to vascular territory maps of each subject. Further, a group average image was formed for each vascular territory across the three subjects.

6.4   Results

Figure 6.19 shows the results of the "all" scan in a single subject, where all inflowing vessels were labelled using a selective label slab placed in the neck, parallel to the imaging slab. This shows high contrast-to-noise perfusion weighted signal in the grey matter, as expected.
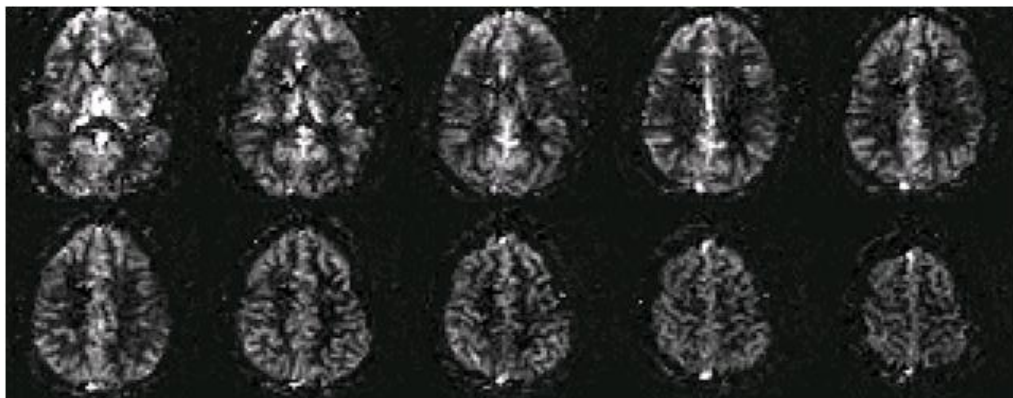
Figure 6.19: Standard ASL using PICORE to label all inflowing vessels in a representative subject.

On the first healthy volunteer, labelling of the basilar artery was not totally successful, but can still be seen. This limited success of labelling of the posterior blood supply is most likely due to the limited coverage of the

transmitting RF coil in the neck at 7 T. Labelling of the right and left internal carotid arteries was highly successful. Figure 6.20 shows a colour coded map of the RICA, LICA and BA territories as acquired at 7 T on the first healthy volunteer.
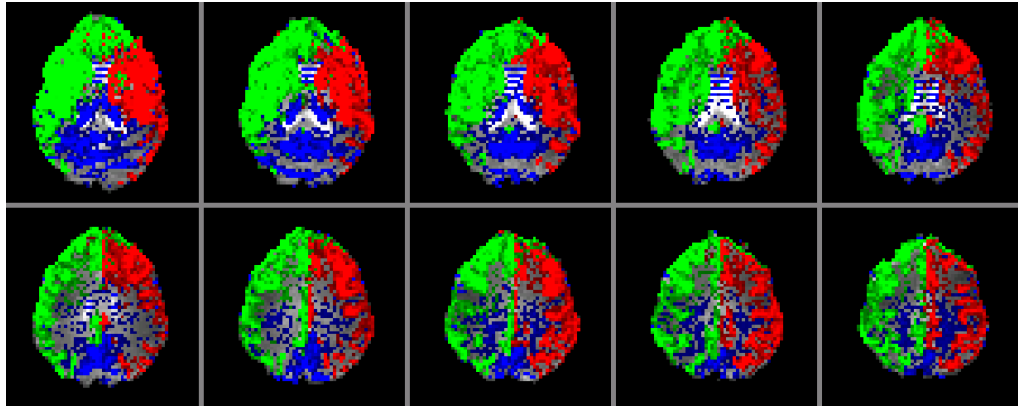
Figure 6.20: Colour coded map of TASL (RICA = green, LICA = red, BA = blue) at 7 T.

Two further subjects were assessed using the same protocol of territorial ASL, this time with greater success in labelling the posterior territory. Mean vascular territory maps for the three subjects are shown in Figure 6.21.
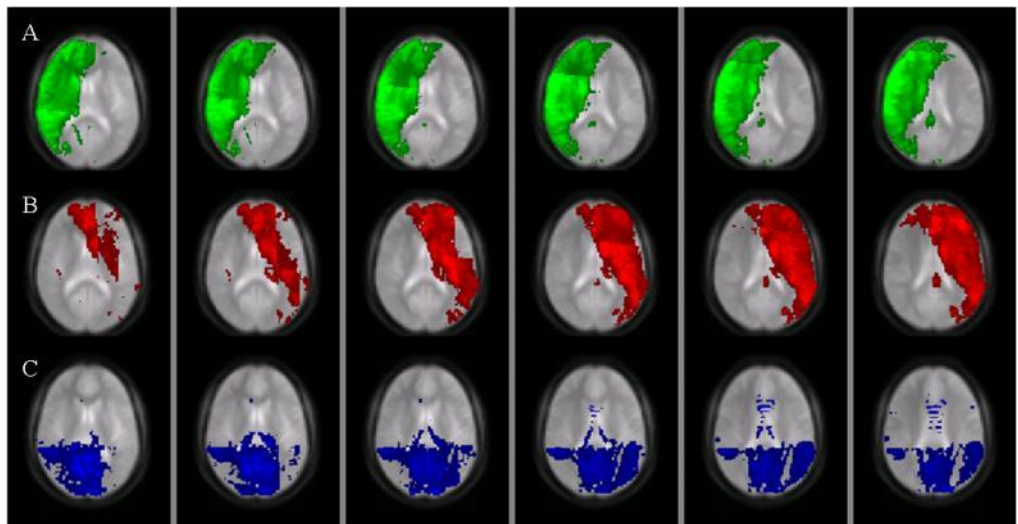
Figure 6.21: Group (n = 3) territorial ASL map displaying the vascular territories of (A) RICA, (B) LICA and (C) BA. Slices shown represent MNI co-ordinates z = 2 to z = 12.

These results highlight the feasibility and potential of using PICORE to perform territorial ASL at ultra-high field.

6.5   Discussion

This chapter has outlined the challenges presented and developments made to the TASL technique for use at ultra-high field. This work has demonstrated that using a PICORE labelling scheme, it is possible to perform Territorial Arterial Spin Labelling at 7 T to selectively label the LICA, RICA and BA.

Success of TASL was found to be highly dependent on the efficiency of the PICORE control condition, which was found to be dependent on the frequency offset, ω_{offset}, of the inversion pulse used. This in turn is dependent on the bandwidth of the pulse ($\Delta\omega$), the thickness of the labelling slab (Δz) and the distance between the centre of the label and image slabs along the direction corresponding to the orientation plane of the label slab (d). TASL geometries with a frequency offset of greater than approximately 1.5 kHz were considered to be successful. Achieving this condition required the use of a high bandwidth pulse and minimising the thickness of the labelling slab, while maximising the distance between the centres of the imaging and labelling slabs, as shown in Figure 6.12 and Figure 6.13.

The use of TASL at 7 T has not previously been reported, due to B_0 and B_1 inhomogeneity, but with careful planning and the use of an optimised sequence it is possible to perform, as has been demonstrated in this chapter (Figure 6.20 and Figure 6.21). This opens up the discussion of the benefits of ultra-high field to TASL.

Ultra-high field potentially provides improvement in contrast-to-noise ratio of any ASL technique, due to lengthened T_1 [8]. In addition, ultra-high field is known to provide higher image signal-to-noise ratio. This allows for images to be acquired at higher spatial resolution, thus providing reduced partial volume effects and finer delineation of vascular territory boundaries. Further developments in the area should assess the improvement to the technique in terms of increased spatial resolution.

The primary limitation to TASL is good labelling efficiency, which can be limited by B_1 inhomogeneities. Recently a method has been suggested for

improved B_1 transmission in the neck through the additional use of dielectric pads containing high permittivity material [24]), which are wrapped around the neck. These have been shown to result in improved B_1 homogeneity at the level of labelling; however, it is uncertain whether this benefit is large enough to enable a sufficient increase in labelling efficiency required for performing TASL.

It would be interesting to see further work using this technique take place in a cohort similar to that described in Chapter 5 of this thesis, where subjects were scanned at 3 T to provide a direct measure of the benefit of increased field strength to the technique. Additionally, the lengthened T_1 values afforded by ultra-high field strength may be exploited to study perfusion in elderly subjects or those with cerebrovascular disease, where blood transit times are likely to be longer [3], as mentioned in Chapter 5 of this thesis. In these cases, a longer post-label delay, TI may be beneficial, or alternatively, the use of a multi-phase readout, used at 3 T in Chapter 5 of this thesis in combination with territorial labelling, as this would provide additional information about the transit time of blood, thus allowing for quantification of perfusion measurements. Having optimised these techniques in a healthy group, it would be of interest in future studies to implement these techniques with a view to studying patients with cerebrovascular impairment.

This chapter reports the use of TASL with gradient-echo (GE) EPI readout only. Alternative image readouts, such as true FISP (true Fast Imaging with Steady-state Precession [25]) may produce images with less distortion at ultra-high field than GE-EPI and so may be more suitable for use in the clinical setting, particularly if the technique is to be applied to high spatial resolution acquisitions.

References

1.   Hendrikse, J, van der Grond, J, Lu, H, van Zijl, PCM, Golay, X. Flow Territory Mapping of the Cerebral Arteries With Regional Perfusion MRI. Stroke 35;882-887 (2004).

2.   Kansagra AP, Wong EC. Quantitative assessment of mixed cerebral vascular territory supply with vessel encoded arterial spin labeling MRI. Stroke. 39(11):2980-5 (2008).

3.   Chng SM, Petersen ET, Zimine I, Sitoh YY, Lim CC, Golay X. Territorial arterial spin labeling in the assessment of collateral circulation: comparison with digital subtraction angiography. Stroke. 39(12):3248-54 (2008).

4.   Dobre MC, Marjanska M, Urgurbil K. Blood T1 measurements at high magnetic field strengths. Proc. Intl. Soc. Mag. Reson. Med. p 1162 (2005).

5.   Detre JA, Wang J. Technical aspects and utility of fMRI using BOLD and ASL. Clin Neurophysiol. 113(5):621-34 (2002).

6.   Lu H, Clingman C, Golay X, van Zijl PC. Determining the longitudinal relaxation time (T1) of blood at 3.0 Tesla. Magn Reson Med. 52(3):679-82 (2004).

7.   Pfeuffer J, Adriany G, Shmuel A, Yacoub E, Van De Moortele PF, Hu X, Ugurbil K. Perfusion-based high-resolution functional imaging in the human brain at 7 Tesla. Magn Reson Med. 47(5):903-11 (2002).

8.   Gardener AG, Gowland PA, Francis ST. Implementation of quantitative perfusion imaging using pulsed arterial spin labeling at ultra-high field. Magn Reson Med. 61(4):874-82 (2009).

9.   Wiesinger F, Van de Moortele PF, Adriany G, De Zanche N, Ugurbil K, Pruessmann KP. Potential and feasibility of parallel MRI at high field. NMR Biomed. 19(3):368-78 (2006).

10.   Teeuwisse WM, Webb AG, van Osch MJ. Arterial spin labeling at ultra-high field: All that glitters is not gold. Int. J. Imag. Syst Tech. Special Issue on Neuroimaging. 20(1):62-70.

11. Holm, DA, Sidaros, K. Slice profile optimization in arterial spin labeling using presaturation and optimized RF pulses. Magn Reson Imaging 24:1229–1240 (2006).

12. Triantafyllou C, Hoge RD, Krueger G, Wiggins CJ, Potthast A, Wiggins GC, Wald LL. Comparison of physiological noise at 1.5 T, 3 T and 7 T and optimization of fMRI acquisition parameters. Neuroimage. 26(1):243-50 (2005).

13. St Lawrence KS, Wang J. Effects of the apparent transverse relaxation time on cerebral blood flow measurements obtained by arterial spin labeling. Magn Reson Med. 53(2):425-33 (2005).

14. Graphical Viewer Version 1.0, Philips Medical Systems Copyright, Philips Healthcare, N.V., Eindhoven, Netherlands.

15. Magnevist, Beyer-Schering-Pharma, Newbury, Berkshire, UK.

16. Wong EC, Buxton RB, Frank LR. Implementation of quantitative perfusion imaging techniques for functional brain mapping using pulsed arterial spin labeling. NMR Biomed. 10(4-5):237-49 (1997).

17. Yongbi MN, Branch CA, Helpern JA. Perfusion imaging using FOCI RF pulses. Magn Reson Med. 40(6):938-43 (1998).

18. Yongbi MN, Yang Y, Frank JA, Duyn JH. Multislice perfusion imaging in human brain using the C-FOCI inversion pulse: comparison with hyperbolic secant. Magn Reson Med. 42(6):1098-105 (1999).

19. Garcia DM, Duhamel G, Alsop DC. Efficiency of inversion pulses for background suppressed arterial spin labeling. Magn Reson Med. 54(2):366-72 (2005).

20. Hendrikse, J, van der Grond, J, Lu, H, van Zijl, PCM, Golay, X. Flow Territory Mapping of the Cerebral Arteries With Regional Perfusion MRI. Stroke 35:882-887 (2004).

21. Matlab version 2009b, The MathWorks Inc., Natick, MA.

22. Montreal Neurological Institute (MNI) Template. Montreal Neurological Institute, Montreal, Canada.

23. FMRIB Software Library (FSL), version 4.1.6, Oxford Centre for Functional MRI of the Brain, UK (2008).

24. Teeuwisse WM, Brink WM, Webb AG. Quantitative assessment of the effects of high-permittivity pads in 7 Tesla MRI of the brain. Magn Reson Med. [Epub ahead of print] (2011).

25. Fenchel M, Martirosian P, Langanke J, Giersch J, Miller S, Stauder NI, Kramer U, Claussen CD, Schick F. Perfusion MR imaging with FAIR true FISP spin labeling in patients with and without renal artery stenosis: initial experience. Radiology. 238(3):1013-21 (2006).

7 Conclusion and discussion

7.1 Summary of work presented in this thesis

This thesis describes technical developments made using the endogenous perfusion contrast, arterial spin labelling (ASL), and further application to pharmacological fMRI studies. Chapter 4 describes the use of blood oxygen level dependent (BOLD) contrast, in combination with the ASL technique of pseudo-continuous arterial spin labelling (PCASL), to study the effect of a peripherally acting beta-blocker on brain activity. The combination of BOLD and ASL allowing better interpretation of the effects of the pharmacological modulation on the underlying haemodynamic changes associated with an emotional visual stimulus, and on resting state brain activity. Chapter 5 describes the use of territorial and multi-phase ASL in combination for the quantitative assessment of cerebral haemodynamics at 3 T. In particular, the location and haemodynamic properties of the cerebral watershed regions are investigated using the two different ASL methods and investigation is enhanced by the use of these methods in conjunction. Chapter 6 describes the development of territorial ASL for use at 7 T, with the challenges of implementing the technique being discussed.

7.2 Discussion of beta-blocker modulation of task induced and resting state brain activity

Chapter 4 of this thesis investigates the effect of administering the peripherally acting beta blocker, nadolol, on task-induced brain activity and resting state functional connectivity. The drug was administered in a randomised placebo controlled crossover study design in 20 healthy subjects. Previous studies have used the centrally acting beta-blocker, propranolol, however, these results are ambiguous as propranolol does not act selectively in the periphery, and thus there may be confounds from direct central modulation. Additionally, previous studies have not assessed resting cerebral blood flow for drug-induced changes. Results from these studies have demonstrated reduced amygdala responsiveness, emotional memory encoding and retrieval

under the influence of the centrally acting beta-blocker, propranolol [1]. The sample size was deemed to be appropriate for testing of statistical significance in line with sample sizes used in other studies [2]. A single 80 mg dose of the peripherally acting beta blocker, nadolol, significantly reduced peripheral reactivity as assessed by mean arterial blood pressure and heart rate compared to a similarly administered placebo. Nadolol did not significantly decrease the resting perfusion or the BOLD response to visual emotional stimuli in a region in the primary visual cortex compared to placebo, thus confirming the peripheral action of the drug and minimising confounds from direct central effects.

Reduction of activity in the anterior insula supports the theory that reduction of peripheral feedback selectively reduces the processing of emotional visual stimuli, in agreement with the James-Lang theory [3] and the two factor theory of emotion [4], and is complementary to previous studies reporting memory impairment of emotional stimuli induced by the centrally acting beta blocker, propranolol [5]. This is also in support of studies where participant groups have experienced blockade of peripheral feedback by means of spinal cord injury [6].

The increase in amygdala activity associated with the administration of nadolol contradicts previously reported findings [1]. It is possible that nadolol causes a hypersensitisation selective to the amygdala due to lack of peripheral feedback, however, there is no previous evidence for this. Alternatively, it may be that the natural processing of emotional visual stimuli involves suppressing the fear / threat response in the amygdala. Nadolol may act to remove this suppressive process, allowing the amygdala to respond freely to emotional visual stimuli as if they were a real threat. This drug induced increase was found to be dominated by the response in the male group however, sample sizes in single gender subgroups were small in this study, and care must be taken in their interpretation. Further investigation in a larger cohort of males may provide more insight into the mechanism behind the modulation.

The acquisition method of dual readout of pseudo-continuous ASL (PCASL) and BOLD allowed the underlying haemodynamics to be assessed in this pharmacological study. The acquisition of a baseline or "off" period between each block of stimuli could be utilised to provide a baseline measure of perfusion and BOLD for calibration of responses, thus possibly eliminating the necessity to acquire an additional baseline perfusion scan in future studies. Alternatively, in order to quantitatively measure drug induced perfusion changes; ASL could be acquired with a multi-phase readout, as described in Chapter 5 of this thesis. Analysis of resting state functional connectivity showed no obvious drug induced changes, but a more rigorous analysis would include additional regression of noise measures.

7.3   Discussion of ASL results at 3 T and 7 T

Chapter 5 of this thesis implemented Territorial Arterial Spin Labelling (TASL) in combination with multiphase ASL for the comparison of vascular territory maps with haemodynamic parameter maps of quantitative CBF and blood transit times. Vascular territories were shown to be highly consistent between subjects. The cerebral watershed regions are known to exhibit lengthened blood transit times and as such are most susceptible to haemodynamic ischaemia. Thus, it is suggested that maps of arterial and capillary transit time can give information on the locations of the watershed regions. Compared to arterial transit time, capillary transit time was found to produce closer delineation of watershed regions by thresholding maps at a fixed value.

Quantitative analysis showed that watershed region masks formed using information from either TASL or multi-phase ASL showed increased capillary transit times and reduced perfusion rates compared to other cortical regions. Definition of the posterior watershed showed adequate delineation in most subjects, whereas assessment of anterior and internal watersheds was limited. However, the combination of the two techniques provided enhanced watershed region definition, thus demonstrating the benefit of the combined use of territorial ASL and multi-phase ASL for the non-invasive assessment of the

cerebral watershed regions, which could provide a means to study the haemodynamic effects on the watershed regions of blood pressure changes or pharmacological intervention, or the processes of healthy ageing or disease.

TASL was implemented and optimised over the course of a pilot study on 11 subjects, during which scanner operators became practiced in positioning of the labelling slabs. However, selective labelling is still highly scanner operator dependent and also dependent on the arrangement of the cerebral vasculature. Recently developed techniques such as super-selective TASL and super-selective ASL angiography may provide superior labelling efficiency, and higher success rates [7, 8]. Further, techniques such as velocity selective ASL [9] remove the dependence on the scanner operator's ability to effectively position labelling slabs.

The combination of territorial ASL with multiphase ASL may provide advantages in clinical groups, and carries the additional advantage of being non-invasive. For example, in asymptomatic subjects, there may be variations in the cerebrovascular architecture that can be explored using TASL and further interrogated using haemodynamic parameter maps provided by multiphase ASL. TASL used in combination with knowledge of the completeness of the Circle of Willis [10, 11] from Time of Flight angiography could provide insight into the effect of asymptomatic variations on the vascular territories and collateral supply. In patients with vascular disease, brain regions exhibiting exceptionally long transit times may signify that blood is supplied to the tissue via an atypical route. Combined assessment using territorial ASL and multi-phase ASL could prove useful for the assessment of patients with arterial occlusion or stenosis [12], or arteriovenous malformation, to assess collateral blood supply, or additionally by making comparisons before and after interventional surgery to determine its success. However, in the older population, blood transit times are longer, suggesting the use of a longer inversion time (TI) than used in this study, or alternatively, the use of a multi-phase readout. Additionally, in patients with cerebrovascular impairment, blood transit times are sometimes sufficiently

long (i.e. $> T_1$ of blood) that the inversion label has completely decayed, making detection of the label impossible.

Keeping in mind the potential applications listed above, the technique of territorial ASL (TASL) was developed for use at 7 T, where longitudinal relaxation times (T_1) increase [13]. As reported in Chapter 6 of this thesis, ultra-high field led to challenges associated with sensitivity to B_1 inhomogeneity, and the labelling efficiency. Use of a PICORE (Proximal Inversion with a Control for Off-Resonance Effects) ASL scheme provided a method for selective labelling and a high bandwidth FOCI (Frequency Offset Corrected Inversion) inversion pulse allowed good profile labelling and high frequency offset from resonance, overcoming issues with the efficiency of the control condition and facilitating the use of TASL at 7 T.

Performing such studies at ultra-high field enables images to be acquired at higher spatial resolution than at lower field, due to the increased signal-to-noise ratio and contrast-to-noise ratio. Additionally, the lengthened T_1 at ultra-high field allows for the imaging of perfusion in cases where blood transit times are exceptionally long. However, limitations of performing this technique at ultra-high field remain in terms of sensitivity to B_1 inhomogeneity and limited coverage of the transmit radiofrequency coil. With additional technical developments, these problems are likely to be overcome, for example, the placement of dielectric pads containing high permittivity material around the neck, improving B_1 delivery below the coverage of the transit coil [14].

References

1. Strange, BA, Dolan, RJ. ß-Adrenergic modulation of emotional memory-evoked human amygdala and hippocampal responses. PNAS, 101(31) 11454-11458 (2004).

2. Carter, CS, Heckers, S, Nichols, T, Pine, DS, Strother, S. Optimizing the Design and Analysis of Clinical Functional Magnetic Resonance Imaging Research Studies. Biol. Psychiatry. 64:842-849 (2008).

3. Fehr, FS, Stern, JA. Peripheral physiological variables and emotion: the James-Lange theory revisited. Psychol Bull, 74(6):411-24 (1970).

4. Schachter, S. and Singer, J. E. Cognitive, social and physiological determinants of emotional states, Psychological Review, 69, 379-399 (1962).

5. Cahill L, Prins B, Weber M, McGaugh JL. Beta-adrenergic activation and memory for emotional events. Nature 371:702-704 (1994).

6. Nicotra, A, Critchley, HD, Mathias, CJ, Dolan, RJ. Emotional and autonomic consequences of spinal cord injury explored using functional brain imaging. Brain, 129, 718–728 (2006).

7. Helle M, Norris DG, Rüfer S, Alfke K, Jansen O, van Osch MJ. Superselective pseudocontinuous arterial spin labeling. Magn Reson Med. 64(3):777-86 (2010).

8. Helle, M, Rüfer, S, Teeuwisse, W, Jansen, O, Norris, DG, van Osch, M. Superselective MR-angiography based on pseudo-continuous arterial spin labeling and first applications in AVM patients. Proc. Intl. Soc. Mag. Reson. Med. 19 (2011).

9. Wong EC, Cronin M, Wu WC, Inglis B, Frank LR, Liu TT. Velocity-selective arterial spin labeling. Magn Reson Med. 55(6):1334-41 (2006).

10. Rothberg M, Mattey WE, Bastidas J. Anomalous internal carotid-posterior cerebral artery circulation: one form of congenital incomplete circle of Willis. AJR Am J Roentgenol. 128(1):153-5 (1977).

11. Kim GE, Cho YP, Lim SM. The anatomy of the circle of Willis as a predictive factor for intra-operative cerebral ischemia (shunt need) during carotid endarterectomy. Neurol Res. 24(3):237-40 (2002).

12. Chng SM, Petersen ET, Zimine I, Sitoh YY, Lim CC, Golay X. Territorial arterial spin labeling in the assessment of collateral circulation: comparison with digital subtraction angiography. Stroke. 39(12):3248-54 (2008).

13. Gardener AG, Gowland PA, Francis ST. Implementation of quantitative perfusion imaging using pulsed arterial spin labeling at ultra-high field. Magn Reson Med. 61(4):874-82 (2009).

14. Teeuwisse WM, Brink WM, Webb AG. Quantitative assessment of the effects of high-permittivity pads in 7 Tesla MRI of the brain. Magn Reson Med. [Epub ahead of print] (2011).

Overcoming Stage Fright

A functional connectivity study of the human brain

We are looking for healthy volunteers for an exciting study looking at how beta-blockers affect brain activity relating to emotions such as fear and nervousness.

Benefits for volunteers:
If you take part in this study, you will:

*   receive an image from the MRI scan of your brain
*   be paid an inconvenience allowance
*   be taking part in cutting edge research!
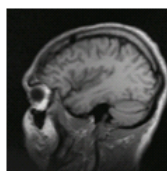
What the study involves:

*   two separate sessions at lease one week apart, each lasting approximately 5 hours
*   Each session will include one non-invasive MRI scan of approximately 40 minutes

Eligibility:
You must be:

*   aged 17 years or over
*   healthy
*   a non-smoker

Division of Academic Radiology
Queens Medical Centre, Nottingham

Contact: Rebecca Dewey
msxrd@nottingham.ac.uk

Contact: Rebecca Dewey
msxrd@nottingham.ac.uk

Contact: Rebecca Dewey
msxrd@nottingham.ac.uk

Contact: Rebecca Dewey
msxrd@nottingham.ac.uk

Contact: Rebecca Dewey
msxrd@nottingham.ac.uk

Contact: Rebecca Dewey
msxrd@nottingham.ac.uk

Contact: Rebecca Dewey
msxrd@nottingham.ac.uk

Contact: Rebecca Dewey
msxrd@nottingham.ac.uk

Contact: Rebecca Dewey
msxrd@nottingham.ac.uk

Contact: Rebecca Dewey
msxrd@nottingham.ac.uk

Appendix B: Safety questionnaire

The University of Nottingham   **On the interaction between pharmacologically reducing bodily feedback and emotion-related brain activity**

MR Volunteer Safety Screening Questionnaire:

NAME	Date of Birth
ADDRESS	Weight
	Height
Phone number	

MR scanning uses strong magnetic fields. For your own safety and the safety of others it is **very important** that you do not go into the magnet halls with any metal in or on your body or clothing. Please answer the following questions carefully and ask if anything is not clear. All information is held in the strictest confidence.

1. Do you have any implants in your body? e.g. replacement joints, drug pumps   Y/N
2. Do you have aneurysm clips (clips put around blood vessels during surgery)?   Y/N
3. Do you have a pacemaker or artificial heart valve? *(These stop working near MR Scanners)* Y/N
4. Have you ever had any surgery? Please give brief details over.   Y/N
   (We do not need to know about uncomplicated caesarean delivery, vasectomy or termination of pregnancy)
5. Do you have any foreign bodies in your body (e.g. shrapnel)?   Y/N
6. Have you ever worked in a machine tool shop without eye protection?   Y/N
7. Do you wear a hearing aid or cochlear implant?   Y/N
8. Could you be pregnant? (Pregnancy tests are available in the female toilets)   Y/N
9. Have you ever suffered from tinnitus?   Y/N
10. Do you wear dentures, a dental plate or a brace?   Y/N
11. Are you susceptible to claustrophobia?   Y/N
12. Do you suffer from blackouts, epilepsy or fits?   Y/N
13. Do you have any tattoos? (If yes, you may be asked to read and sign another form) Y/N
14. Do you have any body piercing jewellery that cannot be removed?   Y/N
15. Do you have any skin patches (trans-dermal patches)?   Y/N
16. Do you have a coil in place (IUD) for contraception? Do you know what type?   Y/N
17. Do you wear glasses to correct your vision? (please state below whether or not you can see without them, and if you can wear contact lenses)   Y/N
18. Do you have any condition that may affect your ability to control your temperature ? Y/N
   (e.g. Do you have a fever, cardiovascular disease, hypertension, diabetes or cerebrovascular disease?)
19. Will you remove all metal including coins, body-piercing jewellery, false-teeth, hearing aids etc. before entering the magnet hall? *(lockers available by the changing rooms)* Y/N
19. Is there anything else you think we should know (please write below)?   Y/N

Appendix C: Psychological questionnaires

Hospital Anxiety and Depression Scale (HADS)

Read these questions and think about how you currently feel. Please choose one response from the four given for each interview.   Please try to give an immediate response and do not think too long about your answers.

I feel tense or 'wound up':

1. Most of the time	2. A lot of the time
3. From time to time, occasionally	4. Not at all

I still enjoy the things I used to enjoy:

1. Definitely as much	2. Not quite so much
3. Only a little	4. Hardly at all

I get a sort of frightened feeling as if something awful is about to happen:

1. Very definitely and quite badly	2. Yes, but not too badly
3. A little, but it doesn't worry me	4. Not at all

I can laugh and see the funny side of things:

1. As much as I always could	2. Not quite so much now
3. Definitely not so much now	4. Not at all

Worrying thoughts go through my mind:

1. A great deal of the time	2. A lot of the time
3. From time to time, but not too often	4. Only occasionally

I feel cheerful:

1. Not at all	2. Not often
3. Sometimes	4. Most of the time

I can sit at ease and feel relaxed:

1. Definitely	2. Usually
3. Not Often	4. Not at all

I feel as if I am slowed down:

1. Nearly all the time	2. Very often
3. Sometimes	4. Not at all

I get a sort of frightened feeling like 'butterflies' in the stomach:

1. Not at all	2. Occasionally
3. Quite Often	4. Very Often

I have lost interest in my appearance:

1. Definitely	2. I don't take as much care as I should
3. I may not take quite as much care	4. I take just as much care as ever

I feel restless as I have to be on the move:

1. Very much indeed	2. Quite a lot
3. Not very much	4. Not at all

I look forward with enjoyment to things:

1. As much as I ever did	2. Rather less than I used to
3. Definitely less than I used to	4. Hardly at all

I get sudden feelings of panic:

1. Very often indeed	2. Quite often
3. Not very often	4. Not at all

I can enjoy a good book or radio or TV program:

1. Often	2. Sometimes
3. Not often	4. Very seldom

Reference:

Zigmond and Snaith (1983)

ERS

This questionnaire asks different questions about how you experience emotions **on a regular basis (for example, each day)**. When you are asked about being "emotional," this may refer to being angry, sad, excited, or some other emotion. Please rate the following statements.

0 Not at all like me	1 A little like me	2 Somewhat like me	3 A lot like me	4 Completely like me

1	When something happens that upsets me, it's all I can think about it for a long time.	0	1	2	3	4
2	My feelings get hurt easily.	0	1	2	3	4
3	When I experience emotions, I feel them very strongly/intensely.	0	1	2	3	4
4	When I'm emotionally upset, my whole body gets physically upset as well.	0	1	2	3	4
5	I tend to get very emotional very easily.	0	1	2	3	4
6	I experience emotions very strongly.	0	1	2	3	4
7	I often feel extremely anxious.	0	1	2	3	4
8	When I feel emotional, it's hard for me to imagine feeling any other way.	0	1	2	3	4
9	Even the littlest things make me emotional.	0	1	2	3	4
10	If I have a disagreement with someone, it takes a long time for me to get over it.	0	1	2	3	4
11	When I am angry/upset, it takes me much longer than most people to calm down.	0	1	2	3	4
12	I get angry at people very easily.	0	1	2	3	4
13	I am often bothered by things that other people don't react to.	0	1	2	3	4
14	I am easily agitated.	0	1	2	3	4
15	My emotions go from neutral to extreme in an instant.	0	1	2	3	4
16	When something bad happens, my mood changes very quickly. People tell me I have a very short fuse.	0	1	2	3	4
17	People tell me that my emotions are often too intense for the situation.	0	1	2	3	4
18	I am a very sensitive person.	0	1	2	3	4
19	My moods are very strong and powerful.	0	1	2	3	4
20	I often get so upset it's hard for me to think straight.	0	1	2	3	4
21	Other people tell me I'm overreacting.	0	1	2	3	4

Other relevant questions/comments:

TAS 20

Answer the following questions as spontaneously as possible. If you get stuck on a question, leave it out and continue with the next. Each question can have one of 5 possible answers. Thank you.

ANSWER SCALE: 1 = strongly disagree – 2 – 3 – 4 – 5 = strongly agree

1. I am often confused about what emotion I am feeling.	1 – 2 – 3 – 4 - 5
2. It is difficult for me to find the right words for my feelings.	1 – 2 – 3 – 4 - 5
3. I have physical sensations that even doctors don't understand.	1 – 2 – 3 – 4 - 5
4. I am able to describe my feelings easily.	1 – 2 – 3 – 4 - 5
5. I prefer to analyze problems rather than just describe them.	1 – 2 – 3 – 4 - 5
6. When I am upset, I don't know if I am sad, frightened, or angry.	1 – 2 – 3 – 4 - 5
7. I am often puzzled by sensations in my body.	1 – 2 – 3 – 4 - 5
8. I prefer to just let things happen rather than to understand why they turned out that way.	1 – 2 – 3 – 4 - 5
9. I have feelings that I can't quite identify.	1 – 2 – 3 – 4 - 5
10. Being in touch with emotions is essential.	1 – 2 – 3 – 4 - 5
11. I find it hard to describe how I feel about people	1 – 2 – 3 – 4 - 5
12. People tell me to describe my feelings more.	1 – 2 – 3 – 4 - 5
13. I don't know what's going on inside me.	1 – 2 – 3 – 4 - 5
14. I often don't know why I am angry.	1 – 2 – 3 – 4 - 5
15. I prefer talking to people about their daily activities rather than their feelings.	1 – 2 – 3 – 4 - 5
16. I prefer to watch "light" entertainment shows rather than psychological dramas.	1 – 2 – 3 – 4 - 5
17. It is difficult for me to reveal my innermost feelings, even to close friends.	1 – 2 – 3 – 4 - 5
18. I can feel close to someone, even in moments of silence.	1 – 2 – 3 – 4 - 5
19. I find examination of my feelings useful in solving personal problems.	1 – 2 – 3 – 4 - 5
20. Looking for hidden meanings in movies or plays distracts from their enjoyment.	1 – 2 – 3 – 4 - 5

BVAQ

On the next page you will find a list of statements about how you react in live generally. Under each statement you find five categories of answers. The categories consist of five boxes. The boxes represent five answers ranging from `This definitely applies' to `This in no way applies'. The purpose of this questionnaire, is to indicate on the scale to what extent your personal way of reacting or responding corresponds to the statement. Put only one cross in one of the boxes.

An example.

Seeing kittens arouses feelings of tenderness

This definitely applies |___|___|___|___|___| This in no way applies

If you think that this statement fully corresponds to the way in which you react or respond, put a cross in the box furthest to the left.

If you think that this statement in no way corresponds with the way in which you react or respond, put a cross in the box furthest to the right.

If you think that the way in which you respond is less clear-cut than is described above, put a cross slightly more to the middle. Only use the centre box in the scale when it is impossible for you to judge the response as described in the statement.

Now you can turn the page and start filling in the questionnaire.

1)	I find it difficult to express my feelings verbally.

This definitely applies |___|___|___|___|___| This in no way applies

2)	Before I fall asleep, I imagine all kinds of events, encounters and conversations.

This definitely applies |___|___|___|___|___| This in no way applies

3)	When I am upset, I know whether I am afraid or sad or angry.

This definitely applies |___|___|___|___|___| This in no way applies

4)	When something unexpected happens, I remain calm and unmoved.

This definitely applies |___|___|___|___|___| This in no way applies

5)	I hardly ever consider my feelings.

This definitely applies |___|___|___|___|___| This in no way applies

6)	I like to tell others about how I feel.

This definitely applies |___|___|___|___|___| This in no way applies

7)	I have few daydreams and fantasies.

This definitely applies |___|___|___|___|___| This in no way applies

8)	When I am tense, it remains unclear from which of my feelings this comes.

This definitely applies |___|___|___|___|___| This in no way applies

9)	When I see somebody crying uncontrollably, I remain unmoved.

This definitely applies |___|___|___|___|___| This in no way applies

10)	You should try to figure out feelings.

This definitely applies |___|___|___|___|___| This in no way applies

11)	Even with a friend, I find it difficult to talk about my feelings.

This definitely applies |___|___|___|___|___| This in no way applies

12)	I often use my imagination.

This definitely applies |___|___|___|___|___| This in no way applies

13)	When things get to be a bit overwhelming, I usually understand why.

This definitely applies |___|___|___|___|___| This in no way applies

14)	When friends around me argue violently, I become emotional.

This definitely applies |___|___|___|___|___| This in no way applies

15) When I feel uncomfortable, I will not trouble myself even more by asking myself why.

This definitely applies |___|___|___|___|___| This in no way applies

16) When I want to express how unhappy I feel, I find it easy to find the right words.

This definitely applies |___|___|___|___|___| This in no way applies

17) I have little interest in fantasies and weird stories.

This definitely applies |___|___|___|___|___| This in no way applies

18) When I feel good, it remains unclear as to whether I am cheerful or elated or happy.

This definitely applies |___|___|___|___|___| This in no way applies

19) Often emotions well up inside me unexpectedly.

This definitely applies |___|___|___|___|___| This in no way applies

20) When I feel uneasy, I try to find out why I feel that way.

This definitely applies |___|___|___|___|___| This in no way applies

21) People often say that I should talk more about my feelings.

This definitely applies |___|___|___|___|___| This in no way applies

22) I hardly ever fantasize.

This definitely applies |___|___|___|___|___| This in no way applies

23) I do not know what's is on my mind.

This definitely applies |___|___|___|___|___| This in no way applies

24) Even when others are wildly enthusiastic about something, I remain unmoved.

This definitely applies |___|___|___|___|___| This in no way applies

25) There is not much to understand as far as emotions are concerned.

This definitely applies |___|___|___|___|___| This in no way applies

26) When I am upset by something, I talk with others about my feelings.

This definitely applies |___|___|___|___|___| This in no way applies

27) I like to think up unusual imaginative stories.

This definitely applies |___|___|___|___|___| This in no way applies

28) When I feel unhappy, I know whether I am afraid or dejected or sad.

This definitely applies |___|___|___|___|___| This in no way applies

29) Unexpected events often overwhelm me with emotion.

This definitely applies |___|___|___|___|___| This in no way applies

30) I think that you should keep in tune with your feelings.

This definitely applies |___|___|___|___|___| This in no way applies

31) I can express my feelings verbally.

This definitely applies |___|___|___|___|___| This in no way applies

32) I think that fantasizing about imaginary things or events is a waste of time.

This definitely applies |___|___|___|___|___| This in no way applies

33) When I am hard on myself, it remains unclear to me whether I am sad or afraid or unhappy.

This definitely applies |___|___|___|___|___| This in no way applies

34) I accept disappointments without emotion.

This definitely applies |___|___|___|___|___| This in no way applies

35) I find it strange that others analyse their emotions so often.

This definitely applies |___|___|___|___|___| This in no way applies

36) When I talk to people, I prefer to talk about daily activities rather than about my emotions.

This definitely applies |___|___|___|___|___| This in no way applies

37) When I don't have much to do, I daydream.

This definitely applies |___|___|___|___|___| This in no way applies

38) When I am in a sunny mood, I know whether I am enthusiastic or cheerful or elated.

This definitely applies |___|___|___|___|___| This in no way applies

39) When I see someone else sobbing heavily, I feel sadness well up inside me.

This definitely applies |___|___|___|___|___| This in no way applies

40) When I am nervous, I want to know exactly where that feeling comes from.

This definitely applies |___|___|___|___|___| This in no way applies

INTERPERSONAL REACTIVITY INDEX

The following statements inquire about your thoughts and feelings in a variety of situations. For each item, indicate how well it describes you by choosing the appropriate letter on the scale at the top of the page: A, B, C, D, or E. When you have decided on your answer, fill in the letter on the answer sheet next to the item number. READ EACH ITEM CAREFULLY BEFORE RESPONDING. Answer as honestly as you can. Thank you.

<u>ANSWER SCALE</u>:

A   B   C   D   E
DOES NOT DESCRIBE ME VERY WELL - DESCRIBES ME VERY WELL

I daydream and fantasize, with some regularity, about things that might happen to me.	A – B – C – D - E
I often have tender, concerned feelings for people less fortunate than me.	A – B – C – D - E
I sometimes find it difficult to see things from the "other guy's" point of view.	A – B – C – D - E
Sometimes I don't feel very sorry for other people when they are having problems.	A – B – C – D - E
I really get involved with the feelings of the characters in a novel.	A – B – C – D - E
In emergency situations, I feel apprehensive and ill-at-ease.	A – B – C – D - E
I am usually objective when I watch a movie or play, and I don't often get completely caught up in it.	A – B – C – D - E
I try to look at everybody's side of a disagreement before I make a decision.	A – B – C – D - E
When I see someone being taken advantage of, I feel kind of protective towards them.	A – B – C – D - E
I sometimes feel helpless when I am in the middle of a very emotional situation.	A – B – C – D - E
I sometimes try to understand my friends better by imagining how things look from their perspective.	A – B – C – D - E
Becoming extremely involved in a good book or movie is somewhat rare for me.	A – B – C – D - E
When I see someone get hurt, I tend to remain calm.	A – B – C – D - E
Other people's misfortunes do not usually disturb me a great deal.	A – B – C – D - E
If I'm sure I'm right about something, I don't waste much time listening to other people's arguments.	A – B – C – D - E
After seeing a play or movie, I have felt as though I were one of the characters.	A – B – C – D - E
Being in a tense emotional situation scares me.	A – B – C – D - E
When I see someone being treated unfairly, I sometimes don't feel very much pity for them.	A – B – C – D - E
I am usually pretty effective in dealing with emergencies.	A – B – C – D - E
I am often quite touched by things that I see happen.	A – B – C – D - E

I believe that there are two sides to every question and try to look at them both.	A – B – C – D - E
I would describe myself as a pretty soft-hearted person.	A – B – C – D - E
When I watch a good movie, I can very easily put myself in the place of a leading character.	A – B – C – D - E
I tend to lose control during emergencies.	A – B – C – D - E
When I'm upset at someone, I usually try to "put myself in his shoes" for a while.	A – B – C – D - E
When I am reading an interesting story or novel, I imagine how I would feel if the events in the story were happening to me.	A – B – C – D - E
When I see someone who badly needs help in an emergency, I go to pieces.	A – B – C – D - E
Before criticizing somebody, I try to imagine how I would feel if I were in their place.	A – B – C – D - E

BODY PERCEPTION QUESTIONNAIRE
(S.W. Porges)

I: AWARENESS

Image how aware you are of your body processes. Select the answer that most accurately describes you. Rate your awareness on each of the characteristics described below using the following 5-point scale:

a) never b) occasionally c) sometimes d) usually e) always

During most situations I am aware of:

1. swallowing frequently	a – b – c – d – e
2. a ringing in my ears	a – b – c – d – e
3. an urge to cough to clear my throat	a – b – c – d – e
4. my body swaying when I am standing	a – b – c – d – e
5. my mouth being dry	a – b – c – d – e
6. how fast I am breathing	a – b – c – d – e
7. watering or tearing of my eyes	a – b – c – d – e
8. my skin itching	a – b – c – d – e
9. noises associated with my digestion	a – b – c – d – e
10. eye fatigue or pain	a – b – c – d – e
11. muscle tension in my back and neck	a – b – c – d – e
12. a swelling of my body or parts of my body	a – b – c – d – e
13. an urge to urinate	a – b – c – d – e
14. tremor in my hands	a – b – c – d – e
15. an urge to defecate	a – b – c – d – e
16. muscle tension in my arms and legs	a – b – c – d – e
17. a bloated feeling because of water retention	a – b – c – d – e
18. muscle tension in my face	a – b – c – d – e
19. goose bumps	a – b – c – d – e
20. facial twitches	a – b – c – d – e
21. being exhausted	a – b – c – d – e
22. stomach and gut pains	a – b – c – d – e
23. rolling or fluttering my eyes	a – b – c – d – e
24. stomach distension or bloatedness	a – b – c – d – e
25. palms sweating	a – b – c – d – e
26. sweat on my forehead	a – b – c – d – e
27. clumsiness or bumping into people	a – b – c – d – e
28. tremor in my lips	a – b – c – d – e
29. sweat in my armpits	a – b – c – d – e
30. sensations of prickling, tingling, or numbness in my body	a – b – c – d – e
31. the temperature of my face (especially my ears)	a – b – c – d – e
32. grinding my teeth	a – b – c – d – e
33. general jitteriness	a – b – c – d – e
34. muscle pain	a – b – c – d – e
35. joint pain	a – b – c – d – e
36. fullness of my bladder	a – b – c – d – e
37. my eye movements	a – b – c – d – e
38. back pain	a – b – c – d – e

39. my nose itching	a – b – c – d – e
40. the hair on the back of my neck "standing up"	a – b – c – d – e
41. needing to rest	a – b – c – d – e
42. difficulty in focusing	a – b – c – d – e
43. an urge to swallow	a – b – c – d – e
44. how hard my heart is beating	a – b – c – d – e
45. feeling constipated	a – b – c – d – e

II: STRESS RESPONSE

Imagine yourself in a very stressful situation or during periods of severe stress. Using the following 5-point scale, rate your awareness of perceived changes due to stress in each of the global response systems described below

a) never b) occasionally c) sometimes d) usually e) always

During stressful situations I am aware of:

46. vascular responses such as my face becoming flushed or pallid, or feeling faint.	a – b – c – d – e
47. body posture shifts such as being hunched over, head down, and knees locked.	a – b – c – d – e
48. muscle tone or tremor such as arms and legs feeling weak, hands shaking, and lips quivering.	a – b – c – d – e
49. breathing more rapidly and shallowly, and having difficulty in catching mybreath.	a – b – c – d – e
50. digestive responses including gastric distress, gas, cramps, and diarrhea.	a – b – c – d – e
51. difficulty in paying attention with my mind wondering or day dreaming.	a – b – c – d – e
52. difficulties in sensory abilities such as problems hearing, seeing, smelling, or feeling touch.	a – b – c – d – e
53. emotional problems such as more frequent feelings of depression, frustration, rage, or anger.	a – b – c – d – e
54. difficulty organizing my thoughts.	a – b – c – d – e
55. difficulty speaking clearly and understandably.	a – b – c – d – e

III: AUTONOMIC NERVOUS SYSTEM REACTIVITY

The autonomic nervous system is the part of your nervous system that controls your cardiovascular, respiratory, digestive, and temperature regulation systems. It is also involved in the experience and expression of emotions.

The autonomic nervous system functions differently among people. This scale has been developed to measure how your autonomic nervous system reacts.

Using the following 5-point scale, rate yourself on each of the statements below:

a) never b)occasionally c) sometimes d)usually e) always

56. I feel nauseous.	a – b – c – d – e
57. I have difficulty coordinating breathing and eating.	a – b – c – d – e
58. My nose is runny, even when I am not sick.	a – b – c – d – e
59. When I am eating, I have difficulty talking.	a – b – c – d – e
60. My heart often beats irregularly.	a – b – c – d – e
61. When I eat, food feels dry and sticks to my mouth and throat.	a – b – c – d – e
62. I have "sour" stomach.	a – b – c – d – e
63. I feel like vomiting.	a – b – c – d – e
64. I feel shortness of breath.	a – b – c – d – e
65. I have difficulty coordinating breathing with talking.	a – b – c – d – e
66. When I eat, I have difficulty coordinating swallowing, chewing, and/or sucking with breathing.	a – b – c – d – e
67. I have a persistent cough that interferes with my talking and eating.	a – b – c – d – e
68. I drool, especially when I am excited.	a – b – c – d – e
69. I gag from the saliva in my mouth.	a – b – c – d – e
70. I produce a lot of saliva even when I am not eating.	a – b – c – d – e
71. I have difficulty adjusting my eyes to changes in illumination.	a – b – c – d – e
72. I have chest pains.	a – b – c – d – e
73. I gag when I eat.	a – b – c – d – e
74. When I talk, I often feel I should cough or swallow the saliva in my mouth.	a – b – c – d – e
75. I am constipated.	a – b – c – d – e
76. I have indigestion.	a – b – c – d – e
77. After eating I have digestive problems.	a – b – c – d – e
78. I have diarrhea.	a – b – c – d – e
79. When I breath, I feel like I cannot get enough oxygen.	a – b – c – d – e
80. I have difficulty controlling my eyes.	a – b – c – d – e
81. I get dizzy when urinating or having a bowel movement.	a – b – c – d – e
82. I have trouble focusing when I go into dimly or brightly illuminated places.	a – b – c – d – e

IV: STRESS STYLE 1

Each of us responds differently to stressful events and conditions. The Stress Style 1 Scale evaluates your style ofresponding to stress.

Using the following 5-point scale, rate yourself on each of the statements below:

a) never b) occasionally c) sometimes d) usually e) always

When I am emotionally stressed because of a specific problem:

83. I approach the problem head-on.	a – b – c – d – e
84. I withdraw.	a – b – c – d – e
85. I know that things will be better later, so I wait until I feel better before acting.	a – b – c – d – e
86. I know that things will go better if I act immediately.	a – b – c – d – e
87. I feel mental tension.	a – b – c – d – e
88. I feel frustrated.	a – b – c – d – e
89. I feel insecure.	a – b – c – d – e
90. I feel aimless.	a – b – c – d – e

V: STRESS STYLE 2

Each of us responds differently to stressful events and conditions. The Stress Style 2 Scale evaluates your style of responding to stress.

Using the following 5-point scale, rate yourself on each of the statements below:

a) never b) occasionally c) sometimes d) usually e) always

When I am emotionally stressed because of a specific problem:

91. I feel dizzy.	a – b – c – d – e
92. I have difficulty speaking.	a – b – c – d – e
93. I feel a tingling in my face.	a – b – c – d – e
94. I feel my blood sugar drop.	a – b – c – d – e

Appendix D: Behavioural questionnaires on pain empathy and facial emotion recognition:

PAIN EMPATHY QUESTIONNAIRE

You will see several pictures depicting persons who suffer from pain.

We ask you to judge:

1. How much pain are <u>they</u> experiencing?

2. How unpleasant do <u>you</u> feel while looking at this picture?

3. How aroused are <u>you</u> while looking at this picture? Or how intense are <u>your</u> bodily reactions in response to the picture?
Please remember: Use the whole range of <u>all</u> scales.

The pictures are similar to those presented in the MRI session.

You can start with your rating while the picture is presented or in the rating period.

Please try to finish every rating and do not leave out any items.

The following scales were presented for each of 15 images shown on

computer screen:

Picture 1:
Experienced pain (Mark the line!)
1_____9
no pain at all   severe pain

Experienced valence (Mark the line!)
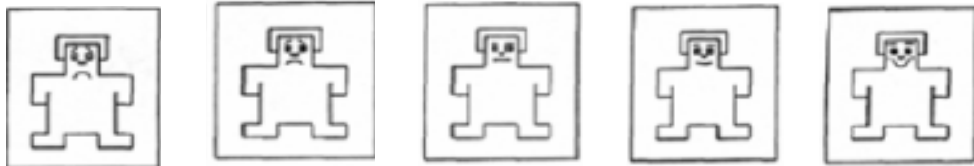
1_____9
very unpleasant   very pleasant

Experienced arousal (Mark the line!)

1_____9
very calm   very aroused

Last question: How long was this picture presentation experiment? (seconds)

Rating of Emotional Faces Questionnaire

You will see several faces with certain emotional and non-emotional expressions.
Please categorize depicted faces according to one of theses categories:

NEUTRAL	HAPPY	FEARFUL	ANGRY	SAD	DISGUSTED

Answer as quick and as correct as possible on the answer sheet by making a cross at the corresponding category.
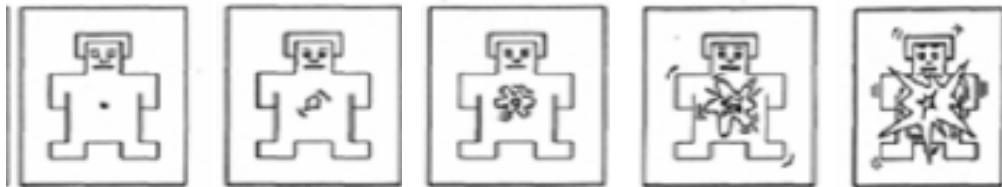**For example when you recognize a happy face:**

NEUTRAL	HAPPY	FEARFUL	ANGRY	SAD	DISGUSTED
	X				

Please start now!

	NEUTRAL	HAPPY	FEARFUL	ANGRY	SAD	DISGUSTED
1						
2						
3						
…						

30 pictures were presented in total, with a short break after the 10th and 20th

pictures.

Appendix E: Tables of activated regions showing BOLD changes

Regions active during neutral stimuli (80mg nadolol)

Peak T Statistic	Cluster Size	MNI Co-ordinates
11.66	984	[-32 -94 8]
11.58	1163	[32 -84 14]
9.69	87	[-22 -36 -4]
9.01	89	[-48 40 16]
7.09	116	[50 28 18]
6.81	67	[22 -34 -4]

Regions active during pleasant stimuli (80mg nadolol)

Peak T Statistic	Cluster Size	MNI Co-ordinates
10.68	1188	[-12 -96 18]
10.14	1400	[44 -82 8]
7.53	36	[-48 22 -2]
6.79	45	[-58 22 12]
6.49	29	[-24 -38 8]

Regions active during unpleasant stimuli (80mg nadolol)

Peak T Statistic	Cluster Size	MNI Co-ordinates
10.47	1631	[42 -80 10]
10.18	1205	[-28 -86 20]
8.65	169	[-22 -36 6]
7.55	96	[22 -36 -4]
6.16	36	[-50 32 10]

Regions active during pleasant > neutral stimuli (80mg nadolol)

Peak T Statistic	Cluster Size	MNI Co-ordinates
10.27	115	[48 -70 10]

Regions active during unpleasant > neutral stimuli (80mg nadolol)

Peak T Statistic	Cluster Size	MNI Co-ordinates
10.29	178	[48 -68 10]
8.17	52	[-52 -68 16]
8.03	27	[-44 -62 22]
7.97	33	[-42 -76 12]

Regions active during neutral stimuli (placebo)

Peak T Statistic	Cluster Size	MNI Co-ordinates
15.30	1370	[-32 -96 10]
11.98	1382	[32 -84 18]
7.64	78	[52 30 14]

Regions active during pleasant stimuli (placebo)

Peak T Statistic	Cluster Size	MNI Co-ordinates
15.20	3407	[-10 -102 14]
10.32	607	[50 30 20]
9.11	120	[24 -30 -4]
7.98	104	[-20 -32 -2]
7.96	110	[-52 30 20]

Regions active during unpleasant stimuli (placebo)

Peak T Statistic	Cluster Size	MNI Co-ordinates
14.78	3814	[-14 -96 8]
11.75	311	[48 30 18]
11.53	104	[-22 -34 -4]
10.08	115	[26 -36 -4]
8.21	97	[50 12 24]
7.40	32	[38 26 -12]

Regions active during pleasant > neutral stimuli (placebo)

Peak T Statistic	Cluster Size	MNI Co-ordinates
9.35	105	[50 -62 4]

Regions active during unpleasant > neutral stimuli (placebo)

Peak T Statistic	Cluster Size	MNI Co-ordinates
8.67	22	[50 -64 6]